The Dissertation Committee for Tingwei Ko Certifies that this is the approved version of the following dissertation:

DEPOSITIONAL, MINERALOGICAL, AND MATURITY CONTROLS ON PORE TYPES, POROSITY, AND PORE-SIZE DISTRIBUTION IN MUDROCKS

Committee:

Robert G. Loucks, Supervisor

Stephen C. Ruppel, Co-Supervisor

William L. Fisher

Peter B. Flemings

Michael D. Lewan

Timothy M. Shanahan

DEPOSITIONAL, MINERALOGICAL, AND MATURITY CONTROLS ON PORE TYPES, POROSITY, AND PORE-SIZE DISTRIBUTION IN MUDROCKS

by

Tingwei Ko, B.S.; M.S.; M.S.

Dissertation

Presented to the Faculty of the Graduate School of

The University of Texas at Austin

in Partial Fulfillment

of the Requirements

for the Degree of

Doctor of Philosophy

The University of Texas at Austin

May 2017

Dedication

To my parents, grandparents, family, friends, and my mentor Dr. Wuu-Liang Huang

Acknowledgements

I would like to express my highest gratitude to my supervisors Dr. Bob Loucks and Dr. Steve Ruppel who patiently guided and helped me become a good researcher. I thank Steve for believing in me the first time when I proposed him the idea of integrating geology and geochemistry and giving me opportunity and funding to work with Bob and him. I would not have gotten here without their encouragement, inspiration, support, and sometimes push over the past five years.

I have benefited from a dissertation committee with their broad expertise in the field of geosciences. Dr. Bill Fisher provided guidance and knowledge in classes that I have taken from him; Dr. Peter Flemings taught me how to do good science and shared his enthusiasm and knowledge on mudstones; Dr. Mike Lewan for his willingness to serve in the committee in the past two years and sharing his knowledge in geochemistry; Dr. Tim Shanahan gave very helpful advice and provided his guidance and encouragement along the way.

Collaborators Deyong Shao (from China) and Paul Hackley (from U.S. Geological Survey) have performed the pyrolysis experiments and organic petrographic analyses on some of my samples. I have learned a lot from Paul's expertise in organic petrology and microscopy.

I thank colleagues of the Mudrock Systems Research Laboratory (MSRL) Group: Kitty Milliken, Tongwei Zhang, Farzam Javadpour, Harry Rowe, Greg Frebourg, Rob Reed, Robert Baumgardner, Sheng Peng, Patrick Smith, and Xun Sun. I have taken Kitty's petrography class and her numerous workshops and discussion groups. It is my privilege and honor to be able to learn a little from her wealth of knowledge. Kitty has also provided support and guidance along the way, just as other committee members. I

have worked closely with Tongwei Zhang whose continued help, enthusiasm, and encouragement are precious. Dr. Harry Rowe generously contributes his time and provided his knowledge on inorganic geochemical analyses and interpretation. Evan Sivil has devoted lots of his time and helped me with the XRF analysis. Employees at the Core Repository Center, including Brandon Williams, Nathan Ivicic and James Donnelly, also deserve my gratitude for handling heavy core boxes with impressive efficiency and friendliness. I appreciate the best graduate coordinator Philip Guerrero and BEG administrative staff Melissa Garcia and Sammy Jacobo for their friendliness and help.

Financial support was provided by Jackson School of Geosciences Merit Scholarship, ConocoPhillips Fellowship, STARR program, and the members of the Mudrock System Research Laboratory (MSRL) Consortium at the Bureau of Economic Geology (BEG), Jackson School of Geosciences. The corporate sponsors include Anadarko, Apache, Aramco Services, BHP Billiton, BP, Cenovus, Centrica, Chesapeake, Cima, Cimarex, Chevron, Concho, ConocoPhillips, Cypress, Devon, Encana, ENI, EOG, EXCO, ExxonMobil, FEI, Geosun, Haimo, Hess, Husky, IMP, Kerogen, Marathon, Murphy, Newfield, Penn West, Penn Virginia, QEP, Repsol, Pioneer, Samson, Shell, Sinopec, Statoil, Talisman, Texas American Resources, The Unconventionals, University Lands, US EnerCorp, Valence, and YPF.

Finally, I would like to extend thanks to my family (particularly my mom) and my friends, both in Taiwan and the United States for their love and support throughout my Ph.D. journey. They believed in me and supported me, cheering me up when I felt defeated and frustrated, sharing my happiness when I made little steps of scientific progress. I thank my fellow UT graduate students: Joel Lundsford, Max Pommer, Susan Ergene, Katy Fry, Lauren Redmond, Michael Nieto, Justin Mauck. Chris Hendrix, Yawen He, and Jinyu Zhang for their kindly support and intellectual discussions.

Abstract

Depositional, Mineralogical, and Maturity Controls on Pore Types, Porosity, and Pore-Size Distribution in Mudrocks

Tingwei Ko, Ph.D.

The University of Texas at Austin, 2017

Supervisor: Robert G. Loucks

Co-Supervisor: Stephen C. Ruppel

Mudrocks act as seals and aquiclude for conventional petroleum systems and sources, seals, and reservoirs for unconventional petroleum resources. They are also candidates for nuclear-waste disposal and carbon capture and storage sites. This investigation improves our understanding of the interplay of depositional, diagenetic, and hydrocarbon generation processes in the origin and evolution of OM-rich mudrock pores by providing (1) a process-based understanding of the origin and control on the formation of different pore types, (2) quantitative methods to characterize pore systems in mudrock reservoirs, and by establishing (3) a link between sediments and depositional processes to pore system variations.

Pore evolution models of mature mudrocks and a classification scheme of OM pores were developed during this research. Four main categories of OM pores comprise the OM-pore network: primary OM pore, convoluted OM pores, OM bubble pore, and OM spongy pore, with the latter two related to thermal maturation processes. The original interparticle and intraparticle mineral pores, which are a function of depositional and early diagenetic processes, determine the mineral pore network before petroleum

generation, expulsion, and migration begin. The mineral pore network constrained petroleum migration and OM redistribution, controlling the modified-mineral-pore and OM-pore network during thermal maturation of OM. After OM maturation, the pore evolution is closely related to OM conversion. The morphology of mineral and OM pores varies with stages of OM maturation. Predominant pore types changed from primary mineral pores, to modified mineral pores containing relic OM, to coexisting modified mineral pores, OM bubble pores, and OM spongy pores, and finally to OM spongy pores.

Pore sizes in OM-rich mudrocks range across at least five orders of magnitude (from 1 nm to approximately 100 μm). In general, OM pores are smaller than mineral pores. OM pores are related to kerogen and maceral types and subsequent thermal maturation processes. Mudrocks with well-sorted and coarse grains contain more abundant mineral pores than those with poorly-sorted and finer grains. Primary mineralogy, texture, and fabric determine diagenesis such as compaction and cementation and could indirectly affect sizes of OM pores up to two orders of magnitude differences.

Table of Contents

List of Tables

List of Figures

Chapter 1: Introduction

BACKGROUND

Mudrocks are fine-grained sedimentary rocks, composed of more than 50% of silt (4 to 62.5 μm) and clay (less than 4 μm)-sized particles (Folk, 1954). Mudrocks comprise about two third of all sedimentary rocks in the Earth's crust. They are seals and barriers for conventional petroleum systems, nuclear-waste disposal, and global geological sequestration (carbon capture and storage), and they are sources, seals, and reservoirs for unconventional petroleum resources. Mudrocks are distinctive in terms of their multiscale heterogeneous character, nano- to micron-scale pore systems, high compressibility (related to the presence of relatively abundant clay minerals and organic matter), and extremely low permeability. The complex variations in the composition, grain assemblages, texture, and fabric of mudrocks are caused by a spectrum of transport and depositional processes (e.g., gravity flows, hemipelagic and pelagic settling, and bottom current reworking) as well as diagenetic history (e.g., compaction, cementation, dissolution, and replacement).

In organic matter- (OM) -rich mudrocks, in addition to mineral diagenesis, the decomposition of kerogen, which begins at approximately 80°C (some initial bitumen can form at temperatures as low as 60°C), also affects rock and fluid properties. Generated and expelled fluids add complexity to the system and make it difficult to predict properties such as porosity, permeability, wettability, and rock strength.

Mudrock porosity declines from 80–90% at the beginning of the burial to 5–10% at depths of 5 km (e.g., Dewhurst et al., 1998; Mondol et al., 2007). Depositional processes determine the original mineral-hosted porosity of mudrocks. Following deposition, porosity decline is predominantly driven by compaction (mechanical

diagenesis). The relative importance of early cementation, involving the formation of authigenic kaolinite, calcite, and calcite concretions, versus compaction on porosity reduction is unclear although compaction appears more important in mudrocks than in sandstones and carbonates (Milliken and Day-Stirrat, 2013). At shallow burial and low temperature, mudrocks compact mainly mechanically, and porosity is reduced as a result of grain rearrangement (grain slippage, rotation) and ductile deformation. The mechanical compaction of mudrocks is a complicated process and compressibility is not only a function of effective stress but also dependent on types of clay minerals present (kaolinite, chlorite, smectite, and illite), the amount of clay minerals, other particles (quartz, mica, calcite, pyrite etc.), pore fluids (oil, gas, water), and pore pressure (hydrostatic or overpressure) (Mondol et al., 2007). At greater depths and temperature (above 65–70°C), chemical diagenesis such as smectite transformation to illite (I/S) (starts at around 65°C), kaolinite to illite (starts at around 120°C), albitization of plagioclase (takes place at 60–100°), albitization of K-feldspar (at 120–150°C), and replacement of calcite cement by ankerite (at about 120°C) dominate (Land and Milliken, 1981; Milliken, 1992; Bjørlykke, 1998; Nadeau et al., 2002; Goulty et al., 2016). Chemical diagenetic processes, including dissolution, replacement, and cementation, also play important roles in causing changes in porosity. In mature OM-rich mudrocks, petroleum generation is another source of porosity generated caused by the transformation from solid kerogen to petroleum (e.g., Jarvie et al., 2007; Loucks et al., 2009).

Characterizing pore types (and their origins), pore structure, and porosity is of critical importance to establish original fluid in place and flow characteristics of the matrix. Total porosity in mudrocks can be measured by helium pycnometry, mercury (mercury injection capillary pressure, MICP) porosimetry, methane, nitrogen and carbon

dioxide adsorption, small angle neutron scattering (SANS) measurements, nuclear magnetic resonance (NMR), scanning electron microscopy (SEM), and transmission electron microscopy (TEM) (Bustin et al., 2008). Helium has greater access to the fine pore structures than larger molecules such as methane and nitrogen. Utilizing gases other than He to measure porosity requires corrections for sorption (Bustin et al., 2008). MICP, gas adsorption, SANS, and NMR analyses all rely on models to infer pore structures, whereas SEM and TEM provides direct evidence. Determining porosity association with organic and mineral components of mudrocks is important but rather difficult without directly observing them.

Scanning electron microscopy (SEM) and/or helium ion microscopy (HIM) on argon (Ar)-ion or broad ion beam (BIB) milled samples provides a means to quantify proportion and distribution of each pore type and controls on pore development and size distribution (Desbois et al., 2009; Loucks et al., 2009; Loucks et al., 2012; Klaver et al., 2012; Houben et al., 2013; Houben et al., 2014). FIB-SEM combines focused ion beam (FIB) milling with SEM and can be used to create a 3D display of a small rock volume by slicing and stacking series of 2D images (Curtis et al., 2012). However, this imaging technique covers too small a portion of the investigated rock volume and is difficult to achieve representation (Kelly et al., 2015). In order to obtain a complete representation of mudrock pores, SEM imaging analysis was used as the main diagnostic tool for pore types, pore-size distribution, and pore volume in this study.

DISSERTATION SCOPE AND RELEVANCE

An important research goal in understanding mudrocks is the characterization and prediction of the type, amount, and distribution of pores and the processes that control their formation, evolution and heterogeneity. A central assumption to this broad research

question is that the distribution of grains and pores within the same stratigraphic interval is dominantly controlled by depositional processes, compaction, and thermal stress. Addressing this wide-ranging topic required subdivision of the research effort into four components that are presented in Chapters 2–5. Each of the main chapters is a stand-alone manuscript for submission to external journals for publication. Several of the manuscripts are in press or have been published.

I integrated different approaches by examining (1) immature marine sapropel samples using the FE-SEM, (2) three suites of laboratory-pyrolyzed mudrock samples to understand how OM pores are developed and evolved as a function of thermal maturation and OM maceral types, (3) variations in pore types, porosity, and pore-size distribution in a suite of organic-rich lacustrine samples in a fluvial-deltaic-lacustrine environment, (4) variations in pore types and porosity in facies along depositional dip, and (5) effects of rock properties such as mineralogy, TOC, texture, and fabric on pore type, size, and distribution in mudrock samples of similar thermal maturity.

In carrying out this research, I developed a model of pore evolution based on thermal maturation and OM maceral types, identified key controls on the development of mineral-hosted pores and OM-hosted pores, and improved understanding of the interplay of depositional, diagenetic, and hydrocarbon generation processes in the origin and evolution of OM-rich mudrock pores.

Summary of Research

In Chapter 2: Pore and Pore Network Evolution of Upper Cretaceous Boquillas (Eagle Ford-equivalent) Mudrocks: Results from Gold Tube Pyrolysis Experiments, I integrated results from laboratory gold-tube pyrolysis, geochemical characterization of generated gas and oil, and Ar-ion milled SEM petrography to develop a descriptive model of how pores evolved in the Upper Cretaceous Boquillas/Eagle Ford.

The major contributions of this research are (1) first successful laboratory simulation of pore development, (2) the identification of important differences among the primary mineral pores, modified mineral pores (mineral pores with migrated pre-oil solid bitumen), and OM pores. I also demonstrated the importance of using detailed geochemical characterization for determining petroleum generation stages. Finally, I provided evidence that pores are mostly associated with relatively coarse calcite grains and crystals in the fecal pellets and mud-sized carbonate aggregates and demonstrated the grain-size control on pore-size distribution and associated fluid migration.

In Chapter 3: Origin and Characterization of Eagle Ford Pore Networks in the South Texas Upper Cretaceous Shelf, I utilized my pore evolution model and pore classification scheme developed in Chapter 2 research to characterize pores in Upper Cretaceous Eagle Ford argillaceous calcareous mudrocks of late oil window maturity. Two quantitative methods were used to quantify the pore volume of each pore type and to derive pore-size distribution: point-count and pore-trace of SEM images. Quantitative results were also compared with nitrogen adsorption analyses and GRI crushed rock helium porosimetry measurements.

Results showed that mineral pore networks dominate the Eagle Ford and appear to contribute most to matrix permeability. More importantly, this research demonstrated (1) that the abundance of OM-hosted spongy pores correlate positively with total-organic-carbon (TOC) content and (2) that mineral pore abundances correlates, albeit weakly, with quartz and feldspar abundance, suggesting that the mineral framework inhibited compaction. In the first study of this kind, I also compared pore measurements from SEM imaging with nitrogen adsorption and showed that results are comparable except some inconsistency is shown for pores in the 30 to 70-nm size range. In the studied upper Eagle Ford marl samples, I observed a systematic change in grain size (less silt-sized grains in

the deeper sample) and pore size [higher percentage of small pores (diameter < 500 nm) in the deeper sample], which could reflect an increase in the supply of silt-sized sediment, an increase in hydrodynamic energy towards shallow interval, or both. Without complication of different thermal maturities, strong micron-scale heterogeneity of rock components and properties (texture, fabric, mineralogy, and TOC abundance) impacts pore types, abundance, and distribution.

Chapter 4: "Pore-Types and Pore Network Evolution in Upper Devonian-Lower Mississippian Woodford and Mississippian Barnett Mudstones: Insights from Integrated Organic Petrography, SEM Petrography, and Laboratory Thermal Maturation" describes research into the question of whether or not differences in mineralogy (siliceous vs. calcareous) exert different catalytic and sorption effects on petroleum generation, pore origin and evolution. This research also investigated the effect of different maceral types on OM pore evolution by integrating and comparing results from organic petrography and SEM petrography on laboratory pyrolyzed Upper Devonian-Lower Mississippian Woodford and Mississippian Barnett mudrock samples.

Results of this research show that OM maceral types, identified using both SEM (platy OM, particulate OM, organic-mineral admixtures, *Tasmanites*) and organic petrology (telalginite, vitrinite, inertinite, amorphous organic matter (AOM), *Leiosphaeridia*, and *Tasmanites*), affect the evolution of OM pores related to differences in generation kinetics and activation energy distribution between *Tasmanites* and AOM and other types of macerals. No catalytic effect of mineralogy on petroleum generation and pore evolution. The relative abundances and types of clay mineral (especially interlayered I/S and smectite) also did not show any signs of significant catalytic or sorption alteration on generated petroleum and affect pore development and evolution.

Chapter 5: "Controls on Pore Types and Pore-Size Distribution in the Upper Triassic Yanchang Formation, Ordos Basin, China: Implications for Pore-Evolution Models of Lacustrine Mudrocks" details research carried out to define the controls on the development of different pore types and sizes in Upper Triassic Yanchang Formation OM-rich argillaceous lacustrine mudrocks. One of the goals of this study was to determine if pore-evolution models developed from marine mudrocks (in Chapters 2 and 4) can be directly applied to lacustrine mudrocks.

A major finding of this research is that sorting and the relative abundance of coarse silt grains affect the preservation and abundance of mineral-hosted pores and mineral-hosted pore-size distribution (PSD) in OM-rich lacustrine mudrocks. Variations in the types of kerogen from proximal (Type II+III) to distal areas (Type I+II) of the lacustrine basin affect the development of OM-hosted pores. No OM pores were developed in early-mature mudrocks with predominantly Type I kerogen because it takes high level of thermal stress to convert Type I kerogen to petroleum. Pore-evolution models developed from marine mudrocks based on thermal maturation process can be applied in lacustrine mudrocks but cautions should to be taken because primary mineralogy and types of kerogen are different in these two depositional settings. Studied marine mudrocks have larger and more abundant mineral and OM pores than studied lacustrine mudrocks, which may be caused by a lack of early cementation during compaction in lacustrine mudrocks, resulting in less lithification and extensive compaction. It is likely that compaction results in sizes of OM pores smaller than those in marine mudrocks because pore sizes are related to the equilibrium pressure outside (overburden pressure of sediments above) and inside (pore-fluid pressure of generated liquid and gas) the pore walls. The sizes of OM pores in these compaction-dominated

lacustrine mudrocks are one to two orders of magnitude smaller than those in marine mudrocks (e.g., in the Eagle Ford) that contain early cements.

Key Contributions to the Science of Organic-Inorganic Interactions in Mudrocks

One of the key contributions of my research was the laboratory study of gold-tube pyrolysis using immature mudrock samples to induce and observe changes of organic matter and pores at different levels of thermal maturity. Laboratory simulation of in situ petroleum formation from isolated kerogen has been used by geochemists since the 1960s to quantify petroleum generation at different temperature and pressure conditions, to understand the kinetics of petroleum generation, and to build mathematical models (e.g., Tissot, 1969; Tissot and Espitalié, 1975; Monthioux et al., 1985). In order to observe pore development in the context of mineral matrix, I implemented the experimental design and successfully created OM pores in a laboratory setting.

This research also led to the development of pore evolution models and a classification scheme of OM pores based on results of laboratory pyrolysis. The original interparticle and intraparticle pores, which are a function of depositional and early diagenetic processes, determined the mineral pore network before petroleum generation and migration begins. The mineral pore network preset and constrained petroleum migration and OM redistribution, controlling the modified-mineral-pore and OM-pore network after thermal maturation of OM. When OM became mature, the pore evolution was closely related to OM conversion. The morphology of mineral and OM pores varied with the stages of OM maturation. From immature to the cracking of early oil to wet gas maturation stage, predominant pore types changed from primary mineral pores, to modified mineral pores with relic OM, to coexisting modified mineral pores, OM bubble pores, and OM spongy pores, and finally to OM spongy pores. The modified mineral

pore with relic OM is commonly misidentified as OM pore because they are in contact with OM. However, they are supported by the surrounding mineral framework and should not be identified as OM pores.

A third key research contribution is the establishment of a link between sediments and depositional processes to pore systems (Figure 1.1). Mineral-hosted pores are a function of sediment sources, depositional and diagenetic (compaction, cementation, dissolution, and replacement) processes. Primary mineralogy, grain assemblage, and texture determine mineral frameworks and subsequent diagenetic processes such as compaction and cementation. A mudrock with well-sorted grains and coarser grains would have higher mineral porosity. OM pores are a function of types of kerogen and macerals, and thermal maturation. In immature mudrocks, the total pore network is dominated by mineral pores. Pore connectivity depends on effective (conncected) pore networks, which are likely composed of interparticle mineral pores. When mudrocks reach oil window maturation, generated petroleum is expelled, then migrates, and pervades the mineral pore network. According to my pore network model, total porosity and mineral composition do not necessarily correlate, nor does total porosity, TOC or thermal maturity. OM porosity should be correlated with measured present-day TOC (TOC_m) when mudrocks have similar types of kerogen and macerals. The correlation between mineral porosity and mineralogy is shown to be much stronger than the correlation between total porosity and mineralogy.

Essential features of pore spaces such as pore shape and connectivity can help improve pore network models. Pore geometry derived from manually-traced pores in the SEM images helps engineers obtain real shape factors (ratio of cross-sectional area to perimeter area squared) as one of the key inputs for pore-network modeling simulation to understand the effective liquid permeability in a mudrock system (e.g., Afsharpoor and

Javadpour, 2016). Most pore network models assume spatially uncorrelated pore sizes (Blunt, 2001). Our result helps recognize geological controls on the possible distribution and connectivity of mineral- and OM-hosted pores in several mudrock systems, providing the spatial correlation of pore types and pore-size distribution. This will promote understanding of relative permeability and multiphase connectivity for a given saturation in a mudrock reservoir.

OPPORTUNITIES FOR FUTURE RESEARCH

The experimental analyses I conducted for this research contribute to the qualitative understanding of pore evolution and thermal maturation. However, the design of laboratory pyrolysis experiments can be improved by adding water in gold tubes because hydrous conditions simulate subsurface condition more realistically than anhydrous conditions (Lewan, 1997). In addition, porosity evolution can be improved by better quantifying the results at each experimental step for mass balance calculation.

My research also found that higher SEM resolution can be obtained, and smaller pores can be observed using uncoated samples. By comparing results of my SEM pore studies with other methods of determining mudrock porosity, I concluded that it is best to utilize at least two to three methodologies to derive a quantitative measure. Porosity measurement among different approaches is seldom compared. A potential research direction is to compare all available methods on the same suite of mudrock samples as done by Loucks et al. (2017).

I made the effort bridging the gap between optical and electron microscopy by examining and describing morphology and characteristics of macerals in this study. Clearly more comparative optical and SEM research needs to be done to close the gap.

Examining recent seafloor sediments and thermally immature mudrocks is one of the important research subjects. When and how mud lithification proceeds and occurs remained unclear. Combining petrophysical data such as bulk density and sonic velocity with petrographic characterization of grain assemblages in sediments can help gain such insight. Also, the relationship between compaction and early cementation in mudrocks needs to be established in immature mudrocks.

Some questions still remain unanswered or not fully answered. A major challenge remaining is to determine the amount of detail regarding of the pore type, size, and configuration necessary to make accurate prediction of macroscopic properties that can be obtained by wireline logs or seismic. A representative elemental area (REA) of SEM images, defined as a smallest sample area over which a measurable attribute of a media renders a value representative of the bulk media itself, that can be used to construct two- or three-dimensional (2D or 3D) simulations is still unknown.

Subjects such as (1) investigating impact of diagenesis on mudrock reservoir properties and mechanical properties, (2) investigating changes in mechanical properties of OM with increasing thermal maturity, and (3) investigating compositional controls on variations of mechanical compaction all deserved more study and research effort.

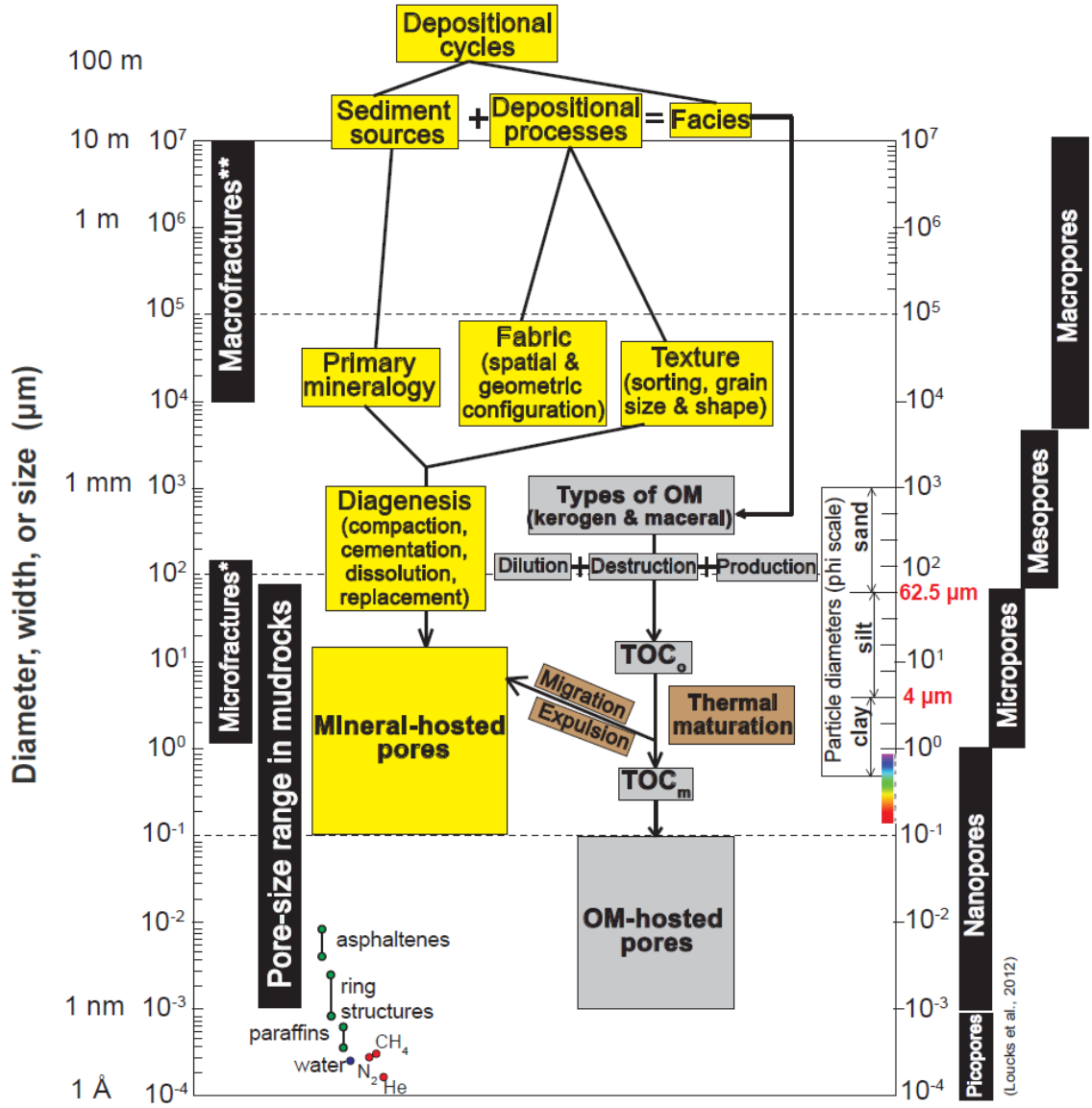

Figure 1.1: Conceptual models of the interrelationships of facies, microstructure, organic matter, and total pore network in mature OM-rich mudrocks on a logarithmic scale covering eleven orders of magnitude. Sizes of pores in a mature OM-rich mudrock range across at least 5 orders of magnitude. Microfracture* is used by structure geologists, refers to a fracture that requires microscopy to detect (length scale of a few millimeters or less), a few tens of microns wide (usually less than 0.1 mm). Microfracture** is used by geophysicists and engineers, refers to large fractures (length scale of centimeter to decimeter). TOC_o: initial TOC; TOC_m: present-day TOC.

REFERENCES

Afsharpoor A. and F. Javadpour, 2016, Liquid slip flow in a network of shale noncircular nanopores, Fuel, v. 180, p. 580–590.

Blunt, M. J., 2001, Flow in porous media — pore-network models and multiphase flow, Current Opinion in Colloid & Interface Science, v. 6, p. 197–207.

Bjørlykke, K., 1998, Clay mineral diagenesis in sedimentary basins e a key to the prediction of rock properties: examples from the North Sea Basin, Clay Minerals, v. 33, p. 15–34.

Bustin, R. M., A. M. M. Bustin, X. Cui, D. J. K. Ross, and V. S. Murthy Pathi, 2008, Impact of shale properties on pore structure and storage characteristics, 2008 SPE Shale Gas Production Conference, Fort Worth, Texas, U.S.A., 16–18 November, SPE 119892

Curtis, M. E., C. H. Sondergeld, R. J. Ambrose, and C. S. Rai, 2012, Microstructural investigation of gas shales in two and three dimensions using nanometer-scale resolution imaging: AAPG Bulletin, v. 96, p. 665–677.

Dale, A., C. M. John, P. S. Mozley, P. C. Smalley, and A. H. Muggeridge, 2014, Time-capsule concretions: Unlocking burial diagenetic processes in the Mancos Shale using carbonate clumped isotopes: Earth and Planetary Science Letters, v. 394, p. 30–37.

Desbois, G., J. L. Urai, and P. A. Kukla, 2009, Morphology of the pore space in claystones- Evidence from BIB/FIB ion beam sectioning and cryo-SEM observations: Earth, v. 4, p. 15–22.

Dewhurst, D. N., S. C. Aplin, J.-P. Sarda, and Y. Yang, 1998, Compaction-driven evolution of porosity and permeability in natural mudstones: an experimental study: Journal of Geophysical Research, v. 103, p. 651–661.

Folk, R. L., 1954, The distinction between grain size and mineral composition in sedimentary-rock nomenclature, The Journal of Geology, v. 62, p. 344–359.

Goulty, N. R., C. Sargent, P. Andras, and A. C. Aplin, 2016, Compaction of diagenetically altered mudstones – Part 1: Mechanical and chemical contributions, Marine and Petroleum Geology, v.77, p. 703–713.

Houben, M. E., G. Desbois, and J. L. Urai, 2013, Pore morphology and distribution in the shaly facies of Opalinus Clay (Mont Terri, Switzerland): insights from representative 2D BIB-SEM investigations on mm to nm scale, Applied Clay Science, v. 71, p. 82–97.

Houben, M. E., G. Desbois, and J. L. Urai, 2014, A comparative study of representative 2D microstructures in shaly and sandy facies of Opalinus Clay (Mont Terri, Switzerland) inferred from BIB-SEM and MIP methods, Marine and Petroleum Geology, v. 49, p. 143–161.

Jarvie, D. M., R. J. Hill, T. E. Ruble, and R. M. Pollastro, 2007, Unconventional shale-gas systems: The Mississippian Barnett Shale of north-central Texas as one model for thermogenic shale-gas assessment, AAPG Bulletin, v. 94, p. 475–499.

Kelly, S., H. El-Sobky, C. Torres-Verdin, and M. T. Balhoff, Assessing the utility of FIB-SEM images for shale digital rock physics, Advances in Water Resources, v. 95, p. 302–316.

Klaver J., G. Desbois, J. L. Urai, and R. Littke, 2012, BIB-SEM study of the pores pace morphology in early mature Posidonia Shale from the Hils area, Germany, International Journal of Coal Geology, v. 103, p. 12–25, doi: 10.1016/j.coal.2012.06.012.

Land, L. S., and K. L. Milliken, 1981, Feldspar diagenesis in the Frio formation, Brazoria County, Texas Gulf Coast, Geology, v. 9, p. 314–318.

Lewan, M. D., 1997, Experiments on the role of water in petroleum formation, Geochimica et Cosmochimica Acta, v. 61, p. 3691–3723.

Loucks, R. G., R. M. Reed, S. C. Ruppel, and D. M. Jarvie, 2009, Morphology, genesis, and distribution of nanometer-scale pores in siliceous mudstones of the Mississippian Barnett Shale: Journal of Sedimentary Research, v. 79, p. 848–861.

Loucks, R. G., R. M. Reed, S. C. Ruppel, and U. Hammes, 2012, Spectrum of pore types and networks in mudrocks and a descriptive classification for matrix-related mudrock pores: AAPG Bulletin, v. 96, p. 1071–1098.

Loucks, R. G., S. C. Ruppel, X. Wang, L. T. Ko, S. Peng, T. Zhang, H. D. Rowe, and P. Smith, 2017, Pore types, pore-network analysis, and pore quantification of the lacustrine shale-hydrocarbon system in the Late Triassic Yanchang Formation in the southeastern Ordos Basin, China, Interpretation, v. 5, p SF63–SF79.

Milliken, K. L., 1992, Chemical behavior of detrital feldspars in mudrocks versus sandstones, Frio Formation (Oligocene), South Texas, Journal of Sedimentary Research, v. 62, p. 790–801.

Milliken, K. L., and R. J. Day-Stirrat, 2013, Cementation in mudrocks: Brief review with examples from cratonic basin mudrocks, *in* J.-Y. Chatellier and D. M. Jarvie, eds., Critical Assessment of Shale Resource Plays: AAPG Memoir 103, p. 133–150.

Milliken, K. L., S. M. Ergene, and A. Ozkan, 2016, Quartz types, authigenic and detrital, in the Upper Cretaceous Eagle Ford Formation, south Texas, USA, Sedimentary Geology, v. 339, p. 273–288.

Mondol, N. H., K. Bjørlykke, J. Jahren, and K. Høeg, 2007, Experimental mechanical compaction of clay mineral aggregates – Changes in physical properties of mudstones during burial, Marine and Petroleum Geology, v. 24, p. 289–311.

Monthioux, M., P. Landais, and J.-C. Monin, Comparison between natural and artificial maturation series of humic coals from the Mahakam delta, Indonesia, Organic Geochemistry, v. 1985, p. 275–292.

Nadeau, P.H., Peacor, D.R., Yan, J., Hillier, S., 2002, I-S precipitation in pore space as the cause of geopressuring in Mesozoic mudstones, Egersund Basin, Norwegian continental shelf, American Mineralogist, v. 87, p. 1580–1589.

Tissot, B. P., 1969, Premières données sur les mécanismes et la cinétique de la formation du pétrole dans les sédiments. Simulation d'un schéma réactionnel sur ordinateur, Revue de l'Institut Français du Pétrole, v. 24, p. 470-501.

Tissot, B. P., and J. Espitalié, 1975, L'évolution thermique de la matière organique des sédiments: application d'une simulation mathématiqueRev, Revue de l'Institut Français du Pétrole, v. 30, p. 743-777.

Chapter 2: Pore and Pore Network Evolution of Upper Cretaceous Boquillas (Eagle Ford-Equivalent) Mudrocks: Results from Gold-Tube Pyrolysis[1]

ABSTRACT

Low-maturity Boquillas Formation (Eagle Ford Formation equivalent) organic-lean calcareous mudrock samples collected from outcrop were heated in gold tubes under confining pressure to investigate the evolution of organic-matter (OM) pores and mineral pores. The majority of OM in the Boquillas samples was migrated petroleum (bitumen) based on evidence from geochemical analyses, solvent extraction, and scanning electron microscopy (SEM) petrography. SEM images showed several diagenetic events—including framboidal pyrite precipitation and euhedral calcite, quartz, kaolinite, and chlorite cementation—that were all interpreted to have occurred prior to petroleum expulsion and pore-scale to bed-scale petroleum (bitumen) migration. Two major pore types were present prior to heating: primary mineral pores and modified mineral pores with migrated relic OM. From heating experiments, pores were found to be associated with stages of OM maturation. During the bitumen generation stage, modified mineral pores were dominant and primary interparticle and intraparticle pores present. During the oil generation stage, modified mineral pores with isopachous OM rim were observed to be the most abundant pore type. During the gas generation stage, both modified mineral pores and nanometer-sized spongy OM pores were predominant. We interpreted the occurrence of modified mineral pores to be the result of (1) Oil and gas filled or partially filled voids that developed during petroleum migration and water expulsion, (2) voids after removing of oil, gas, and water during sample preparation, and (3) trapping of gas

[1]The full content of this chapter is published in *AAPG Bulletin* in 2016.

and/or water molecules. The formation of these nanopores was interpreted to be related to gas generation and structural rearrangement of OM.

2.1 INTRODUCTION

Research on imaging pores in mudrocks (and shales) has defined nanometer- to micrometer-sized pores associated with organic and inorganic (mineral) components (Loucks et al., 2009). Loucks et al. (2009) suggested that thermal maturation of organic matter (OM) with burial is the controlling factor that promotes the development of OM pores. Levels of thermal maturation define different stages of organic matter transformation (Hunt, 1996) and can significantly affect characteristics of organic matter (Tissot and Welte, 1984), thus affecting the original pore network. With increasing thermal stress, immature kerogen starts to crack and transform into first bitumen and then oil and gas, with byproducts such as solid bitumen, pyrobitumen, and char (Tissot and Welte, 1984; Lewan, 1993; Hunt, 1996; Bohacs et al., 2013; Loucks and Reed, 2014). This gradual transformation of organic matter creates multiple co-existing phases (solid, liquid, and gas) in the mudrock and results in significant volume expansion and pressure generation (Tissot and Welte, 1984). Carbon dioxide and organic acids are also released, which may result in intensive fluid-rock interactions in the host mudrock (e.g., Bernard et al., 2013). Organic matter connectivity also changes with increasing thermal stress (Lewan, 1987). Immature organic matter is present in the form of randomly distributed kerogen particles with ‘well-defined boundaries or of discrete, elongated, lamellar masses with or without well-defined boundaries” (Cook and Sherwood, 1991; Loucks et al., 2009; p, 10 in Fishman et al., 2012). The connectivity of immature organic matter is predominantly controlled by its abundance (total organic carbon [TOC]). However, during two key transformation stages—kerogen to bitumen, and then bitumen to oil—

considerable amounts of petroleum fluids are generated and migrated (e.g. Dahl et al., 1989; Selby et al., 2005). Once petroleum migrates into adjacent mineral pores in the mudrock, organic matter connectivity may be significantly increased (Loucks and Reed, 2014). We hypothesized that during organic matter maturation, migrated petroleum and secondary products such as solid bitumen, pyrobitumen, and char may decrease the volume of mineral pores; however, the thermal maturation process will create OM pores in the mudrock system and may change the shape of existing primary OM pores.

To test this hypothesis, laboratory anhydrous gold-tube pyrolysis experiments were conducted on low-maturity (calculated vitrinite reflectance [VR] = 0.6 to 0.7 $\%R_o$) Boquillas Formation (Eagle Ford Formation equivalent) samples under confining pressure (10,000 psi or 68.95 MPa) to induce and observe changes of pore sizes and shapes at different levels of thermal maturity (Hackley et al., 2015). Investigating the relationship between pore evolution and thermal transformation of organic matter in mudrocks will add to the basic understanding of pore networks in unconventional reservoirs.

The main objectives of this research are to observe the evolution of pore types and pore networks in mudrocks and to qualitatively describe and characterize the evolution of pore shape and size distribution at increasing levels of thermal maturity, and to understand the impact of thermal maturity on mudrock-reservoir quality. Laboratory simulation provides a relatively precise, controlled environment for defining petroleum generation related to a single variable (thermal maturity) and can reduce the complexity in outcrop or core samples that display great heterogeneity in bulk mineralogy, TOC content, and lithofacies. Establishing the relationship between thermal maturity and pore evolution provides a basis for developing techniques to predict pore types, abundance, and distribution and model fluid flow in mudrocks.

2.2 REVIEW OF RESEARCH ON OM PORE DEVELOPMENT AND EVOLUTION

Several studies have increased our understanding of storage spaces and potential migration pathways for petroleums in mudrocks (Reed and Loucks, 2007; Ruppel and Loucks, 2008; Desbois et al., 2009; Loucks et al., 2009; Ambrose et al., 2010; Curtis et al., 2010; Passey et al., 2010; Schieber, 2010; Sondergeld et al., 2010; Slatt and O'Brien, 2011; Bernard et al., 2012a, b; Curtis et al., 2012; Fishman et al., 2012; Kanitpanyacharoen et al., 2012; Klaver et al., 2012; Kulia et al., 2012; Loucks et al., 2012; Reed et al., 2012; Bernard et al., 2013; Bohacs et al., 2013; Kulia, 2013; Kulia and Prasad, 2013; Loucks and Reed, 2014). Loucks et al. (2009) documented the occurrence of three types of nanopores in the Barnett Shale and suggested that the abundance of intra-OM pores is related to thermal maturation. They accomplished this study using argon (Ar)-ion milled samples on a scanning electron microscope. Desbois et al. (2009) successfully used cryo-focused ion beam (FIB)-broad ion beam (BIB)-scanning electron microscopic (SEM) methods to investigate pores in Oligocene Boom Clay, Mol Site, Belgium. Desbois et al. (2009) demonstrated that there is unimodal distribution of the clay mineral pores, shape of these pores are elongated and bedding parallel, so clay mineral porosity has a fractal distribution (D = 1.8–1.9, D: fractal dimension). Ambrose et al. (2010) used FIB/SEM imaging to create three-dimensional reconstructions of pores, organic matter, and mineral grains and their connectivity. Kulia et al. (2012) provided evidence that illite-smectite (I/S) clay mineral controls the distribution of the 3 nm pore size peak from nitrogen adsorption measurements and suggested that nanopores in I/S clay minerals, instead of organic matter controls small pore development during low-thermal maturation in the Upper Cretaceous Niobrara Formation, Colorado. Continuing improvements in imaging and characterization techniques not only supported indirect

methods, such as helium and nitrogen adsorption measurements of pore volume and pore size distribution (PSD) (Bustin et al., 2008), but also provided insights into the characteristics of three-dimensional pore connection and controls on the distribution of these nanometer- to micrometer-sized pores. Loucks et al. (2012) compiled observations from previous studies and original research to develop a descriptive classification schemes to categorize pore types and their direct associations. Their concept of interparticle (interP) and intraparticle (intraP) pores was similar to those used in sandstone and carbonate rocks. The first qualitative categorization of OM pores were proposed by Milliken et al. (2013).

It has been widely accepted that OM pores in mudrocks are predominantly controlled by thermal maturation of the organic matter (Loucks et al., 2009; Bernard et al., 2012a, b; Fishman et al., 2012; Klaver et al., 2012; Loucks et al., 2012; Reed et al., 2012; Mastalerz et al., 2013; Milliken et al., 2013; Pommer, 2014; Pommer and Milliken, 2015). However, the stepwise changes in pore size and shape during thermal maturation of organic matter remain unclear and debatable. Thermal maturation measured by vitrinite reflectance cannot document the exact petroleum generation stage because kerogen types (Type I, II, IIS, and III), maceral types (liptinite, alginite, vitrinite, inertinite, etc.), and chemical composition of kerogen (e.g., sulfur content) can all affect changes in relative timing of petroleum generation (Hunt, 1996). Therefore, studying the relationships between pore evolution and organic matter transformation stages can provide significant insights into the timing of mineral-pore and OM-pore evolution.

2.3 DATA AND METHODS

Samples from Upper Cretaceous Boquillas Formation (Eagle Ford Formation equivalent) were collected from outcrops along U.S. Highway 90, west of Del Rio,

Texas, USA. It is worth noted that the Boquillas samples used in the designed experiments are the organic-lean calcite-rich mudrocks (limestone facies), not the commonly seen organic-rich mudrocks (marl facies) of the Boquillas (Eagle Ford-equivalent) Formation. Instead, they are more diagenetically altered "limestone facies". We drilled eight small-diameter rock cylinders (6 mm in diameter and 2-3 cm in length) perpendicular to bedding planes from the outcrop sample (Figure 2.1). These cylindrical samples were pyrolyzed in gold tubes at the laboratory at the Guangzhou Institute of Geochemistry, Chinese Academy of Sciences. It is likely that some irreducible water may have been present in our samples because they were neither vacuum-dried nor oven-dried before being placed in gold tubes.

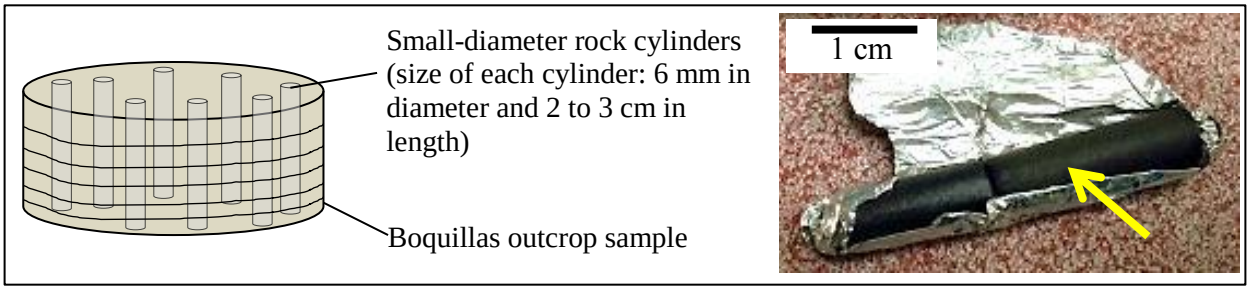

Figure 2.1: Sample preparation. On the left: schematic illustration drilling method to obtain small-diameter rock cylinders perpendicular to the bedding plane. On the right: example of small-diameter rock cylinders (yellow arrow) wrapped in aluminum foil.

Anhydrous gold-tube pyrolysis experiments were completed on each of the eight cylindrical samples. The small-diameter cylinders were pyrolyzed in sealed gold tubes, which were placed in stainless steel autoclaves. The gold tubes had an internal diameter of 6 mm and a wall thickness of 0.45 mm, and each gold tube was between 70 and 75 mm long, giving a total reactor volume of approximately 1.0 mL. Prior to loading the

samples, the open-ended tubes were heated to 600°C to remove any residual organic material on the tubes. The gold tubes were then welded at one end using an argon arc-welder. Each gold tube was placed in a separate stainless steel autoclave and inserted into a pyrolysis oven. The pyrolysis experiments were conducted under isothermal conditions at temperatures of 130, 300, 310, 333, 367, 400, and 425°C for 72 hours reaction time. A constant confining pressure was maintained at approximately 68.95 MPa (10,000 psi) by pumping water through the autoclave during pyrolysis experiments to prevent rupturing of the gold tubes.

When the designated temperature and time was reached for each experimental run, the stainless steel autoclaves were withdrawn from the oven and rapidly quenched to room temperature in cold water. All generated hydrocarbons and non-hydrocarbons (gas, liquid, and solid) were collected for compositional analyses. After the autoclaves were depressurized, the gold tubes were taken out and placed in a vacuum line with a residual pressure of 0.1 Pa. The gold tube was pierced using a needle to allow the product gases (C_1-C_5, CO_2, H_2S, and H_2) to be volatilized into the glass vacuum line. A dry ice and acetone (-80°C) trap was used to collect C_{7-} C_{14} light hydrocarbons. The total numbers of moles of gas were calculated assuming ideal gas behavior. Identification and quantification of individual HC and non-HC gas components were carried out using a two-channel Hewlett-Packard 6890 Series Gas Chromatography (GC) that was custom-configured by Wasson ECE Instrumentation. The details of the GC operation conditions are described by Zhang et al. (2007).

The quantitative yield of light hydrocarbons (C_7-C_{14}) was determined by GC. A known amount of $C_{24}D_{50}$ internal standard (ID) was added in a C_7-C_{14} mixture with CH_2Cl_2 as the solvent, and the ratio of ID content to its GC peak area was defined as a calibration factor. The yield of C_7-C_{14} light oil was derived from the sum of C_7-C_{14} peak

area multiplied by the calibration factor. C_{14+} extractable organic matter (EOM) was collected in 1.5 mL glass vials with a CH_2Cl_2 solvent. After evaporating the solvent, the yield of EOM was determined by the weight difference of the glass vial before and after loading EOM. Saturate, aromatic, resins, and asphaltene (SARA) separation and quantification followed the procedures described by Bastow et al. (2007).

A flat surface was prepared from a third of each post-pyrolysis rock cylinder (without solvent extraction) for SEM analysis by Ar-ion beam milling using a Leica EM TIC020 Triple Ion Beam Miller. Each sample was milled for 10 hours using an accelerating voltage of 8keV and a current of 2.8 mA. Utilizing an FEI Nova NanoSEM 430 microscope, field-emission scanning electron microscopy (FE-SEM) was used to image pores and their association with organic matter and mineral grains under an accelerating voltage of 10–15 keV and a working distance of 4–5 mm. Backscattered electron (BSE), secondary electron (SE), and SE through-the-lens detector (TLD) images were collected at instrument magnifications from 124× (horizontal field width [HFW] = 2.41 mm) to 80,000× (HFW = 0.001 mm). The TLD imaging was used for high-magnification examination. Mosaic images were collected at various scales. The identification of mineral components was completed by X-ray EDS (energy-dispersive spectroscopy detectors) mapping. Two 30 mm^2 Bruker XFlash silicon-drift energy-dispersive X-ray detectors were used, under an accelerating voltage of 15 keV, a spot size of 3.0–3.5, and a total count time of greater than 700 seconds (precision ± 1.0% and accuracy ± 10.0%).

A photo mosaic was taken for each milled sample surface. Because of the multiscale fabrics and associated pore sizes in mudrocks, pictures of 4,700x, 12,000–14,000x, and 21,000x were obtained. Pores were manually traced to derive a statistical pore size distribution using *JMicrovision* (Roduit, 2008). Flow modeling in mudrocks

generally assumes pores have a cylindrical geometry; however, in our samples the shapes of pores were predominantly irregular. Therefore, to assist flow modeling in mudrocks, we reported all pore sizes to the equivalent circular (cylindrical) diameter (ECD) for comparison.

The remaining portion of the pyrolyzed sample was pulverized, and part of the sample was analyzed for Rock-Eval and Leco TOC analyses by GeoMark.

2.4 INTRODUCTION TO PORE TYPES

2.4.1 Review of Loucks et al. (2012) Pore Classification

The mudrock pore classification developed by Loucks et al. (2012) is an objective-based classification that divides pores into three categories (Figure 2.2): (1) interparticle pores (pores between grains), (2) intraparticle pores (pores within a grain or within a composite grain boundary), and (3) organic-matter pores (pores within organic matter whether in-place or migrated). These three categories are first-level divisions. Loucks et al. (2012) recognized various specific types of interparticle and intraparticle pores for which many of the terms assigned to them imply origin. Loucks et al. (2012) did not subdivide OM-pore types but included all OM pores together. However, Loucks and Reed (2014) did recognize that there are different types of OM pores and that some OM pores can be inherited from original kerogen (e.g., original pores in marine vs. lacustrine algae, terrestrial leafy vs. woody tissues) (Teichmuller, 1986; Suarez-Ruiz et al., 2012). Loucks and Reed (2014) also noted that OM pores can form in depositional kerogen (in-place organic matter) and migrated organic matter such as pyrobitumen or char during maturation. The relationship between OM pores and organic macerals was also emphasized by Fishman et al. (2012).

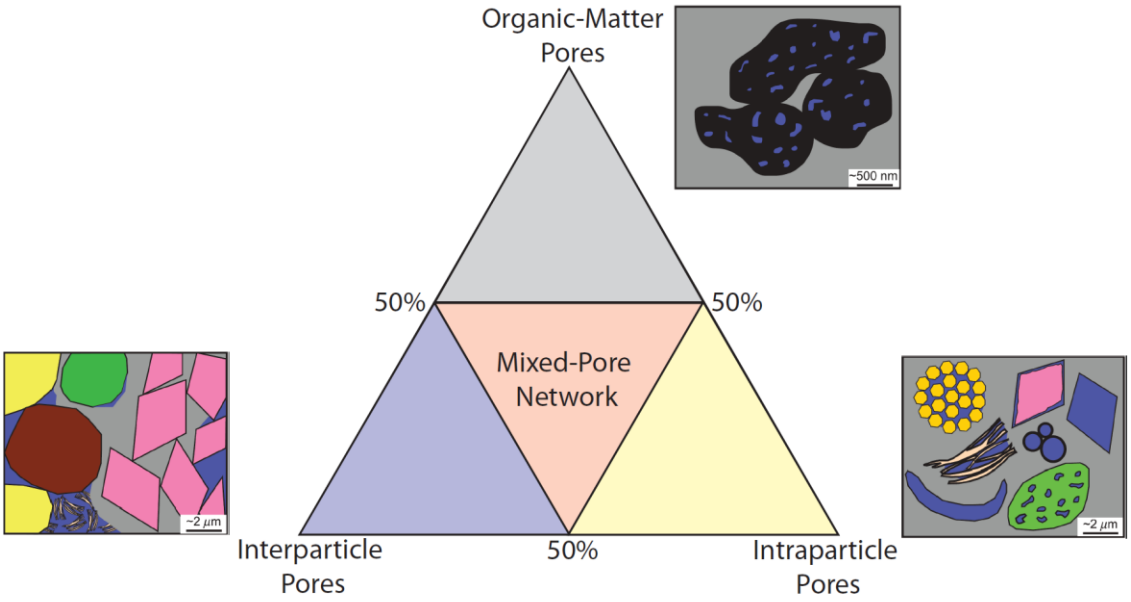

Figure 2.2: The mudrock pore classification ternary diagram from Loucks et al. (2012).

2.4.2 OM Pore Types

In this present study we subdivided OM-pores into several subcategories based on their morphology and interpreted origin (Figure 2.3).

Primary OM pores (Figure 2.3A): Some pores are present in the original organic matter such as cells in wood and leaf fragments or spores. These are considered inherited and are not related to mechanical compaction or thermal maturation.

Convoluted OM pores (Figure 2.3B): These pores form between folded, twisted, or coiled kerogen that is clearly particulate. The pores are related to organic matter in that the deformation of the organic matter produces the pores, not thermal maturation. Pore shape and size are not predictable, but are dependent on variations of its ductile behavior and its relationship with the mineral admixture. Similar pores were found in immature kerogen in the sapropel (Milliken et al., 2014).

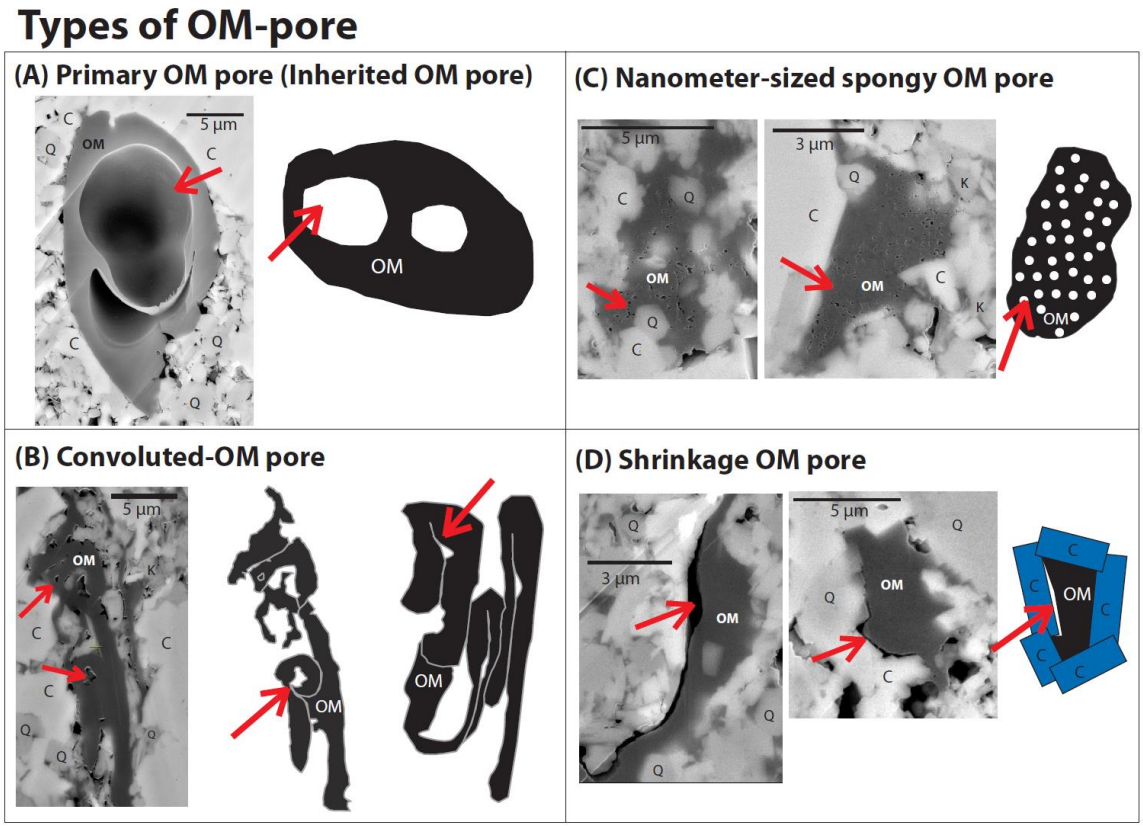

Figure 2.3: Types of OM pore in the Boquillas sample. (A) Primary OM pores are pores inherited from original cellular structure. (B) Convoluted OM pores are found between folded, twisted, or coiled OM. The convoluted OM pores and primary OM pores are related to immature OM (kerogen). (C) Nanometer-sized spongy OM pores are nanopores with rounded, subrounded, or subangular shape. (D) Shrinkage OM pores typically occur between OM and mineral grains. They appear to be related to post-experimental drops in temperature and confining pressure. Such pores are interpreted as artifacts, not likely to occur in the subsurface. Blue: mineral grains; black: organic matter; white with red arrow: pore space. C: calcite; K: kaolinite; Q: quartz. Backscattered electron (BSE) images.

Spongy OM pores (Figure 2.3C): The pores are generally at the nanometer scale, abundant, and closely spaced. They can have a rounded, subrounded, or subangular shape. They are considered to be related to gas generation and are significant at higher stages of maturation.

Shrinkage OM pores (Figure 2.3D): Shrinkage pores commonly occur between organic matter and mineral grains, but some do occur within solid bitumen, pyrobitumen, or char. They appear to be related to post-experimental drops in temperature and confining pressure as noted in this study and to pressure release at surface conditions following coring. Such pores are interpreted as artifacts and may not be present in the subsurface.

2.4.3 Modified Mineral Pores with Relic OM

These pores are modified mineral pores and can be misidentified as OM pore as they are in contact with organic matter. They are not related to organic matter thermal maturation but to petroleum migration in mineral pores and/or leaving mineral pores during migration, post coring, or post sample preparation. Although the pores are either fully or partly lined with organic matter, they are still interparticle or intraparticle mineral pores.

Modified mineral pores in Figure 2.4A are partly in contact with the mineral phase and partly in contact with the organic-matter phase. Shape and size of these pores are controlled by original mineral pores between the coccolith hash or other constituents. These are mineral pores where petroleum migrated into the pore and was later extracted leaving behind a pore with residual organic matter such as solid bitumen. The pore itself is not within the solid bitumen as a true OM pore would be. This pore type and

interparticle mineral pores are the dominant pore types in the unheated Boquillas samples.

Modified mineral pores in Figure 2.4B show a line of isopachous organic matter lining the primary mineral pores. The shape and size of these pores relate to the pore produced by the surrounding framework grains. These pores may result from oil migrating through mineral pores, leaving behind a rim of residual oil (organic matter) or can also be resulted from later extraction leaving behind a pore with isopachous residual organic matter. Pores in Figure 2.4B are different from those in Figure 2.4A as the former one is more abundant in oil generation stage and latter more abundant in bitumen generation stage.

2.5 WORKING DEFINITIONS USED IN THIS DISSERTATION

The geochemical to geological and petrographical definition of organic matter, kerogen, bitumen, solid (or solidified) bitumen, pyrobitumen, and char have been discussed in literature (e.g. Durand, 1980; Tissot and Welte, 1984; Curiale, 1986; Hunt, 1996; Mastalerz and Glikson, 2000; Bernard et al., 2012a, 2012b; Bohacs et al. 2013; Milliken et al., 2014; Loucks and Reed, 2014). These working definitions are related to previously defined pore types for clarification. However, without the use of scanning transmission x-ray microscopy (STXM) to unveil the bonding of carbon in organic compounds in microscopic scale, the exact form of organic matter could not be identified (Bernard et al., 2010, 2012a, b; Romero-Sarmiento et al., 2014).

- Organic matter (OM): a general term referring to any liquid or solid materials enriched in organic carbon. Organic matter can have many forms, such as kerogen, bitumen, solid bitumen, residual (or retained) oil, pyrobitumen, and char,

"only some of which generate hydrocarbons and host pores" (e.g., p.4 in Bohacs et al., 2013; Loucks and Reed, 2014).

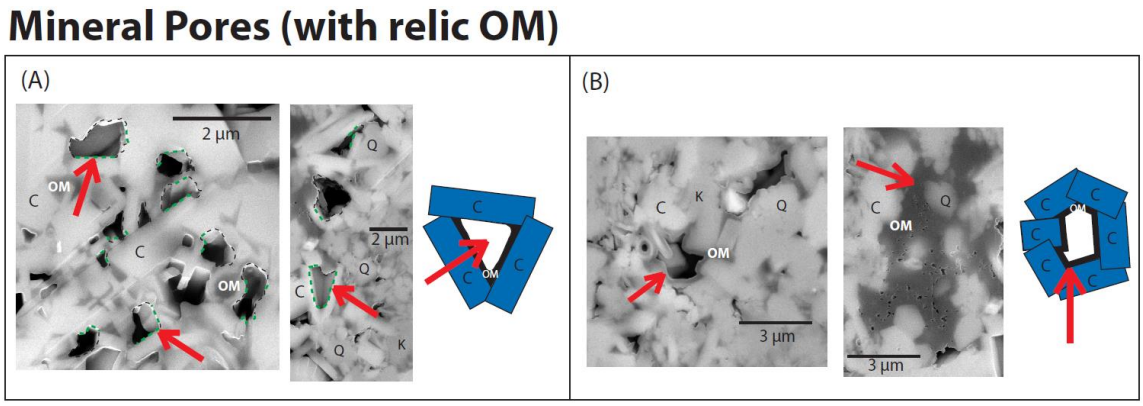

Figure 2.4: Modified mineral pores (with relic OM). (A) Modified mineral pores are defined by their association with both OM phase and mineral (or clay mineral) phase. These pores are commonly observed during bitumen generation with a pore edge in contact with minerals or clay minerals (green dashed line) and another edge in contact with OM (black dashed line). These pores commonly show more than one straight boundary with the mineral grains, and their shapes commonly mimic the pores produced by the surrounding grains. (B) These modified mineral are pores that occur within OM that isopachously coats mineral grains. The OM is residual oil or solid bitumen. They are different from spongy OM pores, as spongy pores are developed in char and pyrobitumen and are not a simple inclusion. These pores are formed during oil generation stage, related to generated oil that has migrated, escaped, and/or extracted. Blue: mineral grains; black: organic matter; white with pointed red arrow: pore space. C: calcite; K: kaolinite; Q: quartz. Backscattered electron (BSE) images.

- Kerogen: insoluble solid organic matter (organic geopolymer), composed of complex polymer structures. Kerogen will be converted in part to petroleum products when subjected to increased thermal maturation. "Kerogen can host pores that are in essence the voids left behind by hydrocarbons that were generated and expelled" or were original pores inherited from its original cell (p.4 in Bohacs et al., 2013). Kerogen can form primary OM pores and convoluted OM pores.
- Bitumen: soluble, viscous, liquid organic matter, derived from thermal cracking of kerogen under immature or low-maturity conditions. It is a generic term and can have a wide range of viscosities (e.g., Bohacs et al., 2013; Loucks and Reed, 2014). Bitumen is NSO-rich, asphaltene-rich, and includes components such as hydrocarbon, resins, and other non-hydrocarbon components (Tissot and Welte, 1984). This term is equivalent to the term "pre-oil bitumen" used by Curiale (1986) and Mastalerz and Glikson (2000). Bitumen is viscous liquid and cannot host pores over long periods of time.
- Solid (or solidified) bitumen: very viscous, difficult to dissolve in organic solvent, also equivalent to "pre-oil bitumen" but solidified in the subsurface (Curiale, 1986; Mastalerz and Glikson, 2000), able to form modified mineral pores with relic OM.
- Pyrobitumen: secondary product from bitumen and/or oil. Pyrobitumen consists of insoluble, nonvolatile, solid organic matter residues that "still retain some petroleum generation capacity upon further heating" and can host pores (p.4 in Bohacs et al., 2013; Loucks and Reed, 2014). This term is equivalent to the term "post-oil bitumen" used by Curiale (1986) and Mastalerz and Glikson (2000).

Bernard et al. (2012) suggested pyrobitumen hosts nanometer-sized spongy OM pores.

- Char: the "ultimate residue of HC generation with minimal hydrogen content and essentially no remaining potential for generating petroleums," derived from further heating of pyrobitumen and petroleum (bitumen) (p.4 in Bohacs et al. 2013). Char can also host nanometer-sized spongy OM pores.
- Residual (or retained) oil: the "liquid oil in subsurface but is solid or highly viscous at surface conditions resulted from expulsion of volatiles on the way up the wellbore and/or during handling and storage" (p. 4 in Bohacs et al., 2013), able to form modified mineral pores with relic OM.

2.6 DESCRIPTION OF BOQUILLAS MUDROCK SAMPLE

2.6.1 Mudrock Texture, Fabric, and Mineralogy

The sample was a laminated, diagenetically altered, coccolith mud-rich packstone with globigerinids and calcispheres (Figure 2.5). The coccolith mud-rich lime packstone lithofacies was commonly laminated. At the millimeter-scale, within laminae, coccolith elements (micrometer-scales rhombs) were randomly orientated and partly cemented.

The predominant minerals in the Boquillas sample, identified by X-ray EDS mapping, included calcite, dolomite, quartz, kaolinite, chlorite, calcium phosphate (apatite), titanium dioxide (possibly anatase or detrital rutile), and pyrite. The samples were very rich in calcite (80–90 wt. % of $CaCO_3$) (Table 2.1). Calcite components included calcispheres, globigerinids, crinoids (saccocomids), coccolith plates (1–15 μm across) and elements, and diagenetic calcite pseudospar. These components commonly occur as aggregates produced by fecal pelletization. Quartz occurs mainly as authigenic

crystals (Ergene, 2014). Kaolinite is also authigenic and has a booklet morphology (Ergene, 2014; Pommer, 2014). Quartz and kaolinite are probably diagenetic products of altered volcanic ash, which is common in the Boquillas Formation. Another source of kaolinite cement might be from the dissolution of feldspar. Pyrite occurs as polyhedral crystals and framboids. Some pyrite has replaced skeletal material.

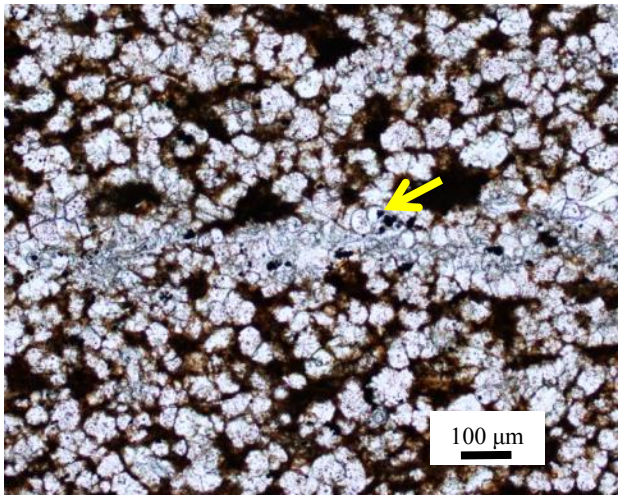

Figure 2.5: Thin-section photomicrograph of outcrop Boquillas Formation using transmitted light. Note cemented calcite crystals and planktonic nanofossils (yellow arrow).

Sample ID	Experimental Temperature (°C)	Percent calcite (wt.%)	Leco TOC (wt. %)	Rock-Eval S_1 (mg HC/g)	Rock-Eval S_2 (mg HC/g)	T_{max} (°C)	Hydrogen Index (HI)	Oxygen Index (OI)	S_1/TOC
EF (1)	outcrop	89.61	1.48	0.77	3.53	437	644	30	52
EF 1-10	130	81.42	2.29	1.99	16.22	432*	708	22	87
EF 1-4	300	82.42	2.07	1.87	14.53	432*	702	34	90
EF 1-6	310	82.28	N/A	N/A	N/A	N/A	N/A	N/A	N/A
EF 1-8	333	85.47	1.68	3.77	11.52	428*	686	44	224
EF 1-12	367	86.94	1.02	2.89	0.84	439*	82	60	283
EF 1-14	400	86.93	1.23	1.67	1.06	430*	86	46	136
EF 1-2	425	80.88	1.38	1.22	0.45	427*	33	38	88

* indicates T_{max} values might not be representative because a low temperature S_2 shoulder was reported in the pyrograms

Table 2.1: Experimental temperature, calcite and TOC contents, and Rock-Eval parameters (S_1, S_2, T_{max}, HI, OI, S1/TOC) of each sample. Rock-Eval S_1 and S_2 are reported as milligram (mg) of S_1 and S_2 per gram of rock. S_1 represents volatile hydrocarbons that have been generated and expelled as free hydrocarbons in the rock. The S_2 represents hydrocarbons that have not been generated and expelled but still have generation potential. T_{max} represents the temperature at which the maximum amount of hydrocarbons released from cracking of kerogen (top of S_2 peak). The T_{max} is an indication of maturation stage of the organic matter. HI (hydrogen index) is calculated as HI = [100 x S_2]/TOC. HI is a parameter used to characterize the origin and type of organic matter in immature rocks. OI (oxygen index) is calculated as OI = [100 x S_3]/TOC. S_3 represents the amount of CO_2 (in milligrams CO_2 per gram of rock) produced during pyrolysis of kerogen and indicates the amount of oxygen in the kerogen. OI is, therefore, a parameter that correlates oxygen to carbon and helps to characterize the origin and type of organic matter in immature rocks as well.

2.6.2 Organic Matter Characterization

Rock-Eval pyrolysis of the Boquillas samples showed that they had undergone early-stage HC generation (T_{max} = 437 °C; ~0.7 $\%R_o$ calculated), and the present-day organic matter had the chemical composition of Type II kerogen (hydrogen index [HI] = 644 mg S_2/g TOC; oxygen index [OI] = 30 mg S_3/g TOC) (Table 1). According to the Rock-Eval data and results from solvent extraction, the organic matter in the sample was predominantly composed of EOM, identified as petroleum (bitumen) (Figure 2.6). Therefore much of the organic matter observed in the samples was migrated bitumen within the Boquillas unit. The distance of migration is unknown but it may have only been at pore-level scale. This implies that the pyrolysis experiments in part simulated the thermal decomposition of bitumen, an intermediate product between kerogen and oil (hydrocarbons) (Lewan, 1993), rather than only the thermal breakdown of kerogen.

Observations from SEM petrography showed that most organic matter was amorphous and some filled original mineral pores (Figure 2.7). Depositional particulate organic matter (POM) was also observed in the Boquillas (Figure 2.8A). The POM was characterized by its discrete shape and boundary, possibly of terrigenous origin.

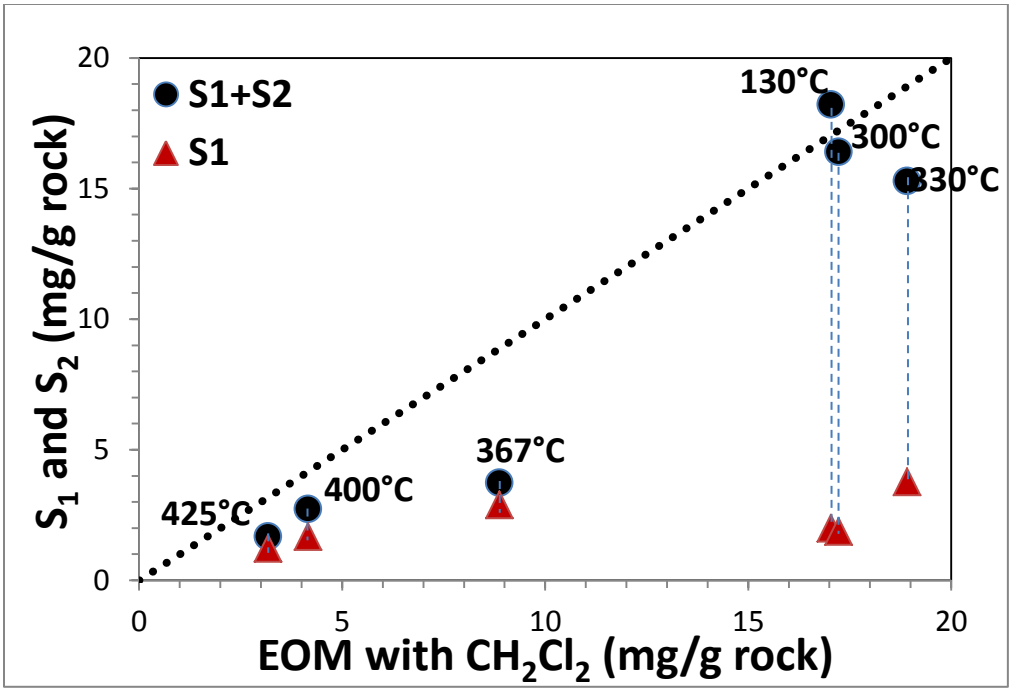

Figure 2.6: Plot of Rock-Eval S_1 and S_1+S_2 against extractable organic matter (EOM) for each sample. Experimental temperature values indicate level of heating. S_1 represents volatile hydrocarbons that have been generated and expelled as free hydrocarbons in the rock. S_2 represents hydrocarbons that have not been generated and expelled but still have generation potential. For low-maturity samples (130 and 300°C), EOM almost equals S_1+S_2 value and Rock-Eval S_2 peak for these two samples (130 and 300°C) is significantly higher and wider than S_1 peak. This implies that hydrocarbon that still has generation potential (S_2) is mostly extractable organic matter (bitumen) instead of non-extractable organic matter.

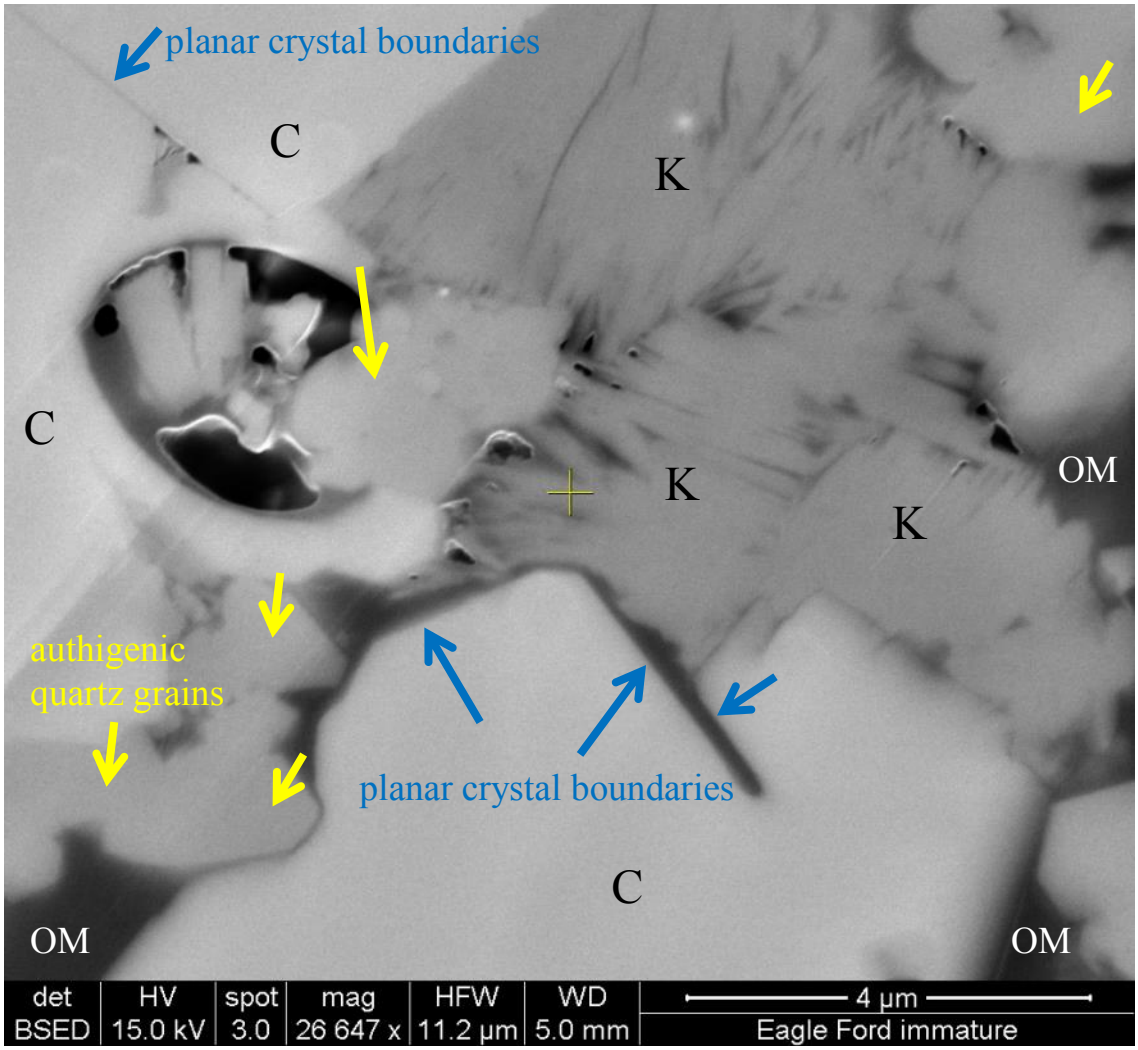

Figure 2.7: SEM photomicrograph of natural (unheated) Boquillas sample. Both calcite (blue arrows) and quartz crystal (yellow arrows) have planar crystal boundaries, indicating they are of authigenic origins. However, some of the calcite edges may be coccolith plate boundaries. Kaolinite booklet morphology also implies it is authigenic. Organic matter (black) likely displaced water and filled pore space after the formation of these authigenic crystals. Therefore, the organic matter here is likely migrated petroleum (bitumen). C: calcite; K: kaolinite; Q: quartz. Backscattered electron (BSE) image.

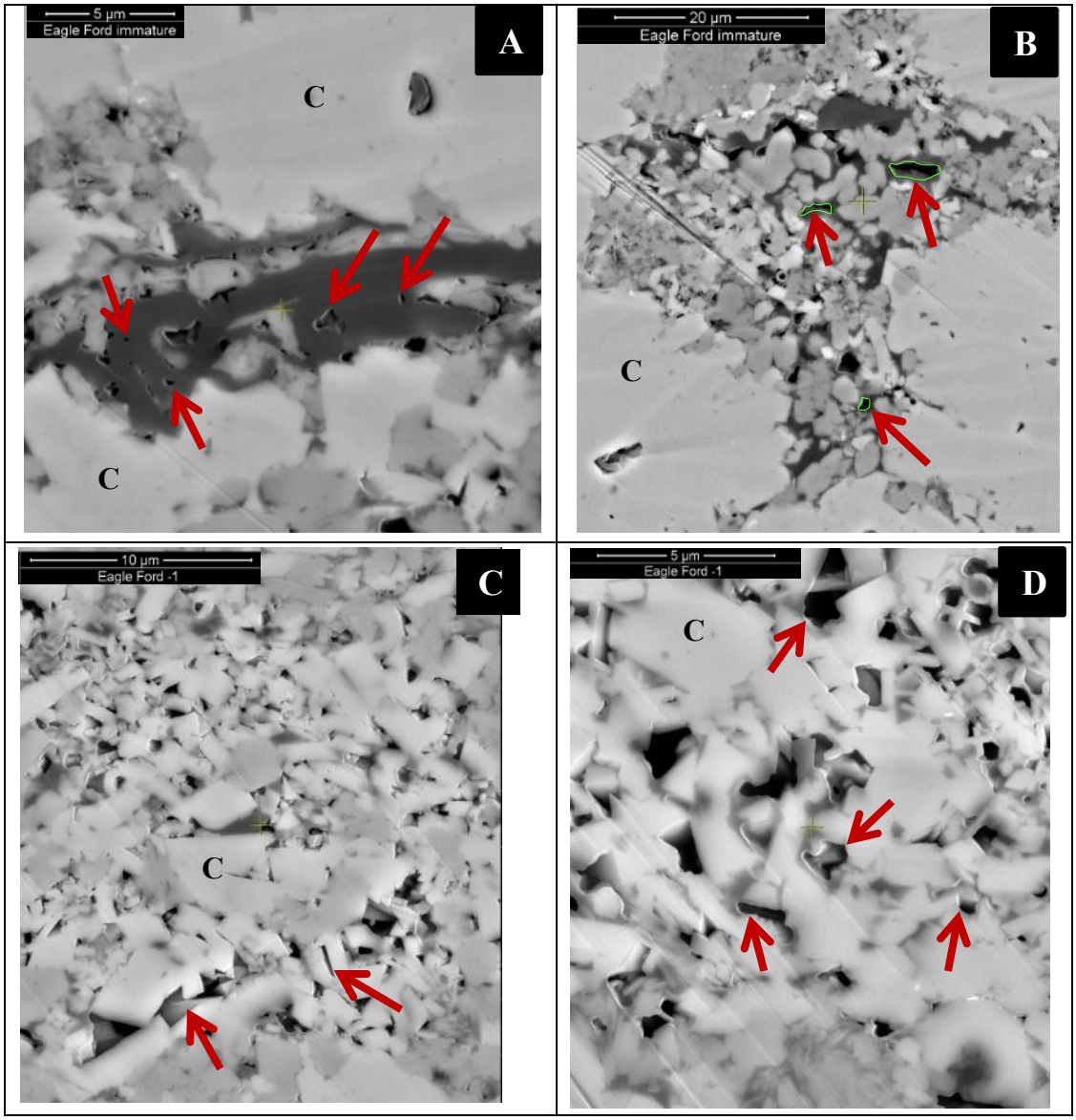

Figure 2.8: SEM photomicrographs from unheated Boquillas showing four types of pore. (A) Convolute OM pores (red arrows). (B) Modified mineral pores with relic OM (white outline, white arrows). (C) Interparticle mineral pores (white arrows). (D) Modified mineral pores (white arrows). Photographs are taken perpendicular to bedding.

2.6.3 Initial Pore Network

The primary interparticle mineral pores and modified interparticle mineral pores were the predominant pore types in the unheated Boquillas samples (Figure 2.8C, D). Rarer intraparticle pores, convoluted OM pores, and primary OM pores were also present. Intraparticle pores can occur as fluid inclusions in mineral grains or within coccolith plates and globigerinids. Primary interparticle pores were present between the allochems, which were predominantly coccoliths and coccolith fragments as well as planktonic foraminifera. Generally, the modified mineral pores ranged from a few to the tens of micrometers with some of the pores in the nanometer scale. Most of the pore shapes were very irregular. Before petroleum migration, the original mineral pores were filled with connate water. The effect of high calcite content in the Boquillas samples prevent significant porosity loss from compaction and preserve much of the primary porosity. Many of these original interparticle pores are now filled or partially filled with petroleum (bitumen) and become modified mineral pores. The abundance of modified mineral pores in the OM-lean calcite-rich Boquillas samples (limestone facies) implied that the migration of petroleum (bitumen) might have formed a continuous petroleum (bitumen) network within the mineral pores setting the stage for a subsequent connected OM pore network, as demonstrated by Loucks and Reed (2014).

2.7 RESULTS FROM GOLD-TUBE PYROLYSIS EXPERIMENTS

2.7.1 Geochemical Characterization of Generated Gases and Liquids

Five oil and gas generation stages are defined based on yields of gas, light oil, EOM, and SARA fractions (Figure 2.9; Tables 2.2 and 2.3). They are (1) bitumen or polar (resins and asphaltenes) generation, (2) early oil generation, (3) oil window and associated gas generation, (4) peak oil generation, and (5) oil cracking to gas. The first

four experimental runs (130, 300, 310, and 333°C) showed little or no further generation of C_1-C_5, CO_2, H_2S gases, and oil saturates, indicating that Boquillas strata from the study area had already reached the early oil generation stage (Figure 2.9). The EOM vs. experimental temperature plot suggested that the original sample had experienced maximum pre-oil bitumen generation from kerogen. No significant increase in EOM was observed (Figure 2.9; Table 2.2). The amount of both light oil (C_{7-14}) and normal oil (C_{14+}) started to increase in the sample heated to 310 and 333°C at the early oil generation and continued to increase significantly to a maximum at 400°C at peak oil generation (Figure 9). When the amount of light oil (C_{7-14}) and normal oil (C_{14+}) started to decrease at 400°C and gaseous HC continued to increase, this was defined as the oil cracking to gas stage from 400 to 425°C (Figure 2.9). SARA fractions also illustrated similar trends. In the sample heated to 333, 367, and 400°C at the oil window, the yields of asphaltene and NSO-compounds decreased, but yields of saturates increased correspondingly (Figure 2.9; Table 2.2). In the sample heated to 400 and 425°C at the oil cracking to gas stage, saturate and aromatic fractions decreased significantly, while NSO and asphaltene were reduced to a lesser extent (Figure 2.9; Table 2.2). CO_2 and H_2S gases showed almost no changes in the sample heated to 130, 300, and 310°C at the bitumen generation stage. Their yields started to increase when the sample was heated to 310 and 333°C at the beginning of oil generation. Then they increased dramatically during the oil window in samples heated to 333, 367, and 400°C, and reached stability at the oil cracking to gas stage at 400 and 425°C (Figure 2.9; Table 2.2).

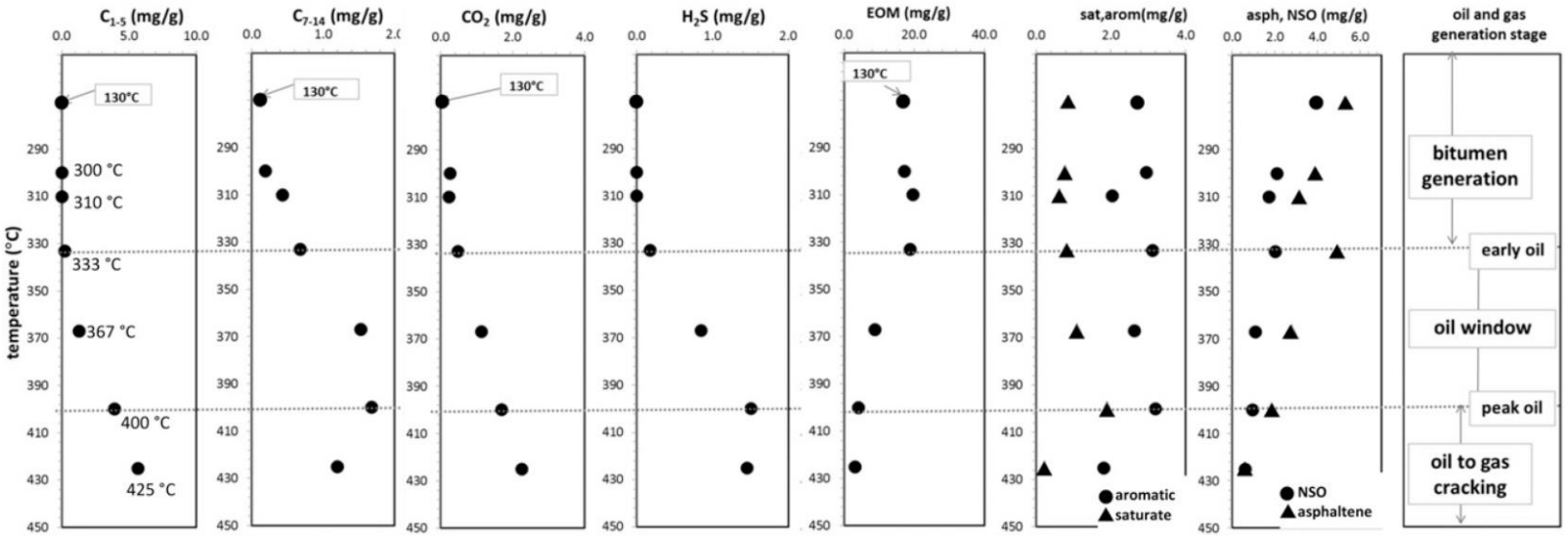

Figure 2.9: Plots of experimental temperatures against generated components (gaseous and liquid hydrocarbons). Five oil- and gas-generation stages are defined by trends from produced gas (C_1-C_5, CO_2, and H_2S), liquids (C_7-C_{14}, C_{14+}), EOM (bitumen), and SARA fractions. Black circles indicate phase abundance at different temperatures (130, 300, 310, 333, 367, 400, 425°C). sat: saturate; arom: aromatic; NSO: nitrogen, sulfur, oxygen, and heavy metals; asph: asphaltene.

Heating Temperature (°C)	C_1-C_3 (mg/g)	C_4-C_5 (mg/g)	C_7-C_{14} (mg/g)	CO_2 (mg/g)	H_2S (mg/g)	EOM (mg/g)	SAT (mg/g)	ARO (mg/g)	NSO (mg/g)	Asphaltene (mg/g)
130	0.0003	0.0002	0.120	0.0098	0.0000	12.693	0.871	2.710	3.912	5.282
300	0.0138	0.0009	0.195	0.1374	0.0000	10.072	0.778	2.950	2.097	3.886
310	0.0238	0.0012	0.433	0.1191	0.0000	7.781	0.625	2.045	1.723	3.171
333	0.1950	0.0113	0.678	0.2447	0.1141	11.201	0.821	3.124	2.038	4.964
367	1.1484	0.1284	1.527	0.5766	0.5560	7.768	1.104	2.637	1.089	2.791
400	3.3867	0.5208	1.677	0.8664	0.9905	8.032	1.907	3.194	0.971	1.865
425	5.1244	0.5403	1.198	1.1517	0.9568	3.306	0.232	1.819	0.622	0.625

Table 2.2: Yields of generated gas and oil components after each experimental run.

Temperature (°C)	Defined HC generation stages	Yields of gas (C_1-C_5, CO_2, H_2S)	Extractable organic matter (EOM) with $C_2H_2Cl_2$	Saturate, aromatic, asphaltene (NSO) separation (SARA)
130	**Bitumen generation**	Low yields of C_1-C_5, CO_2 and no H_2S	TOC directly related to EOM yields	Asphaltene and NSO-compounds are dominant
300				
310				
333	**Early oil generation**	Low yields of C_1-C_5, CO_2 , and H_2S yield	Same as above	Same as above
367	**Oil window and associated wet gas generation**	Yields of C_1-C_5, CO_2 and H_2S increase	EOM, TOC content significantly decrease	Asphaltene and NSO-compounds decrease
400	**The end of oil generation**	Yields of C_1-C_5, CO_2 and H_2S increase	EOM is low	Saturate reaches maximum
425	**Oil cracking to gas**	C_1-C_5 yields greatly increase	EOM is minimum	Saturate starts to decrease

Table 2.3: Petroleum generation stages defined by experimental yields of generated gas and liquid.

2.7.2 Pore Evolution during Thermal Maturation

As previously described, based on our geochemical data (Figure 2.9; Table 2.2), the Boquillas sample had already undergone bitumen generation and possible short-distance migration (at least pore-level scale but likely at bed-scale because these are OM-lean calcareous mudrock). Therefore, the gold-tube pyrolysis experiments performed in this study simulated two key processes: (1) bitumen transformation to oil and (2) early oil thermally cracking to gas (Table 2.2).

Stage I: Bitumen Generation (130, 300, and 310°C/72hrs)

As in the original sample, modified mineral pores were the most abundant type observed in the samples heated to 130, 300, and 310°C. The only difference between the outcrop sample and these heated samples was the appearance of shrinkage OM pores, interpreted as being related to post-experimental process (Figure 2.10). After samples reached the designated temperature and reaction time, they were withdrawn from the oven and rapidly cooled to room temperature by quenching in a water bath. These rapid drops in pressure and temperature were interpreted to result in the internal shrinkage of organic matter and the separation of organic matter from adjacent mineral contacts.

Stage II: Early Oil (333 °C/72hrs) and Oil Window (367°C/72hrs)

Modified mineral pores with isopachous OM rim were the predominant type of pores observed in both early oil and oil window stages (Figures 2.11, 2.12, and 2.13). The size of these modified mineral pores commonly ranged from the tens to hundreds of nanometers to tens of micrometers, and their shape is irregular (without straight boundaries) and mimicked the shape of the framework grains (Figure 2.11B). After petroleum (oil) extracted from the pore after the experimental run, during sample preparation or the vacuum condition, an isopachous coating was left on the pore wall

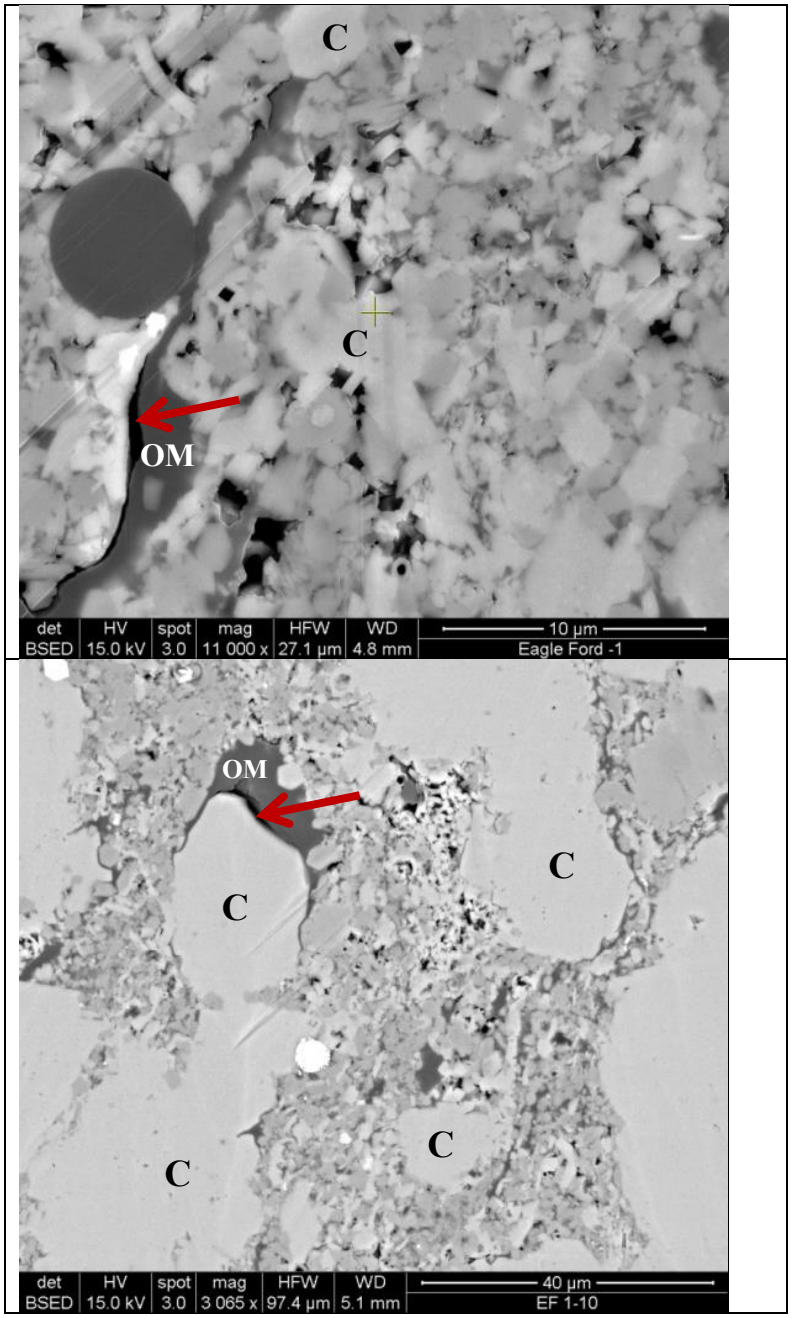

Figure 2.10: SEM photomicrographs from Boquillas sample heated to 130°C for 72 hours showing examples of shrinkage OM pores (red arrows). They are between OM and minerals, related to post-experimental drops in temperature and confining pressure. Such pores have been observed in natural core samples but are related to post-coring (Loucks and Reed, 2014). C: calcite; OM: organic matter. Backscattered SEM images.

(Figures 2.11, 2.12B, D). Compared to pores in the bitumen generation stage, there is a relative decrease in proportions of modified mineral pores, primary interparticle and intraparticle mineral pores. We also observed several possible solidified organic matter residues (perhaps solid bitumen or pyrobitumen) in the coccolith fragment-rich matrix (Figures 2.12A, 2.14). Few modified mineral pores and a few nanometer-sized spongy OM pores were present within the solidified residual organic matter (Figures 2.12A, 2.14). The number and size of these nanometer-sized OM spongy pores increased from the early oil (Figure 2.14) to oil window stage (Figure 2.12A). However, without the use of scanning transmission x-ray microscopy (STXM) to unveil the bonding of carbon in organic compounds in microscopic scale, the exact form of organic matter could not be identified (Bernard et al., 2010, 2012a, b; Romero-Sarmiento et al., 2014).

Stage III: Peak Oil Generation (400 °C) and Cracking of Oil to Gas Stages (425 °C)

Five pore types were found in samples heated to 400 °C at the late oil generation and 425 °C at the oil cracking to gas stages: Modified mineral pores (Figures 2.15A, C, 2.16B, C, D), nanometer-sized spongy OM pores in organic matter residues (Figures 15E, F, 16E), primary interparticle mineral pores (Figure 2.15B, D), and intraparticle pores between clay mineral platelets and between clay mineral and organic matter (Figures 2.15C, 2.16D). The most abundant pore types at this stage were the modified mineral pores nanometer-sized spongy OM pores.

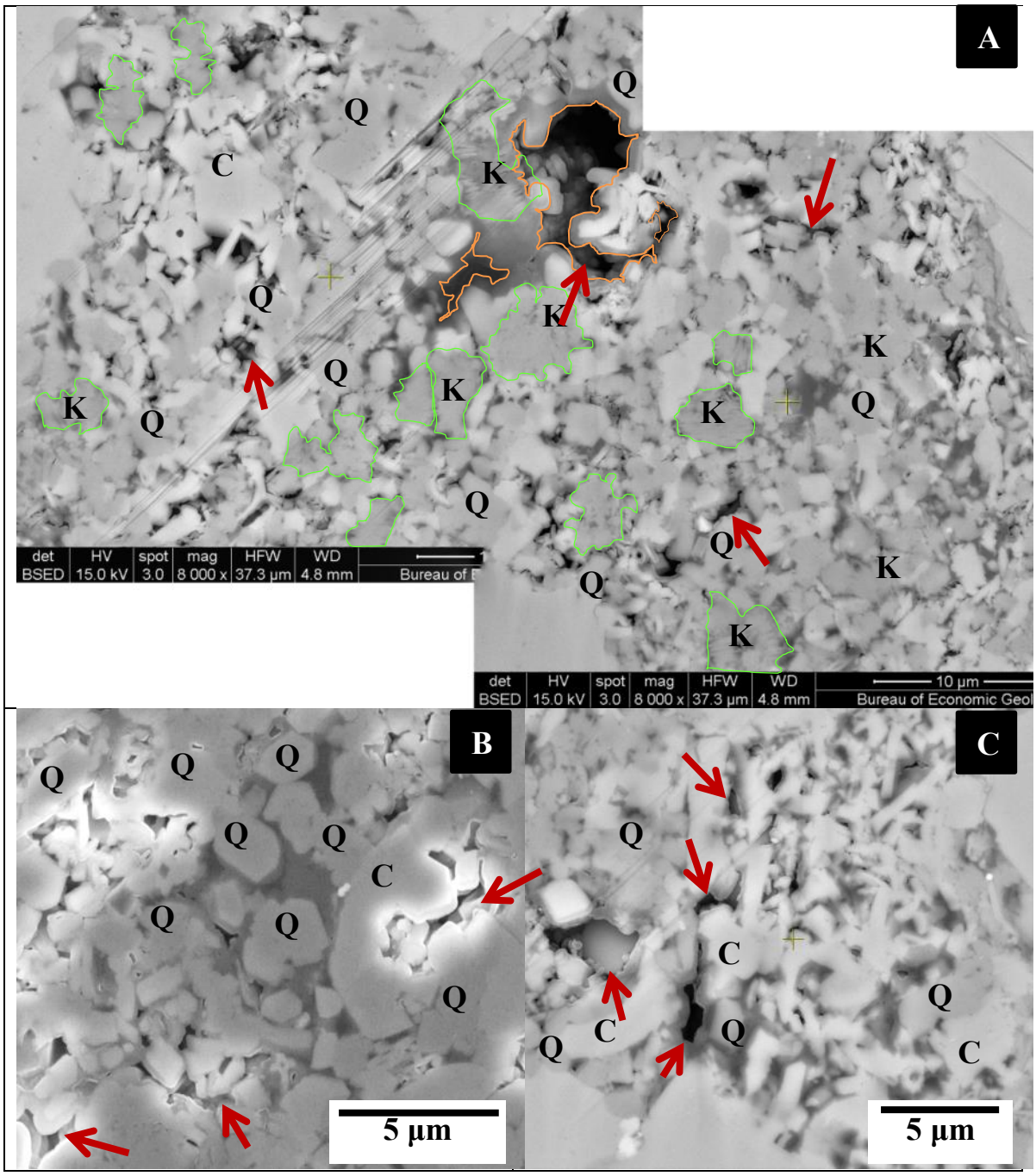
A
B
C
Q
K
C
det HV spot mag HFW WD
BSED 15.0 kV 3.0 8 000 x 37.3 µm 4.8 mm
Bureau of Economic Geol
10 µm
5 µm
5 µm

Figure 2.11: SEM photomicrographs from Boquillas sample heated to 330°C for 72 hours showing modified mineral pores (red arrows) and their associations at early oil generation stage. (A) Modified mineral pores are commonly a few micrometers in length (circled by orange line), within isopachous residual oil-lined mineral grains. Kaolinite booklet (K) circled by green solid line. Backscattered electron (BSE) image. (B) Shape of modified mineral pore (red arrows) is irregular (without straight boundary), mimicking the surface of grains and crystals. Secondary electron (SE) image. (C) OM shows two gray levels, possibly indicating different stages of retained and expelled hydrocarbons with different chemical compositions (see text). Backscattered electron (BSE) images. C: calcite; Q: quartz; K: kaolinite.

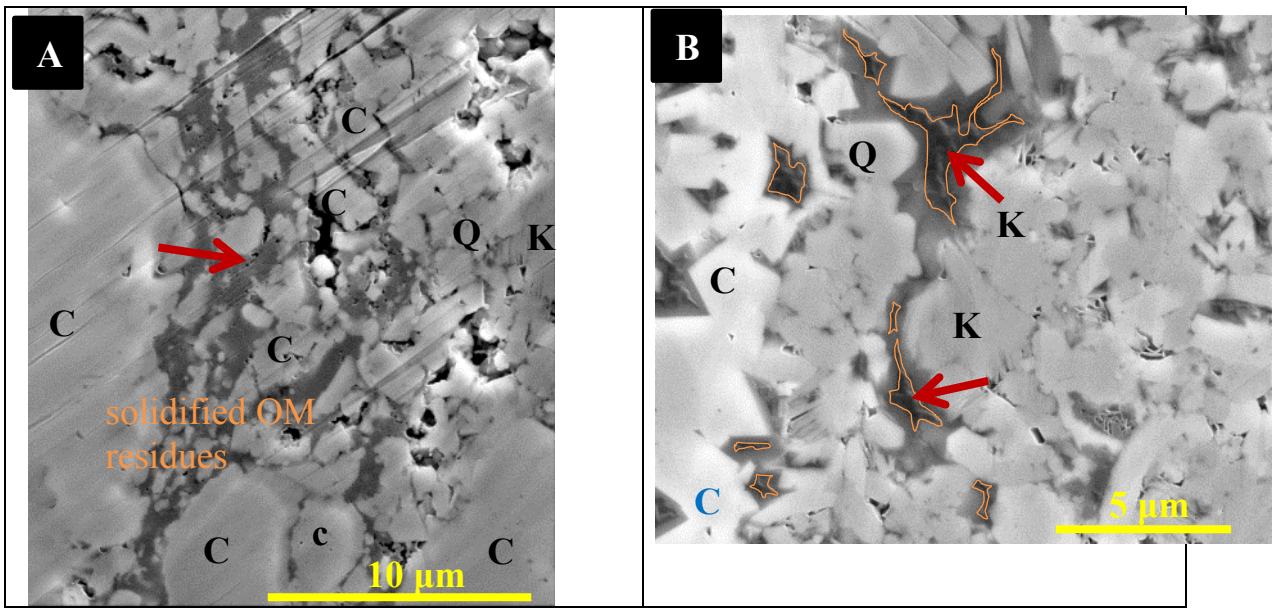

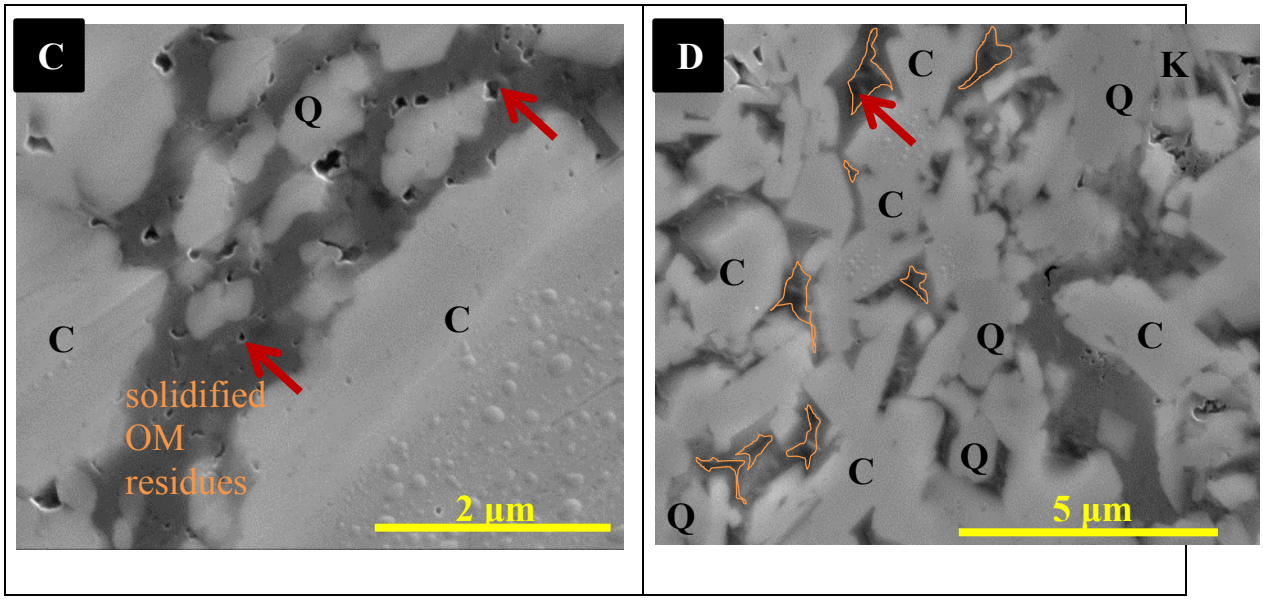

Figure 2.12: SEM photomicrographs of Boquillas sample heated to 367°C for 72 hours, showing modified mineral pores and nanometer-sized spongy OM pores in oil window and associated wet-gas generation stage. (A) Modified mineral pores and nanometer-sized spongy OM pores. (C) Nanometer-sized spongy OM pores in solidified OM residues (likely pyrobitumen). Secondary electron (SE) images. (B) and (D) show modified mineral pores (circled by orange line) within isopachous residual oil-rimmed mineral grains. Dark, undulate surface (within orange line) is interpreted as interface between solid OM residues and remained liquid hydrocarbons. Pore shape is irregular, mimicking the surfaces of surrounding grains and crystals. (B) Backscattered electron (BSE) image; (D) secondary electron (SE) image. C: calcite; Q: quartz; K: kaolinite.

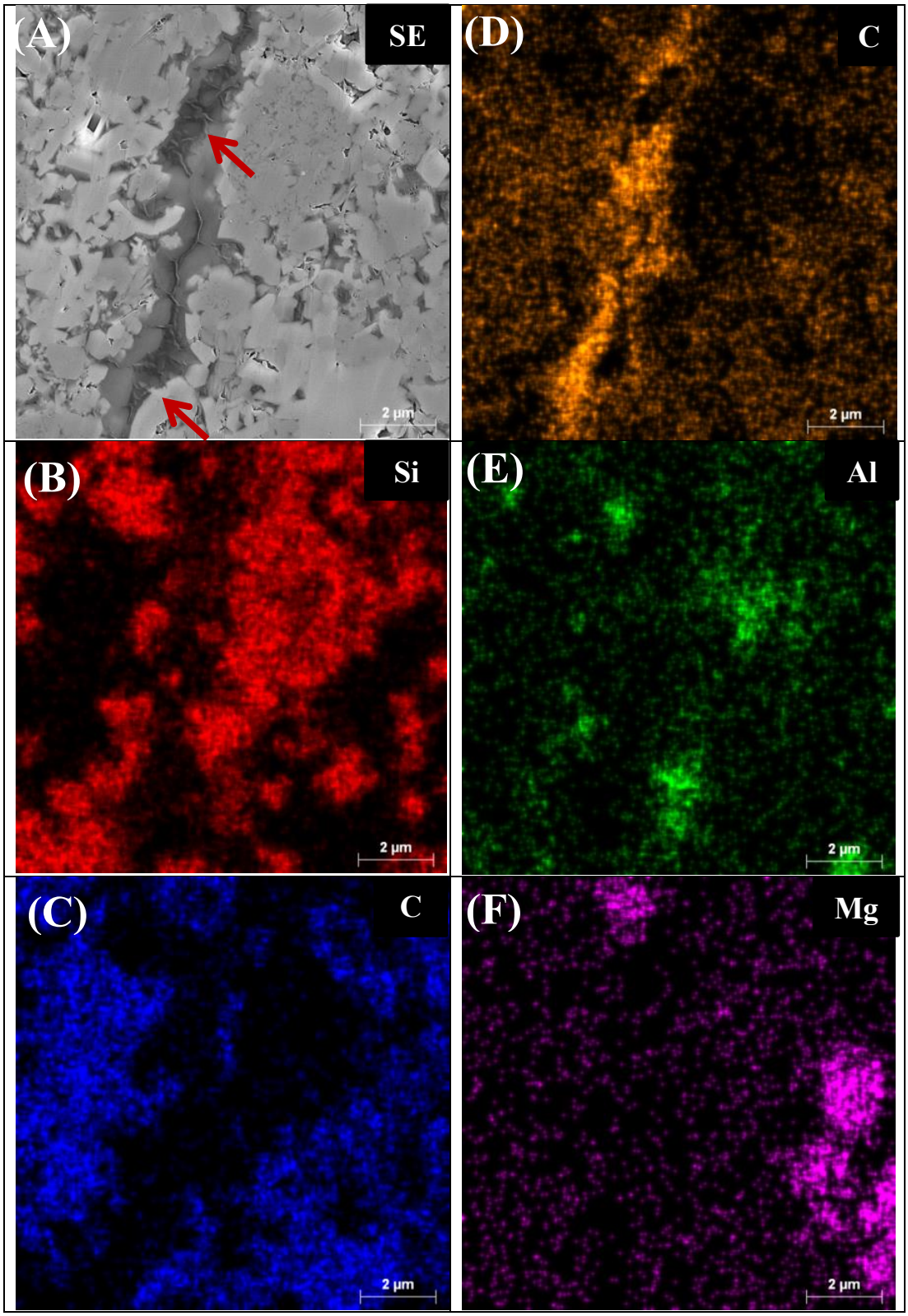
(A)
SE
2 µm
(D)
C
2 µm
(B)
Si
2 µm
(E)
Al
2 µm
(C)
C
2 µm
(F)
Mg
2 µm

Figure 2.13: (A) SEM secondary electron (SE) image showing Boquillas sample in oil window and associated wet-gas generation stage (heated to 367°C for 72 hours). (B) to (F) Corresponding x-ray EDS elemental mapping of carbon (C: orange), silicon (Si: red), aluminum (Al: green), calcium (Ca: blue), and magnesium (Mg: pink). Quartz would contain mainly silicon as shown in (B). Calcite would contain mainly calcium and some carbon, as shown in (C) and (D). Organic matter would contain mainly carbon, as shown in (D). Clay mineral such as kaolinite would contain aluminum and some silicon, as shown in (E). Dolomite would contain calcium and magnesium and chlorite would contain magnesium, aluminum, and silica, as shown in (F). Pores (black arrows) are within residual oil-lined grains. The dark, undulate surface (black arrows) is interpreted as the interface between solid OM residues and remained liquid hydrocarbons

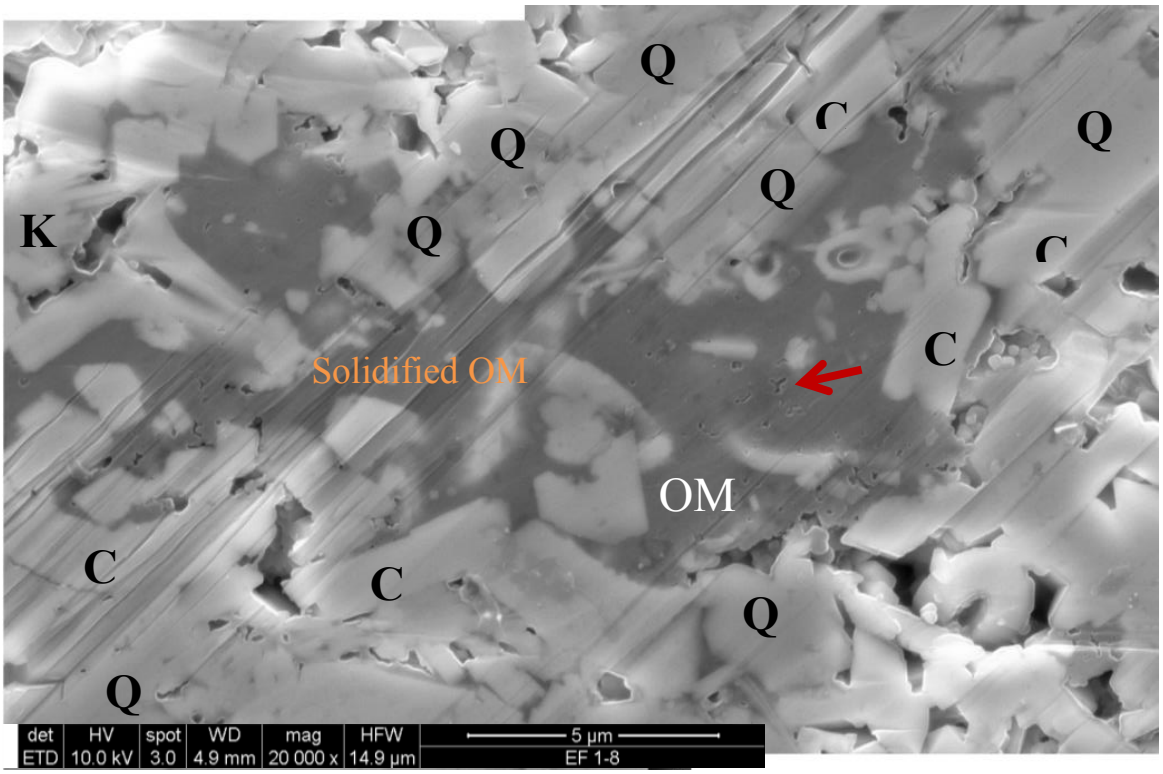

Figure 2.14: SEM photomicrograph of Boquillas sample heated to 330°C for 72 hours showing solidified OM residues (see text) in the early oil-window sample. Some nanometer-sized spongy OM pores (red arrows) are observed in some parts of OM residue (likely pyrobitumen). C: calcite; Q: quartz; K: kaolinite. Secondary electron (SE) image.

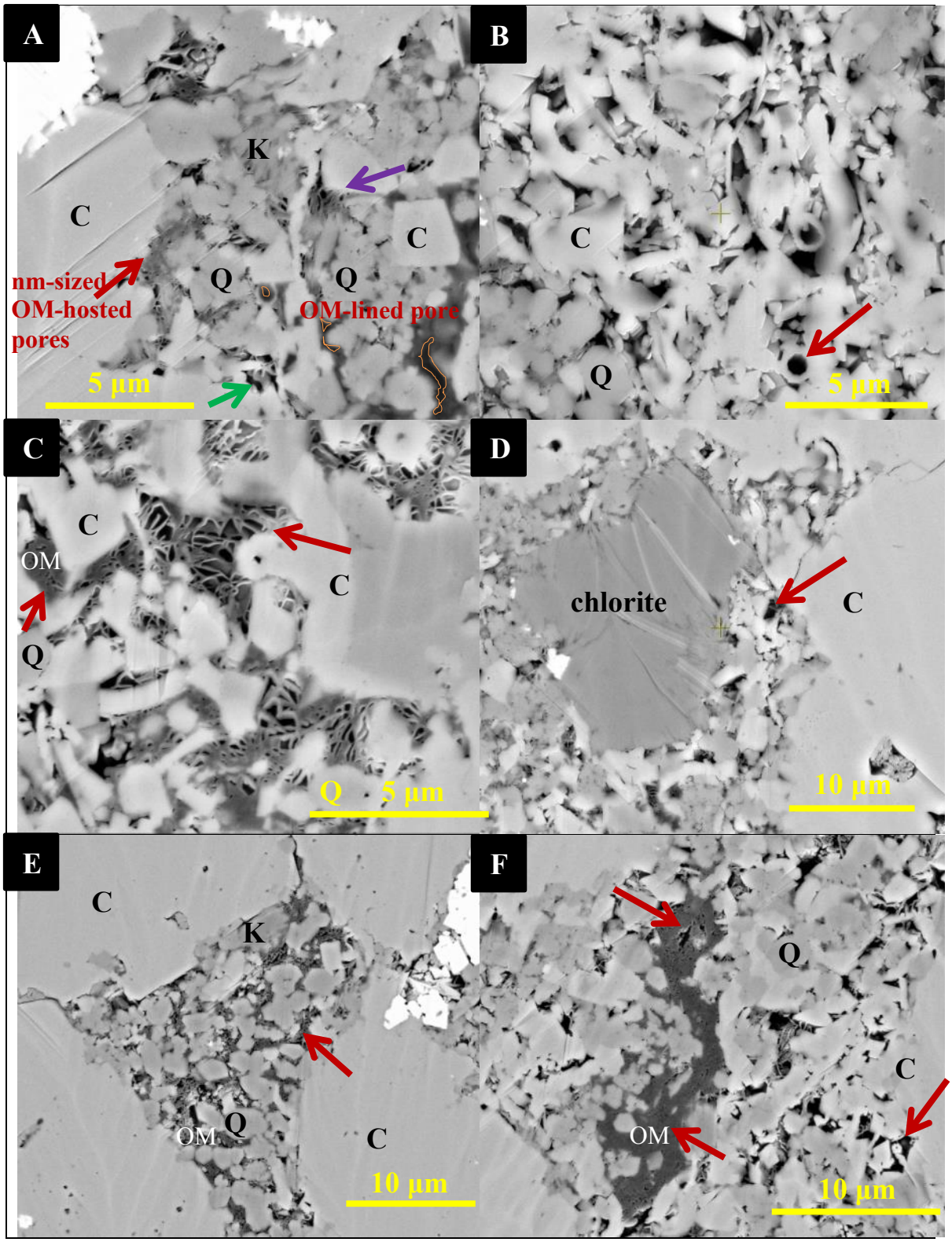
A
K
C
C
nm-sized
OM-hosted
pores
Q
Q
OM-lined pore
5 µm
B
C
Q
5 µm
C
C
OM
C
Q
Q
5 µm
D
chlorite
C
10 µm
E
C
K
Q
OM
C
10 µm
F
Q
C
OM
10 µm

Figure 2.15: SEM photomicrographs of Boquillas sample heated to 400°C for 72 hours, showing different pore types (arrows) at peak oil generation stage. Backscattered electron (BSE) images. (A) Nanometer-sized spongy OM pores, primary interparticle or intraparticle mineral pores, modified intra-clay mineral pores, and modified mineral pores (circled by orange line) are all noted in this figure. (B) Interparticle mineral pore (red arrow) between calcite grains and between calcite and quartz. (C) Modified intra-illite pores or inter-illite and OM pores. (D) Interparticle pore (purple arrow) between illite and calcite. Micrometer-sized authigenic chlorite is present. (E) Nanometer-sized spongy OM pores from thermally cracked OM in quartz-rich matrix. (F) Nanometer-sized spongy OM pores in OM remnants and modified interparticle pores between clay minerals and calcite. C: calcite; Q: quartz; K: kaolinite.

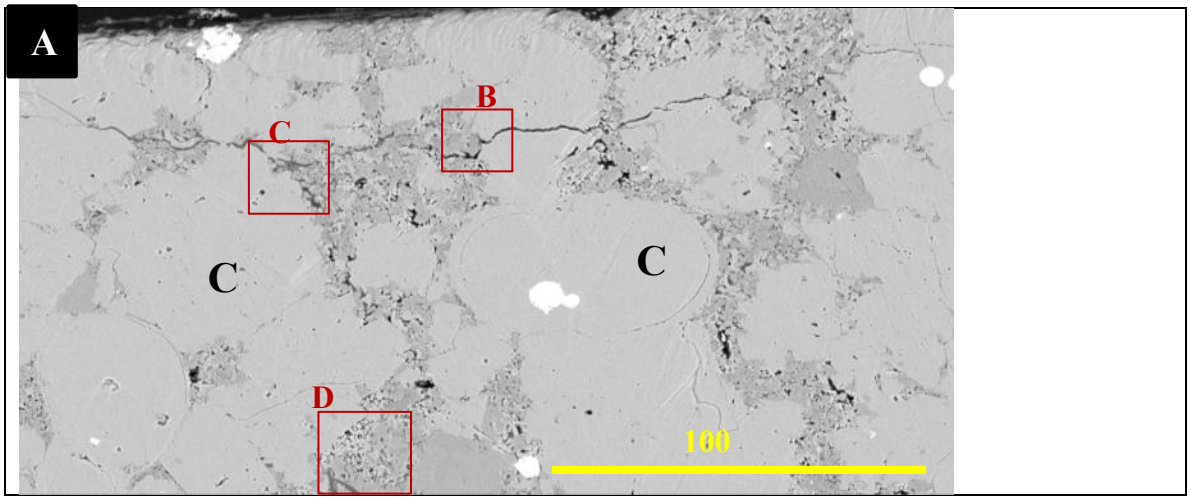

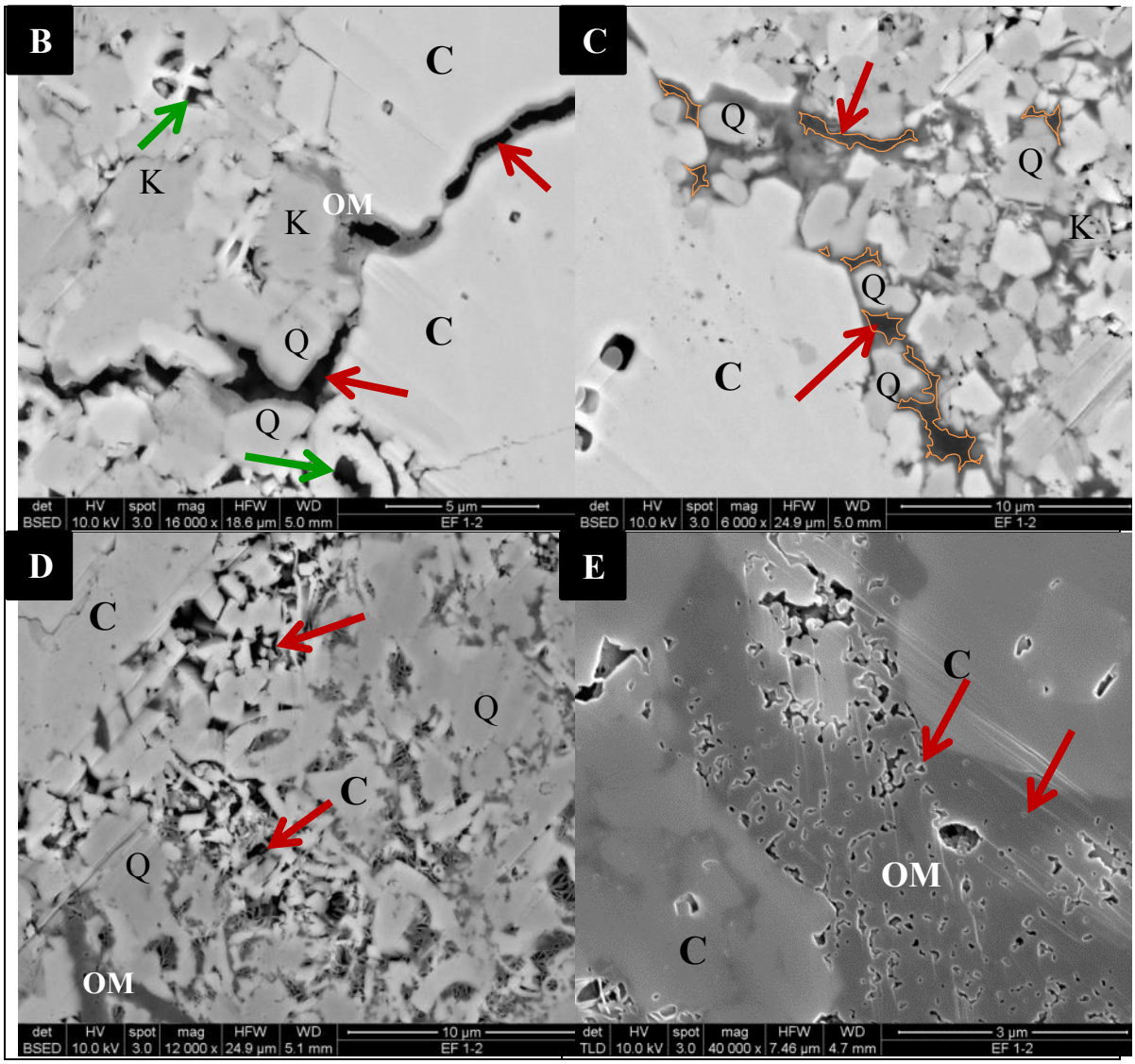

Figure 2.16: SEM photomicrographs of Boquillas sample heated to 425°C for 72 hours showing different pore types (arrows) at the cracking of oil to gas stage. (A) Overview of the backscattered electron (BSE) image area. (B) Modified mineral pores (red arrows) and primary mineral pores (green arrows). (C) Modified mineral pores (circled by orange lines with red arrows). (D) Modified interparticle mineral pores (red arrows) between clay mineral (illite) and grains (calcite and quartz). (E) Nanometer-sized spongy OM pores (red arrows) in OM. Backscattered electron (BSE) images. C: calcite; Q: quartz; K: kaolinite.

2.7.3 Porosity Relationships to Matrix Type

Pore-size distribution (PSD) and porosity were examined in millimeter-scale areas of different rock matrix types within our larger sample for the transitions from bitumen and oil to gas conversion: (1) calcite-dominated (within calcareous fossil fragments), (2) quartz-dominated, (3) mixed (clay mineral-, calcite-, and quartz-dominated), and (4) clay mineral (kaolinite, chlorite)-dominated (Figure 2.17). Areas of samples with the calcite-dominated matrix exhibited the highest porosity and the largest pores. Areas having the mixed matrix (clay mineral-, calcite-, and quartz) showed the second highest porosity and the second largest pores. Areas with the quartz-dominated matrix had lower porosity and the third largest pores. Areas with the clay mineral-dominated matrix showed the lowest porosity and the smallest pores. Observations presented here corroborate that there is a direct link between the matrix type, grain size, and present-day primary porosity.

The influence of grain-size distribution on PSD and permeability had been studied for mudrocks (or shales) (Dewhurst et al., 1998, 1999). Without overprint of petroleum expulsion and migration, the PSD of the coarser-grain matrix will be broader and skewed toward the larger radii during compaction at a given effective stress (Dewhurst et al., 1998). Coarser grains (silt-sized particles) generally have lower compressibility than finer grains (clay-sized particles) (Dewhurst et al., 1998). In general, in our samples, calcite grains and crystals (mostly more than 5 μm) were coarser and much more abundant than authigenic quartz crystals (less than 2 μm) and kaolinite crystals. Therefore, areas with the calcite-dominated matrix were expected to experience less compaction, show the largest pores and broadest PSD. This difference in grain-size distribution (e.g. silt-size to clay-size ratio) affects PSD will later impact petroleum migration in pore spaces and the evolution of mineral and OM pore networks.

Calcite-Dominated Matrix Pore Development

A calcite-dominated matrix is mainly composed of broken coccolith plates and segments with sizes ranging from less than one to tens of micrometers. When these grains form aggregates or floccules (possible pellets) and stack together after deposition, abundant micrometer-scale interparticle pores are formed. These interparticle pore spaces were originally filled with sea water. During bitumen and oil generation, these pores become filled with petroleum.

The generalized schematic diagram showing the evolution of pores in the calcite-dominated matrix in the heated Boquillas sample is presented in Figure 2.18. Pores associated with calcite-dominated matrix were mostly modified mineral pores at the bitumen generation stage (Figures 2.8D, 2.18A). Some interparticle mineral pores were also present (Figure 2.8C). At the early oil and oil window generation stages, modified mineral pores were dominant (Figures 2.10, 2.18B). Grey scale differences of organic matter in BSE maps probably suggested at least two phases of petroleum co-existence in pore spaces—possibly bitumen and oil (Figure 2.11B, C). At the end of the oil window and during the early oil cracking to gas stage, fewer modified mineral pores were present compared to bitumen and oil generation stage (Figure 2.18C). However, the abundance of nanometer-sized spongy OM pores (OM porosity) increased in the residual organic matter (probably pyrobitumen) (Figures 2.15E, F, 2.18C). Those pores were probably filled with gas at the high temperature range (400 and 425°C) of the gold-tube reactor. The gas was then expelled from the pores when the gold-tube reactor was exposed to room temperature and pressure conditions. Some oil expulsion probably occurred, resulting in modified mineral pores in our rock cylinder samples when they were drilled

or prepared for SEM. This expulsion is not expected to happen in similar facies of mudrocks in the subsurface, because the overburden pressure is sufficient to retain generated petroleum in the rock matrix during the gas generation and expulsion stages.

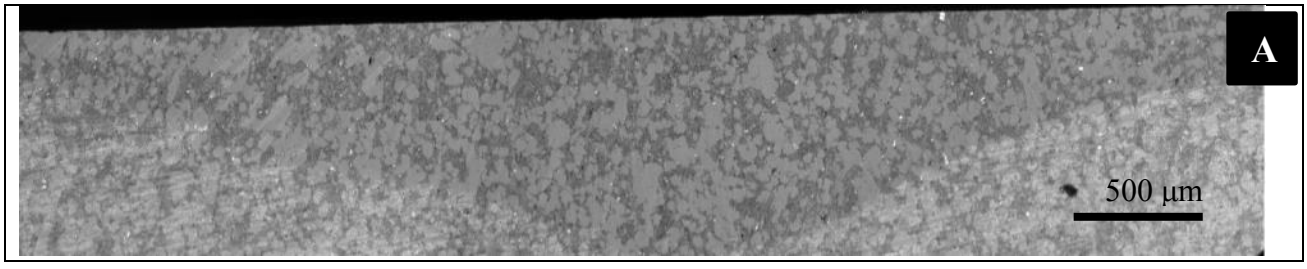

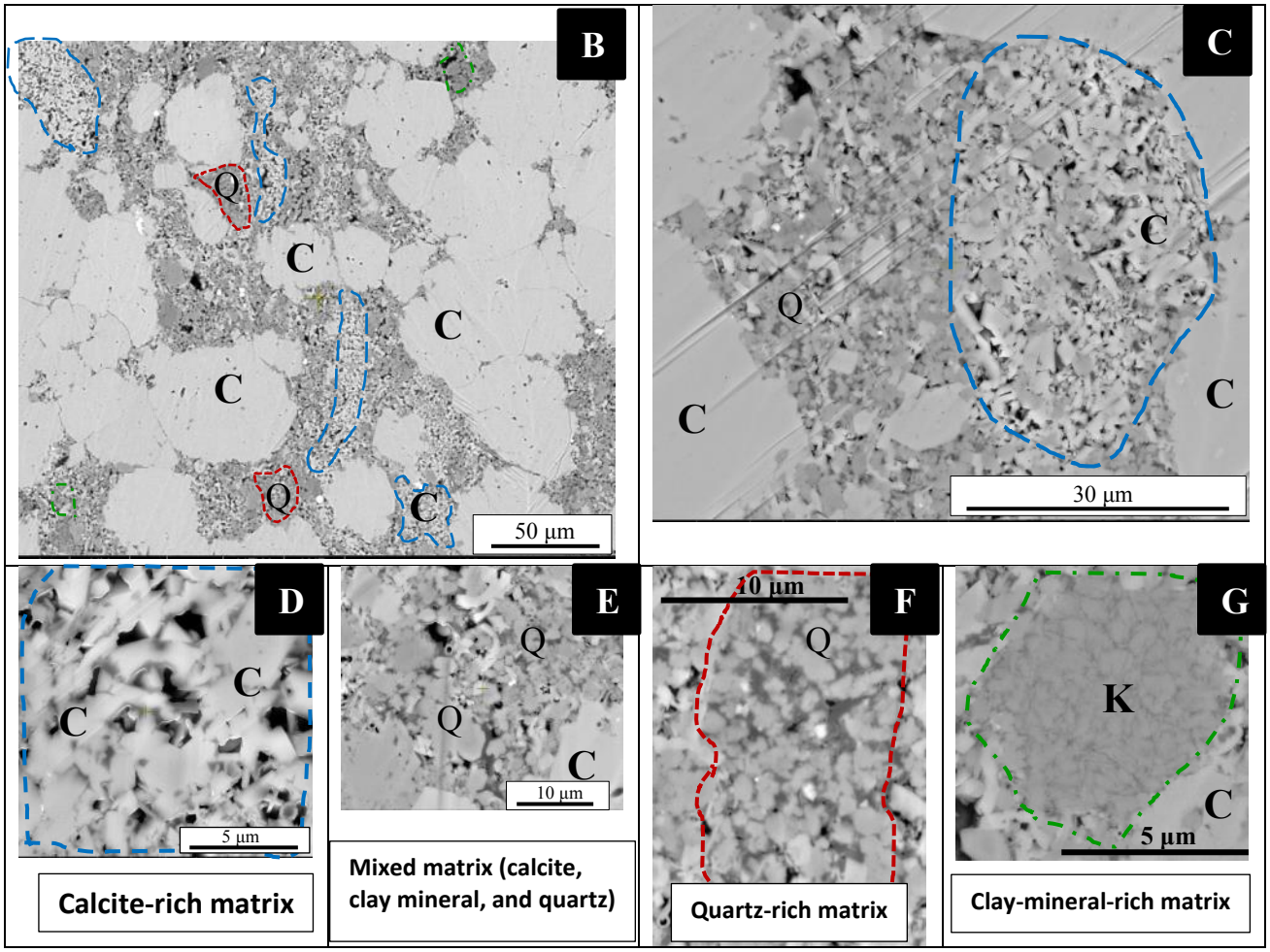

Figure 2.17: SEM photomicrographs of Boquillas sample. (A) Overview of the milled surface. (B) Close-up of a representative area of milled surface (blue dashed outline represents calcite-rich matrix; red dashed outline represents quartz-rich matrix). (C) Calcite-rich matrix (possible fecal pellet). (D) to (G) SEM backscattered electron (BSE) images demonstrating four main types of different matrix composition: (1) Calcite-rich matrix (within calcareous fossil fragment), (2) quartz-rich matrix (within authigenic quartz cement), (3) clay mineral, calcite ,and quartz-mixed mineralogy matrix, and (4) clay-mineral-rich matrix (within kaolinite or chlorite cement). Each matrix type shows different grain- and pore-size distributions and has significant effects on pore network evolution during thermal maturation. Blue-dashed circle: calcite-rich matrix; red-dashed circle: quartz-rich matrix; green-dashed circle: clay mineral-rich matrix. C: calcite; Q: quartz; K: kaolinite.

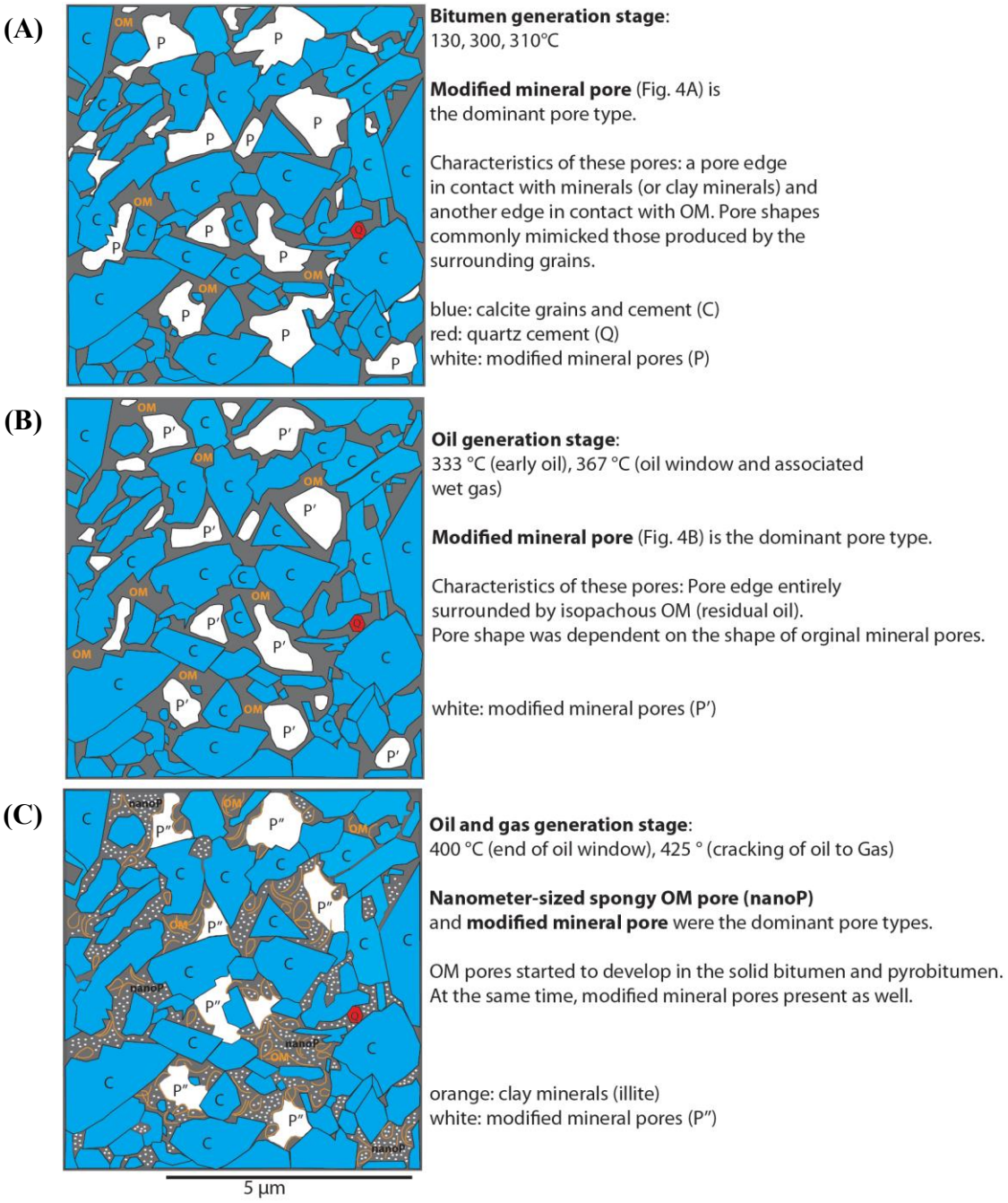

Figure 2.18: Generalized schematic diagram showing pore evolution in calcite-rich matrix area in the heated Boquillas sample. (A) Modified mineral pores are dominant during bitumen generation. (B) Modified mineral pores are dominant during oil generation stage. (C) Nanometer-sized spongy OM pores and modified mineral pores are dominant during the early gas-generation stage.

Quartz-Cement-Dominated-Matrix Pore Development

Examples of pore evolution in the quartz-cement-dominated matrix are shown in Figure 2.19. During the early oil and oil window generation stage, almost no pores were formed in the quartz-cement-dominated matrix (Figure 2.19C, D). At the end of the oil window stage, nanometer-sized spongy OM pores started to appear (Figure 2.19E). At the early oil cracking to gas stage, more OM pores formed among the mineral matrix (Figure 2.19F). Overall porosity in the quartz-cement-dominated matrix increased with thermal maturation.

Mixed Mineralogy Matrix Pore Development

The evolution of pores in the mixed matrix was similar to that in the calcite-dominated-matrix. Modified mineral pores and interparticle mineral pores were the most common pore types during bitumen generation. The pores were up to tens of micrometers in size and in close association with calcite grains. During the oil generation stage, modified mineral pores with isopachous OM rim were most abundant. Similar to pores developed at the bitumen generation stage, these pores were mainly associated with calcareous grains and fragments and had irregular pore shape (Figure 2.13B). At the oil cracking to gas stage, as a result of most of the organic matter being expelled (matured), modified mineral pores were present in the mineral matrix and nanometer-sized spongy OM pores were present in organic matter residues (probably pyrobitumen). Overall porosity in the mixed mineralogy matrix increased with increased thermal maturation.

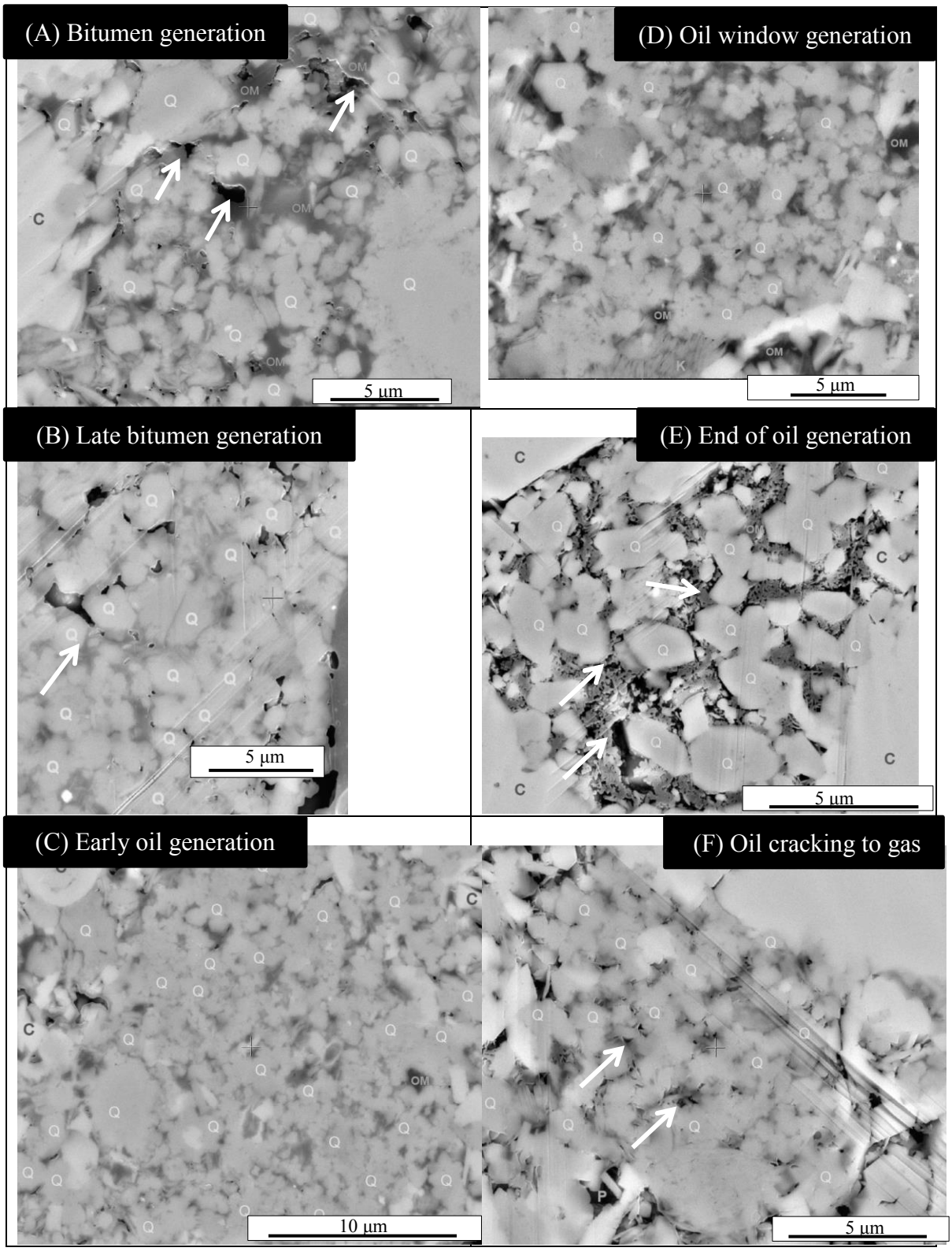
(A) Bitumen generation
(D) Oil window generation
(B) Late bitumen generation
(E) End of oil generation
(C) Early oil generation
(F) Oil cracking to gas
5 µm
5 µm
5 µm
5 µm
10 µm
5 µm

Figure 2.19: Pore evolution in quartz cement dominated matrix. (A) and (B) Few modified mineral pores (white arrows) are developed in quartz-rich matrix at the bitumen generation stage. (C) and (D) No pores were observed during both early oil and oil window generation stages. (E) Peak oil generation stage: OM between quartz crystals converts to oil and gas and form nanometer-sized OM pores (white arrows) in solid OM residue. (F) At the gas-generation stage from oil cracking, modified mineral pores (white arrows) are formed between illite and OM within the quartz cement dominated matrix. C: calcite; Q: quartz; K: kaolinite; P: mineral pores.

Clay-Mineral-Cement-Dominated-Matrix Pore Development

Authigenic kaolinite cement was common in some Boquillas units and Eagle Ford (Loucks et al., 2012; Pommer, 2014). During both bitumen and oil generation stages, almost no pores were observed within kaolinite-dominated matrix areas. During the cracking of oil to gas stage, modified interparticle and intraparticle pores associated with clay mineral platelet were commonly observed. Therefore, in our experiments, overall porosity in the clay-mineral-cement-dominated matrix increased with thermal maturation, as it does in the quartz-cement-dominated matrix.

2.7.4 Quantification of Pore Size Distribution and Porosity

Areas of the calcite-dominated matrix showed the highest porosity and broadest pore size distribution. The mixed mineralogy matrix areas showed the second highest porosity. The quartz-dominated matrix showed the third highest porosity, and the clay mineral-dominated matrix showed the lowest porosity.

We compared pore size distribution and point-count porosity of calcite-dominated and quartz-dominated matrix in the unheated Boquillas sample (Figure 2.20). Results are from manual pore tracing on two backscattered electron images. A total of 300 pore

spaces were traced on each randomly selected image. The point-count porosity is 5.62% in the quartz-dominated matrix and 10.78% in the calcite-dominated matrix.

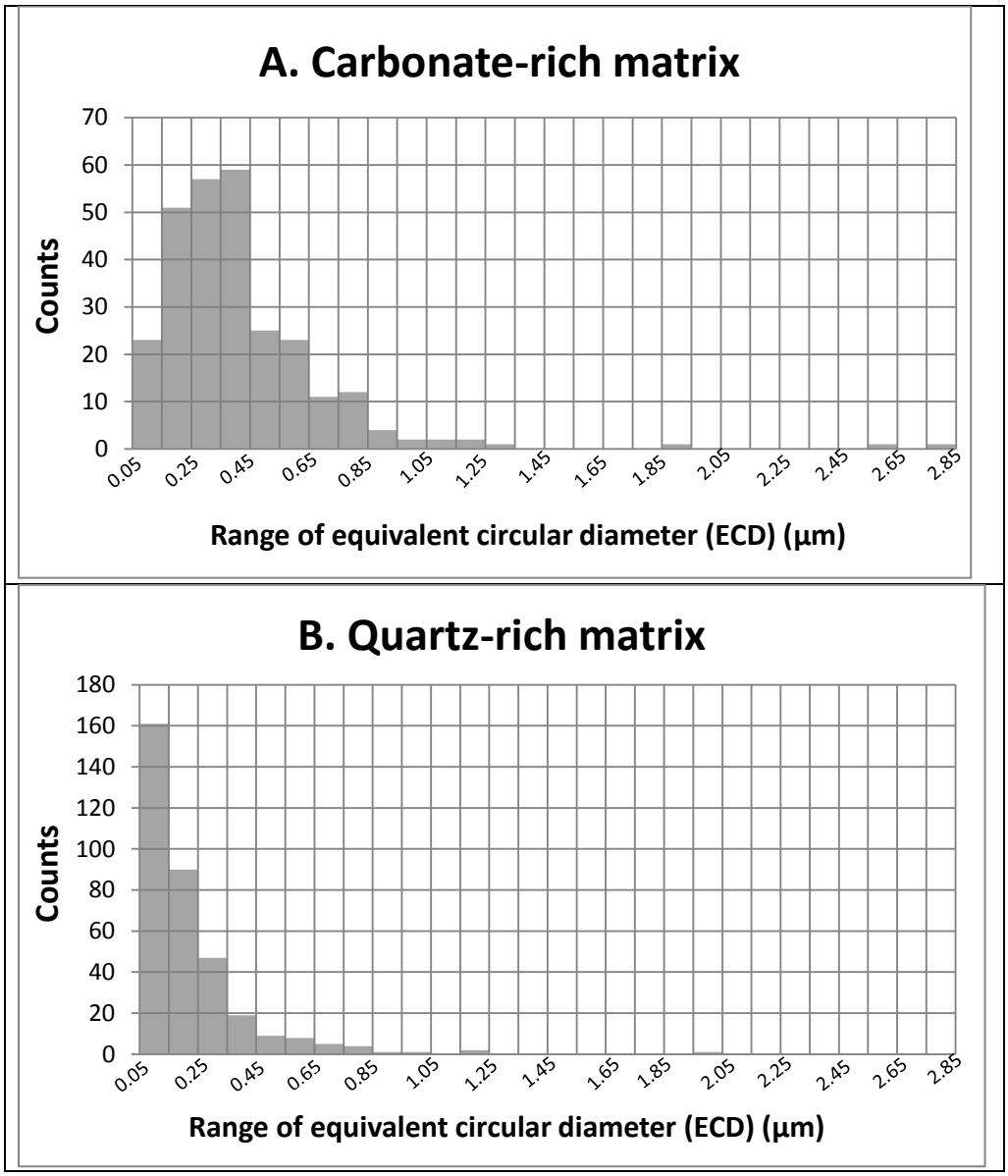

Figure 2.20: Plots comparing pore-size distribution in carbonate-rich matrix (A) and quartz-rich matrix (B) in unheated Boquillas outcrop sample. Results are from manual pore tracing of two backscattered electron images. Point-count porosity is 5.62 % in the quartz-rich matrix and 10.78% in the calcite-rich matrix. Equivalent circular (or cylindrical) diameter (ECD) is the diameter of a circle with the same area as that of the object.

2.8 DISCUSSION

2.8.1 Grain Assemblages in the Unheated Sample

The high carbonate content (>80 wt. %) and rare terrigenous grain assemblage in the studied sample can be explained by high biological productivity of skeletal carbonate and little terrigenous influx from the land. In addition, laminated nature of these Boquillas rocks implies that reworking and winnowing processes on these fine-grained particles are also significant (e.g. Schieber et al., 2007; Schieber and Southard, 2009; Schieber et al., 2010). Abundant cemented calcite grains were observed and are products of diagenetic cement of planktonic nanofossils and recrystallization. Except for cemented calcite grains, the carbonate planktons (blue dashed outline in Figure 2.17C) were the primary contributor to the high carbonate content. The carbonate plankton can settle to the sea floor by fecal pelletization or be deposited as "marine snow," aggregates or flocks of various biogenic materials and POM (Silver et al., 1978; Allderdge and Silver, 1988; Macquaker et al., 2010). The calcareous aggregate was predominantly composed of broken pieces of coccolithophores (planktonic unicellular algae) characterized by its circular or ovoid shape with a cross-shaped interior (Figures 2.8D, 2.11C, 2.15B). This primary sediment may have been nearly pure calcite with little or no aragonite. The original coccolith sediment is diagenetically stable in its early burial history, but will become well cemented with burial.

Two-dimensional cross-cutting relationships observed in SEM photomicrographs revealed part of the paragenetic history of this sample. Calcite, quartz, and kaolinite

cementation were commonly observed. Pore-scale to bed-scale petroleum expulsion and migration probably occurred during or after the precipitation of these cements, because hydrocarbon would have inhibited cementation. The possibility that some petroleum (bitumen) migration might have occurred prior to the cementation also cannot be ruled out. However, the relative timing of quartz and kaolinite cementation and bitumen migration is beyond the scope of this study.

A generalized model was proposed for the formation and evolution of pores, from deposition through bitumen generation (Figure 2.21). Calcite made up to at least 80 wt. % of the rock (Table 2.1) and was the primary constituent upon deposition. Pore spaces at this time were abundant and filled with sea water as shown in Step 1 (Figure 2.21). The cemented euhedral calcite grains suggested a possible dual biogenic and diagenetic origin, although we did not investigate its relative timing of cementation. Nonetheless, extensive diagenetic calcite was identified in other part of the Eagle Ford by Ergene (2014). Euhedral quartz crystals were also identified as cement using SEM-CL (cold-cathode) technique. The pervasively euhedral character of kaolinite booklet crystals was evidence of a diagenetic origin. The precipitation of kaolinite booklets and authigenic quartz cement required the oversaturation of silica and potassium in the formation water. Although the cause of this oversaturation was unclear, it was interpreted as related to dissolution of volcanic ash or detrital feldspar deposited during Boquillas (Eagle Ford-equivalent) deposition (Harbor, 2011; Pommer, 2014). This precipitation of authigenic quartz and kaolinite resulted in a decrease of porosity in the rock as shown in Step 2 (Figure 2.21). In addition, petrographic evidence of pore-scale organic matter (petroleum)

migration inhibiting calcite cementation was noted. Organic matter (possibly solid bitumen) was commonly observed along the boundary among calcite grains (Figure 2.22).

Step 1: Early diagenetic calcite and calcareous fossil fragments were dominant mineral constituents. Interparticle pores (P) were abundant and filled with formation water.
C: calcite; P: pore.

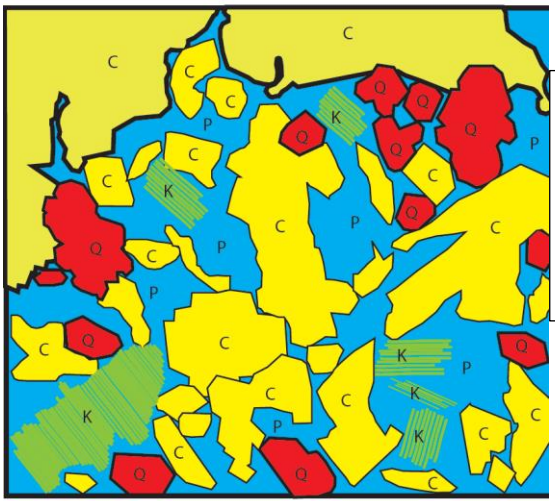

Step 2: Formation water became oversaturated with silicon and potassium likely because of dissolved volcanic ash or feldspar, causing precipitation of authigenic quartz crystals and kaolinite booklets.
Overall porosity has decreased due to compaction and cementation. C: calcite; K; kaolinite; Q: quartz; P: pore.

Step 3: Bitumen was generated, expelled, and migrated into adjacent interparticle pores, displacing formation water. The distribution of bitumen implies that most pores were interconnected. Some irreducible water and gas remained. Modified mineral pores were originally filled with oil, gas, water, or mixture of all.
C: calcite; K; kaolinite; Q: quartz.

Figure 2.21: A generalized model for the formation and evolution of modified mineral pores observed in the bitumen generation stage.

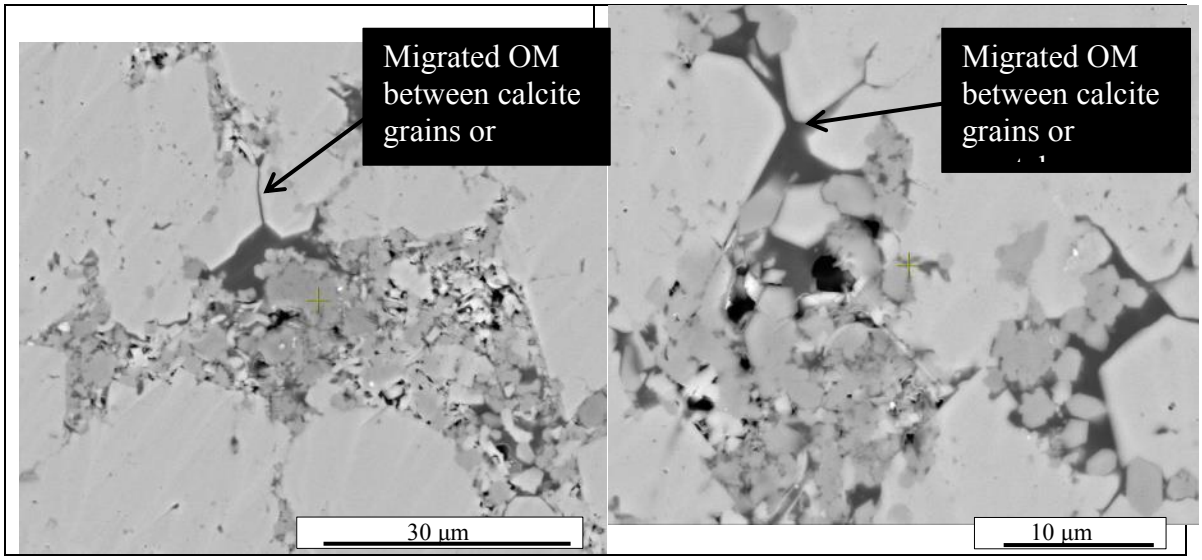

Figure 2.22: Examples of petrographic evidence of pore-scale OM (petroleum) migration inhibiting further calcite cementation.

2.8.2 Origin of Early Formed Pores in Unheated Sample

The proposed model for the formation of modified mineral pores in the unheated Boquillas sample is shown continuously in Figure 2.21. The formation of modified mineral pores was interpreted to be associated with petroleum (bitumen) migration and possible mixing wettability of mineral grains. With increased burial of the Boquillas strata in the outcrop area, kerogen matured with increasing temperature during burial. Bitumen was then generated, expelled, and migrated (on a pore scale) to displace much of the formation water in pores. The pore network was gradually filled with bitumen, but retained some irreducible water. From observations of the sample, the bitumen penetrated almost all the pore spaces, implying that the pores were interconnected. The extent of bitumen also implied that generation pressures created by the kerogen to bitumen transformation probably exceeded the capillary pressure of formation water in the original pore throats. Bitumen, as originally defined, is viscous asphaltene- and NSO-rich

petroleum (mainly C_{15}+ fraction). When bitumen migrated through a pore, framework mineralogy might have had chemical and physical effects on the bitumen. In addition, there could have been changes in the wettability of mineral surfaces as well as physical and chemical adsorptions (Honarpour et al., 2012). It is proposed that the occurrence of modified mineral pores is possibly the result of combined bitumen migration, property changes related to mineralogy, and sample preparation processes.

2.8.3 Comparison of Pores in Naturally Matured and Artificially Heated Samples

Comparison of pores in the calcite-dominated facies in Eagle Ford core samples by Pommer (2014) and in the outcrop Boquillas experimental sample illustrated both similarities and differences in petroleum retention, pore size, and pore shape. Pores in subsurface Eagle Ford cores have been documented by several authors (Driskill et al., 2012, 2013; Jennings and Antia, 2013; Loucks and Reed, 2014; Pommer, 2014; Pommer and Milliken, 2015). Bubble-shaped pores within the organic matter (see center photograph in Figure 27 from Driskill et al., 2012) were similar to the proposed modified mineral pores in both pore size and shape. Intercrystalline pores in replacive limestones (see left photograph in Figure 27 in Driskill et al., 2012) were similar to the interparticle and intraparticle mineral pores in this study. Modified mineral pores with isopachous OM rim were also observed in the Pennsylvanian Caddo Limestone unit in Stephens Country, Texas (Robert Loucks, personal communication, June 6, 2015). The most significant difference regarding pores observed in naturally matured and artificially heated rocks was the high abundance of modified mineral pores in our early gas window samples. Differences in the amount and mechanism of petroleum retention between naturally matured Eagle Ford and artificially heated Boquillas samples might potentially account for this difference in pore development. Even though the confining pressure was designed

to simulate subsurface conditions, the pressure (10,000 psi or 68.95 MPa) exerted on samples in the gold tubes was insufficient to withhold the petroleum generation pressure, especially during the gas window generation. Although the designed confining pressure of the experiments was isotropic and differed from the anisotropic pressure regime in the subsurface (overburden stress >> horizontal stress), the difference in pressure distribution between the subsurface and laboratory should result in no difference in pore size and shape because the rock is well cemented and has a rigid framework. It is possible that the viscosity and mobility of generated oil are not the same in the subsurface versus at the laboratory condition. The loss of generated oil and gas in the rock cylinders led to the abnormal abundance of interparticle mineral pores, which might not occur in mudrocks in the subsurface.

The trapped organic matter observed during gas generation from oil cracking can be particulate organic matter (kerogen of possible terrestrial origin), residual solid bitumen, residual oil, pyrolyzed OM (pyrobitumen or char), or a mixture of at least two of the above. Bernard et al. (2012) suggested that the residual organic matter that hosts nanometer-sized OM pores might be pyrobitumen and the majority of trapped organic matter is possibly pyrobitumen because nanopores are commonly seen. The idea is still debatable because nanometer-sized OM pores are observed in low maturity (0.7 to 0.8% R_o) mudrocks as well (Rob Reed, personal communication, March 20, 2015). More research work will be needed to identify the differences in composition and structure of solid bitumen, pyrobitumen, and char.

2.8.4 Pore Evolution and Connectivity

The petrographic challenges of identifying different kinds of chemically-defined OM (e.g., kerogen, solid bitumen, etc.) using high-resolution SEM petrography have been addressed (Loucks and Reed, 2014; Milliken et al., 2014). However, using combined SEM petrographic observations and geochemical data, the origin and evolution of OM pores and mineral pores can be perceived (Figures 2.21, .2.23, and 2.24). Comparison of Rock-Eval and EOM data (Figure 2.6), yields of gaseous compounds, EOM, and the relative proportions of saturated, aromatic, asphaltene and NSO components (Figure 2.9) suggested that most of the organic matter in the Boquillas sample is primarily bitumen or a mixture of both kerogen and bitumen.

Pore evolution was shown to be closely related to organic matter conversion in the experiments. The morphology of OM-associated Boquillas pores varied with stages of organic matter (predominantly bitumen) conversion. The major types of pores changed from primary mineral pores (immature), to modified mineral pores (related to generation and migration of petroleum - bitumen and oil), and finally to both modified mineral pores and nanometer-sized spongy OM pores (Figures 2.23, 2.24). The formation of nanometer-sized spongy OM pores was interpreted to be related to the cracking of oil to gas or rearrangement of organic matter structure. The mineral-pore network evolution starts from the original interparticle and intraparticle pores before petroleum generation and migration begins, which are a function of depositional and early diagenetic processes (Step 1 and 2 in Figure 2.21). This original mineral pore network preset and constrained petroleum migration and organic matter re-distribution, thus controlling the modified

mineral pore network and OM pore network. Depositional and diagenetic (physical compaction and chemical alteration) processes, as well as steps of organic matter conversion, all affected the pore evolution and distribution.

Bitumen generation stage:
Bitumen generation is dominant, and associated with the earliest gas generation.
Modified mineral pores (P) are most abundant.
These pores are commonly micrometer size.
Pore shape is irregular and mimics the surrounding grain framework.

C: calcite; Q: quartz; K: kaolinite.

Oil generation stage:
Oil generation is the dominant process and gas generation is minor.
Modified mineral pores (P) with isopachous residual OM layers are most abundant.
Pores are commonly micrometer size and subrounded.
Size and number of modified mineral pores decrease compared to bitumen stage.

C: calcite; Q: quartz; K: kaolinite.

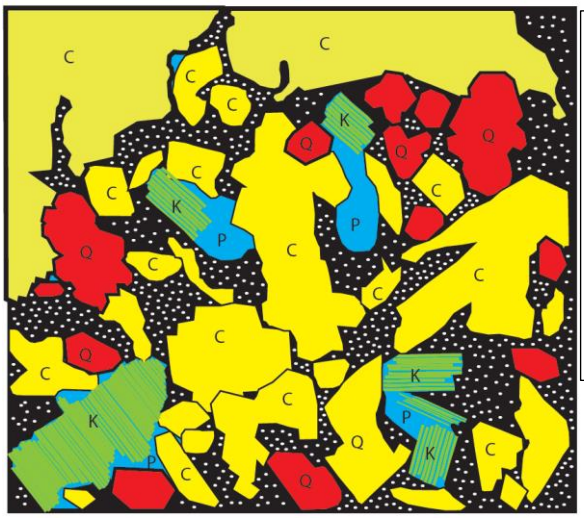

Gas generation stage:
Gas (methane primarily) is the dominant product.
Nanometer-size spongy OM pores (white dots within black OM) are developed and dominant.
Modified mineral pores also present but were filled with oil, gas, water, or mixture of all in the subsurface.

C: calcite; Q: quartz; K: kaolinite.

Figure 2.23: Proposed model for the evolution of pores from bitumen to oil to gas generation stages. (A) Modified mineral pore is the most abundant pore type at bitumen generation stage, (B) Modified mineral pore is the most abundant pore type at oil generation stage, and (C) Modified mineral pore and nanometer-sized spongy OM pores are the most abundant pore types at early gas generation stage.

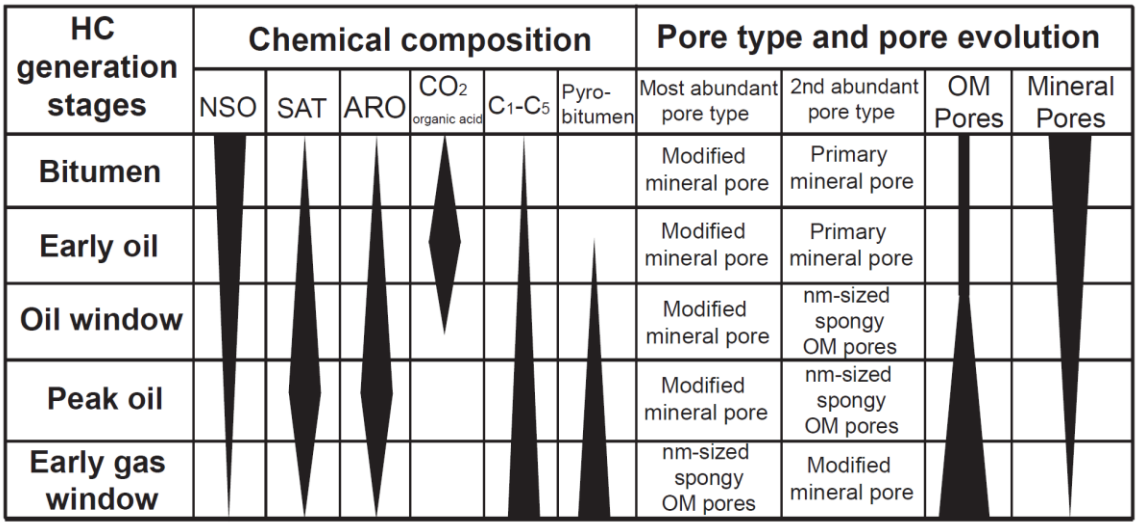

Figure 2.24: Pore evolution can be related to geochemical characterization of generated petroleum components. Four types of OM pores and modified mineral pores were recognized. Their abundance changes during different stages of petroleum generation, affected by chemical composition of generated hydrocarbons.

If the starting material is primarily kerogen instead of bitumen, we expect the pore evolution story to be similar. The pore evolution of kerogen as a starting reactant is also currently under investigation using Mississippian Barnett Shale (cored well in Texas) and Late Devonian–Early Mississippian Woodford Shale (outcrops in Oklahoma) samples.

Four major mineralogy matrix domains at the millimeter scale (calcite-dominated, quartz-dominated, mixed mineralogy-dominated, and clay-mineral-dominated) all showed distinct pore evolution paths in the experiments. In general, as the connectivity of pores in individual matrix types increased, the pore connectivity among domains inside matrix increased as well, along with thermal maturation. During bitumen and oil generation, modified mineral pores were generally developed in areas of calcite grains (calcite-dominated and mixed mineralogy-dominated). During wet-gas and dry-gas generation, nanometer-sized spongy OM pores started to develop in organic matter. The OM porosity correlates with increased maturity. Although the pore evolution that was observed in the Boquillas sample probably was not exactly replicated in naturally matured samples, some insights on pore evolution were obtained. First, there is a likelihood of modified mineral pores being connected to a certain extent. The connectivity could depend on the amount of fluid generated, the distance of pore-scale to bed-scale petroleum migration, and the snap-off effect (Roof, 1970). Second, the abundance of fecal pellets and mud-sized carbonate aggregates (calcite-dominated matrix) significantly influences the porosity and permeability in the rock because the micrometer-sized pores are in close association with the pellets. Third, the nanometer-

sized pores are possibly related to gas generation maturation because they were both found during the gas generation window in the subsurface and artificially heated samples.

2.9 CONCLUSIONS

Combined organic matter heating experiments, geochemical characterization, and SEM petrography of samples from the Upper Cretaceous Boquillas coccolith-rich calcareous mudrocks (limestone facies) documented how pores evolve in mudrocks with increased thermal maturation. Geochemical and petrographical evidence showed that the majority of the organic matter in low-maturity Boquillas samples used in this investigation was in the form of bitumen. Therefore, this study mainly demonstrated how organic matter, OM pores, and mineral pores evolve with increasing levels of maturity. It should be noted that the stages we documented were the major stages of pore development.

Pore evolution can be postulated before and after organic matter maturation. The original interparticle and intraparticle pores, which are a function of depositional and early diagenetic processes, determined the mineral pore network before petroleum generation and migration begins. The mineral pore network preset and constrained petroleum (bitumen and oil) migration and organic matter re-distribution and thus controlled the modified mineral pore and OM pore network after thermal maturation of organic matter. When organic matter became mature, the pore evolution was closely related to gradual organic matter conversion. The morphology of both mineral and OM pores varied with the stages of organic matter maturation. Predominant types of pores

changed from modified mineral pores with relic OM during bitumen generation through oil window. During the early oil cracking into gas, both nanometer-sized spongy OM pores and modified mineral pores are abundant. In conclusion, the occurrence of mineral pores with relic OM was probably the result of combined bitumen, oil, and/or gas migration, wettability property changes of mineral surfaces, and during any sample preparation processes. The modified mineral pores with relic OM were probably associated with gas and liquid (oil or water) inclusions within solid bitumen, pyrobitumen, and char. The formation of nanometer-sized spongy OM pores was interpreted to be related to the cracking of oil or solid bitumen to gas and rearrangement of organic matter structure. We also found several co-existing pore types in the early oil, oil window, and gas generation stages when kerogen, solid bitumen, pyrobitumen, char, gas, oil, and products from secondary cracking all existed in the host mudrock.

Although the pore evolution observed in the Boquillas heated sample might not be perfectly replicated in naturally matured samples, several concepts relative to pore evolution were achieved. First, pore evolution and distribution are affected not only by organic matter conversion, but also by depositional and diagenetic (physical compaction and chemical alteration) processes. Second, there is a strong possibility that the modified mineral pores with migrated relic OM will be connected to a certain extent because organic matter becomes connected by pore-scale to bed-scale petroleum migration. Connectivity depends on the amount of fluid generated, distance of migration, and the snap-off effect. Third, the abundance of fecal pellets and mud-sized carbonate aggregates (calcite-dominated matrix) significantly influences the porosity and permeability of the

rock because the micrometer-sized modified mineral pores are in close association with those calcite grains and crystals. Finally, the nanometer-sized pores are possibly related to gas generation resulting from oil or pyrobitumen cracking, because they were both found in the gas window in naturally matured and artificially heated samples. This study sheds light on the importance of initial pore networks as well as possible change in wettability during thermal maturation in mudrocks. Understanding the changes in pore morphology with organic matter conversion and increasing connectivity of organic matter during petroleum generation can lead to improved fluid flow models and prediction of permeability in mudrock systems.

ACKNOWLEDGMENTS

The outcrop samples for this study were provided by Gregory Frebourg at the Bureau of Economic Geology (BEG) at The University of Texas at Austin. Results of x-ray diffraction analyses were provided by K-T GeoServices,Inc. I would like to thank Patrick Smith for providing argon ion milling and sample coating at the BEG scanning electron microscopy laboratory. I also thank Lanzhou University, China, for carrying out the pyrolysis experiments under the support of the Major State Basic Research Development Program of China (grant 2012CB214701). This study was also financially supported by the National Key Basic Research Program of China (973 Program: 2012CB214701). I thank Kitty Milliken, Max Pommer, Joel Lunsford, Robert Reed, Terri Olson, and Tobi Kosanke for discussions, suggestions, and inspirations during the manuscript preparation. I also would like to thank the Mudrock System Research Laboratory sponsors who

supported this research: Anadarko, BP, Centrica, Cenovus, Chesapeake, Cima, Cimarex, Chevron, Concho, ConocoPhillips, Cypress, Devon, Encana, ENI, EOG, EXCO, ExxonMobil, Hess, Husky, Kerogen, Marathon, Murphy, Newfield, Penn West, Penn Virginia, Pioneer, Samson, Shell, Statoil, Talisman, Texas American Resources, the Unconventionals, US EnerCorp, Valence, and YPF.

ABBREVIATIONS

BIB: broad ion beam
BSE: backscattered electron
CL: cathodoluminescence
D: fractal dimension
ECD: equivalent circular (or cylindrical) diameter
EDS: energy-dispersive spectroscopy detectors
EF: Eagle Ford
EOM: extractable organic matter
FE-SEM: field-emission scanning electron microscopy
FIB: focused ion beam
GC: gas chromatography
HC: hydrocarbon
HFW: horizontal field width
HI: hydrogen index
ID: internal standard
InterP: interparticle
IntraP: intraparticle
I/S: interlayered illite and smectite
NSO: nitrogen, sulfur, oxygen, and heavy metals
OI: oxygen index
OM: organic matter
POM: particulate organic matter
PSD: pore size distribution
SARA: saturate, aromatic, resin, NSO, and asphaltene
SE: secondary electron
SEM: scanning electron microscopy
STXM: scanning transmission X-ray microscopy
TLD: through-the-lens detector
TOC: total organic carbon
VR: vitrinite reflectance

REFERENCES

Alldredge, A. L., and M. W. Silver, 1988, Characteristics, dynamics, and significance of marine snow: Progress in Oceanography, v. 20, p. 41–82.

Ambrose, R. J., R. C. Hartman, M. D. Campos, I. Y. Akkutlu, and C. H. Sondergeld, 2010, New pore-scale considerations for shale gas in place calculations: Society of Petroleum Engineers Unconventional Gas Conference, Pittsburgh, Pennsylvania, February 23–25, 2010, SPE Paper 131772, 17 p.

Bastow, T. P., B. G. K. van Aarssen, and D. Lang, 2007, Rapid small-scale separation of saturate, aromatic, and polar components in petroleum: Organic Geochemistry, v. 38, p. 1235–1250.

Bernard, S., B. Horsfield, H.-M. Schulz, A. Schreiber, R. Wirth, T. T. A. Vu, F. Perssen, S. Könitzer, H. Volk, N. Sherwood, and D. Fuentes, 2010, Multi-scale detection of organic and inorganic signatures provides insights into gas shale properties and evolution: Chemie der Erde - Geochemistry, v. 70, no. S3, p. 119–133.

Bernard, S., B. Horsfield, H.-M. Schulz, R. Wirth, A. Schreiber, and N. Sherwood, 2012a, Geochemical evolution of organic-rich shales with increasing maturity: A STXM and TEM study of the Posidonia Shale (Lower Toarcian, northern Germany): Marine and Petroleum Geology, v. 31, p. 70–89.

Bernard, S., R. Wirth, A. Schreiber, H.-M. Schulz, and B. Horsfield, 2012b, Formation of nanoporous pyrobitumen residues during maturation of the Barnett Shale (Fort Worth Basin): International Journal of Coal Geology, v. 103, p. 3–11.

Bernard, S., R. Wirth, A. Schreiber, L. Brown, A.C. Aplin, E. J. Mathia, H.-M. Schulz, and B. Horsfield, 2013, FIB-SEM and TEM investigations of an organic-rich shale maturation series from the Lower Toarcian Posidonia Shale, Germany: Nanoscale pore system and fluid-rock interactions, in E. D. W. Camp, and B. Wawak, eds., Electron microscopy of shale hydrocarbon reservoirs: AAPG Memoir 102, p. 53–66.

Bohacs, K. M., Q. M. Passey, M. Rudnicki, W. L. Esch, and O. R. Lazar, 2013, The spectrum of fine-grained reservoirs from "shale-gas" to "shale oil"/tight liquids: essential attributes, key controls, practical characterization: International Petroleum Technology Conference (IPTC), Beijing, China, March 26–28, 2013, IPTC Paper 16676, 16 p.

Bustin, R., A. Bustin, A. Cui, and D. Ross, 2008, Impact of shale properties on pore structure and storage characteristics: Society of Petroleum Engineers Shale Gas Production Conference, Fort Worth, Texas, USA, November 16–18, 2008, SPE Paper 119892, 28 p.

Cook, A. C., and N. R. Sherwood, 1991, Classification of oil shales, coals, and other organic-rich rocks: Organic Geochemistry, v. 17, p. 211–222.

Curiale, J. A., 1986, Origin of solid bitumens, with emphasis on biological marker results: Organic Geochemistry, v. 10, p. 559–580.

Curtis, M. E., R. J. Ambrose, C. H. Sondergeld, and C. S. Rai, 2010, Structural characterization of gas shales on the micro- and nano-scales: Canadian Unconventional Resources and International Petroleum Conference, Calgary, Alberta, Canada, October 19–21, 2010, CUSG/SPE Paper 137693, 15 p.

Curtis, M. E., C. H. Sondergeld, R. J. Ambrose, and C. S. Rai, 2012, Microstructural investigation of gas shales in two and three dimensions using nanometer-scale resolution imaging: AAPG Bulletin, v. 96, p. 665–677.

Dahl, J., R. T. Chen, and I. R. Kaplan, 1989, Alum Shale bitumen maturation and migration: implications for Gotland's Oil: Journal of Petroleum Geology, v. 12, p. 465–476.

Desbois, G., J. L. Urai, and P. A. Kukla, 2009, Morphology of the pore space in claystones- Evidence from BIB/FIB ion beam sectioning and cryo-SEM observations: Earth, v. 4, p. 15–22.

Dewhurst, D. N., S. C. Aplin, J.-P. Sarda, and Y. Yang, 1998, Compaction-driven evolution of porosity and permeability in natural mudstones: an experimental study: Journal of Geophysical Research, v. 103, p. 651–661.

Dewhurst, D. N., Y. Yang, and A. C. Aplin, 1999, Permeability and fluid flow in natural mudstones, in A. C. Aplin, A. J. Fleet, and J. H. S., Macquaker, eds., Muds and mudstones: Physical and fluid flow properties: Geological Society (London) Special Publication 158, p. 23–43.

Driskill, B., N. Suurmeyer, S. Rilling-Hall, A. Govert, and A. Garbowicz, 2012, Reservoir Description Of The Subsurface Eagle Ford Formation, Maverick Basin Area, South Texas, USA: Society of Petroleum Engineers Europec/EAGE Annual Conference & Exhibition, Copenhagen, Denmark, June 4–7, 2012, SPE Paper 154528, 23 p.

Driskill, B., J. Walls, S. W. Sinclair, and J. DeVito, 2013, Applications of SEM imaging to reservoir characterization in the Eagle Ford Shale, south Texas, U.S.A., in W. Camp, E. Diaz, B. Wawak, eds., Electron microscopy of shale hydrocarbon reservoirs: AAPG Memoir 102, p. 115–136.

Durand, B., 1980, Kerogen: Insoluble organic matter from sedimentary rocks: Paris, Technip, 519 p.

Ergene, S. M., 2014, Lithologic heterogeneity of the Eagle Ford Formation, South Texas: Austin, The University of Texas at Austin, 203 p.

Fishman, N. S., P. C. Hackley, H. A. Lowers, R. J. Hill, S. O. Egenhoff, D. D. Eberl, and A. E. Blum, 2012, The nature of porosity in organic-rich mudstones of the Upper Jurassic Kimmeridge Clay Formation, North Sea, offshore United Kingdom: International Journal of Coal Geology, v. 103, p. 32–50.

Hackley, P. C., C. V. Araujo, A. G. Borrego, A. Bouzinos, B. Cardott, A. C. Cook, C. Eble, D. Flores, T. Gentzis, P. A. Gonçalves, J. G. Mendonça Filho, M. Hámor-Vidó, I. Jelonek, K.

Kommeren, W. Knowles, J. Kus, M. Mastalerz, T. R. Menezes, J. Newman, M. Pawlewicz, W. Pickel, J. Potter, P. Ranasinghe, H. Read, J. Reyes, G. De La Rosa Rodriguez, I. V. Alves Fernandes de Souza, I. Suarez-Ruiz, I. Sýkorová, B. J. Valentine, 2014, Standardization of reflectance measurements in dispersed organic matter: results of an exercise to improve interlaboratory agreement: Marine and Petroleum Geology, v.59, p. 22-34.

Harbor, R. L., 2011, Facies Characterization and stratigraphic architecture of organic-rich mudrocks, Upper Cretaceous Eagle Ford Formation, South Texas: Austin, The University of Texas at Austin, 195 p.

Honarpour, M. M., N. R. Nagarajan, A. Orangi, F. Arasteh, and Z. Yao, 2012, Characterization of critical fluid, rock, and rock-fluid properties – impact of reservoir performance of liquid-rich shales: Society of Petroleum Engineers Annual Technical Conference and Exhibition, San Antonio, Texas, USA, October 8–10, 2012, SPE Paper 158042, 22 p.

Hunt, J. M., 1996, Petroleum geochemistry and geology: New York, New York, W.H. Freeman and Company, 746 p.

Jennings, D. S., and J. Antia, 2013, Petrographic characterization of the Eagle Ford shale, south Texas: mineralogy, common constituents, and distribution of nanometer-scale pore types, in W. Camp, E. Diaz, B. Wawak, eds., Electron microscopy of shale hydrocarbon reservoirs: AAPG Memoir 102, p. 101–113.

Kanitpanyacharoen, W., F. B. Kets, H.-R. Wenk, and R. Wirth, 2012, Mineral preferred orientation and microstructure in the Posidonia shale in relation to different degrees of thermal maturity: Clay and Clay Minerals, v. 60, p. 315–329.

Klaver, J., G. Desbois, J. L. Urai, and R. Littke, 2012, BIB-SEM study of the pore space morphology in early mature Posidonia Shale from the Hils area, Germany: International Journal of Coal Geology, v. 103, p. 12–25.

Kulia, U., M. Prasad, A. Derkowski, and D. K. McCarty, 2012, Compositional controls on mudrock pore-size distribution: an example from Niobrara Formation: Society of Petroleum Engineers Annual Technical Conference and Exhibition, San Antonio, Texas, USA, October 8–10, 2012, SPE Paper 160141, 16 p.

Kulia, U., 2013, Measurement and interpretation of porosity and pore-size distribution in mudrocks: the whole story of shales: dissertation thesis: Golden, Colorado, Colorado School of Mines, 238 p.

Kulia, U., and M. Prasad, 2013, Specific surface area and pore-size distribution in clays and shales: Geophysical Prospecting v. 61, p. 341–362.

Lewan, M. D., 1987, Petrographic study of primary petroleum migration in the Woodford shale and related rock units, in B. Doligez Ed., Migration of Hydrocarbons in Sedimentary Basins: Paris, Editions Technip, p. 113–130.

Lewan, M. D., 1993, Laboratory simulation of petroleum formation, hydrous pyrolysis, in M. S. A. Engel M.H., ed., Organic Geochemistry Plenum Press, p. 419–442.

Loucks, R. G., R. M. Reed, S. C. Ruppel, and D. M. Jarvie, 2009, Morphology, genesis, and distribution of nanometer-scale pores in siliceous mudstones of the Mississippian Barnett Shale: Journal of Sedimentary Research, v. 79, p. 848–861.

Loucks, R. G., R. M. Reed, S. C. Ruppel, and U. Hammes, 2012, Spectrum of pore types and networks in mudrocks and a descriptive classification for matrix-related mudrock pores: AAPG Bulletin, v. 96, p. 1071–1098.

Loucks, R. G., and R. M. Reed., 2014, Scanning-electron-microscope petrographic evidence for distinguishing organic-matter pores associated with depositional organic matter versus migrated organic matter in mudrocks: GCAGS Journal, v. 3, p. 51–60.

Macquaker, J. H. S., M. A. Keller, and S. J. Davies, 2010, Algal blooms and "marine snow": Mechanisms that enhance preservation of organic carbon in ancient fine-grained sediments: Journal of Sedimentary Research, v. 80, p. 934–942.

Mastalerz, M., and M. Glikson, 2000, In-situ analysis of solid bitumen in coal: Examples from the Bowen Basin and the Illinois Basin: International Journal of Coal Geology, v. 42, p. 201–220.

Mastalerz, M., A. Schimmelmann, A. Drobniak, and Y. Chen, 2013, Porosity of Devonian and Mississippian New Albany Shale across a maturation gradient: Insights from organic petrology, gas adsorption, and mercury intrusion: AAPG Bulletin, v. 97, p. 1621–1643.

Milliken, K. L., M. Rudnicki, D. N. Awwiller, and T. Zhang, 2013, Organic matter-hosted pore system, Marcellus Formation (Devonian), Pennsylvania: AAPG Bulletin, v. 97, p. 177–200.

Milliken, K. L., L. T. Ko, M. Pommer, and K. M. Marsaglia, 2014, SEM petrography of eastern Mediterranean sapropels: Analogue data for assessing organic matter in oil and gas shales: Journal of Sedimentary Research, v. 84, p. 961–974.

Passey, Q. R., K. M. Bohacs, W. L. Esch, R. Klimentidis, and S. Sinha, 2010, From oil-prone source rock to gas-producing shale reservoirs - geological and petrophysical characterization of unconventional shale-gas reservoirs: Society of Petroleum Engineers CPS/SPE International Oil and Gas Conference and Exhibition, Beijing, China, June 8–10, 2010, SPE Paper 131350, 29 p.

Pommer, M. E., 2014, Quantitative assessment of pore types and pore size distribution across thermal maturity, Eagle Ford Formation, South Texas: Austin, The University of Texas at Austin, 239 p.

Pommer, M., and K. Milliken, 2015, Pore types and pore-size distribution across thermal maturity, Eagle Ford Formation, southern Texas: AAPG Bulletin, v. 99, p. 1713–1744.

Reed, R.M., and R. G. Loucks, 2007, Imaging nanoscale pores in the Mississippian Barnett Shale of the northern Fort Worth Basin (abs): American Association of Petroleum Geologists, Annual Convention, Abstracts Volume, v. 16, p. 115.

Reed, R. M., R. G. Loucks, and K. L. Milliken, 2012, Heterogeneity of shape and microscale spatial distribution in organic-matter-hosted pores of gas shales: AAPG Annual Convention and Exhibition.

Roduit, N., 2008, JMICROVISION Version 1.2.7: Image analysis toolbox for measuring and quantifying components of high-definition images: http://www.jmicrovision.com (accessed November 1, 2012).

Romero-Sarmiento, M.-F., J. -N. Rouzaud, S. Bernard, D. Deldicque, M. Thomas, and R. Littke, 2014, Evolution of Barnett Shale organic carbon structure and nanostructure with increasing maturation: Organic Geochemistry, v. 71, p. 7–16.

Roof, J. G., 1970, Snap-off of oil droplets in water-wet pores: Society of Petroleum Engineers Journal, v. 249, p. 85-90.

Ruppel, S. C., and R. G. Loucks, 2008, Black mudrocks: Lessons and questions from the Mississippian Barnett Shale in the southern Midcontinent: The Sedimentary Record, v. 6, p. 4–8.

Selby, D., R. A. Creaser, K. Dewing, M. Fowler, 2005, Evaluation of bitumen as ^{187}Re-^{187}Os geochronometer for hydrocarbon maturation and migration: A test case from Polaris MVT deposit, Canada: Earth and Planetary Science Letters, v. 235, p. 1-15.

Schieber, J., J. B. Southard, and K. Thaisen., 2007, Accretion of mudstone beds from migrating
floccule ripples: Science, v. 318, p. 1760–1763, doi: 10.1126/science.1147001.

Schieber, J., and J. B. Southard, 2009, Bedload transport of mud by floccule ripples – Direct observation of ripple migration processes and their implications: Geology, v. 37, p. 483-486, doi: 10.1130/G25319A

Schieber, J., 2010, Common themes in the formation and preservation of intrinsic porosity in shales and mudstones -illustrated with examples across the Phanerozoic: Society of Petroleum Engineers Unconventional Gas Conference, Pittsburgh, Pennsylvania, USA, February 23–25, SPE Paper 132370, 10 p.

Schieber, J., J. B. Southard, and A. Schimmelmann, 2010, Lenticular shale fabrics resulting from intermittent erosion of water-rich muds – Interpreting the rock record in the light of recent flume experiments: Journal of Sedimentary Research, v. 80, p. 119-128. doi: 10.2110/jsr.2010.005

Silver, M. W., A. L. Shanks, and J. D. Trent, 1978, Marine snow: Microplankton habitat and source of small-scale patchiness in pelagic populations: Science, v. 201, p. 371–373.

Slatt, R. M., and N. R. O'Brien, 2011, Pore types in the Barnett and Woodford gas shales: Contribution to understanding gas storage and migration pathways in fine-grained rocks: AAPG Bulletin, v. 95, p. 2017–2030.

Sondergeld, C. H., R. J. Ambrose, C. S. Rai, and J. Moncrieff, 2010, Micro-structural studies of gas shales: SPE Unconventional Gas Conference, Pittsburgh, Pennsylvania, USA, Society of Petroleum Engineers Unconventional Gas Conference, Pittsburgh, Pennsylvania, USA, February 23-25, SPE Paper 131771, 17 p.

Suárez-Ruiz, I., D. Flores, J. G. M. Filho, P. C. Hackley, 2012, Review and update of the applications of organic petrology: Part 1, geological applications: International Journal of Coal Geology, v. 99, p. 54-112.

Teichmüller M., 1986, Organic petrology of source rocks, history and state of the art: Organic Geochemistry, v.10, p. 581-599.

Tissot, B. P., and D. H. Welte, 1984, Petroleum formation and occurrence, 2nd ed.: Berlin, Heidelberg, Germany, Springer-Verlag, 699 p.

Zhang, T., G. S. Ellis, K. Wang, C. C. Walters, S. R. Kelemen, B. Gillaizeau, and Y. Tang, 2007, Effect of hydrocarbon type on thermochemical sulfate reduction: Organic Geochemistry, v. 38, p. 897–910.

Chapter 3: Origin and Characterization of Eagle Ford Pore Networks in the South Texas Upper Cretaceous Shelf[2]

ABSTRACT

Recent studies have shown that the loss of primary pores and the development of secondary pores in mudrocks are primarily controlled by burial diagenesis of the mineral matrix and thermal maturation of organic matter (OM). However, the lack of quantitative data on micrometer- to nanometer-scale rock properties has limited the ability to define and predict petrophysical properties and fluid flow in these fine-grained rocks. To upscale these rock properties, quantitative data are needed at multiple scales.

Representative Eagle Ford samples were collected from continuous cores taken from two adjacent oil-producing wells in Karnes County, Texas, to investigate small-scale variations in mineralogy, diagenesis, and pore type. Point-count and pore-tracing methods were used to systematically quantify pore types and determine the size and shape of the identified pores. The Eagle Ford in these two cores is dominated by modified mineral pores, although secondary OM pores in migrated petroleum (bitumen) are also important. The mineral pore network includes (1) primary mineral pores originally saturated with formation water and (2) modified mineral pores containing migrated petroleum (bitumen and/or residual oil). The OM pore network includes (1) primary OM pores and (2) secondary OM pores including relatively large, less abundant OM bubble pores and relatively small, more abundant OM spongy pores. The abundance of OM

[2]The full content of this chapter is published in *AAPG Bulletin* in 2017.

spongy pores correlates positively with total organic carbon (TOC) content, and that of mineral pores weakly correlates with volume of quartz plus feldspar. Studied samples have similar thermal maturities, although samples from one deeper core are slightly more mature than the other. Except for thermal maturation, the strong micrometer-scale heterogeneity of rock components and properties (texture, fabric, mineralogy, and TOC) impacts the abundance, distribution, and type of pores. This micrometer-scale heterogeneity in porosity and pore networks would, in turn, significantly impact matrix permeability.

3.1 INTRODUCTION

Since the 1980s, millimeter- to centimeter-scale heterogeneity of mudrocks in terms of lithofacies, fabric, texture, grain assemblage, and mineralogy have been investigated, but only over the past 10 years has it become economic to study these shale oil and shale gas resources at smaller scales (e.g. Macquaker and Gawthorpe, 1993; Wignall, 1994a, 1994b; Schieber et al., 1998; Macquaker and Howell, 1999; Schieber, 1999; Potter et al., 2005; Macquaker et al., 2007; Milliken et al., 2007; Loucks et al., 2009; Schieber and Southard, 2009; Aplin and Macquaker, 2011; Milliken et al., 2012a, Bohacs et al., 2013; Hart et al., 2013; Schieber et al., 2013; Plint, 2014; Lazar et al., 2015). Consequently, there is little documentation of the nanometer- to micrometer-scale rock properties that are fundamental to defining mudrock storage capacity and creating fluid-flow models. The complex variations in facies and textures of these fine-grained sediments have been described and interpreted in the rock record (e.g. Frébourg et al., 2016) according to transport and depositional processes, including pelagic and hemipelagic settling, gravity flows, nepheloid flow, bottom currents, storm events,

internal waves, etc. (e.g., Young and Southard, 1978; Rine and Ginsburg, 1985; Myrow and Southard, 1996; Stow et al., 2002; Schieber et al., 2007; Ichaso and Dalrymple, 2009; Macquaker et al., 2010; Schieber et al., 2013). The depositional processes and sources of sediment supply (extrabasinal vs. intrabasinal) affect grain assemblages, mineralogy, and types of kerogen deposited. These factors, together with maturity (burial) and diagenesis, contribute to the complexity and heterogeneity of mudrock pore types and morphology, which directly impact reservoir quality.

The main objectives of this study are to (1) define the pore types in the Eagle Ford strata, (2) interpret the origin of mineral pores and organic matter (OM) pores, (3) quantify the abundance, size, and morphology of pore types, (4) define the factors controlling the origin of pores, and (5) define scales of heterogeneity, as well as the parameters that influence the heterogeneity of pore types and their distribution.

The Upper Cretaceous Eagle Ford Group is one of the most prolific shale oil resource plays in the United States, having produced an average of more than 700 barrels of oil and more than 1,900 thousand cubic feet of gas per well per day (EIA Drilling Productivity Report as June 8, 2015). Karnes County, the location of the studied cores, is part of this Eagle Ford producing trend and is located in the area of wet gas, condensate, and oil production (Figure 1). Economic oil production indicates that the pore network in the Eagle Ford in this area is of high enough quality for liquid production. Previous studies have suggested that interparticle (interP) and OM pores are dominant in mature Eagle Ford mudrocks (Driskill et al., 2012, 2013; Jennings and Antia, 2013; Pommer and Milliken, 2015). Pore development in mudrocks is controlled by both primary depositional and diagenetically modified processes (interparticle and intraparticle mineral pores) and thermal maturation of organic matter (OM pores) (Ruppel and Loucks, 2008; Loucks et al., 2009, 2012; Bernard et al., 2012a, 2012b; Fishman et al., 2012; Mastalerz

et al., 2013; Milliken et al., 2013; Ko et al., 2014; Romero-Sarmiento et al., 2014). It is important to describe and quantify the type, shape, distribution, and abundance of pores as input parameters for fluid dynamics modeling of Newtonian fluid flow (Afsharpoor and Javadpour, 2016) that define the producibility of these mudrock reservoirs.

3.2 DATA AND METHODS

Figure 3.1 shows the location of the studied wells (designated K1 and K2) in Karnes County, Texas. The Eagle Ford section in the K2 well is slightly deeper than it is in the K1 well. Representative samples were collected from these two closely spaced (~4 miles apart) oil-producing wells (Figures 3.1 and 3.2) and analyzed to define and quantify pore networks. Sample contamination is negligible because the drilling mud was water-based and the samples were not experienced any solvent extraction. Nine samples were taken from the K1 core, and seven from the K2 core. Samples were chosen on the basis of lithofacies defined from core description and mineralogy trends defined by X-ray fluorescence (XRF) (Figure 3.2). Division of the Eagle Ford into upper (UEF) and lower (LEF) parts is based on uranium abundance, which is observed on the spectral gamma log and which correlates with changes in molybdenum concentration and total organic carbon (TOC) (Pierce et al., 2016).

An aliquot of Eagle Ford samples was analyzed by GeoMark using Rock-Eval pyrolysis to obtain their geochemical parameters and thermal maturity (Table 3.1). TOC content was obtained using the LECO TOC approach (Table 3.1).

A flat surface was prepared on each sample for SEM analysis by Ar-ion beam milling using a Leica EM TIC020 Triple Ion Beam Miller. Each sample was milled for

10 hr using an accelerating voltage of 8 keV and a current of 2.8 mA. A thin, conductive coating of iridium (Ir) was applied to samples to reduce charging and improve image quality using a Leica EM ACE600 High Vacuum Coater. An FEI Nova NanoSEM 430 field-emission scanning electron microscope (FE-SEM) was used to image pores and their association with organic matter and mineral grains under an accelerating voltage of 10 to15 keV and a working distance of 4 to 5 mm.

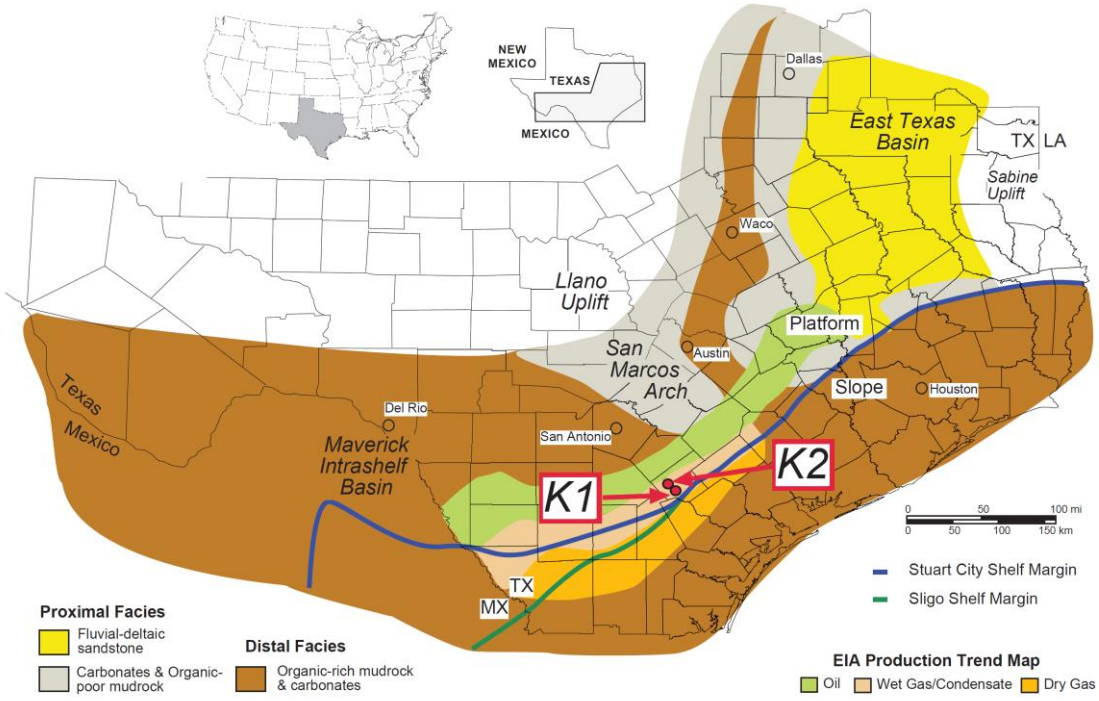

Figure 3.1: Paleogeographic map of south Texas region showing general facies distribution during the Late Cenomanian and locations of K1 and K2 wells in Karnes County. Boundaries of oil, condensate, and gas production are also shown. EIA = Energy Information Administration. Modified after Fairbanks et al., (2016).

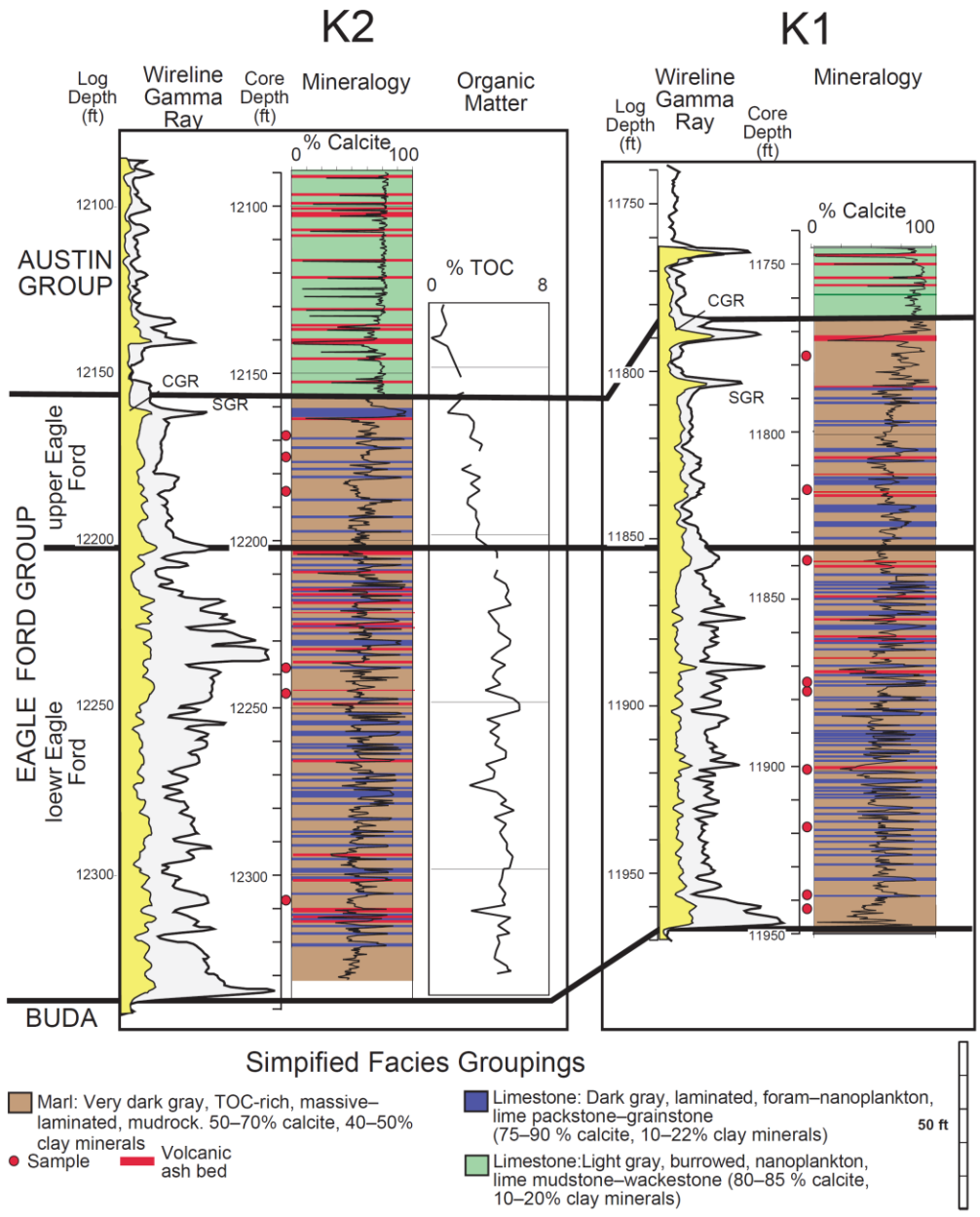

Figure 3.2: General facies stacking pattern and correlation of the K1 and K2 cored Eagle Ford wells. Subdivision of the upper and lower Eagle Ford is based on gamma-ray log response and corresponding changes in redox conditions (Denne et al., 2014). Cores are approximately 4 miles apart. CGR = compensated gamma ray (uranium-free); SGR = spectral gamma ray; TOC = total organic carbon.

Well	EF sections	Depth (ft)	S_1 (mg HC/g)	S_2 (mg HC/g)	T_{max} (°C)	LECO TOC (wt. %)
K1	UEF	11,778	2.55	1.79	463	1.71
K1	UEF	11,818	6.15	2.88	461	2.85
K1	LEF	11,838	7.14	4.49	466	4.05
K1	LEF	11,875	10.67	4.35	442	2.86
K1	LEF	11,878	11.25	5.50	461	5.50
K1	LEF	11,901	7.37	2.66	460	2.56
K1	LEF	11,918	9.91	4.54	462	4.92
K1	LEF	11,939	7.55	3.47	460	3.72
K1	LEF	11,943	3.69	4.07	464	4.63
K2	UEF	12,169	6.09	2.51	460	3.39
K2	UEF	12,174	7.12	2.58	459	3.17
K2	UEF	12,185	5.80	2.54	458	3.33
K2	LEF	12,238	1.57	0.84	452	1.10
K2	LEF	12,246	7.71	3.17	473	5.06
K2	LEF	12,247	0.88	0.63	465	1.14
K2	LEF	12,308	5.57	1.73	465	3.29

S_1, S_2, T_{max} are Rock-Eval parameters. Rock-Eval S_1 and S_2 are reported as milligrams of S_1 and S_2 per gram of rock. Volatile hydrocarbons (HCs) that have been generated and expelled as free HCs in the rock are represented by S_1. The HCs that have not been generated and expelled but still have generation potential are represented by S_2. The temperature at which the maximum amount of HCs released from cracking of kerogen (top of S_2 peak) is represented by T_{max}. The T_{max} value is an indication of maturation stage of the organic matter.

Table 3.1: Geochemical parameters and thermal maturity values of the studied Eagle Ford samples in the K1 and K2 cores.

3.2.1 SEM Imaging Scales for Pore Networks

Backscattered electron (BSE), secondary electron (SE), and SE through-the-lens detector (TLD) images were collected at instrument magnifications of 5,000X, 15,000X, and 120,000X to cover a broad range of visible pore sizes (as small as 5 nm) (Figure 3.3).

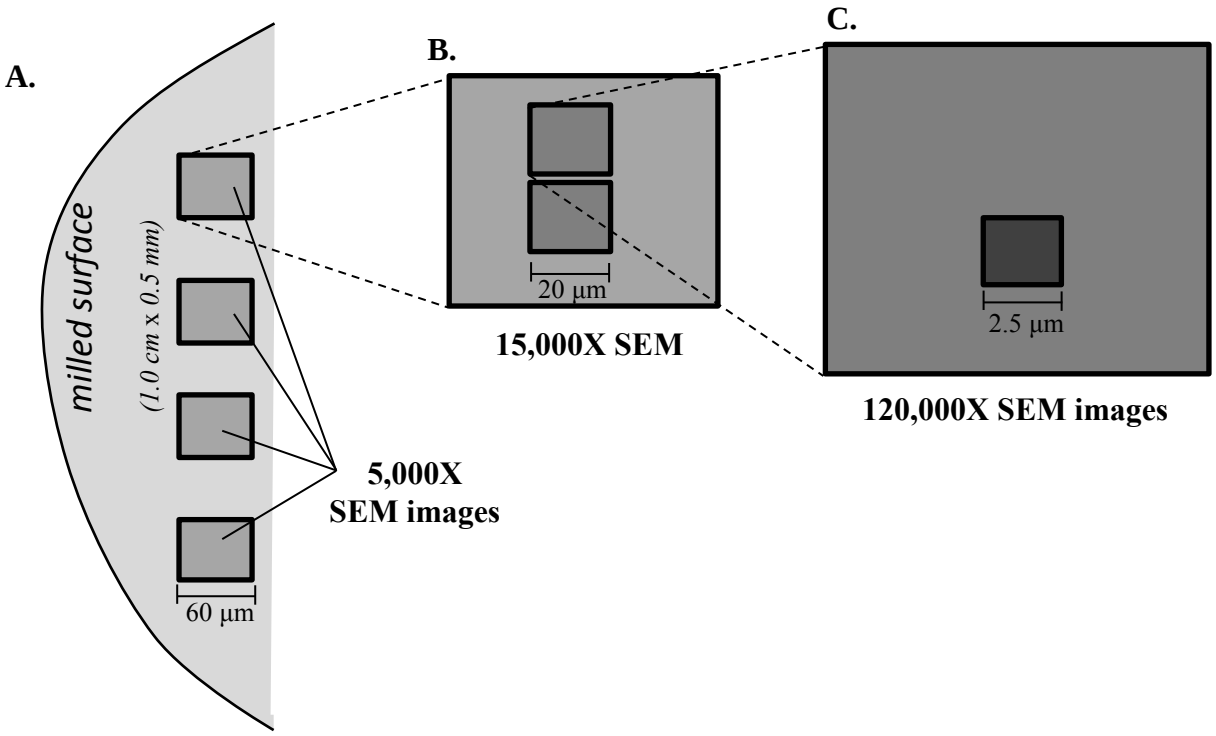

Figure 3.3: Diagram showing sampling and analysis protocols. (A) Four 5,000X SEM photomicrographs were taken perpendicular to the bedding on each milled surface. Areas having anomalously large allochems, grains, and recrystallized crystals were avoided. (B) For each 5,000X photo, two 15,000X SEM photomicrographs were taken. (C) For each 15,000X photo, two high-resolution 120,000X photos were taken across bedding planes. If foraminifera were included in the 5,000X photo, one high-resolution image would zoom into the OM inside the foraminifera chamber and another one would be taken in the matrix area outside the foraminifera chamber.

The TLD imaging was used for 120,000X high-magnification examination. Four 5,000X (machine magnification) SEM photomicrographs were acquired perpendicular to bedding planes for each milled surface and uniformly distributed along that surface. For

each 5,000X photomicrograph, two 15,000X (machine magnification) SEM photomicrographs were taken perpendicular to bedding planes and two high-resolution 120,000X (machine magnification) SEM photomicrographs were taken to image the detailed size and shape of OM pores and mineral pores. Where foraminifera were included in the 15,000X photograph, one high-resolution image was taken of the OM inside the foraminifera chamber and another was taken of the matrix outside the chamber. At least twenty images were collected for each sample, including four 5,000X, eight 15,000X, and eight 120,000X SEM photomicrographs. Areas having anomalously large allochems, grains, and crystals were intentionally avoided. Corrections of counted porosity can be made on the basis of visual estimation of the area percentage of anomalously large grains versus that of the bulk matrix.

3.2.2 Compositional Analysis (XRD and SEM X-Ray EDS)

Mineral components were identified by X-ray energy-dispersive spectroscopy (EDS) mapping. Two 30-mm^2 Bruker XFlash silicon-drift energy-dispersive X-ray detectors were used, under an accelerating voltage of 15 keV, a spot size of 3.0 to 3.5 micrometers, and a total count time of greater than 700 s. X-ray diffraction (XRD) analyses of the studied Eagle Ford samples were completed by K-T GeoServices (Gunnison, Colorado).

3.2.3 Point-Count and Pore-Trace Methods

One thousand points were counted on each backscattered SEM image using JMicroVision software (Roduit, 2008). Five point-count categories were used: minerals,

organic matter, OM pore, interparticle (interP) pore, and intraparticle (intraP) pore (Loucks et al., 2012). The size of each point is 5 pixels in each photomicrograph (5 pixels equivalent to 290 nm in 5,000X photomicrographs; 95 nm in 15,000X photomicrographs; 12 nm in 120,000X photomicrographs). The final estimated "visible total porosity" is derived by multiplying point-count data times (1-[visual estimation of the area percentage of anomalously large particles]). Here, we used "visible total porosity" instead of "total porosity" to refer to the image-derived porosity because the representative elementary area or volume (REA or REV) is yet unknown. The REA or REV is defined as the smallest sample area or volume over which a measured attribute of a media can be made that will yield a value representative of the whole.

All visible pores in the 5,000X photomicrographs were also manually traced using the JMicroVision program (Roduit, 2008). The pore-tracing methods at all three scales were applied to two samples — K1: 11,918 ft (3,633 m), marl, LEF; K2: 12,174 ft (3,711 m), marl, UEF. Visible total porosity and morphological information on the pores such as area, perimeter, aspect ratio, and equivalent circular diameter (ECD) were obtained from the pore trace. This study uses manual tracing method in favor of automated image analysis tool to avoid artifacts such as curtaining and grooves which caused by uneven ablation of sample surfaces by Ar ions and can result in misidentification of pores by automated software (Sondergeld et al., 2010). Another concern while using automated tool to segment pores is related to under- or over-estimation of pore sizes caused by applying thresholding that uses the normal distribution of gray scale in SEM images (e.g., Houben et al., 2013, 2014). Usually, the normal distribution of gray scale is not sufficient

enough to separate the similar color scale identified within pores and on organic matter surfaces, mineral surfaces, and/or sample artifacts. Additional concern such as grain plucking or possible "smearing" effects from ion milling processes which might redeposit milled materials, plugging a portion of large pores or masking the entire small pores, also needs to be considered. The grain plucking or redeposited materials can be identified in SEM images, so manual pore tracing method can eliminate the possible overestimation or underestimation of pore sizes.

3.2.4 Nitrogen-Gas Adsorption Analyses

Pore-size distribution analyses were performed using an Autosorb-iQ-MP instrument (Quantachrome Instruments) equipped with a vacuum pump capable of reaching 5E-7 Pa (7.25E-11 psi). Samples were crushed to 20–50 mesh size, and the residual oil was removed by CH_2Cl_2 solvent extraction. At least 500 mg samples were placed into 6-mm-stem quartz sample cells and degassed for 12 hours at 110°C under vacuum. Nitrogen at 77 K (-196.15°C) was used as the probe gases for all experiments. Surface areas were calculated using the best linear range between 0.05–0.3 P/P_o of N_2 sorption, with a minimum of 5 points used in the Brunauer–Emmett–Teller (BET) surface-area analysis. Pore-size distributions were obtained using both the density functional theory method (DFT) and the Barrett, Joyner, and Halenda (BJH) method, both of which are available within the ASiQwin instrument software package (v. 2.02).

3.2.5 Helium Porosity Measurement

Porosity was measured using crushed sample with mesh size of 20/50 using GRI method (Gas Research Institute, Luffel and Hopkins, 1993). GRI method involves a helium expansion process from which initial and equilibrium pressures can be measured.

With volumes of reference cell and sample cell, grain volume of the sample can be measured. Bulk volume of the samples was measured using a 3D laser scanner (Peng and Loucks, 2016). Porosity can be calculated as 1 – (grain volume/bulk volume).

3.3 REGIONAL GEOLOGY AND LITHOFACIES

The interbedded marl (defined as compact, impure, argillaceous limestone) and limestone of the studied Eagle Ford sections were deposited on the Late Cretaceous shelf, southwest of the San Marcos Arch, during the early Cenomanian and Turonian (Figure 3.1; Ruppel et al., 2012; Denne et al., 2014; Eldrett et al., 2015). This area is characterized by starvation of siliciclastic sediment input and abundant carbonate sedimentation (Ruppel et al., 2012; Denne et al., 2014).

Four basic facies were recognized in the Eagle Ford section, on the basis of mineralogy and thin-section petrography: (1) Globigerinid-bearing, laminated wackestone-packstone, (2) globigerinid-bearing, laminated mudstone-wackestone, (3) globigerinid-bearing, laminated packstone, and (4) skeletal-debris (inoceramids and echinoderms), globigerinid-bearing, laminated wackestone-packstone (Tables 3.2 and 3.3, Figure 3.4). In general, the upper Eagle Ford section is dominated by marls with relatively less TOC, limestone, and relatively uncommon ash beds, whereas the lower Eagle Ford section shows alternating cyclic OM-rich marls and limestone beds with relatively common ash beds. Three samples were taken from the limestone facies, and thirteen samples from the marl facies.

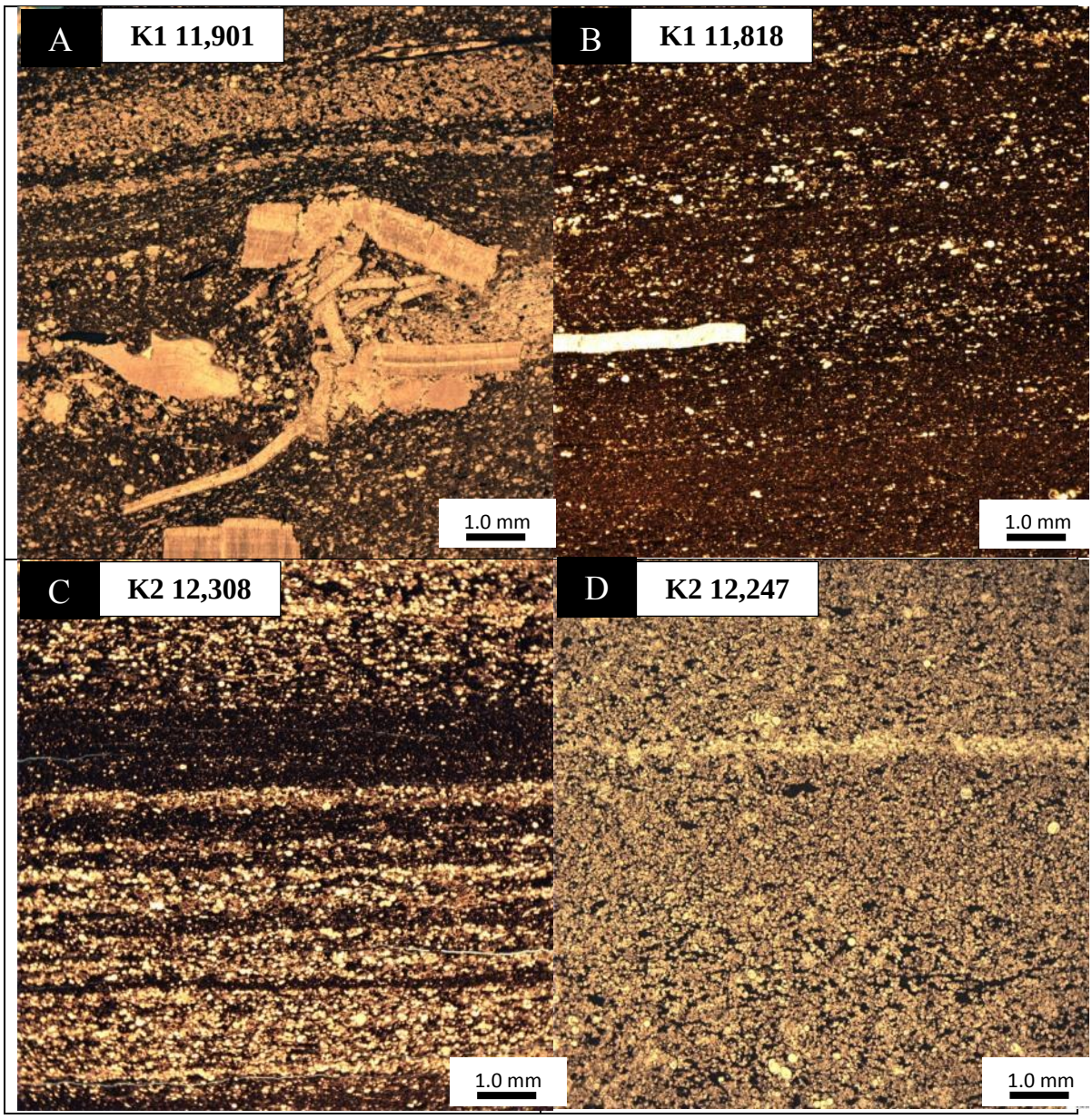

Figure 3.4: Thin-section photomicrographs of major Eagle Ford facies in the K1 and K2 cores. (A) Skeletal-debris, globigerinid-bearing, laminated wackestone-packstone, K1 well, 11,901 ft. (B) Globigerinid-bearing, laminated mudstone-wackestone, K1 well, 11,818 ft. (C) Globigerinid-bearing, laminated wackestone-packstone, K2 well, 12, 308 ft. (D) Globigerinid-bearing, laminated packstone, K2 well, 12, 247 ft.

Sample ID	EF sections	Core description facies	Mineralogy-defined facies	XRD mineralogy (volume %)									
				Quartz	K-Feldspar	Plagioclase	Calcite	Dolomite	Pyrite	Marcasite	Apatite	Clay mineral	Total
K1 11,778	**UEF**	OM-poor marl	Calcareous mudrock	11.4	0.5	4.3	76.1	0.6	0.5	0.2	0.0	6.3	100
K1 11,818	**UEF**	OM-rich marl	Calcareous mudrock	15.1	0.6	4.2	68.0	0.5	1.4	0.2	0.0	10.0	100
K1 11,838	**LEF**	OM-rich marl	Calcareous mudrock	15.6	1.1	3.7	57.4	0.4	1.3	0.2	0.0	20.4	100
K1 11,875	**LEF**	OM-rich limestone	Calcareous mudrock	3.1	0.4	0.7	92.1	1.0	0.2	0.0	0.0	2.5	100
K1 11,878	**LEF**	OM-rich marl	Calcareous mudrock	19.8	0.7	4.3	60.9	1.2	1.5	0.0	0.0	11.5	100
K1 11,901	**LEF**	OM-rich marl	Calcite-rich siliceous mudrock	34.6	0.5	6.2	31.4	3.6	2.0	0.0	0.5	21.2	100
K1 11,918	**LEF**	OM-rich marl	Calcareous mudrock	17.5	0.3	1.3	62.5	2.7	1.5	0.0	0.0	14.2	100
K1 11,939	**LEF**	OM-rich marl	Calcareous mudrock	10.1	0.2	0.7	67.0	0.0	1.7	0.0	0.0	20.3	100
K1 11,943	**LEF**	OM-rich marl	Calcite-rich argillaceous mudrock	17.7	0.8	0.6	36.5	0.4	3.1	1.4	0.0	39.6	100
K2 12,169	**UEF**	OM-rich marl	Calcareous mudrock	16.1	0.8	7.5	59.1	0.7	1.0	0.6	0.0	14.3	100
K2 12,174	**UEF**	OM-rich marl	Calcareous mudrock	15.5	1.1	5.6	65.2	0.5	0.9	0.4	0.0	10.9	100
K2 12,185	**UEF**	OM-rich marl	Calcareous mudrock	15.8	0.9	5.4	63.5	0.4	1.1	0.8	0.0	12.2	100
K2 12,238	**LEF**	OM-poor limestone	Calcareous mudrock	8.0	0.5	1.0	88.4	0.3	0.2	0.0	0.0	1.6	100
K2 12,246	**LEF**	OM-rich marl	Calcareous mudrock	22.5	0.6	4.2	58.7	0.0	1.6	0.0	0.0	12.3	100
K2 12,247	**LEF**	OM-poor limestone	Calcareous mudrock	6.0	0.4	1.1	89.0	0.0	0.2	0.0	0.0	3.2	100
K2 12,308	**LEF**	OM-rich marl	Calcareous mudrock	18.1	0.5	4.0	65.5	1.6	1.7	0.2	0.0	8.4	100

*OM-poor (TOC < 2.0 wt%); OM-rich (TOC > 2.0 wt%)

Table 3.2: X-ray diffraction mineralogy data and mineralogical facies in the studied Eagle Ford section. A 2.0 wt% cutoff was used to differentiate OM-poor (<2 wt%) and OM-rich (>2 wt%) marl.

Sample ID	Facies names (at various scales of observation)		
	Core description facies	**Mineralogy (XRD) facies**	**Thin section petrography-defined facies**
K1 11,778	OM-poor marl	Calcareous mudrock	Globigerinid-bearing, laminated wackestone-packstone
K1 11,818	OM-rich marl	Calcareous mudrock	Globigerinid-bearing, laminated mudstone-wackestone
K1 11,838	OM-rich marl	Calcareous mudrock	Globigerinid-bearing, laminated mudstone-wackestone
K1 11,875	OM-rich limestone	Calcareous mudrock	Globigerinid-bearing, laminated packstone
K1 11,878	OM-rich marl	Calcareous mudrock	Globigerinid-bearing, laminated mudstone-wackestone
K1 11,901	OM-rich marl	Calcite-rich siliceous mudrock	Skeletal-debris, globigerinid-bearing, laminated wackestone-packstone
K1 11,918	OM-rich marl	Calcareous mudrock	Globigerinid-bearing, laminated mudstone-wackestone
K1 11,939	OM-rich marl	Calcareous mudrock	Globigerinid-bearing, laminated mudstone-wackestone
K1 11,943	OM-rich marl	Calcite-rich argillaceous mudrock	Globigerinid-bearing, laminated wackestone-lime mudstone
K2 12,169	OM-rich marl	Calcareous mudrock	Globigerinid-bearing, laminated mudstone-wackestone
K2 12,174	OM-rich marl	Calcareous mudrock	Globigerinid-bearing, laminated mudstone-wackestone
K2 12,185	OM-rich marl	Calcareous mudrock	Globigerinid-bearing, laminated mudstone-wackestone
K2 12,238	OM-poor limestone	Calcareous mudrock	Globigerinid-bearing, laminated packstone
K2 12,246	OM-rich marl	Calcareous mudrock	Globigerinid-bearing, laminated wackestone-packstone
K2 12,247	OM-poor limestone	Calcareous mudrock	Globigerinid-bearing, laminated packstone
K2 12,308	OM-rich marl	Calcareous mudrock	Globigerinid-bearing, laminated wackestone-packstone

Table 3.3: Facies names at various scales of observation in the studied Eagle Ford section.

3.4 MINERALOGY, FABRIC, AND TEXTURE

The dominant mineral constituent throughout the Eagle Ford section is calcite, quartz, clay minerals, and feldspar (Table 3.2). Most samples fall in the carbonate field (greater than 50% carbonate). Clay minerals constitute generally 20% or less and quartz plus feldspar is generally 30% or less (Table 3.2, Figure 3.5). From thin-section and SEM petrography, quartz and feldspar are in the clay and silt size range. Pyrite, dolomite, kaolinite, marcasite, and chlorite are accessory minerals.

Micrometer-scale mineral distribution (fabric) is illustrated by the SEM-EDS maps shown in Figure 6. The matrix is dominated by globigerinid foraminifera, coccolith debris, and clay minerals. Dolomite, albite, and feldspar are also common. Calcite, pyrite, kaolinite, and Mg-chlorite are present as cements in the globigerinid chambers (Figure 3.6). Higher magnification SEM photomicrographs (Figure 3.7) show the coccolith elements with calcite overgrowths.

The bulk mineralogy of the UEF marl samples is similar (Figure 3.8A, B); however, the LEF marl samples demonstrate much more variations, especially in the relative amounts of quartz, albite, dolomite, and clay minerals (Figure 3.8C–F). SEM-EDS maps and SEM- cathodoluminescence (CL) show that quartz can be detrital (rounded shape, bright-color CL) or authigenic (euhedral shape, dull-color CL) in origin. Dolomite is generally rhombic in shape (Figure 3.6B). SEM petrography shows that albite can be cement (euhedral shape) or a replacement product, but some albite can be of detrital origin (Figure 3.6B). The amount of kaolinite, mixed layered illite/mica, illite,

and smectite varies among these samples, with sample 11,943 ft (3,640 m) (K1 core) having the highest amount of clay minerals and sample 12,308 ft (3,751 m) (K2 core) the lowest. A significant increase in the relative abundance of kaolinite and chlorite was noted from the upper to lower Eagle Ford (Figure 3.8).

Texture and fabric were obtained by detailed examination and documentation using thin-section and SEM petrography. Broken inoceramids, echinoderms, and globigerinids range up to sand and pebble size. Some marl samples consist of alternating silt- and clay-sized continuous laminae in the core (Figure 3.4). Bioturbation is rare. Within the UEF in the K2 core, the proportion of millimeter-scale silt-grain-bearing laminae systematically increases, as does the size of the foraminifera from the lower to upper UEF samples. Intergranular and intragranular cementation of calcite, dolomite, kaolinite, Mg-chlorite, quartz, and pyrite is significant in the Eagle Ford mudrocks and has affected the texture and fabric of the originally deposited sediments during compaction. The authigenic calcite and kaolinite cementation observed within the foraminifera chambers is considered early diagenetic event because it has prevented their collapsing before significant compaction had occurred. Extensive quartz cementation is another major diagenetic event in the Eagle Ford. Euhedral quartz crystals were widely dispersed in the matrix. Milliken et al. (2016) have reported that approximately 85% of total quartz (12.6 volume %) in the Eagle Ford is interpreted as authigenic. These widely dispersed microquartz, re-precipitated from dissolved silica released by dissolved radiolarians and volcanic glass, have prevented significant compaction and preserved much pore spaces (Milliken et al., 2016).

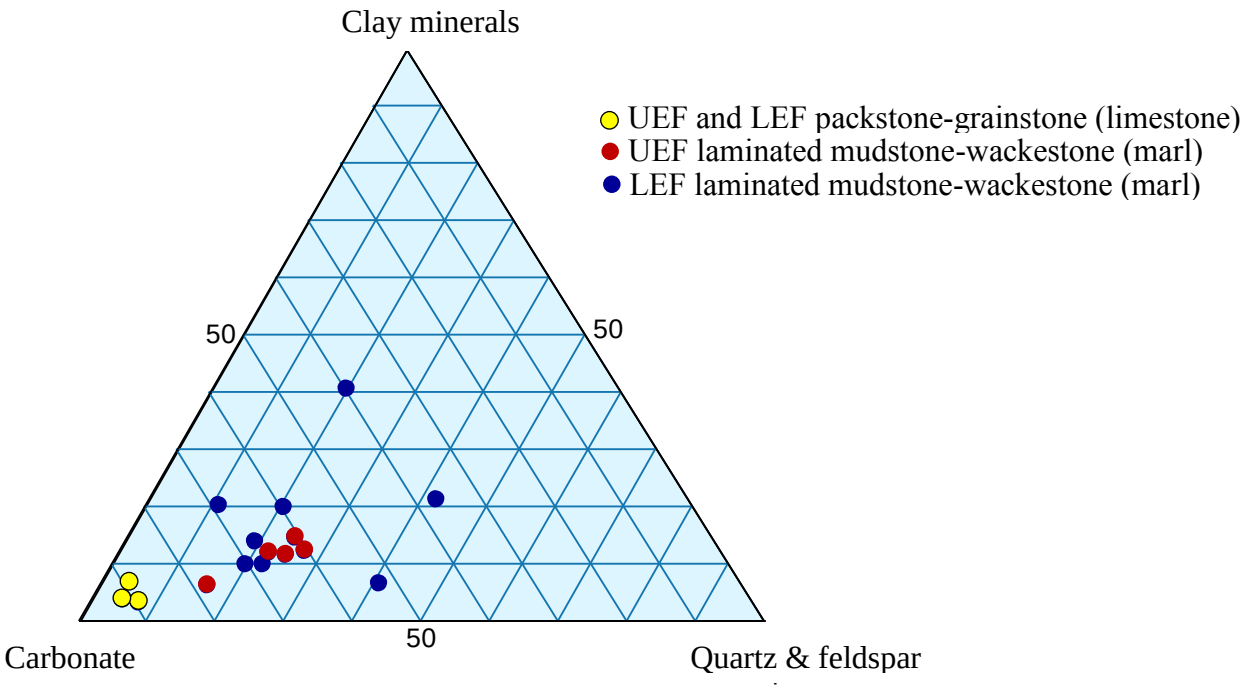

Figure 3.5: Ternary plot showing general mineralogy of the Eagle Ford samples. UEF = upper Eagle Ford Group; LEF = lower Eagle Ford Group.

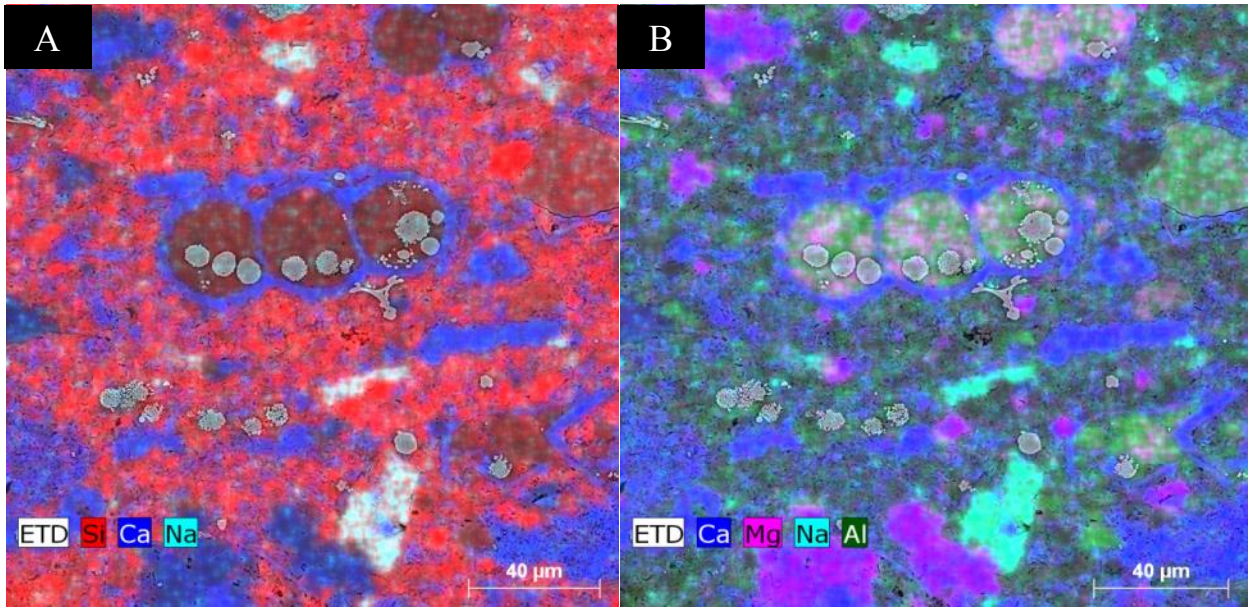

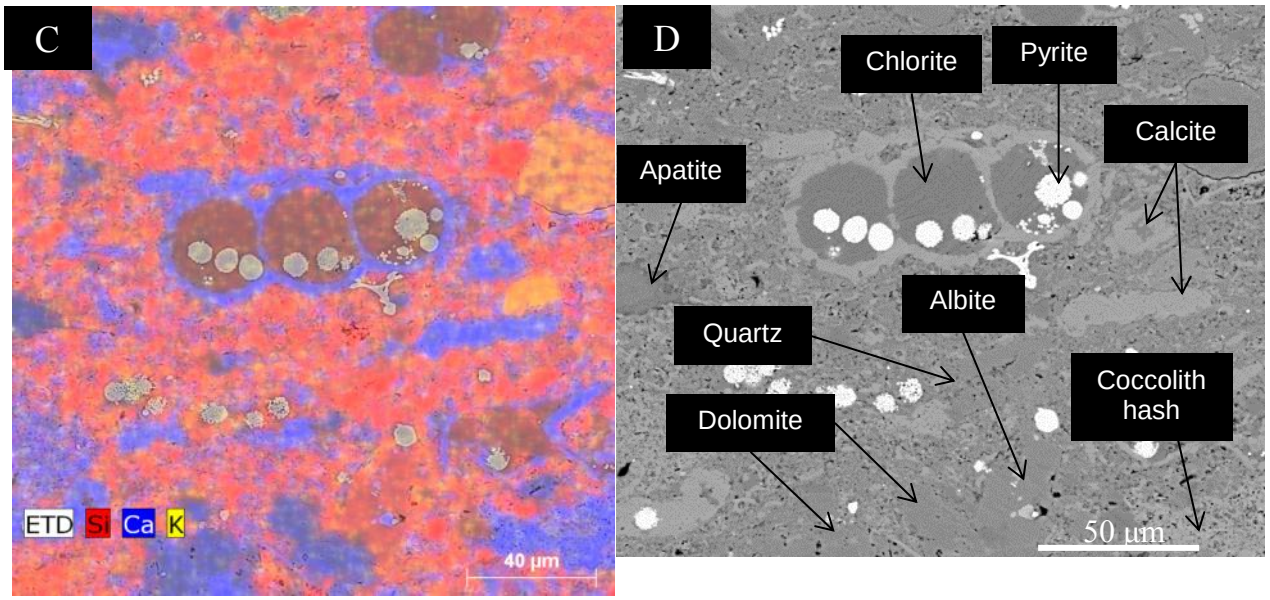

Figure 3.6: SEM-EDS elemental maps showing mineral fabric of the Eagle Ford sample at a depth of 11,901 ft (3,627 m) in the K1 core. (A) Composite map of silicon (Si), calcium (Ca), and sodium (Na) abundance showing the distribution of quartz, calcite, and albite, respectively. (B) Composite map of Ca, magnesium (Mg), Na, and aluminum (Al) abundance documenting the distribution of calcite, dolomite, plagioclase/feldspar, and clay minerals, respectively. (C) Composite map of Si, Ca, and potassium (K) abundance identifying feldspar. (D) Backscattered electron (BSE) composite map showing minerals identified by elemental maps. ETD: Everhart Thornley Detector (for secondary electron and/or backscatter election images).

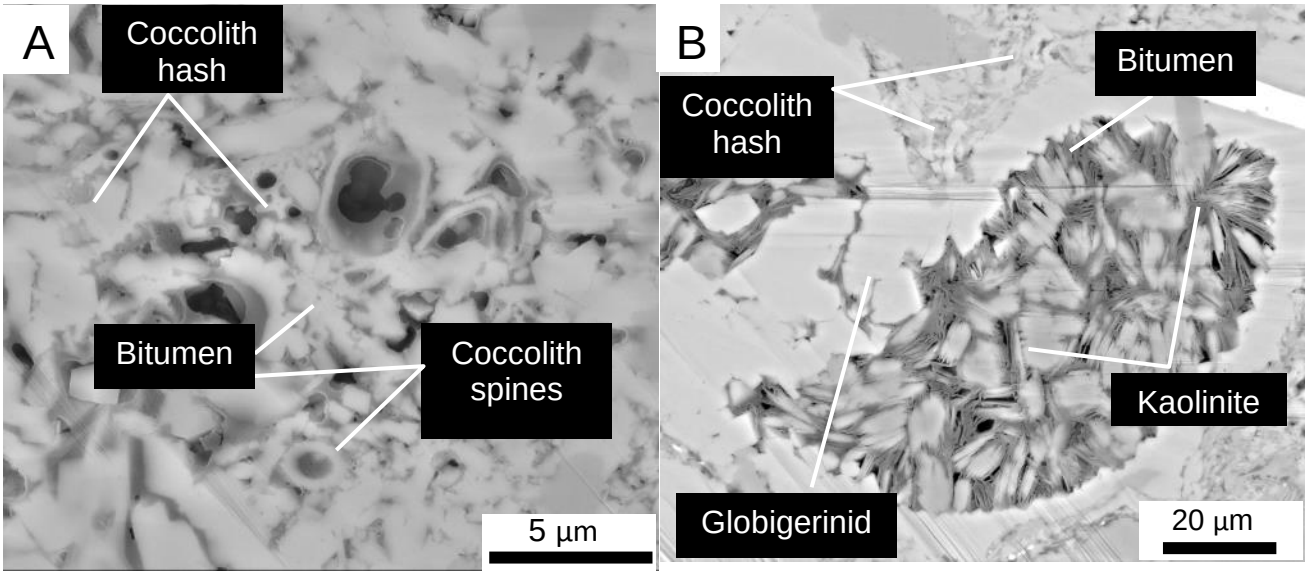

Figure 3.7: SEM-photomicrographs showing (A) coccolith matrix and (B) globigerinid foraminifera filled with kaolinite booklets and bitumen.

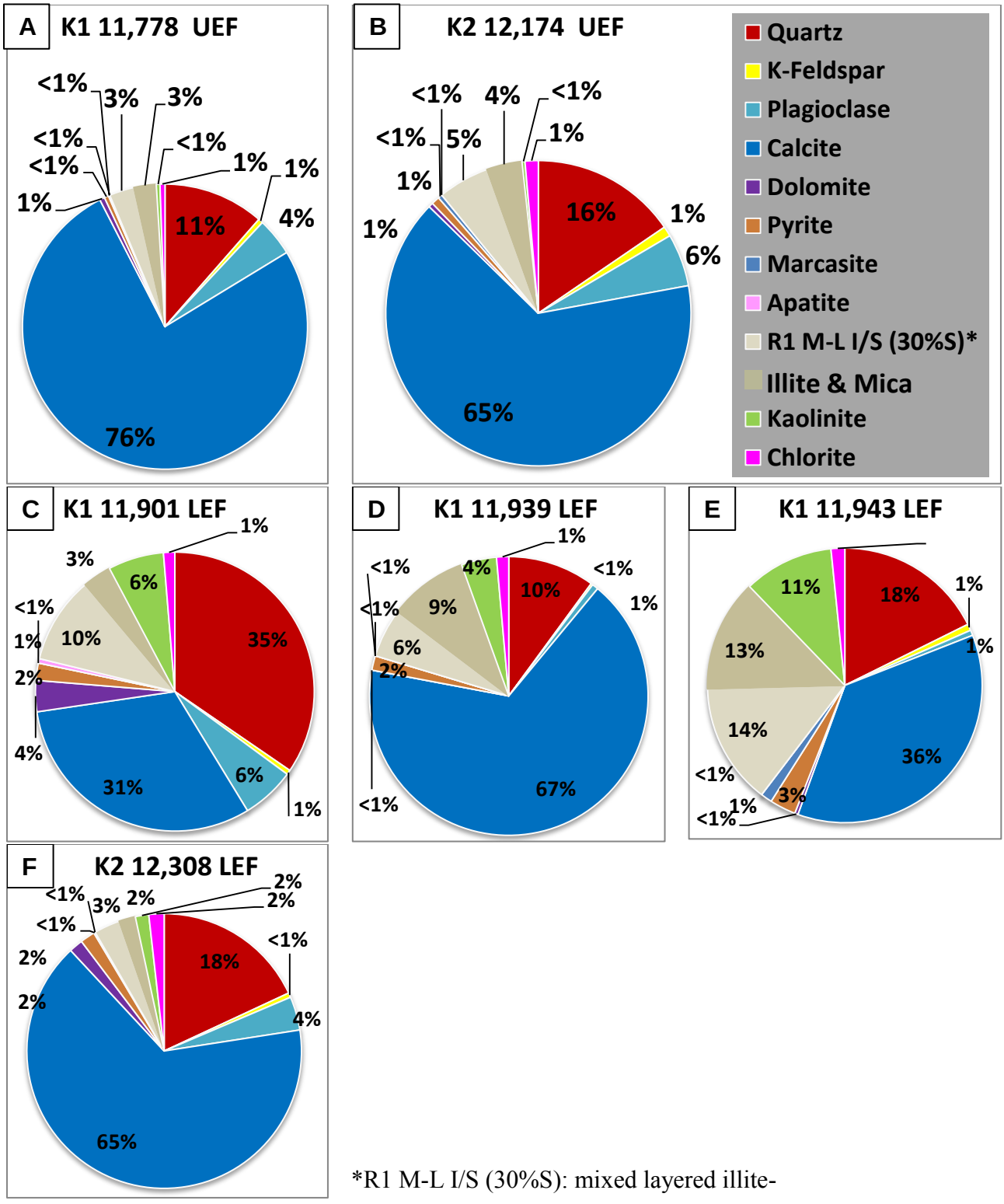

*R1 M-L I/S (30%S): mixed layered illite-

Figure 3.8: Pie charts showing XRD bulk mineralogy (volume %) of upper and lower Eagle Ford Group (UEF and LEF) marl facies. UEF marls in K1 and K2 cores show very similar bulk mineralogy.

3.5 CHARACTERIZATION OF ORGANIC MATTER

Rock-Eval and LECO TOC analyses were performed on all samples. The average TOC value is 3.33 wt %, with a range of 1.10 to 5.50 wt %. In the studied sample set, marl facies of the LEF has higher TOC content than do the marls in the UEF (Figure 3.9A, B). Rock-Eval S_1 and S_2 values were normalized to per gram of TOC. Both cores show higher S_1 than S_2, indicating that much of the petroleum have been generated and expelled, and the rocks at present retain limited generation potential. Overall, K1marl facies display slightly higher S_2 values than does in the K2 core, meaning that K1 marls have higher generation potential than K2 marls and also that K1 marls are thermally less mature than K2 marls. The average T_{max} value among the studied samples is approximately 461°C, with a range of 442 to 473°C (Table 3.1). Calculated vitrinite reflectance (R_o) based on T_{max} (calculated $R_o = 0.018*T_{max}-7.16$) averages ~1.16%. Both production index (PI) versus T_{max} plot and calculated R_o imply that these two cores have almost reached the end of oil generation (condensate and gas window) (Figure 3.10). Vitrinite reflectance measurement as a means to determine thermal maturation is not feasible because vitrinite particles are derived from partly decomposed high plant tissues which are difficult to find in marine mudrocks. Because the majority of marine kerogen has been converted to petroleum and solid bitumen at the condensate and gas window level of thermal maturation, solid bitumen reflectance instead of vitrinite reflectance can

be measured. We did not measure solid bitumen reflectance but used biomarker (Sun, unpublished data, April 2015) and Rock-Eval hydrogen index (HI = [100 x S_2]/TOC), oxygen index (OI = [100 x S_3]/TOC), production index (PI = S_1/ [S_1+S_2]), and T_{max} to determine the relative levels of thermal maturities. The original type of kerogen is difficult to identify because of thermal maturation. However, the remains of original maceral and kerogen can possibly be identified using organic petrology or biomarker analyses. Sun et al. (2016) have applied biomarker analysis on the residual oil in the organic-rich marls of the Eagle Ford and identified predominantly Type II kerogen throughout the Eagle Ford, with LEF containing some Type II-S kerogen and UEF containing minor amount of Type III kerogen.

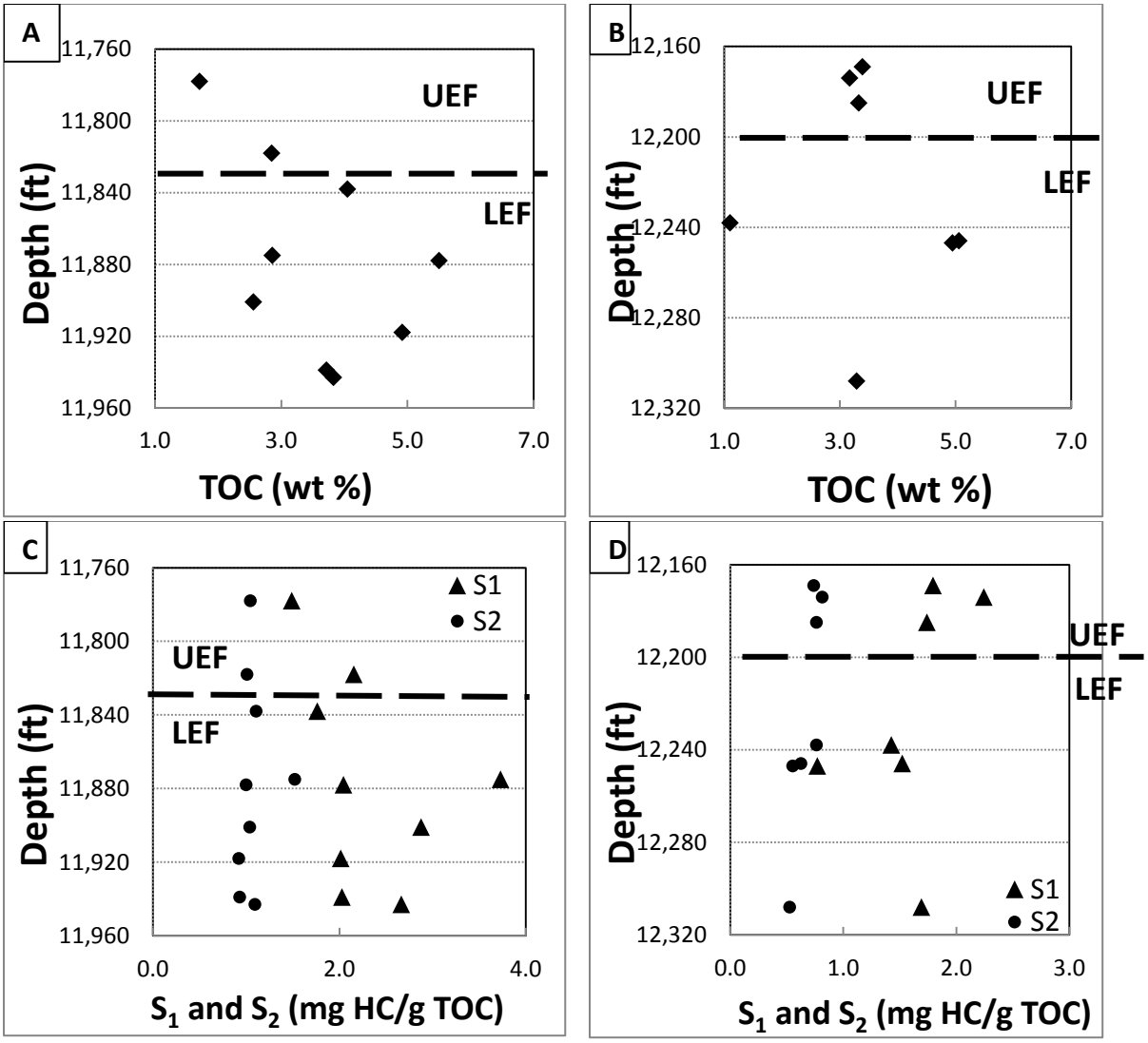

Figure 3.9: Plots of total organic carbon (TOC) and Rock-Eval S_1, and S_2 against depths for Eagle Ford samples. (A) Depth vs. TOC in K1 cores. (B) Depth vs. TOC in K2 cores. In both K1 and K2 cores, the marl facies from the lower Eagle Ford (LEF) have higher TOC content than those from the upper Eagle Ford (UEF). (C) Depth vs. S_1 and S_2 (expressed in milligrams of hydrocarbons per gram of TOC [mg HC/g TOC]) in K1 cores. (D) Depth vs. S_1 and S_2 in K2 cores. Both cores have higher S_1 than S_2 values, indicating most hydrocarbons have already been generated and expelled. Overall, K1 cores have slightly higher S_2 values than K2 cores.

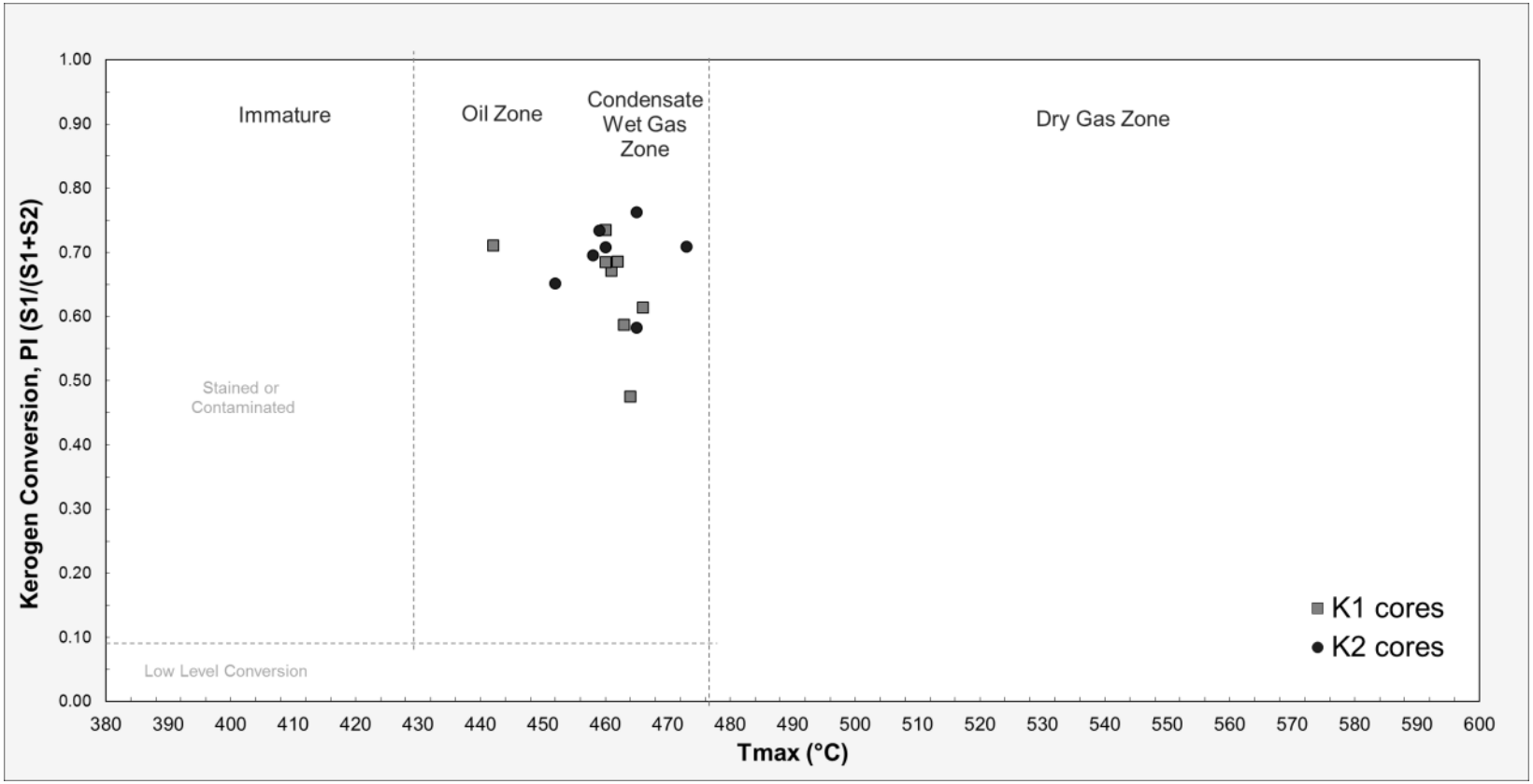

Figure 3.10: Plot of Rock-Eval production index (PI = S_1/S_1+S_2) versus Tmax (°C) indicating that majority of the Eagle Ford samples are in condensate and wet gas maturation. Two limestone samples K1:11,875 ft (3,620 m) and K2: 12,238 ft (3,730 m) are in oil window maturation.

3.6 PORE TYPES AND PORE NETWORKS

Pores observed in the Eagle Ford samples are in the nanometer- to micrometer pore-size range (Figures 3.11 and 3.12). The mudrock pore classification of Loucks et al. (2012) and a proposed modified version based on our laboratory experiments were used to classify the pores observed in the Eagle Ford samples (Tables 3.4 and 3.5, Ko et al., 2016).

3.6.1 Mineral Pores

Interparticle Pores: Interparticle pores are defined as pores that occur between grains and crystals. Interparticle pores are primary mineral pores and are generally well connected, forming an effective pore network that can contribute to permeability. Figure 3.11A and 3.11B illustrates interparticle pores between coccolith elements in the Eagle Ford that have been significantly compacted and cemented. Many of the original grains have calcite overgrowths (Figure 3.7). The interparticle pores in the Eagle Ford range from less than 1 to 9 μm (Figure 3.11A).

Intraparticle Pores: Intraparticle pores occur within grain and crystal boundaries; for examples, as molds, within body cavities of globigerinid foraminifera, within pyrite framboids, and within clay mineral platelets (Figure 3.11C, D). Some of the pores within clay mineral platelets are the result of clay mineral deformation (Figure 3.10C). Clay minerals are soft and ductile, easily bent around rigid grains during compaction. The shape and size of the intraparticle pores are commonly controlled by their origin. These intraparticle pores are relatively isolated and may not contribute to permeability.

Modified Primary Mineral Pores:

We separated modified mineral pores from primary interparticle and intraparticle pores to ensure that they are not misinterpreted and misidentified as OM pores. It is important to recognize that modified mineral pores correctly when quantifying pore types. These pores are variations of primary mineral pores, although the pores are in contact with OM (Figure 3.11E, F). These pores can result from two different processes: (1) Oil and gas can leave the original mineral pore, most likely during sample preparation at various conditions. A rim of residual oil is formed when heavy-component oil is adsorbed on the mineral surface. The shape and size of these pores are related to the pore formed by the surrounding framework grains or the original mineral pores (Figure 3.11E), (2) Pores can also form from petroleum (bitumen) migration and infill of surrounding mineral pores, trapping early gas or connate water on the edge and/or tip of minerals (e.g., Löhr et al., 2015) (Figure 3.11F). These pores are characterized as being in contact with both minerals and OM (Figure 3.11F). The occurrence, shape, and location of these pores are controlled by the wettability of the mineral surface. Generally these pores range from a few micrometers to tens of micrometers in diameter, some of the pores falling in the nanometer scale. Most of the pore shapes are irregular, but some pores are rounded. The pore itself is not within the solid bitumen, as a true OM pore would be.

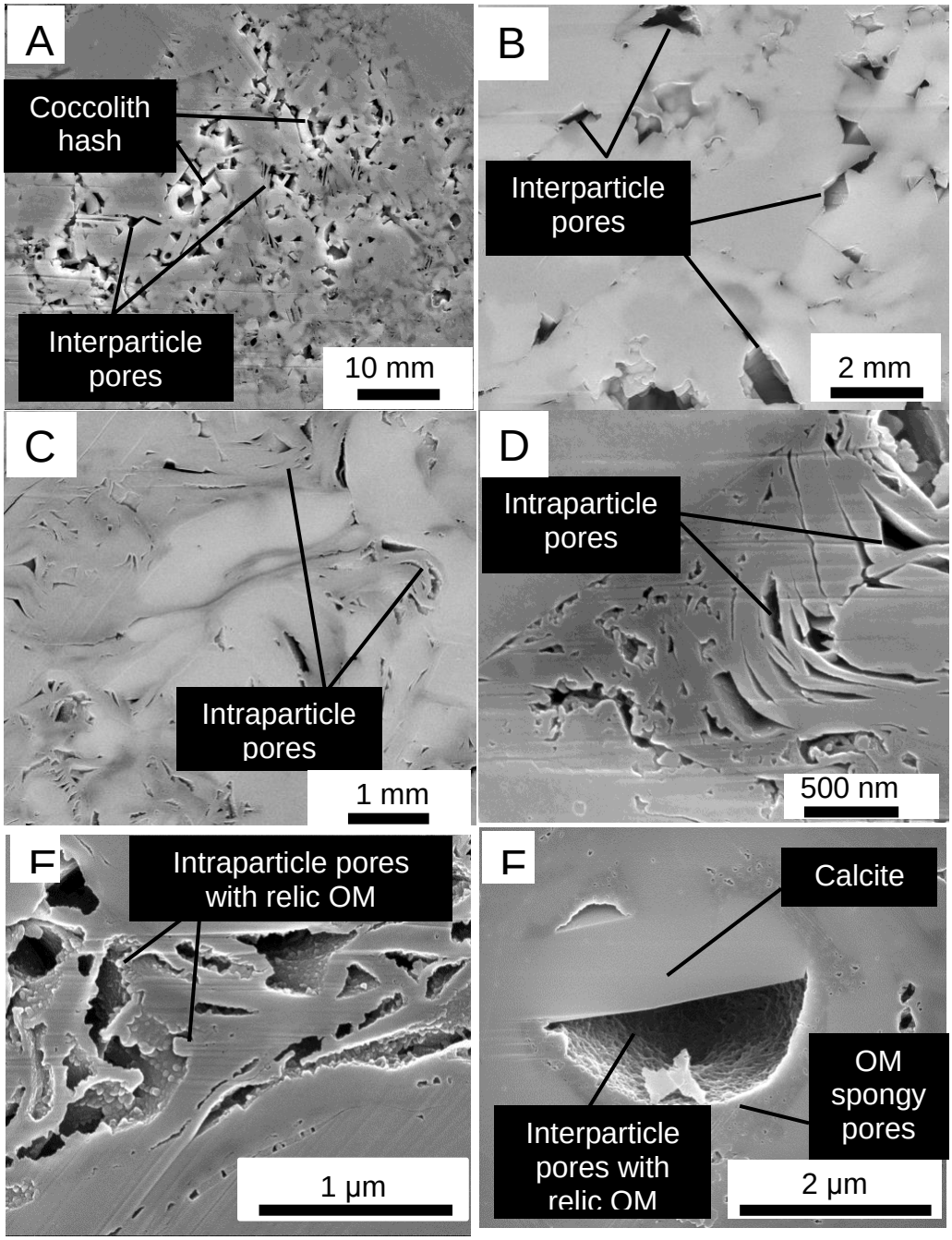

Figure 3.11: SEM photomicrographs showing examples of three different pore types: interparticle, intraparticle, and secondary OM pores. (A) Interparticle pores within coccolith hash. (B) Interparticle pores between cemented coccolith hash. (C) Intraparticle pores within compacted clay platelets. (D) Elongated intraparticle pore within clay platelet. (E) Intraparticle pores with organic matter (OM) remnant. (F) Interparticle pores with OM remnant that has OM spongy pores.

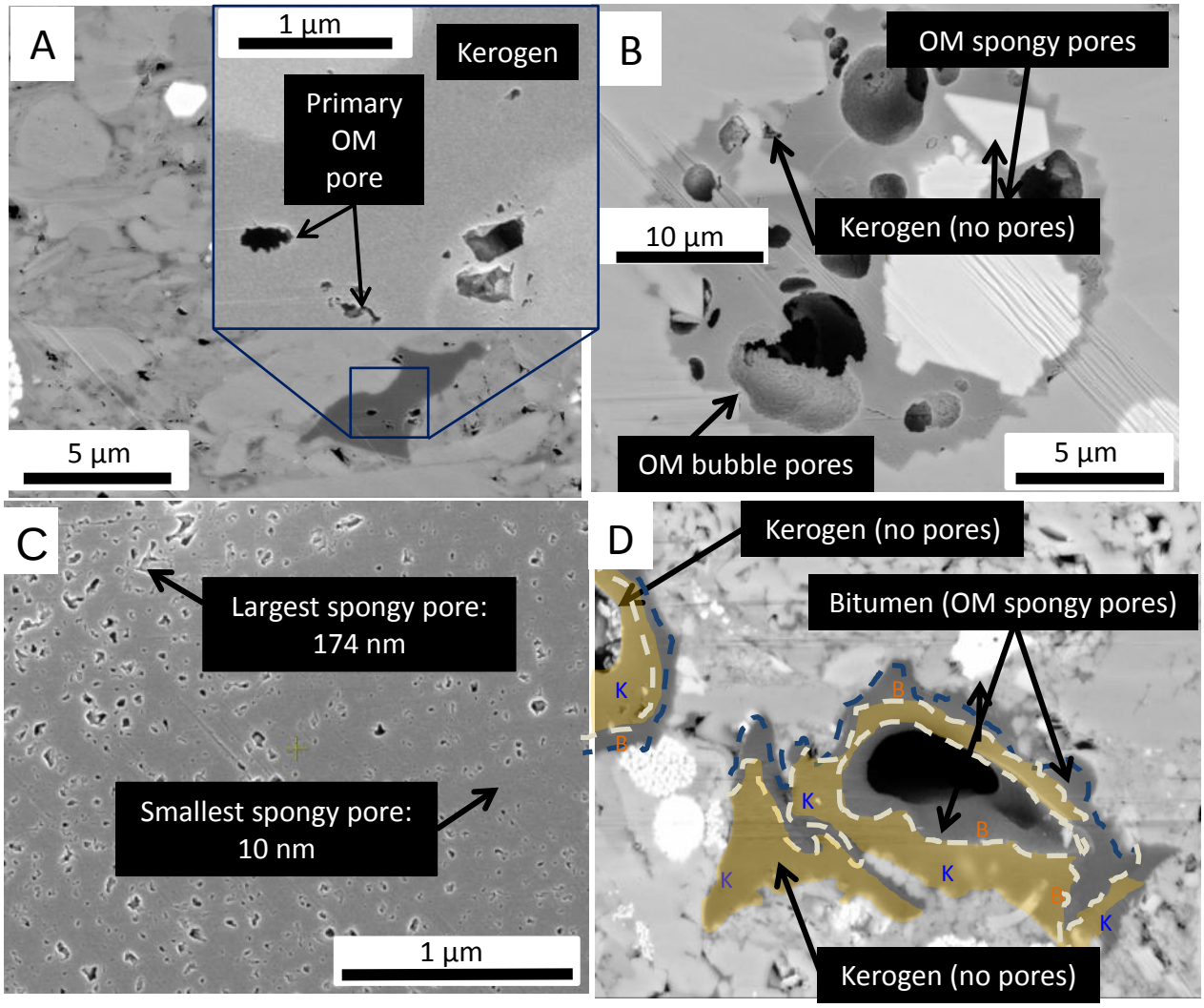

Figure 3.12: SEM photomicrographs showing three types of organic matter (OM) pore and OM complex (kerogen + bitumen). (A) Primary OM pores in compacted kerogen. (B) OM bubble pores in bitumen within the globigerinid chamber. Bitumen followed calcite precipitation in the chamber, as indicated by crystal faces. (C) OM spongy pores in the bitumen inside a foraminifera chamber. (D) OM pores in kerogen plus solid bitumen complex. B = bitumen (dark gray); K = kerogen (yellow).

3.6.2 Organic-Matter (OM) Pores

OM pores comprise both primary and secondary OM pores, which include OM bubble pores and OM spongy pores (Figure 3.12). OM pores can be subdivided into three categories on the basis of their morphology and interpreted origins. Primary OM pores are related to the original structure of kerogen; OM bubble pores and OM spongy pores are the result of OM maturation (Ko et al., 2016) (Table 3.4). In addition, there is special occurrence of OM pores related to their location rather than origin: OM pores in kerogen and bitumen complex.

Primary OM Pores: These pores include those present in the original OM (kerogen) such as cells in wood and leaf fragments or spores (Figure 3.12A). The organic matter is commonly particulate and less compactible (rigid cell structures). Primary OM pores are considered inherited and are not related to thermal maturation.

OM Bubble Pores: These pores are generally rounded to subrounded and can range from hundreds of nanometers to a few micrometers in size (Figure 3.12B). The occurrence of OM bubble pores is related to thermal maturation of organic matter. The OM bubble pores have been interpreted to result from bitumen cracking to oil and gas (Loucks and Reed, 2014; Table 3.5).

OM Spongy Pores: These pores are generally smaller (nanometer scale: 2.5 to 200 nm) and are much more abundant than OM bubble pores (Figure 3.12C). They have a rounded, subrounded, or subangular shape. They have been interpreted to be related to gas generation at higher stages of maturation (Loucks et al., 2012; Table 3.5). OM spongy pores are most commonly found in migrated solid bitumen, pyrobitumen, or char (Bernard et al., 2012a, 2012b; Loucks and Reed, 2014).

OM pores in kerogen and solid bitumen complex: This is not a new type of OM pore. Rather, this kerogen and solid bitumen complex is a special but common

occurrence in mudrocks. These OM spongy pores were formed in migrated solid bitumen and/or pyrobitumen trapped within kerogen or adsorbed onto the surface of kerogen, forming a kerogen and bitumen complex (Figure 3.12D). The kerogen may have its primary pore structure or may lack pores within. A kerogen and bitumen complex suggests that the kerogen is most likely oil wet, so the migrated bitumen can be absorbed or trapped within or on the kerogen particles. The separation of assumed kerogen and bitumen is based on working definitions and experimental works in Ko et al. (2016). Without using scanning transmission x-ray microscopy (STXM) to understand the bonding of carbon in organic compounds in SEM scale, the exact form of organic matter could not be confirmed (Bernard et al., 2012a, b; Romero-Sarmiento et al., 2014).

General pore types	Pore types	Sub types	Basic attributes	Illustration
Mineral pore	Primary mineral pore	Interparticle pore	Occur between grains and crystals. Size and shape vary but many are triangular in two dimensions and are filled with connate water (Loucks et al., 2012)	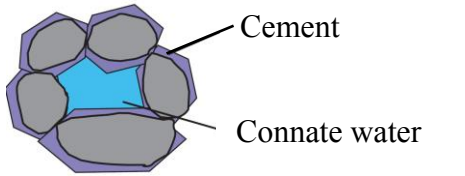
		Intraparticle pore	Occur within boundaries of grains and crystals, e.g., as molds or intrafossil pores or within clay mineral platelets and pyrite framboids. Pore size and shape are variable and are related to origins of particles and crystals (Loucks et al., 2012)	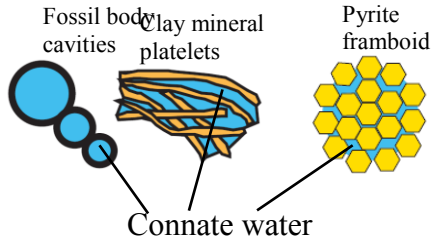
	Modified mineral pores. These can be misidentified as OM pores because they are in contact with organic matter.		Pores are in contact with both minerals and organic matter.	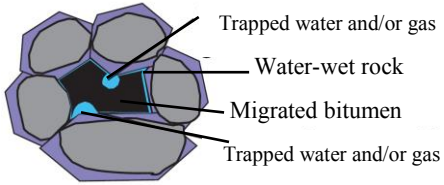
			Residual oil within pores. Pores are entirely in contact with organic matter but are supported by mineral framework. Pore shape and size are controlled by the original mineral pores.	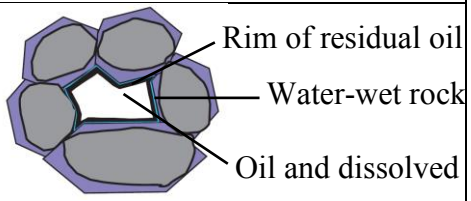

Organic matter (OM) pore	Primary OM pore		Inherited primary pores in the original organic matter (kerogen) such as cells in wood and leaf fragments or spores. Pore size and shape varies. Pores not related to thermal maturation.	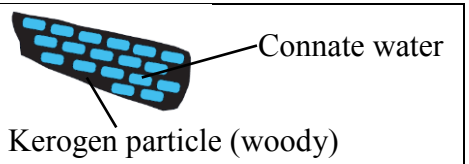
	Secondary OM pore	OM bubble pore	Generally sub-micrometer to micrometer scale (hundreds of nanometers to a few micrometers). Rounded shape. Related to thermal maturation.	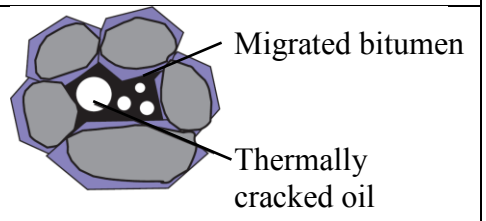
		OM spongy pore	Generally smaller and more abundant than bubble pores. Pores are nanometer scale and homogeneously distributed. Rounded, subrounded, or subangular shape. Related to thermal maturation.	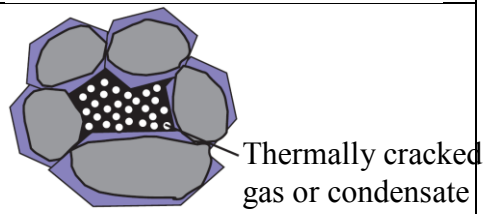

Table 3.4: Types of pores in the Eagle Ford mudrocks.

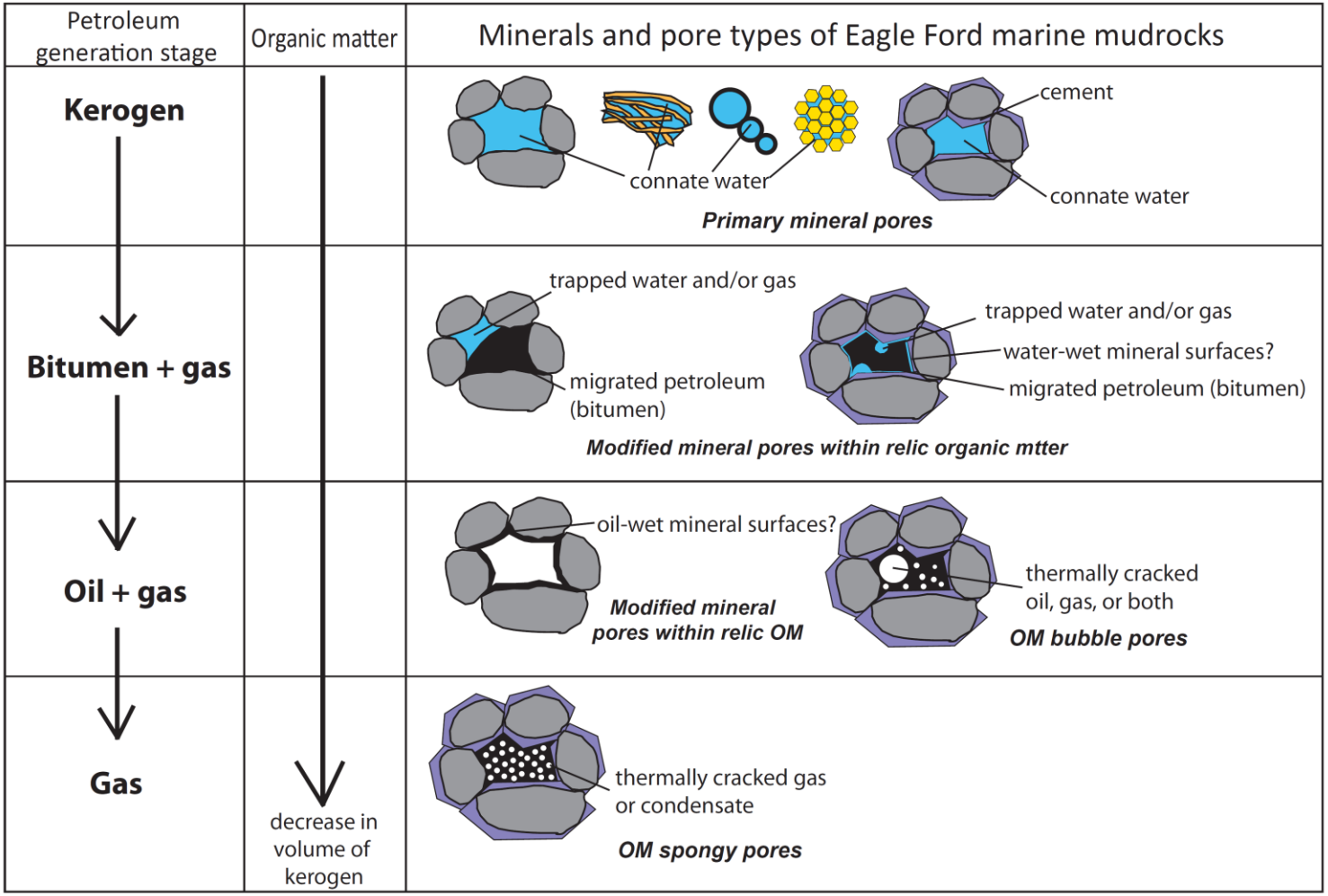

Table 3.5: Evolution of minerals and pore types in the Eagle Ford marine mudrocks.

3.6.3 Porosity and Pore Networks

Figure 3.13 shows the range of point-count-derived visible total porosity values at magnifications of 5,000X (horizontal field width [HFW] = 60 μm), 15,000X (HFW = 20 μm), and 120,000X (HFW = 2.5 μm) for all samples in the K1 and K2 cores. Visible total porosity is higher at higher magnification because smaller pores can be resolved. Figure 14 shows point-count visible total porosity values of marl and limestone facies in the K1 and K2 cores. The four points shown for each sample reflect porosity measurements in four SEM photomicrographs for each sample at 5,000X (Figure 3.14). The spread of the data points shows the heterogeneity at the microscale in the matrix within each sample. The point-count porosity of the marl facies is slightly higher in the lower Eagle Ford (LEF) than in the upper Eagle Ford (UEF). The limestone facies samples have the lowest visible total porosity.

In addition to visible total porosity, it is important to understand variations in pore type. Mineral porosity includes primary mineral pores and modified mineral pores. Figures 3.15 and 3.16 show plots of point-count visible OM porosity, mineral porosity, and total porosity at 5,000X and 15,000X magnification, respectively. A key observation is that most of the visible total porosity is contributed by mineral porosity. OM spongy pores are also an important contributor to visible total porosity but cannot be resolved at 5,000X machine magnification. In the Eagle Ford, mineral pores are generally larger than OM pores (assumed to be connected by larger pore throats) and therefore assumed to

control permeability. It should be noted, however, that one UEF sample (K1: 11,838) is dominated by OM pores instead of mineral pores.

Figure 3.17 shows the pore-size distribution of the marl facies in the upper and lower Eagle Ford. The distribution was determined from manually traced pores on 5,000X SEM images. The frequency of counts of pore-size range was normalized to 100% in order to compare differences in pore-size distribution. The *x*-axis depicts the equivalent circular diameter (ECD), which, by definition, is the diameter of a circle having the same area as that of the object (Figure 3.17). In the UEF samples, smaller pore sizes (ECD = 250 to 500 nm) dominate at deeper burial depths, and the abundance of relatively larger pore sizes (ECD > 500 nm) increase at shallower depths. This systematic increase in relative proportion of small and large pore sizes with depth in the UEF can possibly be attributed to gradual changes in grain size, because (1) the mineral pore network is dominated in the Eagle Ford and (2) the size and abundance of mineral pores are partly controlled by size and abundance of silt- and clay-sized grains (Figure 18). The silt content increases from 12,185 ft (3,714 m) (K2) to 11,778 (3,590 m) (K1) ft (Figure 3.18). Increasing silt-sized grain sediment supplies and increasing hydrodynamic depositional energy could cause increased abundance and size of grains. No pore-size distribution trends are observed in the LEF. Similar pore-size distribution is observed between 12,169, 12,174, and 11,838, and 11,878, 12,246, and 12,308 ft (3,709, 3,711, 3,608, 3,620, 3,733, 3,751 m).

Figure 3.19 shows pore-size distribution of two marl samples (K1: 11,918 ft [3,633 m] and K2: 12,174 ft [3,711 m]). Pore-size distribution was obtained from

manually traced pores at all three scales of SEM photomicrographs. These two samples show similar pore-size distribution with the sample taken at 11,918 ft (3,633 m) (LEF) having more pores smaller than 35 nm (ECD).

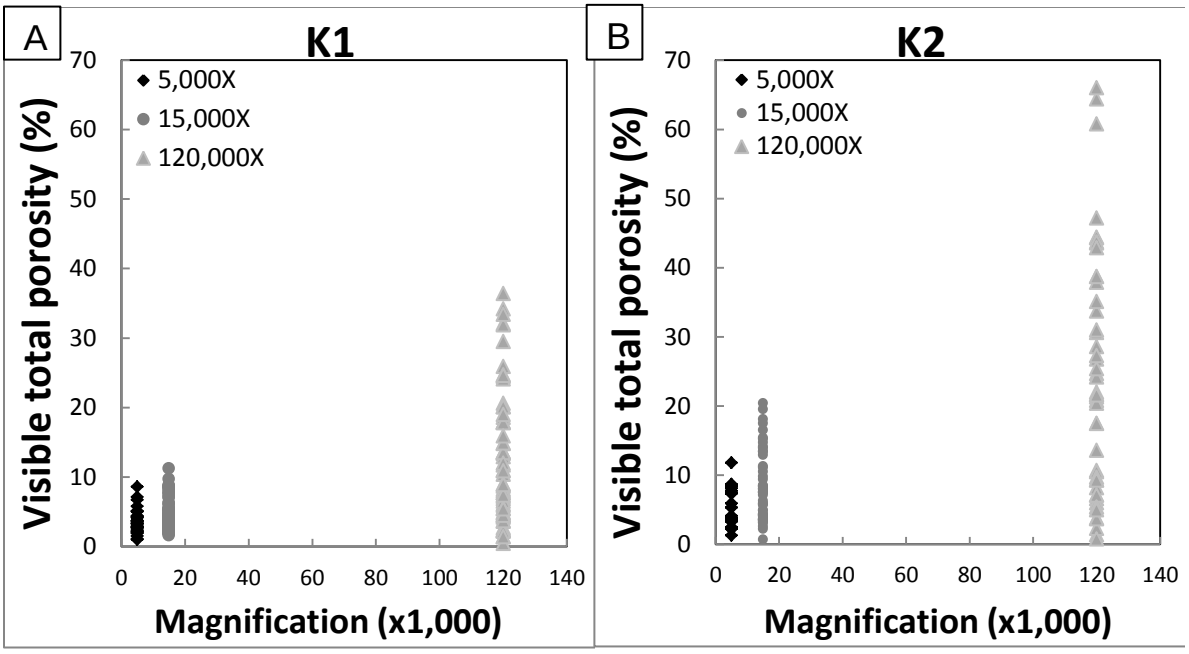

Figure 3.13: Plots showing point-count derived visible total porosity at 5,000X, 15,000X, and 120,000X magnifications. (A) K1 core. (B) K2 core. At higher magnification, counted visible total porosity is higher and data variance is greater.

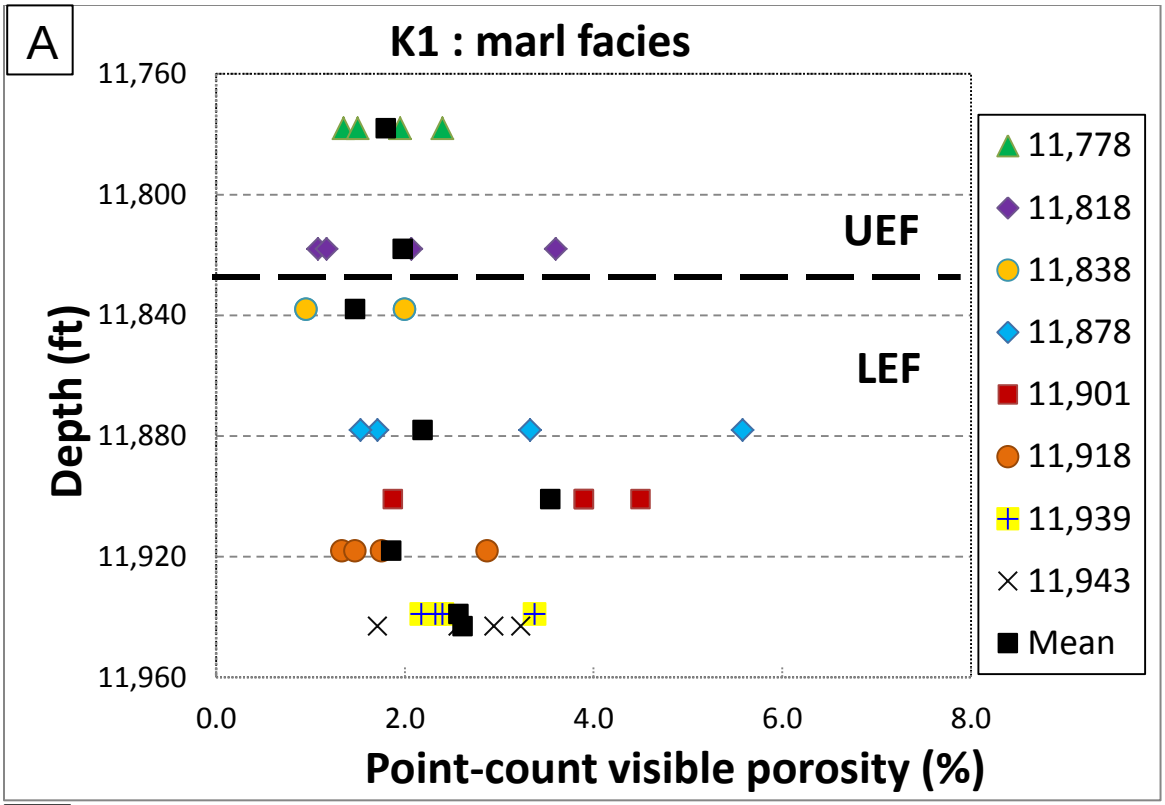
A
K1 : marl facies
11,760
11,800
11,840
11,880
11,920
11,960
Depth (ft)
UEF
LEF
0.0
2.0
4.0
6.0
8.0
Point-count visible porosity (%)
11,778
11,818
11,838
11,878
11,901
11,918
11,939
11,943
Mean

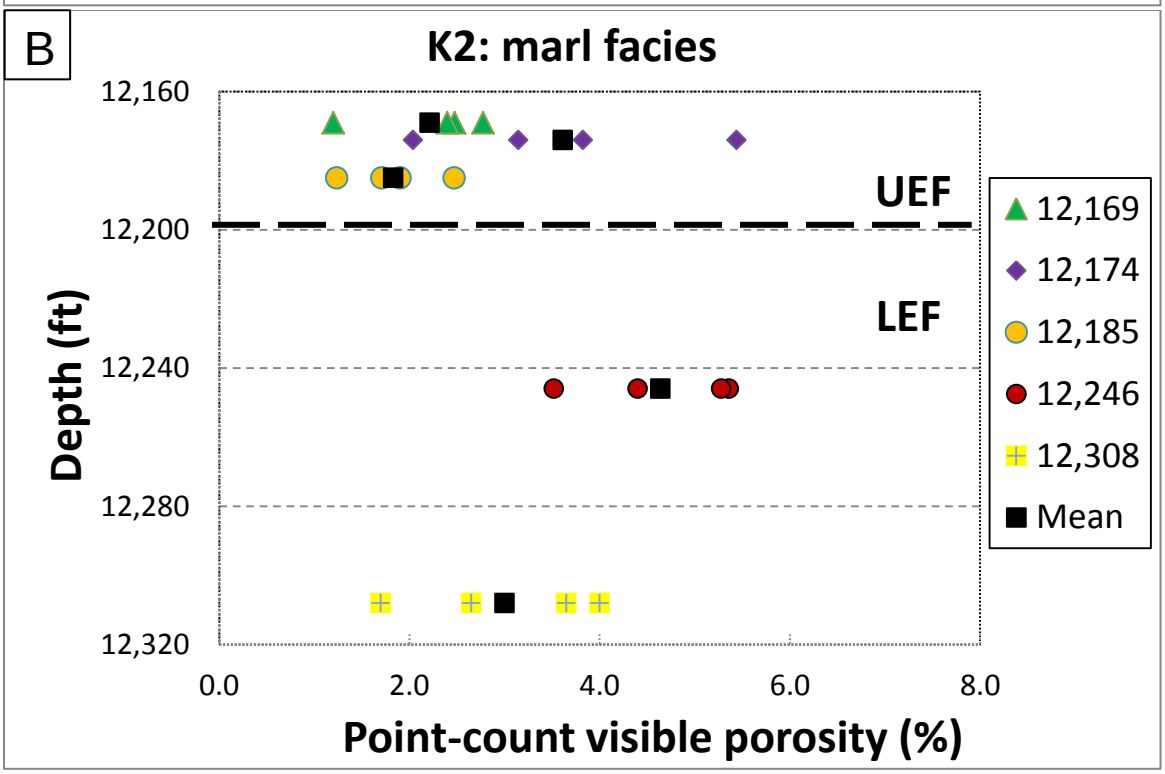
B
K2: marl facies
12,160
12,200
12,240
12,280
12,320
Depth (ft)
UEF
LEF
0.0
2.0
4.0
6.0
8.0
Point-count visible porosity (%)
12,169
12,174
12,185
12,246
12,308
Mean

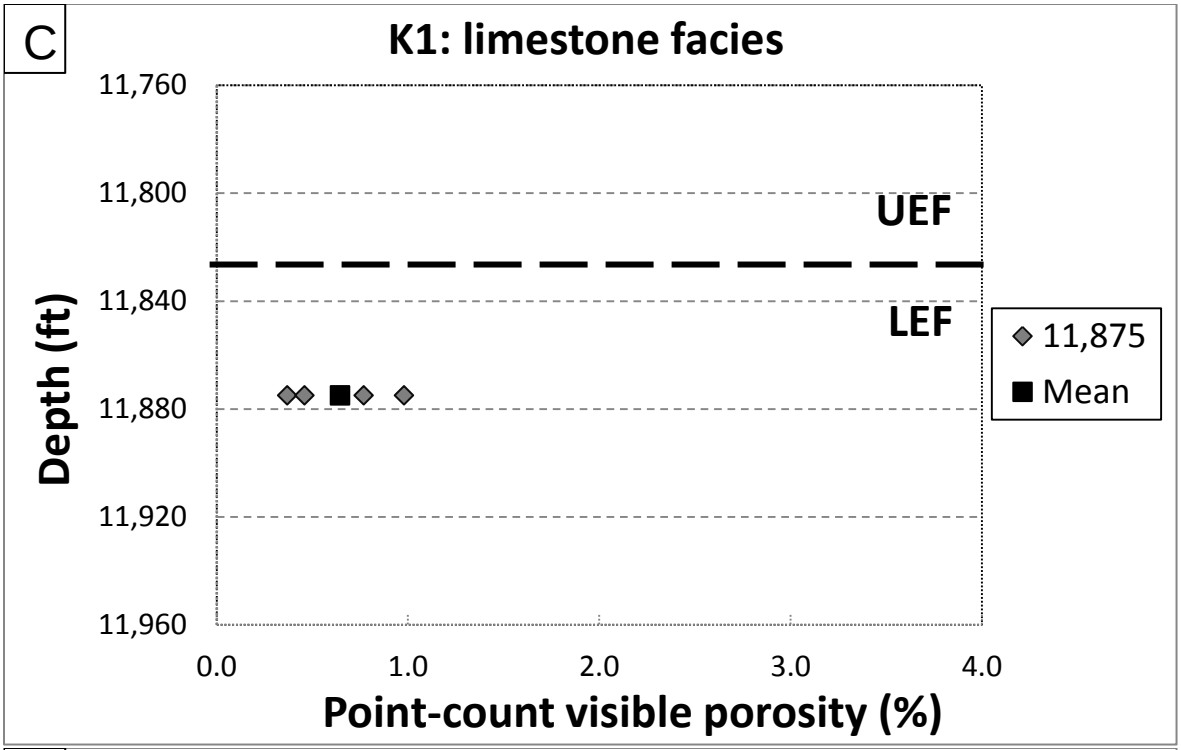
C
K1: limestone facies
11,760
11,800
11,840
11,880
11,920
11,960
Depth (ft)
UEF
LEF
11,875
Mean
0.0
1.0
2.0
3.0
4.0
Point-count visible porosity (%)

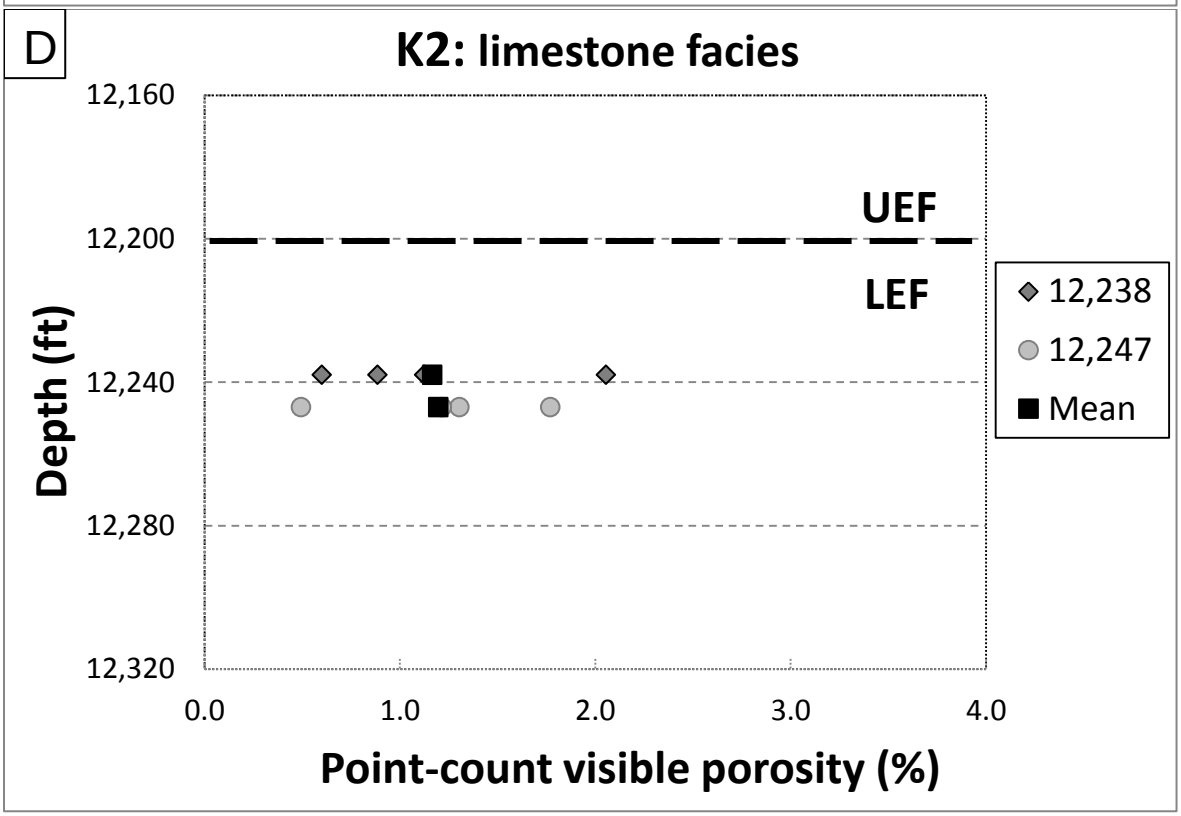
D
K2: limestone facies
12,160
12,200
12,240
12,280
12,320
Depth (ft)
UEF
LEF
12,238
12,247
Mean
0.0
1.0
2.0
3.0
4.0
Point-count visible porosity (%)

Figure 3.14: Plots showing point-count based visible total porosity measured at 5,000X magnification. (A) K1: marl facies. (B) K2: marl facies. (C) K1: limestone facies. (D) K2: limestone facies. K1 and K2 cores are in the late oil (condensate and gas) window. Mean visible total porosity of marl facies increases from upper Eagle Ford (UEF) to lower Eagle Ford (LEF). Each sample has four points that represent visible total porosity estimation from point counting of four different SEM photos.

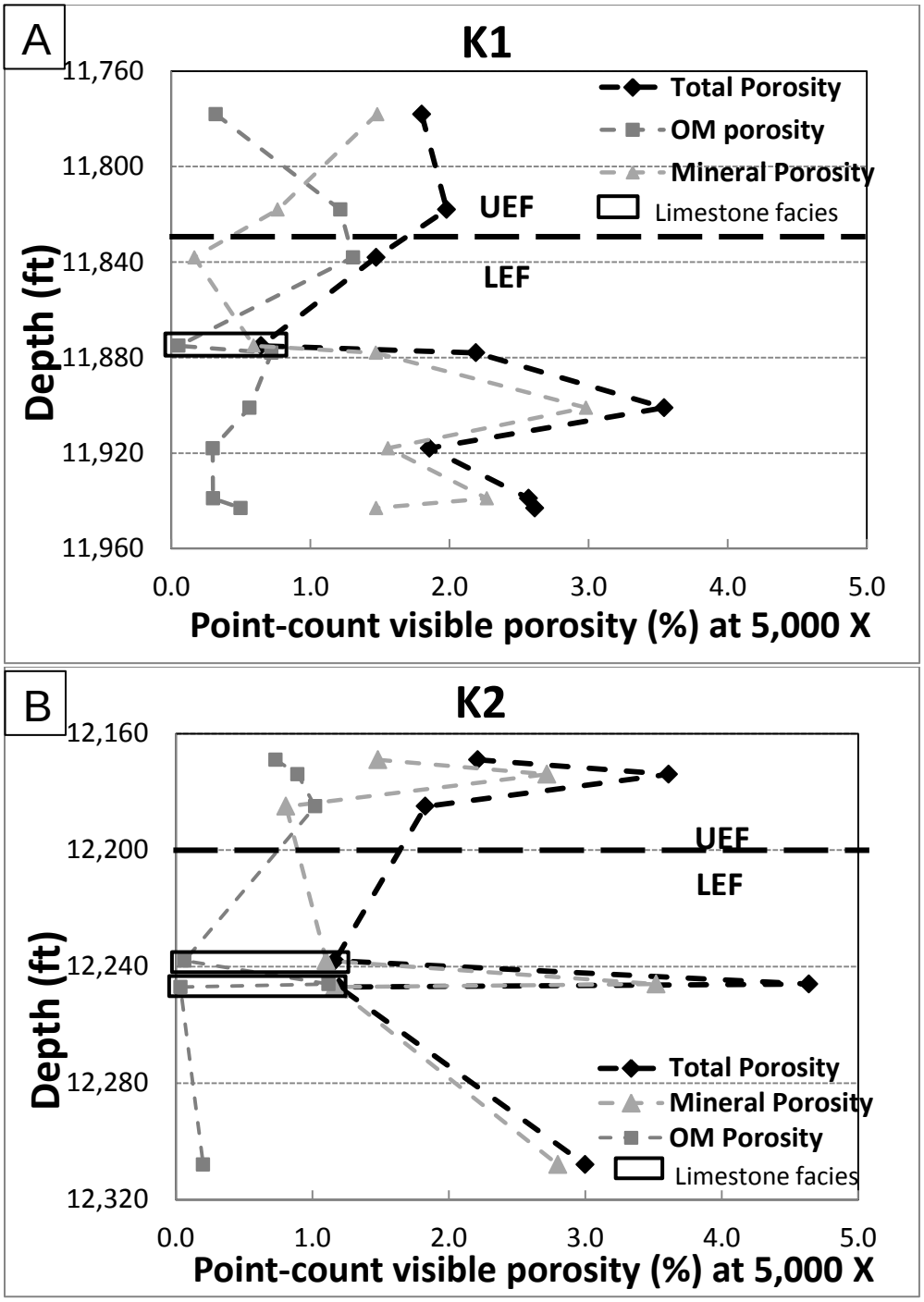

Figure 3.15: Plots of point-count visible organic matter (OM) porosity, mineral porosity, and total porosity for (A) K1 and (B) K2 cores at 15,000X magnification. Most of the visible total porosity is contributed by mineral porosity. UEF = upper Eagle Ford; LEF = lower Eagle Ford.

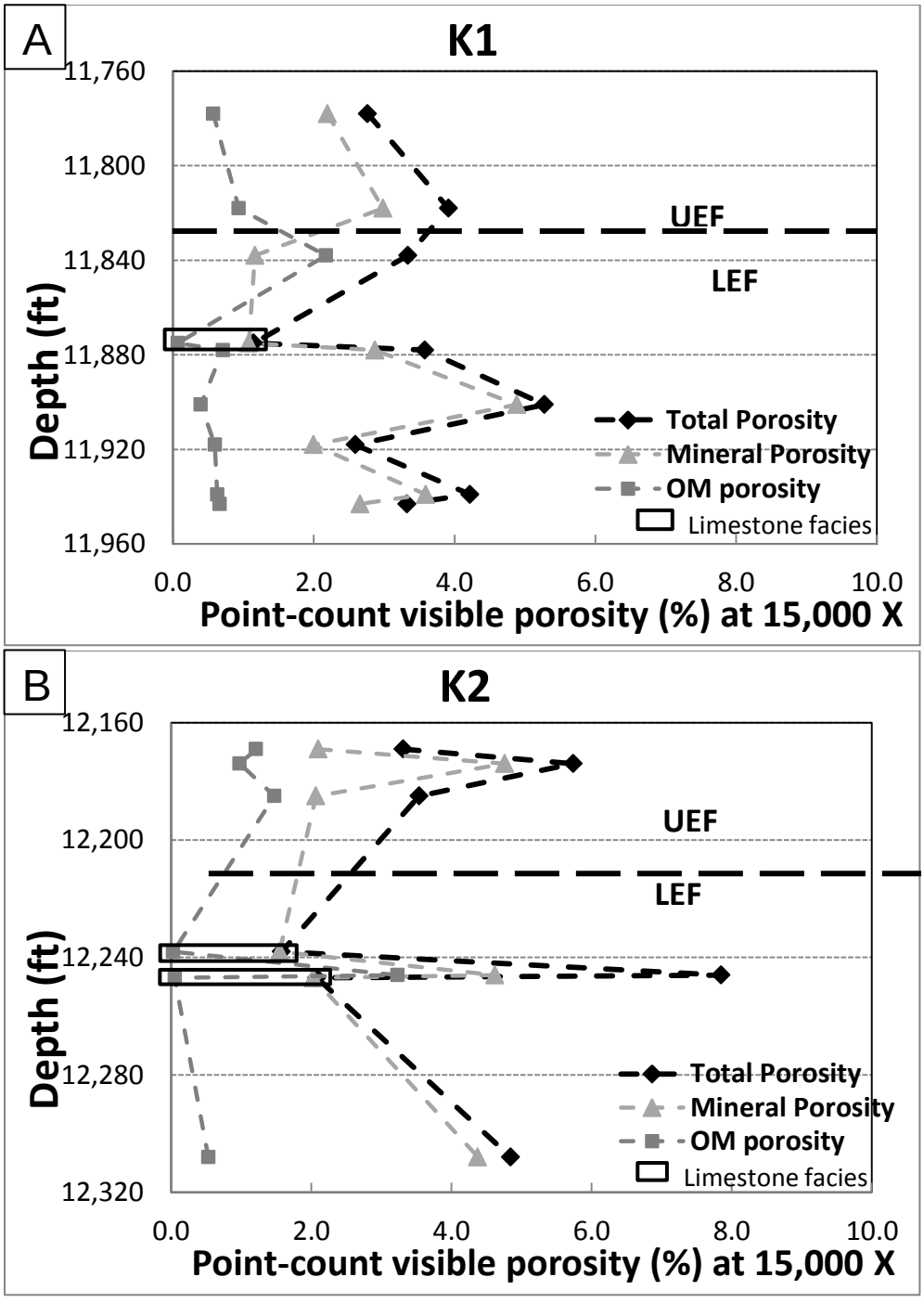

Figure 3.16: Plots of point-count visible organic matter (OM) porosity, mineral porosity, and total porosity for (A) K1 and (B) K2 cores at 5,000X magnification. Limestone facies are outlined as rectangles. UEF = upper Eagle Ford; LEF = lower Eagle Ford.

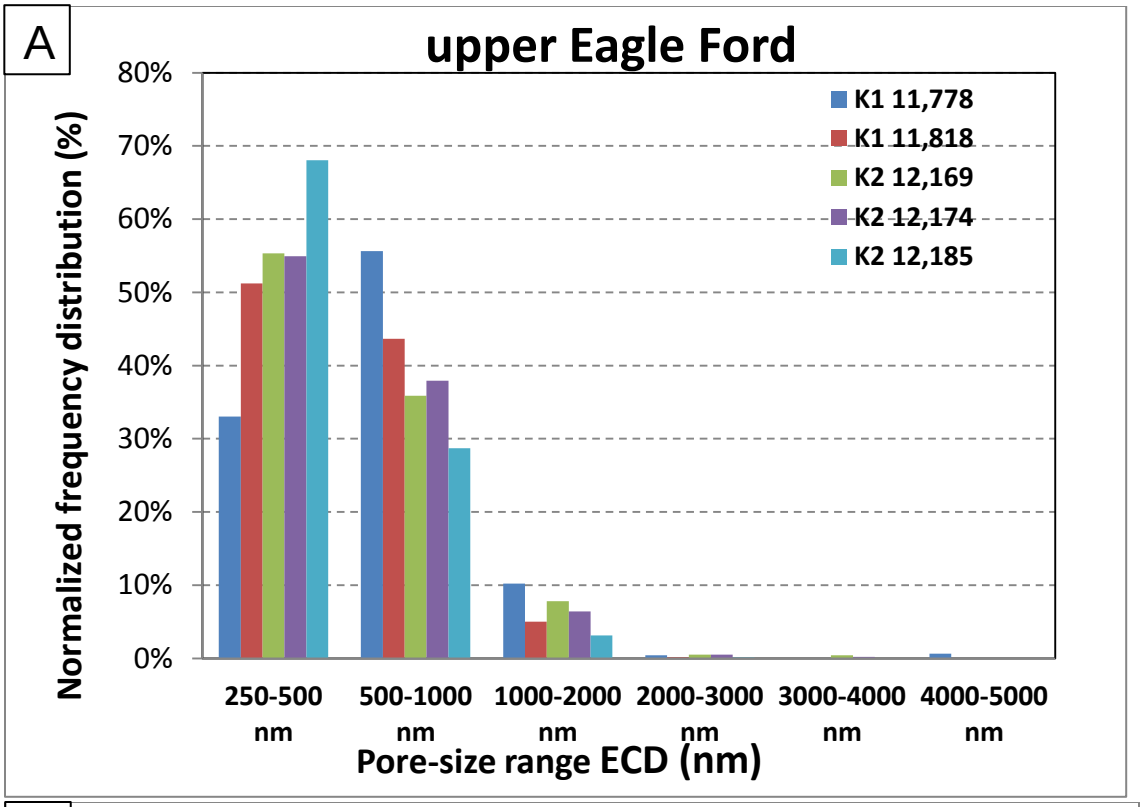
A
upper Eagle Ford
80%
70%
60%
50%
40%
30%
20%
10%
0%
Normalized frequency distribution (%)
K1 11,778
K1 11,818
K2 12,169
K2 12,174
K2 12,185
250-500 nm
500-1000 nm
1000-2000 nm
2000-3000 nm
3000-4000 nm
4000-5000 nm
Pore-size range ECD (nm)

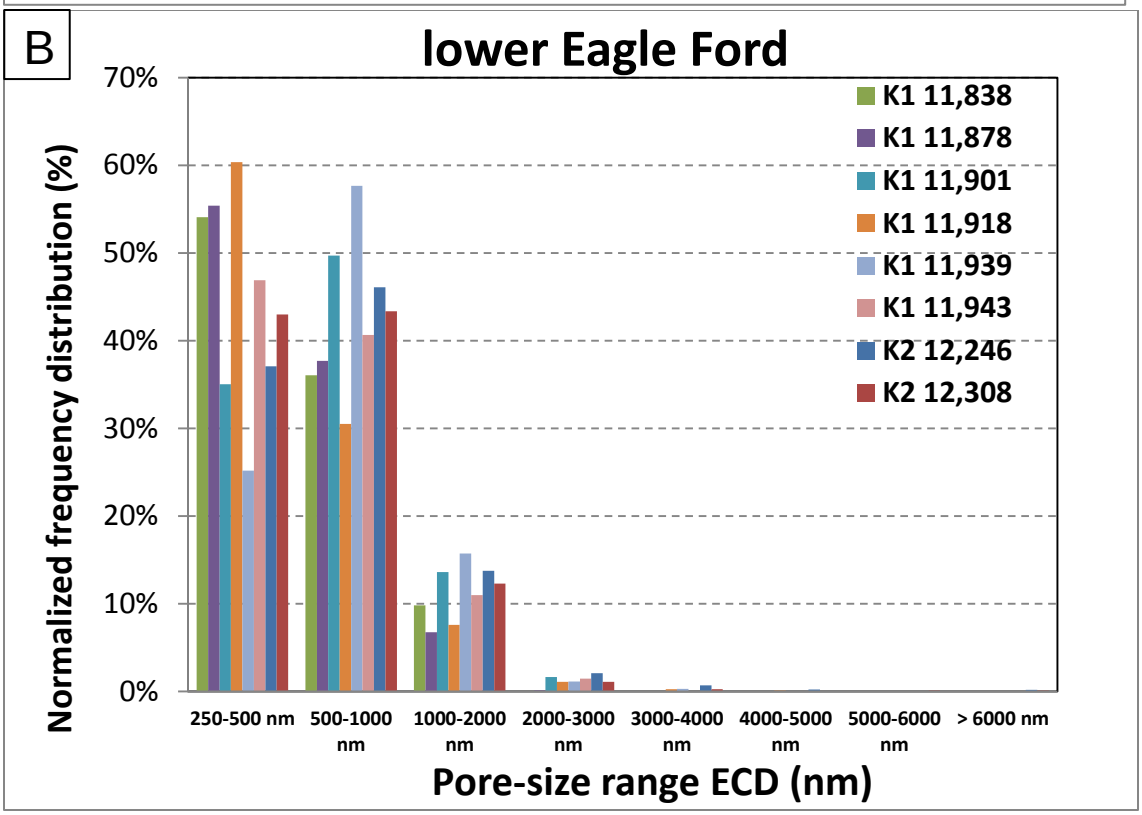
B
lower Eagle Ford
70%
60%
50%
40%
30%
20%
10%
0%
Normalized frequency distribution (%)
K1 11,838
K1 11,878
K1 11,901
K1 11,918
K1 11,939
K1 11,943
K2 12,246
K2 12,308
250-500 nm
500-1000 nm
1000-2000 nm
2000-3000 nm
3000-4000 nm
4000-5000 nm
5000-6000 nm
> 6000 nm
Pore-size range ECD (nm)

Figure 3.17: Plots of normalized pore-size frequency distribution of marl facies from (A) upper Eagle Ford (UEF) and (B) lower Eagle Ford (LEF) sections in K1 and K2 cores. Pore-size distribution data were obtained from manually traced pores on 5,000X SEM images. The frequency was normalized to 100% in order to compare differences. Note that in the UEF, smaller pores are increasingly abundant with depth, whereas large pores show the opposite trend. No trends are apparent in the LEF. ECD = equivalent circular diameter.

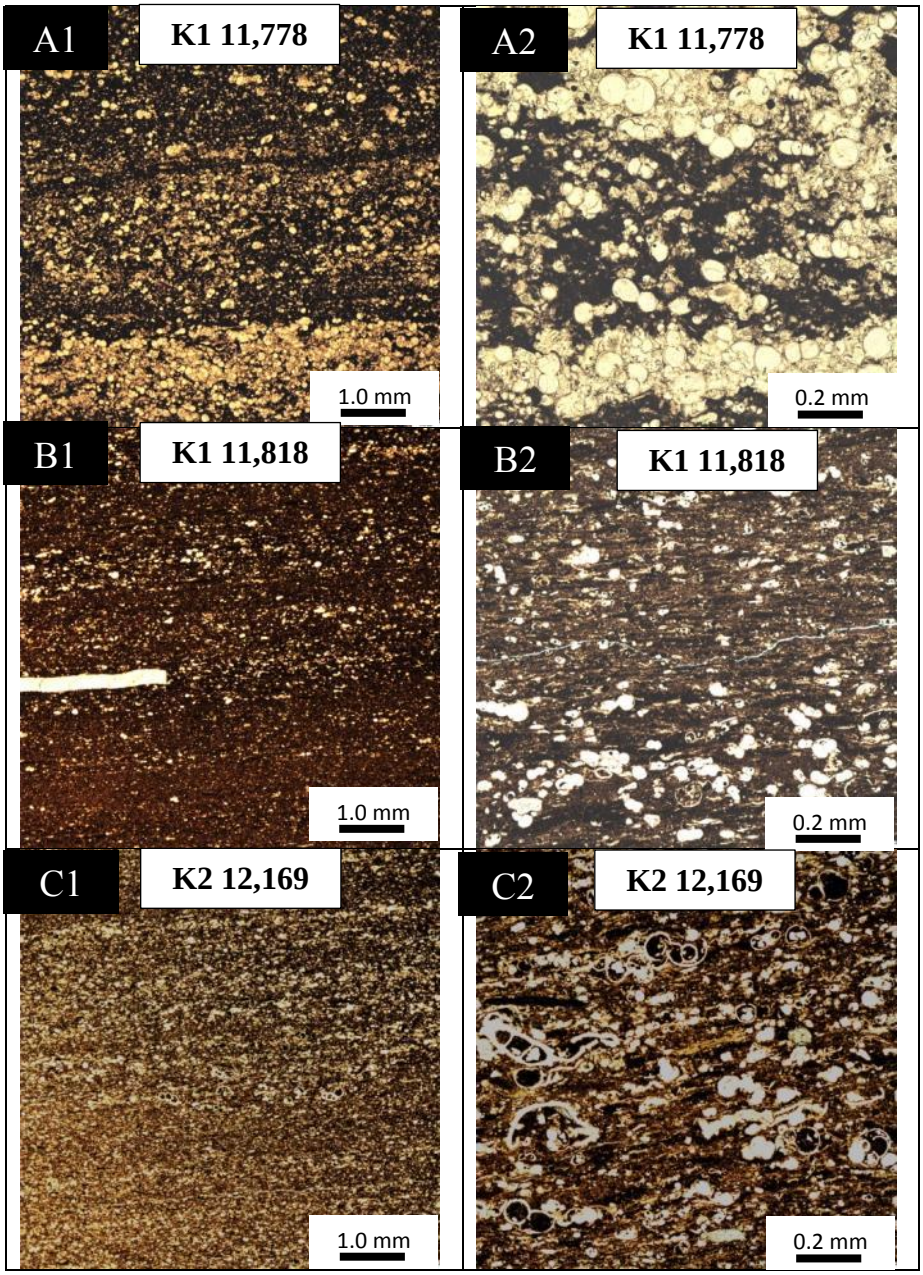

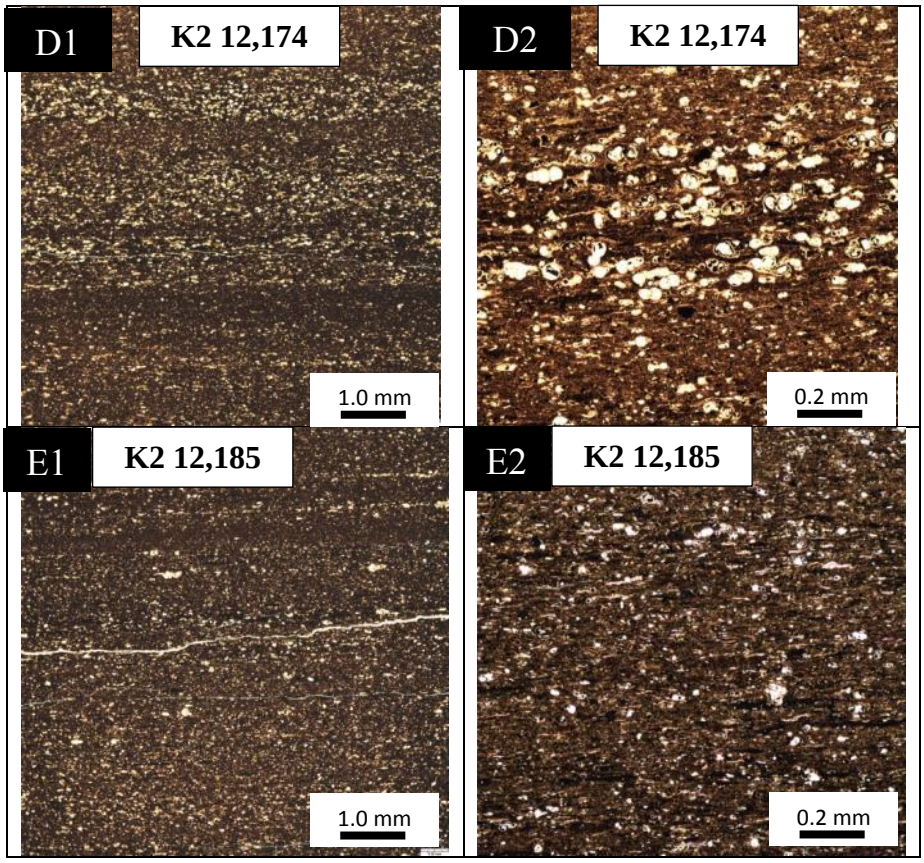

Figure 3.18: Thin section photomicrographs of upper Eagle Ford samples in the K1 and K2 cores, Karnes County, showing increased silt-sized grain proportions towards shallower depths of UEF. A1-A2: globigerinid-bearing, laminated wackestone-packstone. K1: 11,778 ft (3,590 m). B1-B2: globigerinid-bearing, laminated mudstone-wackestone. K1: 11,818 ft (3,602 m). C1-C2: globigerinid-bearing, laminated mudstone-wackestone. K2: 12,169 ft (3,709 m). D1-D2: globigerinid-bearing, laminated mudstone-wackestone. K2: 12,174 ft (3,711 m). E1-E2: globigerinid-bearing, laminated mudstone-wackestone. K2: 12,185 ft (3,714 m).

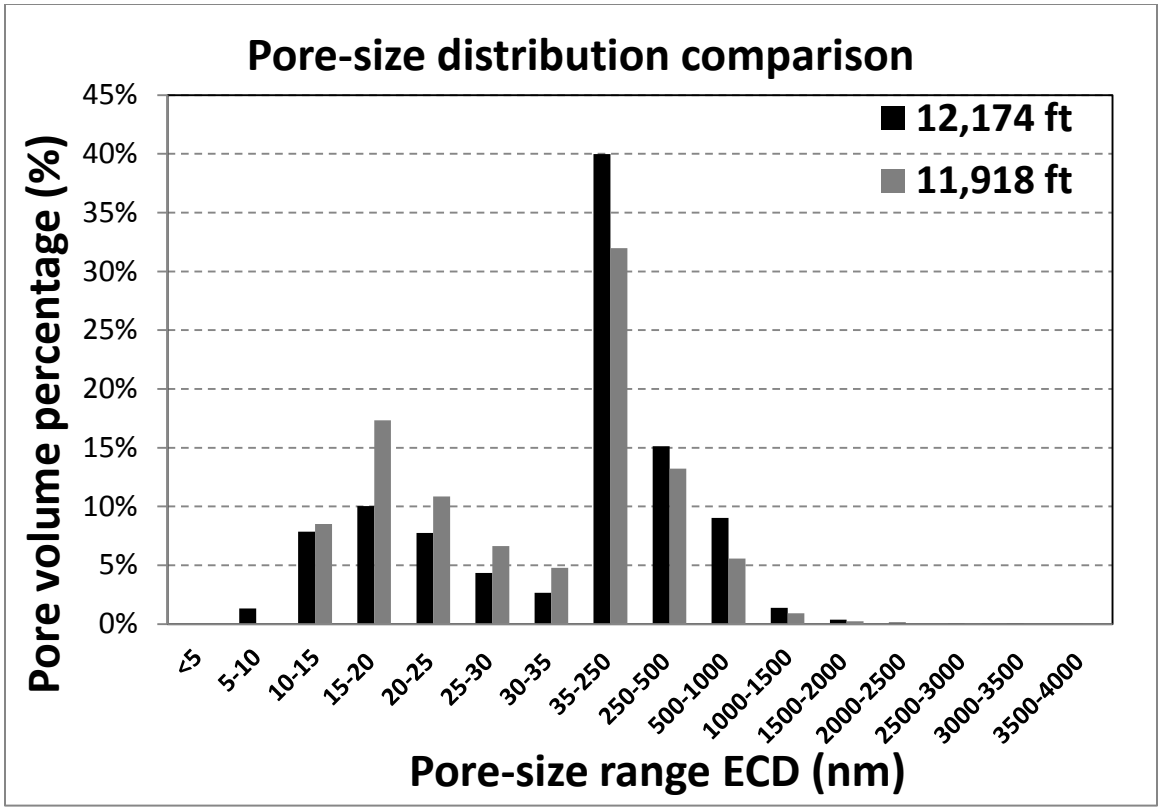

Figure 3.19: Plots showing comparisons of pore-size distribution in two marl samples (K1: 11,918 ft, lower Eagle Ford; K2: 12,174 ft, upper Eagle Ford) at 5,000X, 15,000X, and 120,000X scales. ECD = equivalent circular diameter.

3.7 COMPARISON OF VISIBLE TOTAL POROSITY AND PORE-SIZE DISTRIBUTION

3.7.1 Porosity

Comparisons of visible total porosity derived from point-count and pore-traced methods are shown in Figures 3.20 and 3.21. The point-count method resulted in slightly higher porosity totals for most images counted (Figure 3.20). However, the differences decrease in higher magnification images (Figure 3.21). Commonly in the Eagle Ford mudrocks, the interval between counted points is smaller than the largest pores. If one pore is hit twice, the pore is counted twice, etc. Error associated with point count method is related to the amount and size of points and components counted (Folk, 1980). Pore sizes in the Eagle Ford mudrocks range across approximately five orders of magnitude, and a total of one thousand points were counted on each image. For a set amount and size of points, because more components and more size variations are included in lower magnification images, higher percentage of errors would be expected to see towards the lower magnification images. Error associated with pore tracing methodology is most likely from pixel resolution and tracing precision. Therefore, error from pore trace data is expected to be less than point count data. In addition, although each spongy pore volume is relatively insignificant, once the OM spongy pore is counted, it contributes 0.1% (1 point/1000 points) to the visible total porosity. The numbers of OM spongy pores are the most abundant and these pores can be resolved at 15,000X and sometimes 5,000X images. Therefore, point count methodology tends to slightly overestimate the visible total porosity than the pore trace at low magnification images.

Both porosity calculation approaches have advantages and disadvantages. The advantages of using the point-count method are that it (1) is less time-consuming, and (2) allows pores as small as 2.5 nm to be recognized. The disadvantage of this method is that

a grid of points (five pixels for each point in JMicroVision) was used to count pore sizes across four to five orders of magnitude, and the preset 1,000 grid points for this study might actually count the larger pores but not the smaller pores. The advantage of the pore-tracing method is that it provides geometry information for geostatistical use. Disadvantages of this method are that it is (1) time-consuming, and (2) limited to pores greater than 24 nm.

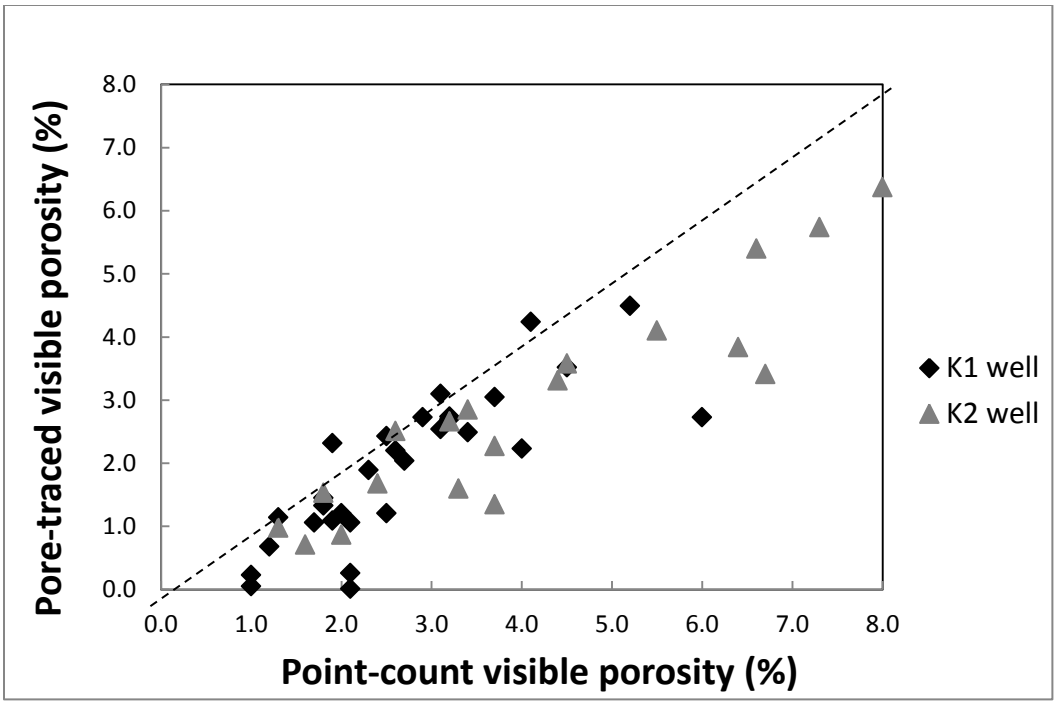

Figure 3.20: Comparison of pore-traced visible total porosity and point-count visible total porosity at all magnifications. In general, point-count visible porosity values are higher than pore-traced visible porosity values.

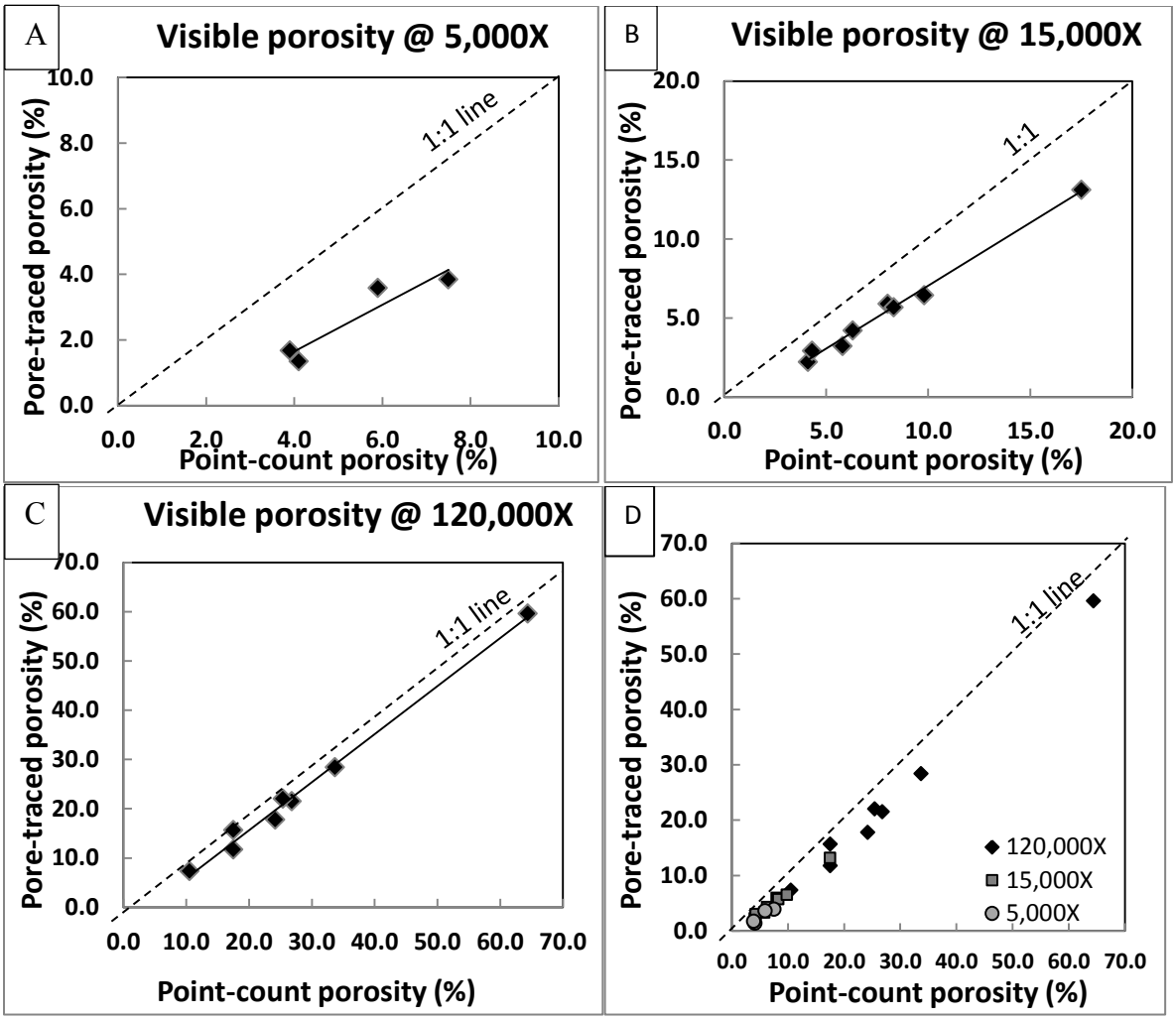

Figure 3.21: Pore-traced visible total porosity versus point-count-derived visible total porosity of a marl sample (K2: 12,174, UEF) at three scales of investigation (A) 5,000X (B) 15,000X (C) 120,000X (D) all scales. Point-count visible porosity is higher than pore-traced visible porosity, although the difference decreases at higher-magnification

3.7.2 Pore-Size Distribution

Figure 3.22 compares the pore-size distribution derived from three scales of SEM imaging and pore tracing, and nitrogen-gas adsorption analysis. Note that pore tracing resolves pore diameters from 20 nm to 15 μm (largest pore observed), whereas nitrogen

adsorption only measures pores from 0.3 to 200 nm. In one sample (Figure 3.22A), the techniques show very similar PSD. In a second sample (Figure 22B), the agreement between the results of the two methods is less.

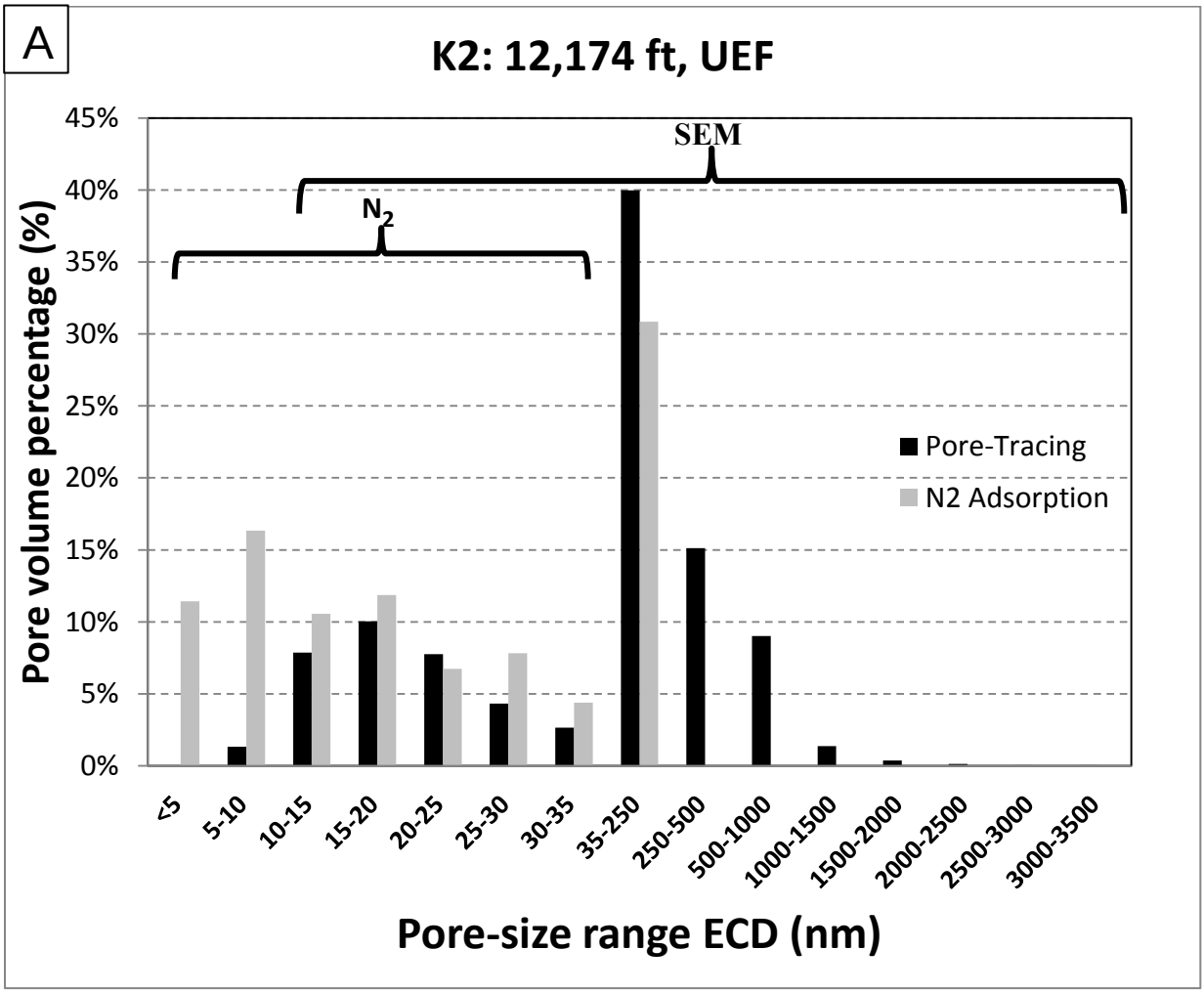

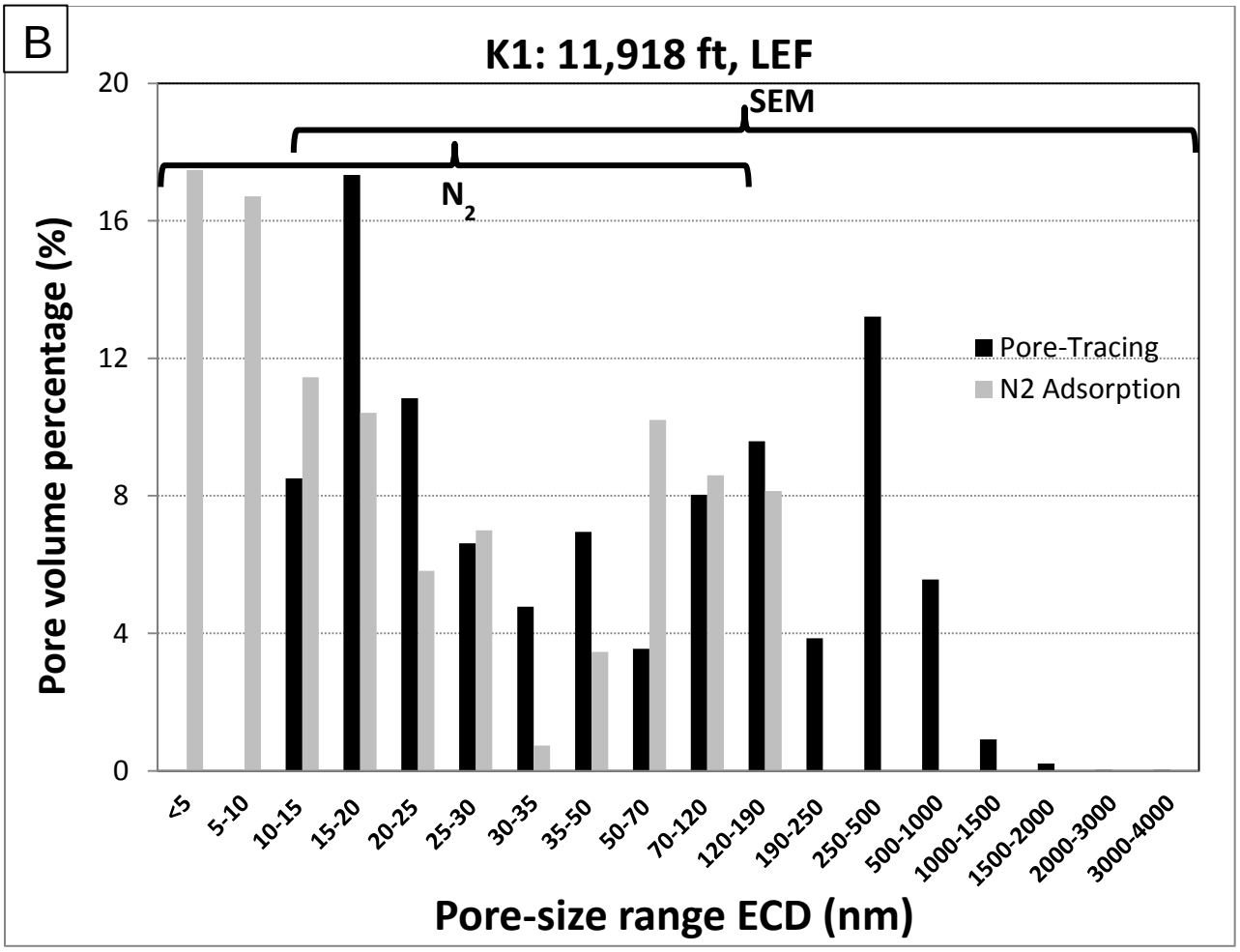

Figure 3.22: Comparison of pore-size distribution of marl samples from pore-tracing and nitrogen-gas-adsorption measurement. (A) K2: 12,174 ft (3,711 m), upper Eagle Ford (UEF). The two techniques show very similar pore-size distribution. (B) K1: 11,918 ft (3,633 m), lower Eagle Ford (LEF). Differences in the two techniques are large owing to the differences in scale resolution between the techniques. ECD = equivalent circular diameter.

3.8 RELATIONSHIPS BETWEEN TOTAL VISIBLE POROSITY, OM-PORE MORPHOLOGY, TOC, AND MINERALOGY

3.8.1 Total Visible OM Porosity and OM-pore Morphology

Eagle Ford mudrock samples are dominated by modified interparticle pores. OM bubble and OM spongy pores contribute less to visible total porosity but are important because they also affect permeability. Because OM spongy pores are best resolved at 120,000X magnification, the OM pore percentage in total organic matter was renormalized and ranked in each SEM photomicrograph. We observed that the morphology and types of OM pores significantly impact the total visible OM porosity. The combination of anomalously large micrometer-sized OM bubble pores plus OM spongy pores contributes the most to total OM porosity, a few smaller bubble pores (hundreds of nanometer-sized pores) plus OM spongy pores contributing the next largest amount, and the primary OM pores contributing the least (Figure 3.23).

3.8.2 Visible OM Porosity and TOC

Generally, no strong correlation exists between visible OM porosity and TOC at the lowest SEM magnification (5,000X). However, one positive correlation trend is apparent between average visible OM porosity at 120,000X and TOC: the upper trend shows no correlation ($R^2 = 0.12$) while the lower one shows strongly positive correlation ($R^2 = 0.81$) (Figure 3.24A). These two trends can be related to the pore morphology as suggested in Figure 3.23. The lower trend is primarily affected by the abundance of OM spongy pores, whereas the lower trend is controlled by the occurrence and mixture of primary OM pores, OM bubble pores, and OM spongy pores. No correlation is apparent

between average visible OM porosity at 5,000X (R^2 = 0.20) and TOC as well as at 15,000X and TOC (R^2 = 0.28) (Figure 3.24B).

3.8.3 Visible Mineral Porosity and Mineralogy

Mineralogical variation (volume percentage) at different sample depths is shown in Table 3.2. Plots of visible mineral porosity against volume percentage of quartz plus feldspar, calcite, and clay minerals are shown in Figure 3.25. No correlation can be established between average visible mineral porosity and the volume percentage of calcite and clay minerals (Figure 3.25A, C). There is a weak positive correlation between average visible mineral porosity at 15,000X and the volume percentage of quartz and feldspar (R^2 = 0.40) (Figure 3.25B). This positive correlation is interpreted to be related to the rigidity of these framework grains, which inhibited compaction of pores. No correlations were found between average visible mineral porosity at 5,000X and 120,000X and the volume percentage of quartz and feldspar.

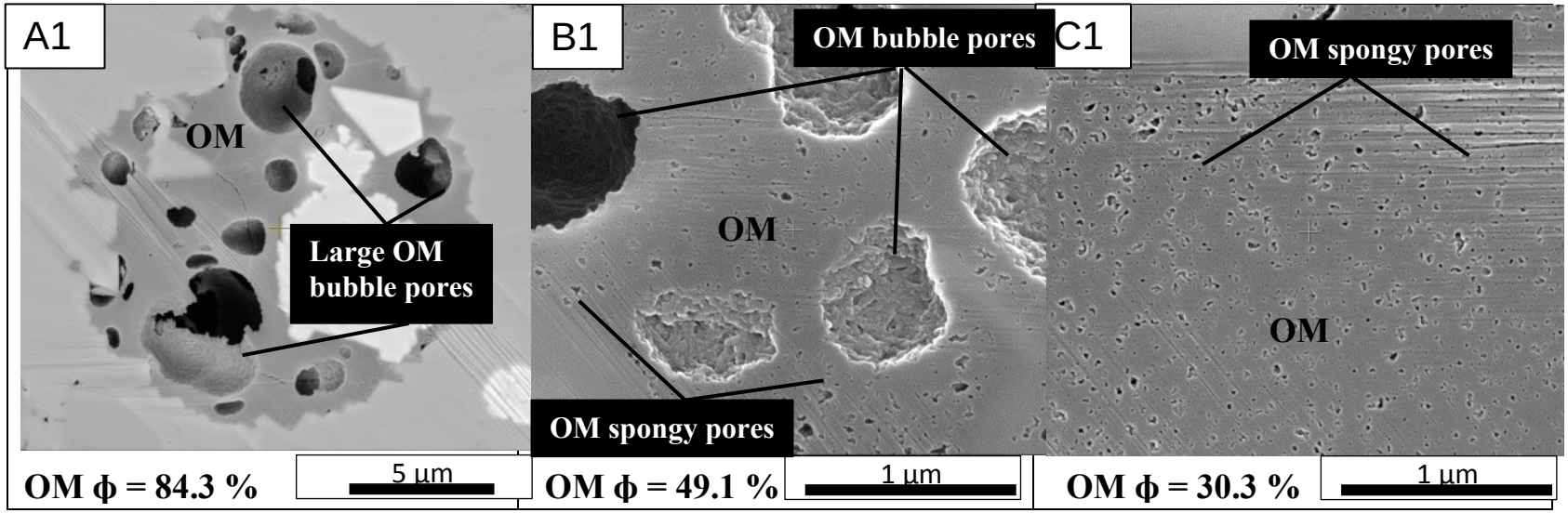
A1
OM
Large OM bubble pores
OM ϕ = 84.3 %
5 µm
B1
OM bubble pores
OM
OM spongy pores
OM ϕ = 49.1 %
1 µm
C1
OM spongy pores
OM
OM ϕ = 30.3 %
1 µm

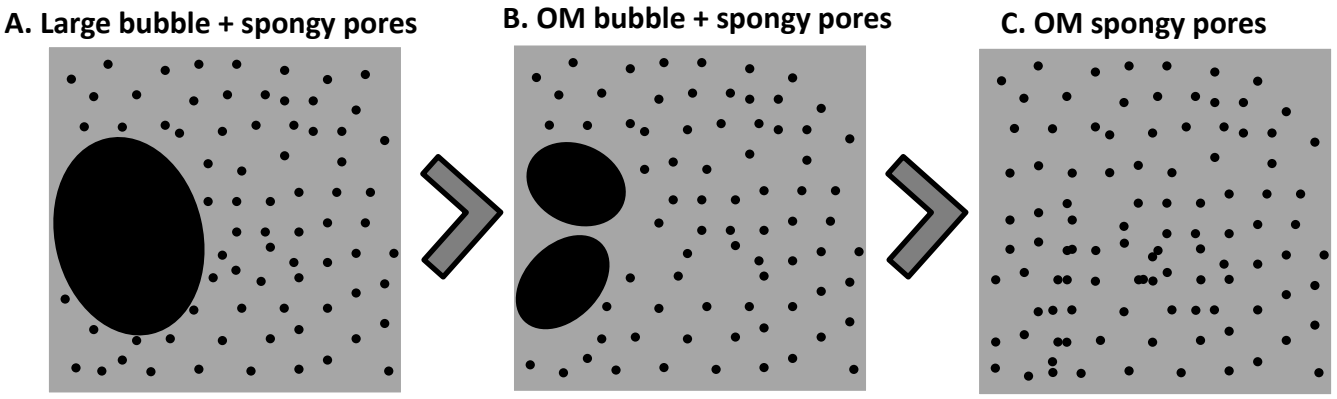
A. Large bubble + spongy pores
B. OM bubble + spongy pores
C. OM spongy pores

Figure 3.23: SEM photomicrographs showing examples of OM pore morphology and different sizes of OM bubble pores (A1) Large OM bubble pores and OM spongy pores with visible OM porosity = 84.3 %, K2: 12,246 ft (3,733 m), lower Eagle Ford (LEF). (B1) OM bubble and spongy pores with visible OM porosity = 49.1 %, K2: 12,169 ft (3,709 m), upper Eagle Ford (UEF). (C1) OM spongy pores with visible OM porosity = 30.3 %, K2: 12,169 ft (3,709 m), upper Eagle Ford (UEF). (A, B, and C) Schematic diagram showing the impact of OM pore morphology on visible total porosity. The larger OM bubble pores contribute the most to the visible total porosity but not necessarily to total permeability. Black = pores; gray = organic matter.

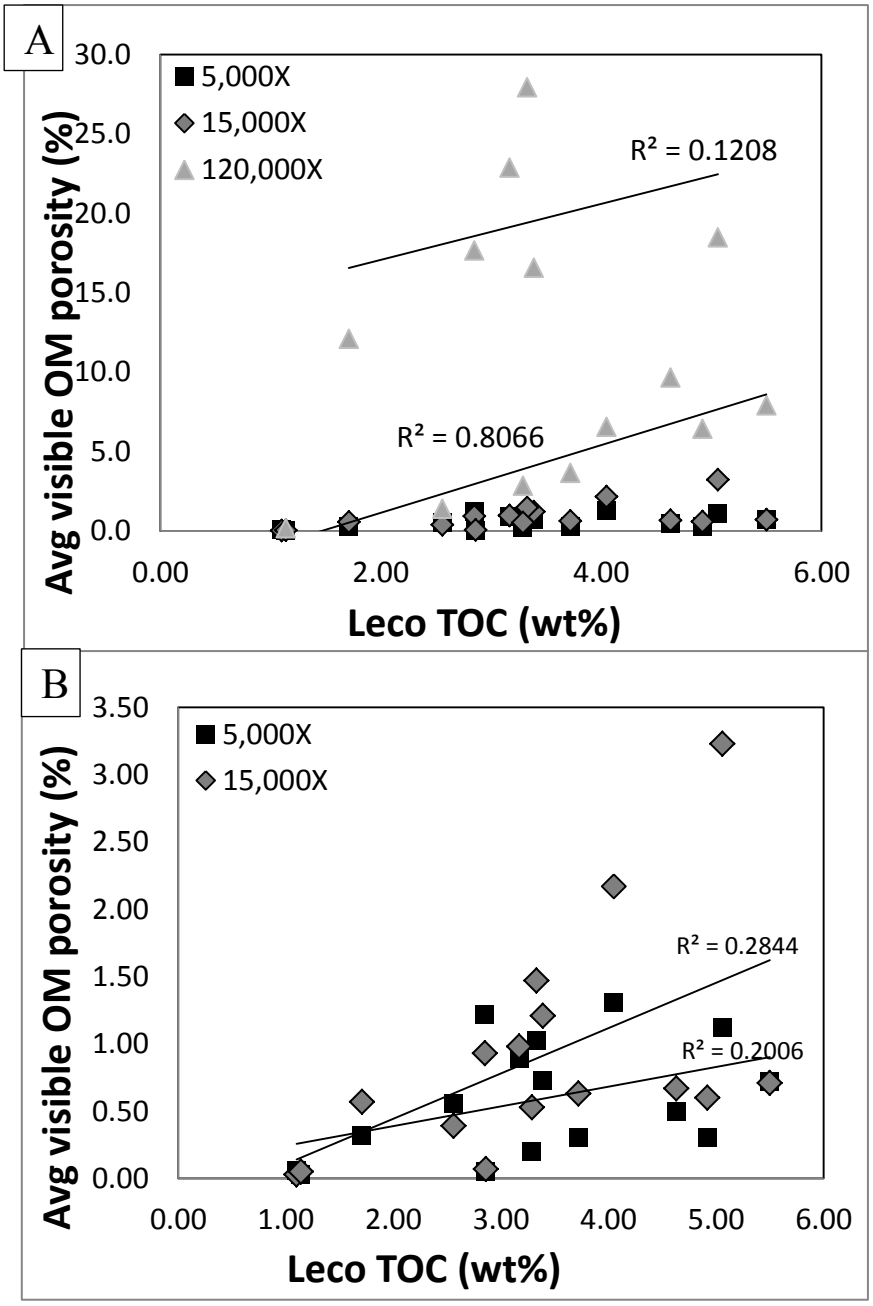

Figure 3.24: Plots showing relationship between average visible OM porosity and total organic carbon (TOC). (A) One positive correlation ($R^2 = 0.8$) was found between average visible OM porosity at 120,000X and TOC. (B) No correlation was found between average visible OM porosity at 15,000X and TOC ($R^2 = 0.3$) and at 5,000X and TOC ($R^2 = 0.2$).

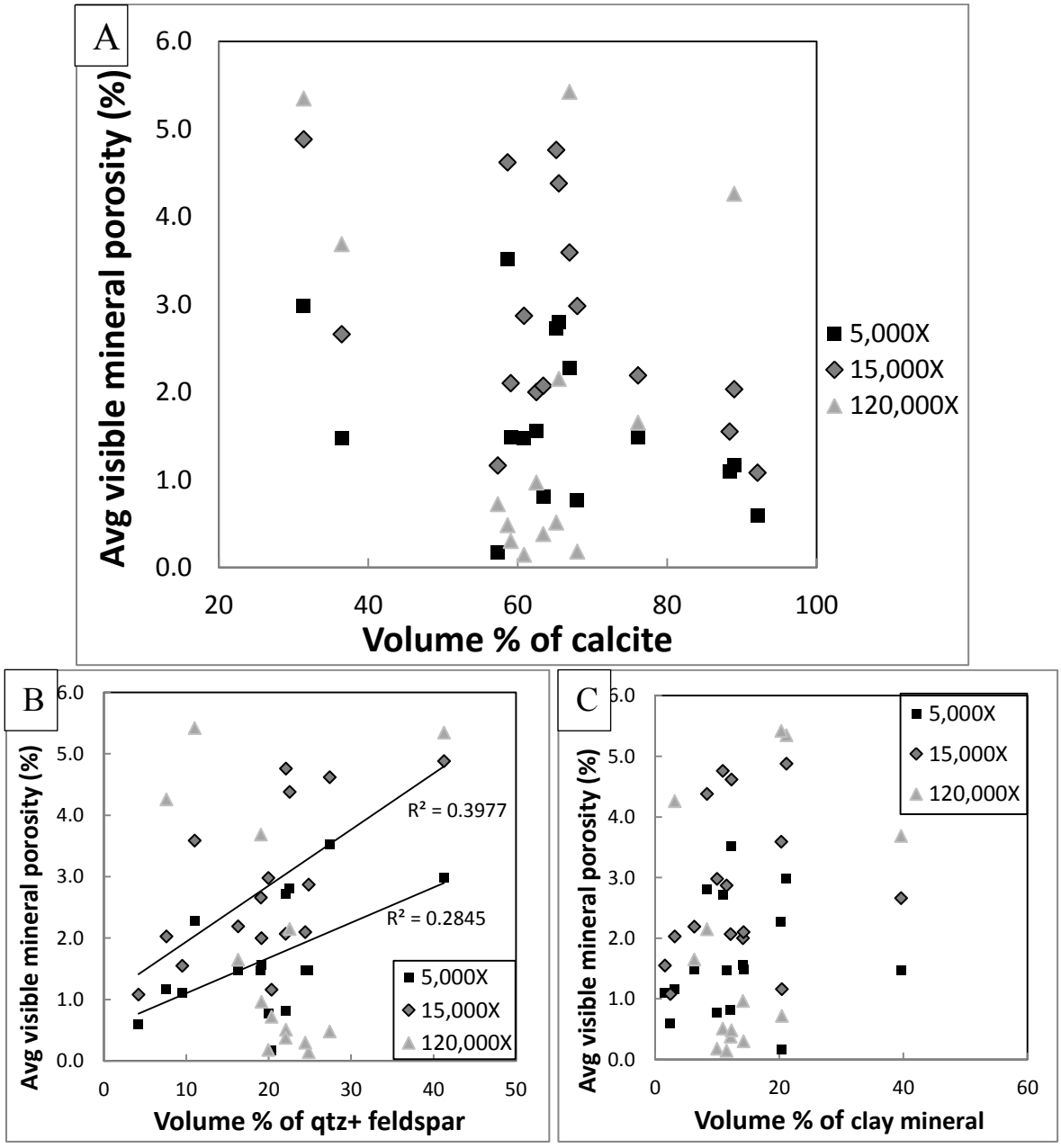

Figure 3.25: Plots showing relationship between average visible mineral porosity and major mineral abundance. (A) No correlation is apparent between visible mineral porosity and calcite. (B) A weakly positive correlation exists between visible mineral porosity at 15,000X and quartz (qtz) and feldspar ($R^2 = 0.4$). (C) No correlation is apparent between visible mineral porosity and total clay minerals. Mineral volumes from XRD analyses.

3.9 DISCUSSION

3.9.1 Significance of OM Bubble Pores

This study demonstrates that mineral pore networks are dominant in the Eagle Ford section in Karnes County (Figures 3.15 and 3.16). The only exception among the samples is marl at K1: 11,838 ft (3,608 m). To confirm that our data are representative of the samples and, more broadly, of the Eagle Ford Group, we examined the entire milled area of each sample in detail. It is intriguing to find that more than 90% of the observed pores are OM spongy pores in the marl at K1: 11,838 ft (3,608 m). In areas containing coccolith hash, where most OM bubble pores and modified interparticle pores are observed, the OM spongy pores are still the only pore type found. This raises the question of what controls the formation and preservation of OM bubble pores and modified mineral pores. In addition to the previously proposed mechanisms for the formation and development of OM bubble pores and modified mineral pores, there may be other controls on OM bubble pores. We suspect that because the marl sample at K1: 11,838 ft (3,608 m) has a relatively high content of clay minerals and likely has the highest clay to silt ratio, this would lead to significant physical compaction effect. Alternative interpretations are proposed for developing and preserving OM bubble pores and modified mineral pores: (1) OM bubble pores are interpreted to be resulted from bitumen cracking to oil and gas. In addition to that, pore sizes of OM bubble pores imply a pressure equilibrium state of the outer overburden pressure and inner pore pressure. Extensive compaction means relatively higher overburden pressure than the pore pressure; therefore, it might be difficult for OM bubble pores to form or be preserved

while compaction and overburden are significant. (2) The modified mineral pores are related to petroleum migration and/or water and gas trapping. If petroleum migration is inhibited or limited because the capillary pressure of the pore throat is too high, the modified mineral pores cannot be formed. The high capillary pressure can be related to high content of ductile clay-sized particles such as organic matter and clay minerals. If petroleum migration is inhibited or limited, more primary mineral pores should be preserved within the coccolith hash. However, we did not observe more primary mineral pores in sample K1: 11,838 ft (3,608 m). Future investigation is required to understand the other processes that might be involved.

3.9.2 Reservoir Quality of Eagle Ford Mudrocks

Total porosity is one of several very important factors determining reservoir quality in mudrocks (i.e., TOC, maturity, brittleness, pressure, etc). The pore networks in Eagle Ford mudstones can be separated into two main categories: mineral pore and OM pore networks. The mineral pore networks comprise the network of primary mineral pores and modified mineral pores within residual migrated petroleum (bitumen and/or oil). Concentrated areas of fecal pellets (composed of coccolith hash) and broken foraminifera bodies are the major allochems that host the interparticle pores. Because those pores are commonly better connected than intraparticle pores, they generally contribute more to permeability (Lucia, 2007; Loucks et al., 2012). This finding that calcite is highly correlated with the occurrence of interparticle pore is not entirely

corrected, though, as calcite cement also contributes to the volume of calcite (Figure 25A).

Meanwhile, connectivity within OM pore networks is controlled by the original and the resulting three-dimensional distribution of kerogen after generation and expulsion of bitumen, oil, and gas (Loucks and Reed, 2014; Milliken et al., 2014). Migrated and retained bitumen will crack into oil, gas, pyrobitumen (solid bitumen) and char, forming OM spongy pores (Bernard et al. 2012b), which are the dominant OM pore type observed. Because OM spongy pores are best resolved under the highest 120,000X images, TOC and average visible OM porosity of OM spongy pores is positively correlated (Figure 3.24). Because mineral pores are relatively large (tens of nanometers to tens of micrometers) and more likely to be connected, they should contribute more to oil storage and liquid flow. The majority of OM pores are in the nanometer size range; therefore, these pores are thought to be related to gas storage and gas flow.

Micrometer-scale heterogeneity of bulk mineralogy, TOC, and nanometer- to micrometer-scale porosity is significant within these representative Eagle Ford mudrocks, even though they have similar thermal maturation levels. Mineralogy within the UEF samples does not show significant variation, although texture, fabric, and TOC content vary among each sample. Heterogeneity within the LEF samples shows remarkable dissimilarity in mineralogy, TOC, texture, and fabric related to pronounced diagenetic alteration processes. The effect of initial deposited kerogen types is not discussed here because mature samples do not directly correspond to the original kerogen composition. However, it should be taken into consideration as another impact on heterogeneity.

Several studies have demonstrated that variations in maceral composition and kerogen types along the depositional profile affect geochemical characteristics of kerogen and its produced oil and gas, as well as thermal and pore evolution in the Eagle Ford and other shales and mudrocks (e.g., Fishman et al., 2012; Mastalerz et al., 2012; Ko et al., 2015; Sun et al., 2016).

The most important diagenetic processes in the Eagle Ford are compaction and cementation. Early cementation processes such as calcite, pyrite framboids, and kaolinite cement precipitation retards compaction and prevent collapse of pelagic foraminifers (globigerinids), preserving intragranular and intergranular porosity (e.g., Ergene, 2014; McAllister et al., 2015). Other possibly late cementation processes include phosphate, authigenic quartz, and Mg-chlorite (possibly clinochlore) cement precipitation (e.g., Ergene, 2014; McAllister et al., 2015; Milliken et al., 2016). Precipitation of euhedral quartz crystals is common and its cementation significantly increases the mechanical properties of the Eagle Ford mudrocks. Mg-chlorite cements, similar to early kaolinite cements, infills mostly intraparticle pores within pelagic foraminifers and skeletal grains. Grain dissolution and replacement was also observed, including albite, pyrite, marcasite, and dolomite replacement. Quantifying and understanding the relative timing of each diagenetic effect is important but beyond the scope of this study.

3.9.3 Differences in Pore-Size Distribution

Efforts have been made to measure pore abundance, pore-throat diameters, and pore-size distribution in fine-grained sediments by applying techniques such as mercury

intrusion, nitrogen gas adsorption, two-dimensional broad ion beam scanning electron microscopy (2D BIB-SEM) images, three-dimensional focused ion beam scanning electron microscopy (3D FIB-SEM), X-ray μ-CT, crushed rock GRI analysis, ultrasmall-angle neutron scattering and small-angle neutron scattering (USANS/SANS), and nuclear magnetic resonance spectroscopy (NMR) (Bustin et al., 2008; Desbois et al., 2009; Ross and Bustin, 2009; Chalmers et al., 2012; Klaver et al., 2012; Kulia et al., 2012; Clarkson et al., 2013; Kulia and Prasad, 2013; Ruppert et al., 2013; Houben et al., 2014; Hemes et al., 2015). Pore-size distribution in fine-grained sediments ranges across approximately six orders of magnitude, from subnanometer to tens of micrometers. Each technique has its limitations in measuring and accessing a certain size range of pores. For example, the widely used nitrogen adsorption technique fails to measure larger pores (pore diameter > 200 nm). The optimal resolution for an SEM image is around 2 to 5 nm, so a pore size of less than 2 to 5 nm cannot be resolved. Qualitative description and classification of pores using SEM are commonly seen in the literature (Loucks et al., 2009, 2012; Curtis et al., 2010; Schieber, 2010; Sondergeld et al., 2010; Slatt and O'Brien, 2011; Loucks and Reed, 2014; Pommer and Milliken, 2015). Quantitative analyses are rare because the characterization method is relatively time- and labor-intensive. Figure 3.22A demonstrates that PSD derived from SEM imaging and nitrogen-gas adsorption is straightforward in comparison. However, Figure 3.22B shows some inconsistency between the two methods for pores in the 30- to 70-nm size range. These data raise some concerns regarding the reliability of either method.

3.9.4 Differences in Total Porosity Measurements

Figure 3.26 compares point-count-derived visible total porosity total porosity at three SEM scales versus measured helium porosity based on the GRI method (Luffel and Guidry, 1992). Visible total porosity measured by point-count methods at 5,000X and 15,000X generally underestimates visible total porosity when compared with helium-porosity measurement. The underestimation can be explained by the limitation of SEM photomicrographs that pores smaller than 50 nm at 5,000X and 20 nm at 15,000X magnification cannot be resolved. On the other hand, helium-porosity measurements can resolve pores as small as 0.28 nm (2.8 Angstrom) in diameter, close to the size of many gas molecules. These small pores are likely storage spaces for oil and gas and contribute very little to fluid flow (mainly gas diffusion process).

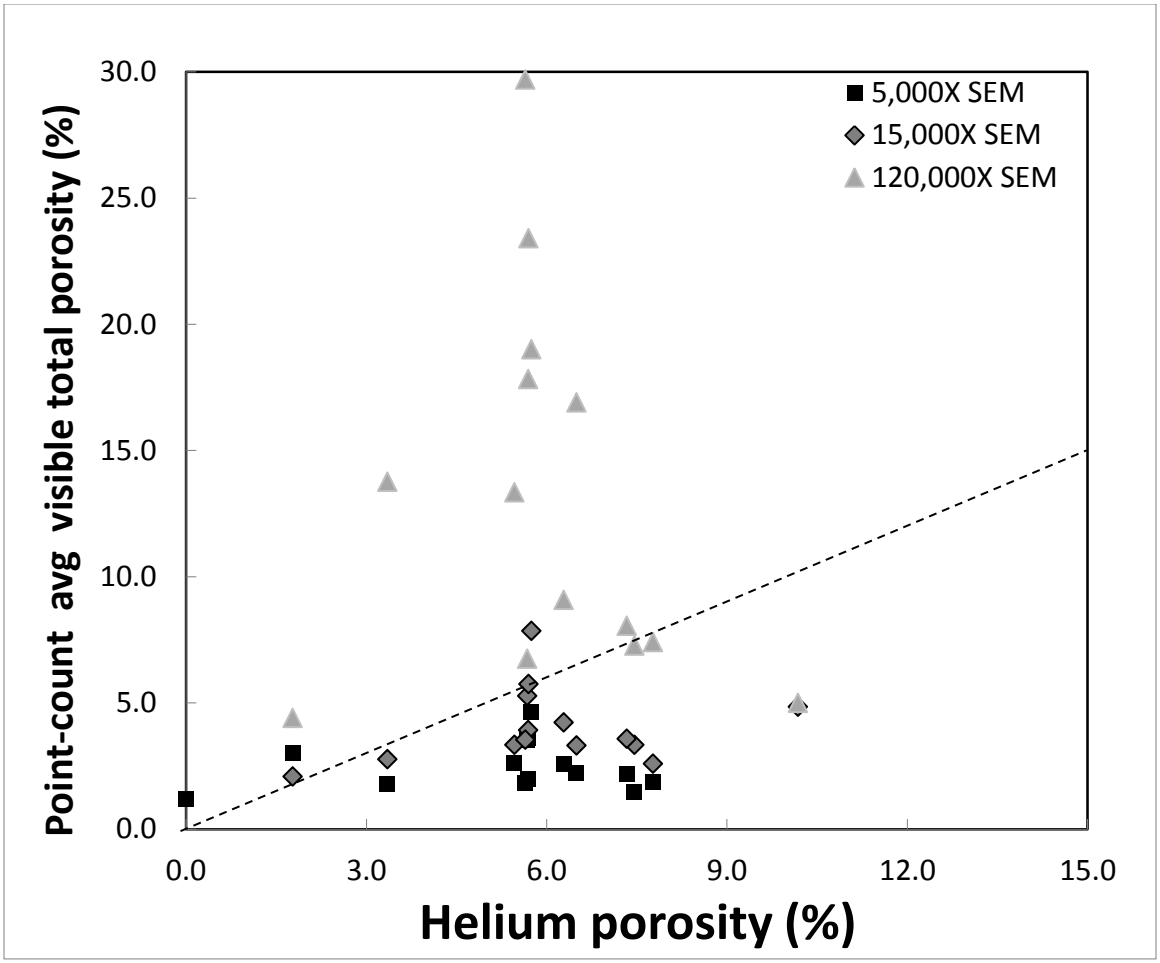

Figure 3.26: Plot comparing visible total porosity from point-count methods and helium-porosity from crushed-rock GRI analysis.

3.10 CONCLUSIONS

The studied Eagle Ford samples obtained from the closely spaced K1 and K2 cores in Karnes Country, Texas are in the late oil (condensate and gas) window, the K2 core being slightly more mature than the K1 core. Quantification of mineral and OM pore networks in the Eagle Ford samples using the point-count approach requires correct understanding of the origins of mineral and OM pores and detailed characterization of different pore types. An organic matter and mineral pore network for the Eagle Ford

reservoir was proposed. The mineral pore network consists of (1) primary mineral pores originally saturated with formation water and (2) modified mineral pores that contain migrated petroleum (bitumen and/or residual oil). The OM pore network comprises (1) primary OM pores and (2) secondary OM pores including relatively large, less abundant OM bubble pores and relatively small, more abundant OM spongy pores. The total pore network of the Eagle Ford mudrocks is mainly contributed by mineral pore network because the visible total porosity of the Eagle Ford samples is controlled by the modified mineral porosity. The visible OM porosity of OM spongy pores is positively correlated to the TOC content. There are likely multiple factors that play a role in the distribution of OM porosity, not just TOC. The visible mineral porosity shows a weak positive correlation with the volume of quartz plus feldspar. This positive correlation is interpreted to be related to the rigidity of the mineral framework that inhibited compaction of mineral pores and later allowed petroleum (probably bitumen) to migrate within the intergranular pores of mudrocks.

The bulk mineralogy of the UEF marl samples is similar; however, the LEF marl samples demonstrate much more variations, especially in the relative amounts of quartz, albite, dolomite, and clay minerals, possibly related to diagenetic alteration processes. A significant increase in the relative abundance of kaolinite and chlorite was noted from the upper to lower Eagle Ford. Within the upper Eagle Ford marls, deeper samples have a higher percentage of smaller pores (diameter < 500 nm), and the abundance of relatively larger pore sizes (diameter > 500 nm) increase at shallower depths. This systematic change in pore size could be partly controlled by changes in grain size, which could

reflect an increase in the supply of silt-sized sediment or an increase in hydrodynamic energy toward the top of the upper Eagle Ford (without entirely overprinting by diagenetic processes on rocks) or both.

Quantitative visible total porosity measured by point-count methods at 5,000X and 15,000X generally underestimates visible total porosity when compared with helium porosity measurement. The underestimation can be explained by the limitation of SEM photomicrographs that pores smaller than 50 nm at 5,000X and 20 nm at 15,000X magnification cannot be resolved. Quantitative pore-size distribution data derived from SEM imaging and nitrogen-gas adsorption is straightforward in comparison although some inconsistency is shown between the two methods for pores in the 30- to 70-nm size range. These data raise some concerns regarding the reliability of either method. Although each method (helium pycometer, nitrogen adsorption, and image-based point-count, and pore-tracing) measures different ranges of pore sizes, they enhance the understanding of pore types, distribution, and abundance in mudrocks. The integration and comparison of each data set on the same sample set are needed to accurately and fully characterize the pore system of mudrocks.

Results show that even without the complication of different thermal maturity, strong micrometer-scale heterogeneity of rock components and properties (texture, fabric, mineralogy, and TOC) impacts the occurrence, abundance, distribution, and types of mineral and OM pores. Pore development in mudrocks is primarily controlled by depositional and diagenetically modified processes (first order) and thermal maturation of organic matter (second order). Diagenetic processes such as compaction and cementation

significantly impacts texture and fabric in these marine mudrocks, as well as alters their mineralogical and mechanical properties, which are critical for hydraulic fracturing. Understanding the relative timing of each diagenetic process and quantifying their contributions are critical and will improve the reservoir quality prediction. The micrometer-scale heterogeneity and complexity would, in turn, significantly impact matrix permeability and fluid flow behaviors in the Eagle Ford mudrocks.

ACKNOWLEDGEMENTS

I would like to thank Marathon Oil Company for providing the cores used in this study. Results of X-ray diffraction analyses were provided by K-T GeoServices, Inc. Geochemical and mineralogical analyses were partially supported by the State of Texas Advanced Oil and Gas Resource Recovery (STARR) program. I also thank Dr. Joan Spaw, Dr. Kitty Milliken, Dr. Robert Reed, Dr. Farzam Javadpour, Dr. Xun Sun, and Dr. Athma Bhandari for discussions, suggestions, and inspirations during manuscript preparation. The Mudrock System Research Laboratory (MSRL) members supported this research: Anadarko, Apache, BHP Billiton, BP, Cenovus, Centrica, Chesapeake, Chevron, Cima, Cimarex, Concho, ConocoPhillips, Cypress, Devon, Encana, Eni, EOG, EXCO, ExxonMobil, FEI, Hess, Husky, IMP, Kerogen, Marathon, Murphy, Newfield, Oxy, Penn Virginia, Penn West, Pioneer, QEP, Samson, Shell, Statoil, Talisman, Texas American Resources, The Unconventionals, US EnerCorp, Valence, and YPF.

REFERENCES

Afsharpoor, A. and F. Javadpour, 2016, Liquid slip flow in a network of shale noncircular nanopores: Fuel, v. 180, p. 580–590.

Aplin, A. C., and J. H. S. Macquaker, 2011, Mudstone diversity: Origin and implications for source, seal, and reservoir properties in petroleum systems: AAPG Bulletin, v. 95, p. 2031–2059, doi:10.1306/03281110162.

Bernard, S., B. Horsfield, H.-M. Schulz, R. Wirth, A. Schreiber, and N. Sherwood, 2012a, Geochemical evolution of organic-rich shales with increasing maturity: A STXM and TEM study of the Posidonia Shale (Lower Toarcian, northern Germany): Marine and Petroleum Geology, v. 31, p. 70–89, doi:10.1016/j.marpetgeo.2011.05.010.

Bernard, S., R. Wirth, A. Schreiber, H.-M. Schulz, and B. Horsfield, 2012b, Formation of nanoporous pyrobitumen residues during maturation of the Barnett Shale (Fort Worth Basin): International Journal of Coal Geology, v. 103, p. 3–11, doi:10.1016/j.coal.2012.04.010.

Bohacs, K. M., Q. M. Passey, M. Rudnicki, W. L. Esch, and O. R. Lazar, 2013, The spectrum of fine-grained reservoirs from "shale-gas" to "shale oil"/tight liquids: Essential attributes, key controls, practical characterization: International Petroleum Technology Conference (IPTC), Beijing, China, March 26–28, 2013, IPTC Paper 16676, 16 p.

Bustin, R., A. Bustin, A. Cui, and D. Ross, 2008, Impact of shale properties on pore structure and storage characteristics: Society of Petroleum Engineers Shale Gas Production Conference, Fort Worth, Texas, USA, November 16–18, 2008, SPE Paper 119892, 28 p.

Chalmers, G. R., R. M. Bustin, and I. M. Power, 2012, Characterization of gas shale pore systems by porosimetry, pycnometry, surface area, and field emission scanning electron microscopy/transmission electron microscopy image analyses: Examples from the Barnett, Woodford, Haynesville, Marcellus, and Doig units: AAPG Bulletin, v. 96, p. 1099–1119, doi:10.1306/10171111052.

Clarkson, C. R., N. Solano, R. M. Bustin, A. M. M. Bustin, G. R. L. Chalmers, L. He, Y. B. Melnichenko, A. P. Radliński, and T. P. Blach, 2013, Pore structure characterization of North American shale gas reservoirs using USANS/SANS, gas adsorption, and mercury intrusion: Fuel, v. 103, p. 606–616, http://dx.doi.org/10.1016/j.fuel.2012.06.119.

Curtis, M. E., R. J. Ambrose, C. H. Sondergeld, and C. S. Rai, 2010, Structural characterization of gas shales on the micro- and nano-scales: Canadian Unconventional Resources and International Petroleum Conference, Calgary, Alberta, Canada, October 19–21, 2010, CUSG/SPE Paper 137693, 15 p.

Denne, R. A., R. E. Hinote, J. A. Breyer, T. H. Kosanke, J. A. Lees, N. Engelhardt-Moore, J. M. Spaw, and N. Tur, 2014, The Cenomanian-Turonian Eagle Ford Group of South Texas: Insights on timing and paleoceanographic conditions from geochemistry and micropaleontologic analyses: Palaeogeography, Palaeoclimatology, Palaeoecology, v. 413, p. 2–28, http://dx.doi.org/10.1016/j.palaeo.2014.05.029.

Desbois, G., J. L. Urai, and P. A. Kukla, 2009, Morphology of the pore space in claystones—Evidence from BIB/FIB ion beam sectioning and cryo-SEM observations: Earth, v. 4, p. 15–22, doi:10.5194/ee-4-15-2009.

Driskill, B., N. Suurmeyer, S. Rilling-Hall, A. Govert, and A. Garbowicz, 2012, Reservoir description of the subsurface Eagle Ford Formation, Maverick Basin area, South Texas, USA: Society of Petroleum Engineers Europec/EAGE Annual Conference & Exhibition, Copenhagen, Denmark, June 4–7, 2012, SPE Paper 154528, 23 p.

Driskill, B., J. Walls, S. W. Sinclair, and J. DeVito, 2013, Applications of SEM imaging to reservoir characterization in the Eagle Ford Shale, south Texas, U.S.A., *in* W. Camp, E. Diaz, B. Wawak, eds., Electron microscopy of shale hydrocarbon reservoirs: AAPG Memoir 102, p. 115–136.

Eldrett, J. S., C. Ma, S. C. Bergman, A. Ozkan, D. Minisini, B. Lutz, S.-J. Jackett, C. Macaulay, and A. M. Kelly, 2015, Origin of limestone-marlstone cycles: Astronomic forcing of organic-rich sedimentary rocks from the Cenomanian to early Coniacian of the Cretaceous Western Interior Seaway, USA: Earth and Planetary Science Letters, v. 423, p. 98–113, http://dx.doi.org/10.1016/j.epsl.2015.04.026

Ergene, S. M., 2014, Lithologic heterogeneity of the Eagle Ford Formation, south Texas: unpublished Master Thesis, The University of Texas at Austin, 182 pp.

Fairbanks, M. D., S. C. Ruppel, and H. Rowe, 2016, High-resolution stratigraphy and facies architecture of the Upper Cretaceous (Cenomanian–Turonian) Eagle Ford Group, Central Texas: AAPG Bulletin, v.100, p. 379–403.

Fishman, N. S., P. C. Hackley, H. A. Lowers, R. J. Hill, S. O. Egenhoff, D. D. Eberl, and A. E. Blum, 2012, The nature of porosity in organic-rich mudstones of the Upper Jurassic Kimmeridge Clay Formation, North Sea, offshore United Kingdom: International Journal of Coal Geology, v. 103, p. 32–50, http://dx.doi.org/10.1016/j.coal.2012.07.012.

Folk, R. L., 1980, Petrology of sedimentary rocks: Hemphill Publication Company, Austin, Texas 78703.

Frébourg, G., S. C. Ruppel, R. G. Loucks, and J. Lambert, Depositional controls on sediment body architecture in the Eagle Ford/Boquillas system: Insights from outcrops in West Texas, USA: AAPG Bulletin, v. 100, p. 657–582.

Hart, B. S., J. H. S. Macquaker, and K. G. Taylor, 2013, Mudstone ("shale") depositional and diagenetic processes: Implications for seismic analyses of source-rock reservoirs: Interpretation, v. 1, p. B7–B26.

Hemes, S., G. Desbois, J. L. Urai, B. Schröppel, and J.-O. Schwarz, 2015, Multi-scale characterization of porosity in Boom Clay (HADES-level, Mol, Belgium) using a combination of X-ray μ-CT, 2D BIB-SEM and FIB-SEM tomography: Microporous and Mesoporous Materials, v. 208, p. 1–20.

Houben, M. E., G. Desbois, and J. L. Urai, 2013, Pore morphology and distribution in the Shaly facies of Opalinus Clay (Mont Terri, Switzerland): Insights from representative 2D BIB-SEM investigations on mm to nm scale: Applied Clay Science, v. 71, p. 82–97.

Houben, M. E., G. Desbois, and J. L. Urai, 2014, A comparative study of representative 2D microstructures in Shaly and Sandy facies of Opalinus Clay (Mont Terri, Switzerland) inferred form BIB-SEM and MIP methods: Marine and Petroleum Geology, v. 49, p. 143–161, http://dx.doi.org/10.1016/j.clay.2012.11.006.

Ichaso, A. A., and R. W. Dalrymple, 2009, Tide- and wave-generated fluid mud deposits in the Tilje Formation (Jurassic), offshore Norway: Geology, v. 37, p. 539–542, doi:10.1130/G25481A.1.

Jennings, D. S., and J. Antia, 2013, Petrographic characterization of the Eagle Ford shale, south Texas: Mineralogy, common constituents, and distribution of nanometer-scale pore types, *in* W. K. Camp, E. Diaz, B. Wawak, eds., Electron microscopy of shale hydrocarbon reservoirs: AAPG Memoir 102, p. 101–113.

Klaver, J., G. Desbois, J. L. Urai, and R. Littke, 2012, BIB-SEM study of the pore space morphology in early mature Posidonia Shale from the Hils area, Germany: International Journal of Coal Geology, v. 103, p. 12–25, doi:10.1016/j.coal.2012.06.012.

Ko, L. T., T. Zhang, R. G. Loucks, S. C. Ruppel, and D. Shao, 2014, Boquillas (Eagle Ford) Formation pore evolution results from laboratory heating experiments: Unconventional Resources Technology Conference (URTeC), Denver, Colorado, August 25–27, 2014, URTeC 1935124, 7 p.

Ko, L. T., T. Zhang, R. G. Loucks, S. C. Ruppel, and D. Shao, 2015, Pore evolution in the Barnett, Eagle Ford (Boquillas), and Woodford mudrocks based on gold-tube

pyrolysis thermal maturation, AAPG 2015 Annual Convention and Exhibition, Denver, Colorado, May 31–June 3rd, Search and Discovery Article #51228 (2016)

Ko, L. T., R. G. Loucks, T. Zhang, S. C. Ruppel, and D. Shao, 2016, Pore and pore network evolution of Upper Cretaceous Boquillas (Eagle Ford-equivalent) mudstone: Results from gold-tube pyrolysis experiments: AAPG Bulletin, v. 100, p. 1693–1722.

Kulia, U., and M. Prasad, 2013, Specific surface area and pore-size distribution in clays and shales: Geophysical Prospecting v. 61, p. 341–362, doi:10.1111/1365-2478.12028.

Kulia, U., M. Prasad, A. Derkowski, and D. K. McCarty, 2012, Compositional controls on mudrock pore-size distribution: An example from Niobrara Formation: SPE Annual Technical Conference and Exhibition, San Antonio, Texas, USA, Society of Petroleum Engineers, p. 16.

Lazar, O. R., K. M. Bohacs, J. H. S. Macquaker, J. Schieber, and T. M. Demko, 2015, Mudstone primer: Lithofacies variations, diagnostic criteria, and sedimentologic/stratigraphic implications at lamina to bedset scale: Concepts in Sedimentology and Paleontology, v. 12, SEPM, 198 p.

Löhr, S. C., E. T. Baruch, P. A. Hall, and M. J. Kennedy, 2015, Is organic pore development in gas shales influenced by the primary porosity and structure of thermally immature organic matter?: Organic Geochemistry, v. 87, p. 119–132, doi:10.1016/j.orggeochem.2015.07.010

Loucks, R. G., and R. M. Reed, 2014, Scanning-electron-microscope petrographic evidence for distinguishing organic-matter pores associated with depositional organic matter versus migrated organic matter in mudrocks: GCAGS Journal, v. 3, p. 51–60.

Loucks, R. G., R. M. Reed, S. C. Ruppel, and U. Hammes, 2012, Spectrum of pore types and networks in mudrocks and a descriptive classification for matrix-related mudrock pores: AAPG Bulletin, v. 96, p. 1071–1098, doi:10.1306/08171111061.

Loucks, R. G., R. M. Reed, S. C. Ruppel, and D. M. Jarvie, 2009, Morphology, genesis, and distribution of nanometer-scale pores in siliceous mudstones of the Mississippian Barnett Shale: Journal of Sedimentary Research, v. 79, p. 848–861, doi:10.2110/jsr.2009.092.

Loucks, R. G., and S. C. Ruppel, 2007, Mississippian Barnett Shale: Lithofacies and depositional setting of a deep-water shale-gas succession in the Fort Worth Basin, Texas: AAPG Bulletin, v. 91, p. 579–601, doi:10.1306/11020606059.

Lucia, F. J., 2007, Carbonate reservoir characterization: An integrated approach, 2nd ed.: New York, Springer-Verlag, 336 p., doi: 10.1007/978-3-540-72742-2.

Luffel, D. L., and C. W. Hopkins, 1993, Matrix permeability measurement of gas productive shales: Society of Petroleum Engineers (SPE) Annual Technical Conference and Exhibition, October 3-6th, Houston, Texas, SPE-26633-MS, p. 261–270.

Macquaker, J. H. S., and R. L. Gawthorpe, 1993, Mudstone lithofacies in the Kimmeridge Clay Formation, Wessex Basin, southern England: Implications for the origin and controls of the distribution of mudstones: Journal of Sedimentary Petrology, v. 63, p. 1129–1143.

Macquaker, J. H. S., and J. K. Howell, 1999, Small-scale (<5.0 m) vertical heterogeneity in mudstones: Implications for high-resolution stratigraphy in siliciclastic mudstone successions: Journal of Geological Society, London, v. 156, p. 105–112, doi: 10.1144/gsjgs.156.1.0105.

Macquaker, J. H. S., K. G. Taylor, and R. L. Gawthorpe, 2007, High-resolution facies analyses of mudstones: Implications for paleoenvironmental and sequence stratigraphic interpretations of offshore ancient mud-dominated successions: Journal of Sedimentary Research, v. 77, p. 324–339, doi:10.2110/jsr.2007.029.

Mastalerz, M., A. Schimmelmann, G. P. Lis, A. Drobniak, and A. Stankiewicz, 2012, Influence of maceral composition on geochemical characteristics of immature shale kerogen: Insight from density fraction analysis: International Journal of Coal Geology, v. 103, p. 60–69, http://dx.doi.org/10.1016/j.coal.2012.07.011

Mastalerz, M., A. Schimmelmann, A. Drobniak, and Y. Chen, 2013, Porosity of Devonian and Mississippian New Albany Shale across a maturation gradient: Insights from organic petrology, gas adsorption, and mercury intrusion: AAPG Bulletin, v. 97, p. 1621–1643, doi:10.1306/04011312194.

McAllister, R. T., K. G. Taylor, and B. Garcia-Fresca, 2015, Diagenetic evolution of the Eagle Ford Formation, SW Texas: Impacts upon reservoir quality and rock properties: Unconventional Resources Technology Conference (URTeC), San Antonio, Texas, July 20–22, 2015, URTeC 2153115, 12 p.

Milliken, K. L., 2013, SEM-based cathodoluminescence imaging for discriminating quartz types in mudrocks: Unconventional Resources Technology Conference (URTeC), Denver, Colorado, August 12–14, 2013, URTeC 1582467, 9 p.

Milliken, K. L., S.-J. Choh, P. Papazis, and J. Schieber, 2007, "Cherty" stringers in the Barnett Shale are agglutinated foraminifera: Sedimentary Geology, v. 198, p. 221–232, doi:10.1016/j.sedgeo.2006.12.012.

Milliken, K. L., R. J. Day-Stirrat, P. K. Papazis, and C. Dohse, 2012a, Carbonate lithologies of the Mississippian Barnett Shale, Fort Worth Basin, Texas, *in* J. A. Breyer, ed., Shale reservoirs—Giant resources for the 21st century: AAPG Memoir 97, p. 290–321, doi:10.1306/13321473M97252.

Milliken, K. L., L. T. Ko, M. Pommer, and K. M. Marsaglia, 2014, SEM petrography of eastern Mediterranean sapropels: Analogue data for assessing organic matter in oil and gas shales: Journal of Sedimentary Research, v. 84, p. 961–974, doi:http://dx.doi.org/10.2110/jsr.2014.75.

Milliken, K. L., M. Rudnicki, D. N. Awwiller, and T. Zhang, 2013, Organic matter-hosted pore system, Marcellus Formation (Devonian), Pennsylvania: AAPG Bulletin, v. 97, p. 177–200, doi:10.1306/07231212048.

Milliken, K. L., S. M. Ergene, and A. Ozkan, 2016, Quartz types, authigenic and detrital, in the Upper Cretaceous Eagle Ford Formation, south Texas, USA: Sedimentary Geology, v. 339, p. 273–288.

Myrow, P. M., and J. B. Southard, 1996, Tempestite deposition: Journal of Sedimentary Research, v. 66, p. 875–887.

Peng, S. and R. G. Loucks, 2016, Permeability measurements in mudrocks using gas-expansion methods on plug and crushed-rock samples: Marine and Petroleum Geology, v. 73, p. 299–310.

Pierce, J. D., S. C. Ruppel, and D. F. Stockli, 2016, U-Pb geochronology of the Late Cretaceous Eagle Ford Shale, Texas: Defining chronostratigraphic boundaries and volcanic ash source, GCAGS Journal, *in press*.

Plint, A. G., 2014, Mud dispersal across a Cretaceous prodelta: Storm-generated, wave-enhanced sediment gravity flows inferred from mudstone microtexture and microfacies: Sedimentology, v. 61, p. 609–647, doi:10.1111/sed.12068.

Pommer, M., and K. Milliken, 2015, Pore types and pore-size distributions across thermal maturity, Eagle Ford Formation, southern Texas: AAPG Bulletin, v. 99, p. 1713–1744, doi:10.1306/03051514151.

Potter, P. E., B. Maynard, and P. J. Depetris, 2005, Mud and mudstones: Introduction and overview: Berlin; London, Springer, 297 p.

Rine, J. M., and R. N. Ginsburg, 1985, Depositional facies of a mud shoreface in Suriname, South America—A mud analogue to sandy, shallow-marine deposits: Journal of Sedimentary Petrology, v. 55, p. 633–652.

Roduit, N., 2008, JMICROVISION Version 1.2.7: Image analysis toolbox for measuring and quantifying components of high-definition images: http://www.jmicrovision.com (accessed December 1, 2014).

Romero-Sarmiento, M.-F., J.-N. Rouzaud, S. Bernard, D. Deldicque, M. Thomas, and R. Littke, 2014, Evolution of Barnett Shale organic carbon structure and nanostructure with increasing maturation: Organic Geochemistry, v. 71, p. 7–16, http://dx.doi.org/10.1016/j.orggeochem.2014.03.008.

Ross, D. J. K., and R. M. Bustin, 2009, The importance of shale composition and pore structure upon gas storage potential of shale gas reservoirs: Marine and Petroleum Geology, v. 26, p. 916–927, doi:10.1016/j.marpetgeo.2008.06.004.

Ruppel, S. C., and R. G. Loucks, 2008, Black mudrocks: Lessons and questions from the Mississippian Barnett Shale in the southern Midcontinent: The Sedimentary Record, v. 6, p. 4–8.

Ruppert, L. F., R. Sakurovs, T. P. Blach, L. He, Y. B. Melnichenko, D. F. R. Mildner, and L. Alcantar-Lopez, 2013, A USANS/SANS study of the accessibility of pores in the Barnett Shale to methane and water: Energy & Fuels, v. 27, p. 772–779, dx.doi.org/10.1021/ef301859s.

Schieber, J., 1999, Distribution and deposition of mudstone facies in the Upper Devonian Sonyea Group of New York: Journal of Sedimentary Research, v. 69, p. 909–925.

Schieber, J., 2010, Common themes in the formation and preservation of intrinsic porosity in shales and mudstones—Illustrated with examples across the Phanerozoic: Society of Petroleum Engineers Unconventional Gas Conference, Pittsburgh, Pennsylvania, USA, February 23–25, SPE Paper 132370, 10 p.

Schieber, J., and J. B. Southard, 2009, Bedload transport of mud by floccule ripples—Direct observation of ripple migration processes and their implications: Geology, v. 37, p. 483–486, doi:10.1130/G25319A.

Schieber, J., J. B. Southard, P. Kissling, B. Rossman, and R. Ginsburg, 2013, Experimental deposition of carbonate mud from moving suspensions: Importance of flocculation and implications for modern and ancient carbonate mud deposition: Journal of Sedimentary Research, v. 83, p. 1025–1031, doi:10.2110/jsr.2013.77.

Schieber, J., J. B. Southard, and K. G. Thaisen, 2007, Accretion of mudstone beds from migrating floccule ripples: Science, v. 318, p. 1760–1763, doi:10.1126/science.1147001.

Schieber, J., W. Zimmerle, and P. S. Sethi, 1998, Shales and mudstones: Petrography, Petrophysics, Geochemistry, and Economic Geology, v. 2: Stuttgart, E. Schweizerbart, 296 p.

Slatt, R. M., and N. R. O'Brien, 2011, Pore types in the Barnett and Woodford gas shales: Contribution to understanding gas storage and migration pathways in fine-grained rocks: AAPG Bulletin, v. 95, p. 2017–2030, doi:10.1306/03301110145.

Sondergeld, C. H., R. J. Ambrose, C. S. Rai, and J. Moncrieff, 2010, Micro-structural studies of gas shales: Society of Petroleum Engineers Unconventional Gas Conference, Pittsburgh, Pennsylvania, USA, February 23–25, SPE Paper 131771, 17 p.

Stow, D. K. V., J.-C. Faugeres, J. A. Howe, C. J. Pudsey, and A. R. Viana, 2002, Bottom currents, contourites, and deep-sea sediment drifts: current state-of-the-art: Geological Society, London, Memoirs 2002, v. 22, p. 7–20, doi:10.1144/GSL.MEM.2002.022.01.02.

Sun, X., T. Zhang, Y. Sun, K. L. Milliken, and D. Sun, 2016, Geochemical evidence of organic matter source input and depositional environments in the lower and upper Eagle Ford Formation, south Texas: Organic Geochemistry, v. 98, p. 66–81.

Wignall, P. B., 1994a, Black shales: Oxford monographs on geology and geophysics, v. 30: New York, Oxford University Press Inc., 127 p.

Wignall, P. B., 1994b, Mudstone lithofacies in the Kimmeridge Clay Formation, Wessex Basin, Southern England: Implications for the origin and controls of the distribution of mudstones—Discussion: Journal of Sedimentary Research, v. a64, p. 927–929.

Young, R. N., and J. B. Southard, 1978, Erosion of fine-grained marine sediments: Sea-floor and laboratory experiments: Geological Society of America Bulletin, v. 89, p. 663–672, doi:10.1130/0016-7606.

Chapter 4: Pore-Types and Pore Network Evolution in Upper Devonian-Lower Mississippian Woodford and Mississippian Barnett Mudstones: Insights from Laboratory Thermal Maturation and Organic Petrology[3]

ABSTRACT

Pore evolution models from immature organic-rich Barnett (0.42 $\%R_o$) and Woodford (0.49 $\%R_o$) mudrocks were compared with those previously developed from low-maturity OM-lean Boquillas (Eagle Ford-equivalent) mudrocks to investigate whether (1) different mineralogy (siliceous vs. calcareous) exerts different catalytic and sorption effects and influences OM-pore origin and evolution (2) different types of OM maceral show different OM pore evolution history. Laboratory gold-tube pyrolysis, scanning electron microscopy (SEM) and thin-section petrography, organic petrography, and geochemical characterization were used to investigate the role of bulk mineralogy, total organic content (TOC), organic matter (OM) maceral type, and thermal maturation. Results suggest that mineralogy has little impact on OM pore development and evolution. OM macerals, identified using both SEM (platy OM, particulate OM, organic-mineral admixtures, *Tasmanites*) and organic petrology [telalginite, vitrinite, inertinite, amorphous organic matter (AOM), *Leiosphaeridia*, and *Tasmanites*], do affect the origin and evolution of OM pores owing to differences in generation kinetics and activation energy distributions between *Leiosphaeridia*, *Tasmanites,* AOM, and other types of macerals. Woodford mudrock samples containing *Leiosphaeridia* and *Tasmanites* exhibit

[3]Written for submission to *International Journal of Coal Geology*

a delay in onset and a shorter period of petroleum generation and pore development compared to Barnett mudrock samples which contain mostly AOM. Pre-oil solid bitumen was observed to have migrated into initial primary mineral pore networks at bitumen generation stage in both Barnett and Woodford mudrocks. The abundance of mineral pores partially filled with residual OM (modified mineral pores) in the Barnett and Woodford mudrocks implies good inter-connectivity of pore spaces. At higher levels of thermal maturation, the volume of primary mineral pores decreases and the pore volume composed of modified mineral pores and OM pores became greater. Pore evolution and pore type heterogeneity in these mudrocks is a function of the initial mineral pore network, types of kerogen and macerals, and generation kinetics of individual maceral upon thermal maturation.

4.1 INTRODUCTION

It has been well documented that the formation of OM pores in mudrocks is predominantly affected by thermal maturation processes (e.g., Loucks et al., 2009; Bernard et al., 2012a, b; Bohacs et al., 2013; Curtis et al., 2012; Milliken et al., 2013; Mastalerz et al., 2013; Bernard and Horsfield, 2014; Pommer and Milliken, 2015; Ko et al., 2016). The change in size and shape of OM pores is related to stepwise transformation of organic matter and can be associated with generated pre-oil solid bitumen (Curiale, 1986; Mastalerz and Glikson, 2000), post-oil solid bitumen, oil, gas, pyrobitumen, and char (e.g., Bernard et al., 2012a; Loucks and Reed, 2014; Löhr et al., 2015; Cardott et al., 2015; Wood et al., 2015; Ko et al., 2016).

The importance of mineralogy (in particular clay minerals) in affecting the composition and yield of generated petroleum, has been known for decades caused by differences in mineral adsorption and catalytic capacities (e.g., Johns, 1979; Goldstein, 1983; Tannenbaum and Kaplan, 1985; Tannenbaum et al., 1986; Huizinga et al., 1987a, b; Hetényi, 1995; Wei et al., 2006a, b; Pan et al., 2010). Catalytic cracking of kerogen or pre-oil bitumen by interaction of minerals with organic matter has been proposed by many previous studies (Johns, 1979; Espitalié et al., 1980, 1984; Horsfield and Douglas, 1980; Tannenbaum and Kaplan, 1985; Tannenbaum et al., 1986; Hetényi, 1995). Minerals in sediments can catalyze chemical reactions (i.e. C-C bond cleavage, defunctionalization, condensation, oxidation, and reduction) occurring during the maturation of kerogen. Much effort has been made to investigate the role of minerals on petroleum composition during the thermal maturation of kerogen, specifically in regard to the presence or absence of minerals such as calcite, pyrite, quartz, calcium sulfate, illite, kaolinite, and montmorillonite (i.e. smectite). For example, montmorillonite shows a pronounced catalytic effect, significantly changing the chemical composition and yield of oil from kerogen, whereas other minerals such as calcite, pyrite, quartz, and calcium sulfate shows a weaker or no effect (e.g., Tannenbaum et al., 1986; Lao et al., 1989). This is related to montmorillonite having a high surface area and exposed cations on its surface (Johns, 1979) and most importantly, it contains sites where organic reactions can be catalyzed (Johns, 1979; Wei et al., 2006). Both montmorillonite and illite can alter pre-oil bitumen composition by adsorbing a considerable amount of asphaltene and polar compounds, whereas calcite and other minerals show little or no adsorption (Tannenbaum

and Kaplan, 1985; Huizinga et al., 1987). These studies have shown effects of mineralogy on petroleum composition. However, the role of bulk mineralogy on pore development in unconventional reservoirs during maturation has received comparatively little investigation.

The process by which pores evolve with different macerals during thermal maturation also remains unclear. Schieber (2010), Curtis et al. (2012), Loucks et al. (2012), and Milliken et al., (2013) have suggested that type of organic matter (Type I, II, III, IV kerogen) might play a role in formation of pores during thermal maturation. Mastalerz et al. (2012) showed that variations in relative proportion of macerals can affect geochemical properties of bulk organic matter. Only in the last several years, has the idea that OM pores may vary as a function of maceral type been introduced and the importance of integrating organic petrology with SEM petrography to distinguish different organic matter type (solid bitumen vs. different types of maceral) been recognized (Fishman et al., 2012; Mastalerz et al., 2013; Cardott et al., 2015; Hackley and Cardott, 2016).

To investigate if bulk mineralogy, total organic content (TOC), kerogen and maceral types, and thermal maturation affect changes in shape and size of OM pores and the evolution of OM-pore and mineral-pore networks, laboratory gold-tube pyrolysis, mineralogical and geochemical characterization, organic petrology, and SEM petrography methods were applied in this study. The pore evolution model developed by Ko et al. (2016, 2017) for OM-lean Upper Cretaceous Eagle Ford mudrocks is compared to pore evolution in the Woodford and Barnett mudrocks analyzed in this study. Specific

research questions examined include: (1) Do differences in maceral type affect OM pore development and evolution, and (2) Does bulk mineralogy, especially clay mineralogy, affect the timing of OM transformation and pore evolution?

4.2 DATA AND METHODS

4.2.1 Core and Outcrop Samples

The Devonian-Mississippian Woodford chert and mudrock samples used in this study were collected by Dr. Geoffrey S. Ellis at the U.S. Geological Survey (Denver, CO) from a well- studied (e.g., Ham, 1973; Kirkland et al., 1992; Krystyniak , 2005; Aufill, 2007; Paxton and Cardott; 2008) road cut along Interstate 35 on the south flank of the Arbuckle Anticline in Carter County, Oklahoma, USA (also see Fig. 1, Fishman et al., 2013). The outcrop has been and detailed stratigraphic and sedimentological analyses have been done. Chert and siliceous mudstone are the two major lithofacies in the Woodford Formation. We sampled both chert and mudstone lithofacies but focused on the pore evolution of the siliceous mudstone sample for this study.

Mississippian Barnett mudrock subsurface core samples were collected from a shallow core, Houston Oil and Minerals, Lee, Sam, No.C-5-1, located in Brown Country, Texas (in the southwestern Fort Worth Basin) (Figure 4.1). A sample (2.0 inches by 1.5 inches) was collected from the core at 1,278 ft.

4.2.2 Organic Petrography

Thin sections and polished pellets were made from outcrop (Woodford) and core (Barnett) samples for organic petrographic analysis. Organic petrographic analysis was

completed using a Zeiss Axio Imager A1m microscope equipped with white incident and

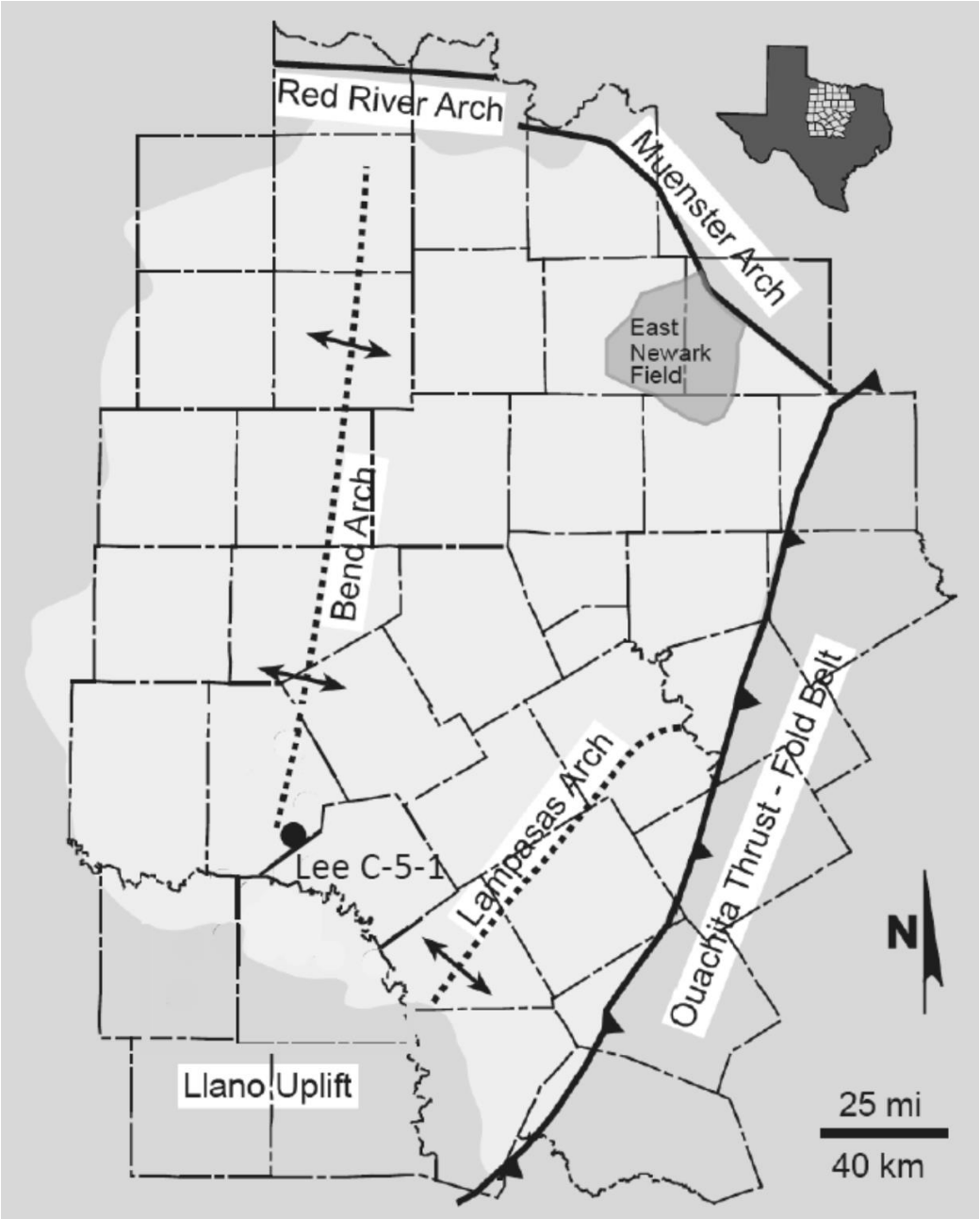

Figure 4.1: Map of the Fort Worth Basin (FWB) showing the distribution of the Barnett Formation, the general structural features, and the location of the core (Lee C-5-1, Brown County, Texas) used in this study. Modified after Loucks and Ruppel (2007) and Redmond (2016).

transmitted light and epifluorescence illumination. Imaging was accomplished with a Zeiss MRc digital camera at total magnifications of 200-500x with highest magnification using a 1.0 NA oil immersion objective.

An aliquot of 1 g or less crushed and sieved rock sample was mounted and polished to form pellets for analyses via ASTM D2797 (ASTM, 2016a). Polished pellets are best for examining organic matter in incident light despite exhibiting high surface roughness, typically up to about 1 μm of relief in individual fragments as determined from atomic force microscopy (AFM) measurements. Maceral identification and reflectance measurement (via ASTM D7708; ASTM, 2016b) was performed on these polished pellets. We used a Leica DM4000 microscope with LED illumination and monochrome camera detection for reflectance analysis with computer program DISKUS-FOSSIL by Hilgers Technisches Buero and a Klein and Becker YAG calibration standard (0.908% R_o). Preparation of thin sections achieves a relatively flat surface but does not allow as high a polish of organic matter as in pellet preparation. However, OM macerals still can be identified in incident and transmitted light petrography of thin sections.

4.2.3 Artificial Gold-Tube Anhydrous Pyrolysis and Geochemical Analysis

Eight small-diameter rock cylinders (6 mm in diameter and 2–3 cm in length) were drilled perpendicular to bedding planes from each collected sample (Barnett siliceous mudstone, Woodford chert, and Woodford siliceous mudstone). A total of 24 samples were drilled, and one original sample from each lithofacies was used as a control group. Twenty-one cylindrical samples were pyrolyzed in gold tubes at the Guangzhou

Institute of Geochemistry, Chinese Academy of Sciences. Samples were neither vacuum-dried nor oven-dried before being placed in gold tubes, so it is possible that some irreducible water may have been present.

Anhydrous gold-tube pyrolysis experiments were conducted on fourteen Barnett and Woodford cylindrical samples (seven for each). The gold tubes had an internal diameter of 6 mm and a wall thickness of 0.45 mm, and each was between 70 and 75 mm long, giving a total reactor volume of approximately 1.0 mL. Prior to loading the samples, the open-ended tubes were heated to 600°C to remove any residual organic material contaminating the tubes. The tubes were then welded at one end using an Argon arc-welder. Each gold tube was placed in a separate stainless steel autoclave and inserted into a pyrolysis oven. The anhydrous pyrolysis experiments were conducted under isothermal conditions at temperatures of 130, 300, 310, 333, 367, 400, and 425°C for 72 hours reaction time. A constant confining pressure was maintained at approximately 68.85 MPa (10,000 psi) by pumping water through the autoclave during pyrolysis to prevent rupturing of the gold tubes.

When the 72 hours duration was reached, the autoclave was withdrawn from the oven and rapidly quenched to room temperature in cold water. All generated petroleum (gas, liquid, and solid) were collected for compositional analyses. After the autoclaves were depressurized, the gold tubes were taken out and placed in a vacuum line with a residual pressure of 0.1 Pa. The gold tube was pierced using a needle to allow the product gases (C_1-C_5, CO_2, H_2S, and H_2) to be volatilized into the glass vacuum line. A dry ice and acetone (-80°C) trap was used to collect C_7-C_{14} light hydrocarbons. The total number

of moles of gas were calculated assuming ideal gas behavior. Identification and quantification of individual HC and non-HC gas components were carried out using a two-channel Hewlett-Packard 6890 Series Gas Chromatography (GC) that was custom-configured by Wasson ECE Instrumentation. The details of the GC operation conditions are described by Zhang et al. (2007).

The yield of light hydrocarbons (C_7-C_{14}) was determined by GC. A known amount of $C_{24}D_{50}$ internal standard (ID) was added in a C_7-C_{14} mixture with CH_2Cl_2 as the solvent, and the ratio of ID content to its GC peak area was defined as a calibration factor. The yield of C_7-C_{14} light oil was derived from the sum of C_7-C_{14} peak area multiplied by the calibration factor. C_{14+} extractable organic matter (EOM) of the pyrolysis residues was Soxhlet-extracted with a CH_2Cl_2 solvent and collected in 1.5 mL glass vials. After evaporating the solvent, the yield of EOM was determined by the weight difference of the glass vial before and after loading EOM. Saturate, aromatic, resins, and asphaltene (SARA) separation of the extract and quantification of extract fractions followed the procedures described by Bastow et al. (2007).

A portion of the pyrolyzed cylindrical sample was pulverized. Part of the pulverized sample was analyzed for Rock-Eval and Leco TOC (GeoMark) and the remaining sample was analyzed by nitrogen adsorption to investigate pore sizes ranging from 3 to 200 nm.

4.2.4 SEM Petrography

A flat surface was prepared from a portion of each post-pyrolysis Barnett and Woodford rock cylinder (without solvent extraction) for SEM analysis by Ar-ion beam milling using a Leica EM TIC020 Triple Ion Beam Miller. The Woodford chert samples were solvent (CH_2Cl_2) extracted. Therefore, these chert samples will not be used to discuss their pore evolution. Each sample was milled for 10 hours using an accelerating voltage of 8 keV and a current of 2.8 mA. An FEI Nova NanoSEM 430, field-emission scanning electron microscope (FE-SEM) located at the Bureau of Economic Geology in Austin, Texas, was used to image pores and their association with organic matter and mineral grains under an accelerating voltage of 10–15 keV and a working distance of 4–5 mm. Backscattered electron (BSE), secondary electron (SE), and SE through-the-lens detector (TLD) images were collected at various instrument magnifications ranging from 124x (horizontal field width [HFW] = 2.41 mm) to 80,000x (HFW = 0.001 mm). The TLD imaging was used for high-magnification examination.

4.2.5 Mineralogical Characterization

Samples were sent to KT GeoServices Inc., CO for X-ray diffraction (XRD) analysis of bulk mineralogy (Table 1). Identification of mineral components was completed by thin-section petrography and SEM X-ray EDS (energy-dispersive spectroscopy) detectors mapping. Two 30 mm^2 Bruker XFlash silicon-drift energy-dispersive X-ray detectors were used for elemental identification, under an accelerating

voltage of 15 keV, a spot size of 3.0–4.0, and a total count time of greater than 700 seconds.

4.3 GEOLOGICAL SETTING

4.3.1 Woodford Mudstones

Upper Devonian-Lower Mississippian Woodford mudstones in southern Oklahoma were deposited in an epicontinental sea during global sea-level transgression, within a failed aulacogen structure (Nicholas and Rozendal, 1975; Ham, 1973; Cardott and Chaplin, 1993; Lambert, 1993; Blakey, 2009). From the Cambrian through Permian, the basin was primarily filled with carbonates and marine shales. The Woodford marine shale was deposited in a deeper-water euxinic environment and is siliceous, containing chert and subordinate amounts of greenish-gray shale, sandstone, dolostone, phosphate nodules, and pyrite (Cardott and Chaplin, 1993; Comer, 2007). In general, chert, composed of radiolarian remains and diagenetic silica, is more abundant in distal parts of the basin; mudstone, siltstone, and sandstone are more abundant in proximal areas. Chert, composed primarily of microcrystalline, cryptocrystalline, and microfibrous quartz, and siliceous mudstones are the two main lithofacies in the Woodford Formation. Woodford Formation rocks are, in general, stratigraphically equivalent to other OM-rich shale deposits include the Chattanooga Shale in the Black Warrior Basin, the Antrim Shale in the Michigan Basin, the New Albany Shale in the Illinois Basin, the Marcellus Shale in the Appalachian Basin, and the Bakken Formation in the Williston Basin (Meissner, 1978; Blakey, 2009). The Woodford Shale has long been known as the source of most

Oklahoma's petroleum reserves and has become an active target for shale-gas and shale-oil development in the Anadarko, Arkoma, and Marietta-Ardmore basins (Cardott, 2011). In area of investigation, Woodford mudstone is conformably overlain by the Mississippian Sycamore Formation, composed of silty limestone interbedded with dark shale and unconformably overlies the Silurian and Lower Devonian Hunton Group (Ham, 1973; Fishman et al., 2013).

4.3.2 Barnett Mudstones

Mississippian Barnett siliciclastic mudstones were deposited in a deeper water foreland basin, the Fort Worth Basin (FWB), during the late Paleozoic Ouachita orogeny as the Gondwana plate approached the Laurussia craton (Meckel et al., 1992; Loucks and Ruppel, 2007). Barnett mudstones reach a maximum thickness of about 1,000 ft in the northeast near the Muenster arch and thin to the west and south (Montgomery et al., 2005; Pollastro et al., 2007). The Ouachita thrust-fold belt bounds the FWB to the east. Muenster, Red River, Bend, and Lampasas Arches, and the Llano Uplift bound the FWB on the west and north (Montgomery et al., 2005; Pollastro et al., 2007). The Barnett Shale is composed of a mixture of siliceous mudstone, calcareous siliceous mudstone, argillaceous limestone, skeletal packstone, and phosphatic packstone to grainstone facies (Loucks and Ruppel, 2007; Redmond, 2016). The Barnett Shale in the northern FWB has been studied extensively and developed as a general gas-shale reservoir model based on many pioneering studies (Bowker, 2007; Loucks and Ruppel, 2007; Milliken et al., 2007; Milliken et al., 2012a, b; Montgomery et al., 2005; Pollastro et al., 2007). Natural gas

was first produced from Barnett strata started in 1981 (Bowker, 2007). The Forestburg limestone subdivides the Barnett in the northern FWB into upper and lower units but is absent in the southern FWB (Montgomery et al., 2005; Pollastro et al., 2007; Loucks and Ruppel, 2007). The Barnett Formation unconformably overlies the Ordovician Ellenburger, Simpson, and Viola shelf carbonates and is directly overlain by the phosphatic glauconitic lime packstone unit and Pennsylvanian Marble Falls Group carbonates (Montgomery et al., 2005; Wood, 2013). In the southern FWB, the Barnett is shown to unconformably overly the Mississippian Whites Crossing unit, the Devonian Houy Formation, or the Lower Ordovician Ellenburger Group (Redmond, 2016).

4.4 RESULTS

4.4.1 Sample Lithofacies, Mineralogy, Texture, and Fabric

4.4.1.1 Barnett Mudstone

The Barnett sample is a siliceous mudstone, the most common lithofacies in the Barnett strata. These rocks are comprised of 25 to 40% clay minerals [illite and mica, interlayer illite and smectite (I/S), chlorite, and kaolinite] and 30 to 50 % quartz (Table 4.1, Redmond, 2016). Feldspar, carbonate, phosphate, and pyrite are minor components (Table 4.1). This facies is rich in organic matter, with an average TOC value of 4.5 wt.% (range 1.6 to 10.6 wt.%) (Table 4.2, Redmond, 2016). Texturally, the mudstone is laminated, composed of silt-sized quartz, feldspar, and clay minerals, with less abundant silt-sized carbonate grains (Figure 4.2). Phosphate (apatite) grains form peloids or are dispersed and admixed in the matrix with organic matter and other minerals (Figure 4.2).

				Carbonates					*Clay minerals*					
Sample #	Quartz	Plagioclase	K-feldspar	Calcite	Dolomite	Ankerite	Siderite	Pyrite	Illite + mica	I/S mixed-layer	Smectite	Kaolinite	Chlorite	TOTAL
Barnett siliceous mudstone	**40**	**2**		**2**	**2**		**4**	**10**	**25**	**10**			**5**	**100**
Woodford siliceous mudstone	**50**		**8**	**3**		**1**		**3**	**15**	**15**		**5**		**100**
Woodford chert	**93**							**2**	**5**					**100**

Table 4.1: Bulk mineralogy of the Barnett and Woodford mudrocks.

Immature or low-maturity samples	Woodford chert	Barnett siliceous mudstone	Woodford siliceous mudstone
% carbonate	3.33	11.43	4.25
Leco TOC (wt %)	6.22	9.70	16.7
Rock-Eval S_1 (mg/g TOC)	0.89	1.14	1.93
Rock-Eval S_2 (mg/g TOC)	38.04	53.72	89.74
Rock-Eval T_{max} (°C)	432	421	425
Calculated R_o (%)	0.60	0.42	0.49
Hydrogen Index (HI)	612	554	537
Oxygen Index (OI)	6	15	4
Solid bitumen reflectance	0.40	0.43	0.38

Table 4.2: Rock-Eval, Leco TOC analyses, and solid bitumen reflectance measurement of immature Barnett and Woodford mudrocks.

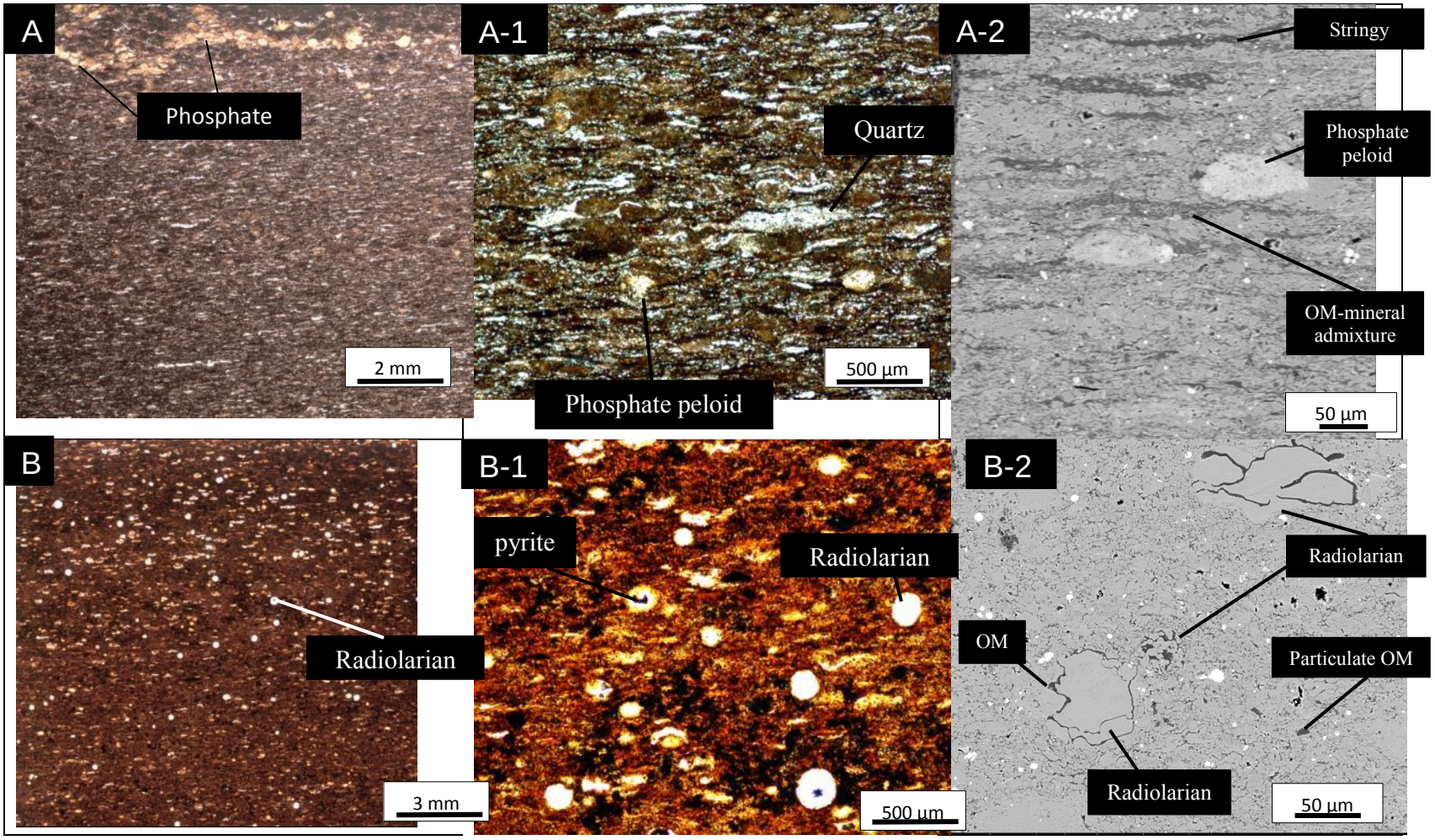
A
Phosphate
2 mm
A-1
Quartz
Phosphate peloid
500 µm
A-2
Stringy
Phosphate peloid
OM-mineral admixture
50 µm
B
Radiolarian
3 mm
B-1
pyrite
Radiolarian
500 µm
B-2
Radiolarian
OM
Particulate OM
Radiolarian
50 µm

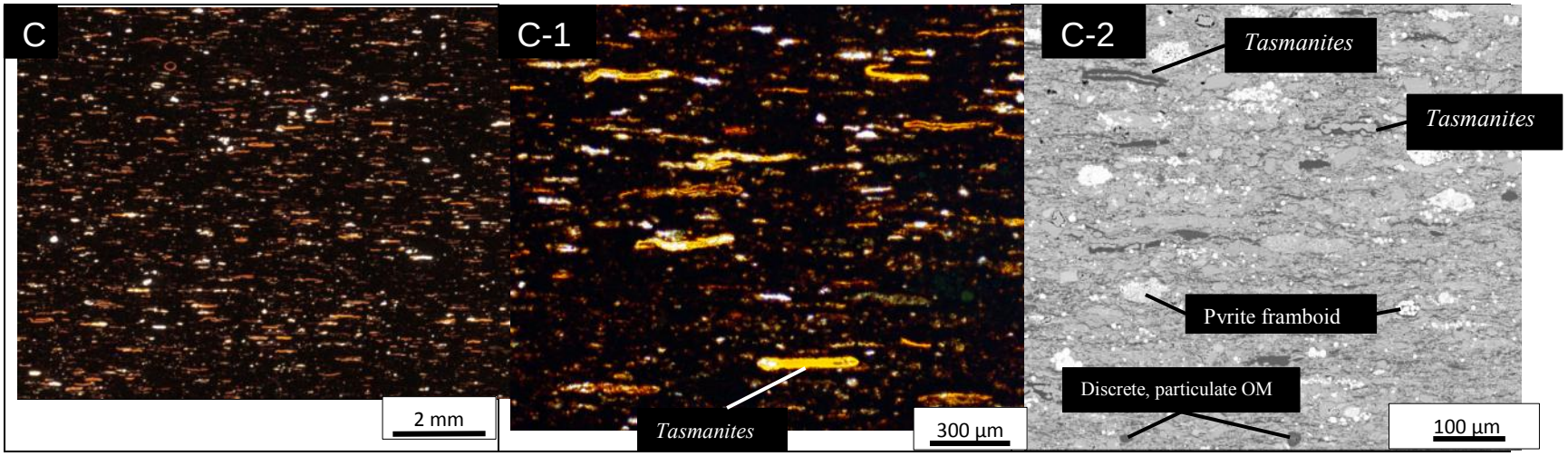

Figure 4.2: Thin-section and SEM photomicrographs of representative areas under plane polarized light (PPL) of Barnett and Woodford mudstones. Photomicrographs showing (A) Barnett Shale, laminated siliceous mudstone facies. (A-1) Matrix is mainly composed of quartz, clay minerals, and organic matter (OM). (A-2) OM-rich, silty, argillaceous, siliceous mudstone. Organic matter is largely amorphous. (B) Woodford Shale, weakly laminated chert facies. (B-1) Radiolarian microfossils. Some radiolaria are filled and replaced by calcite or partly replaced by pyrite. (B-2) Radiolaria within mixed illite, organic matter, and microcrystalline quartz matrix. Some radiolaria are filled with OM. (C) Woodford Shale, laminated siliceous mudstone facies. (C-1) Abundant compressed *Tasmanites* OM are the dominant form of OM in the Woodford siliceous mudstone. (C-2) Silty, *Tasmanites*-rich, argillaceous, siliceous mudstone. Some *Tasmanites* are filled with quartz. Abundant pyrite framboids are in the matrix.

Authigenic minerals include pyrite, dolomite, and phosphate. Thin-section petrography reveals that both detrital and biogenic quartz (sponge spicules) contribute to total quartz content. Agglutinated foraminifera were observed.

4.4.1.2 Woodford Chert and Siliceous Mudstone

The Woodford chert and siliceous mudstone facies are both laminated (Figure 4.2). The chert facies contained between 85% to 95% quartz and less than 5% clay minerals (mainly illite), whereas the mudstone facies contains 60 to 70% quartz and 20 to 35% clay minerals based on XRD analysis (Table 4.1, Fishman et al., 2013). Some of the chert was recrystallized from dissolved radiolarian tests and possibly from sponge spicules that were both originally opal A. Thin-section petrography shows a few intact recrystallized radiolarian microfossils and suggests that the diagenesis could have occurred very early. Recrystallized biogenic silica and subhedral to euhedral microscrystalline quartz compose the chert; however, the sizes of these crystallites are non-uniform in SEM. The silt-size quartz crystals in the Woodford samples were investigated using cathodoluminescence microscopy (CL) techniques (Milliken, 2012b; Milliken, 2000). CL patterns show that the chert is dominated by authigenic quartz (dull luminescence) (Figure 4.3). CL analysis of the Woodford mudstone facies shows quartz in both detrital and authigenic forms (Figure 4.4). Many brightly luminescent detrital grains have dull luminescent authigenic rims (Figure 4.4 C, D), implying detrital quartz with authigenic microcrystalline quartz overgrowth is common. Most silt-sized grains are quartz and the rest are K-feldspar and dolomite. These silt grains are angular to

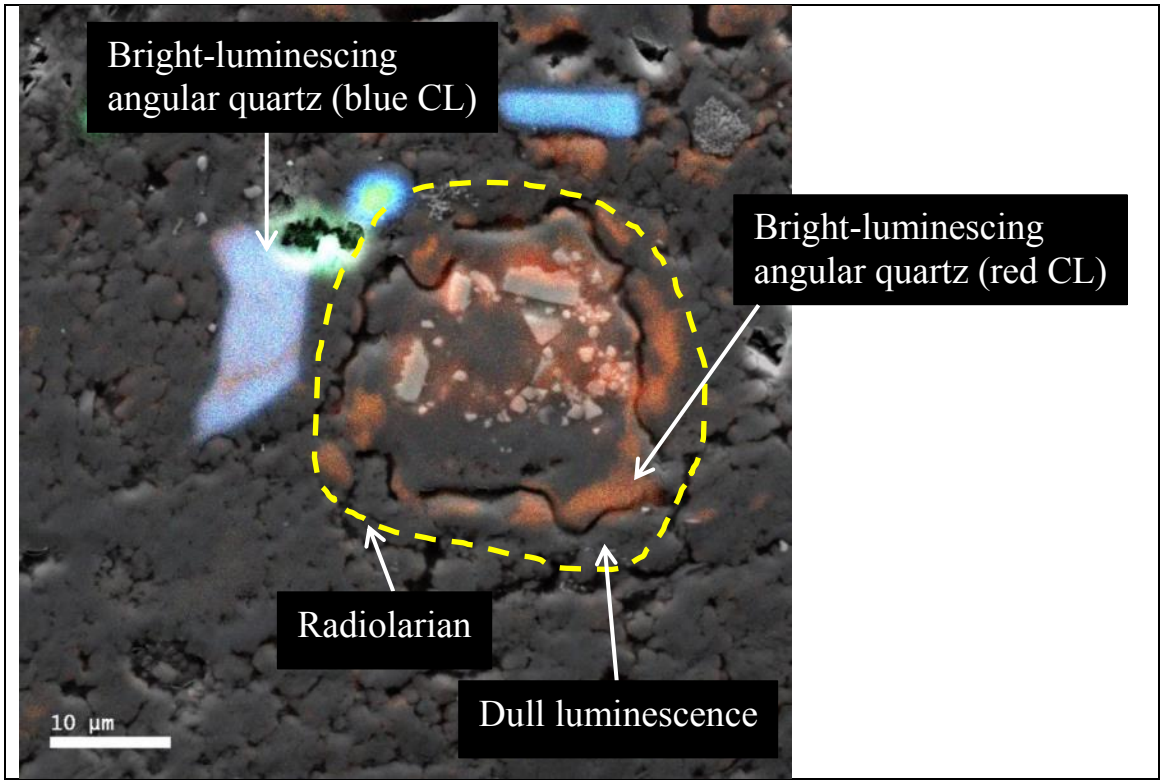

Figure 4.3: SEM-CL image showing quartz (more than 97%) in the Woodford chert sample. Radiolarian (yellow dashed line) composed of angular quartz silt particles cemented by dark luminescing authigenic quartz. Next to the radiolarian, the angular bright-luminescing quartz showed blue to violet CL and was interpreted to represent quartz phenocrysts from volcanic rock or high-grade metamorphic quartz.

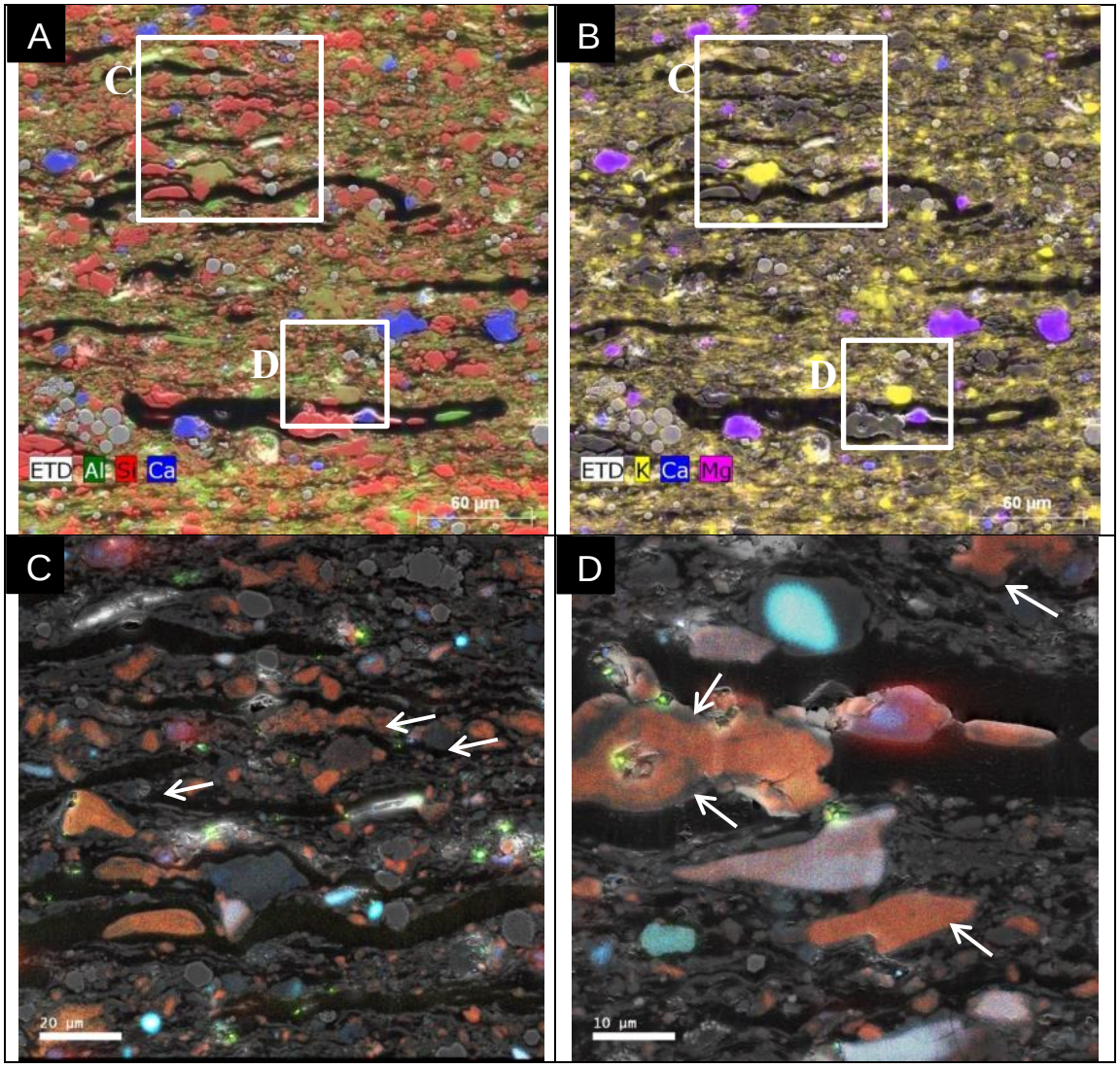

Figure 4.4: SEM-EDS and SEM-CL images showing varieties of quartz silt. (A, B) X-ray maps of elements (Al, Si, Ca, K, Mg) based on EDS with a secondary electron signal displaying distribution of quartz (red), dolomite (purple), feldspar, anad clay minerals in the Woodford siliceous mudstone facies. Bedding is horizontal. (C, D) Quartz in multichannel electron cathodoluminescence (SE/CL) image. Brightly luminescent detrital grains (red and blue CL) have dull luminescent rims (white arrows), representing quartz of detrital and authigenic origins, respectively.

subrounded and are of detrital origin. Clay-sized minerals include illite, kaolinite, quartz, pyrite, and dolomite.

4.4.2 Organic-Matter Macerals, TOC, and Thermal Maturity

4.4.2.1 Barnett Mudstone

The Barnett sample has a TOC content of 9.7 wt.% (Table 4.2). Solid bitumen reflectance is 0.43 $\%R_o$ (30 measurements, standard deviation = 0.06), and the Rock-Eval T_{max} temperature is approximately 420°C or less (Table 4.2). Based on these data, the Barnett sample is immature.

The Barnett siliceous mudstone sample contains scattered telalginite particles visible via fluorescence (Figure 4.5A, B). Telalginite is a minor part of the overall organic matter component which is dominated by faintly fluorescent amorphous organic matter (AOM), that is commonly oriented parallel to bedding (Figure 4.5A, B). The AOM is sometimes identified as bituminite, the organic petrographers' catch-all term for amorphous organic matter (e.g., Fishman et al., 2012), although it is generally understood that the terms AOM and bituminite are used interchangeably to describe structureless kerogen (e.g., Hackley and SanFilipo, 2016; Hackley et al., 2016). Bituminite (or AOM) in the Barnett sample ranges from discrete lamellae with bright fluorescence and a relatively homogeneous gray reflecting surface to more scattered accumulations with less fluorescence (or non-fluorescent) and a greater admixture of mineral grains (Figure 4.5). Additionally, scattered inertinite and vitrinite are present in the Barnett sample. There is also some micrinite associated with gray reflecting solid bitumen (Figure 4.5D). The

presence of micrinite may indicate early conversion of amorphous kerogen to petroleum (Taylor and Liu, 1989).

Using SEM petrography, four general types of kerogen can be identified in the immature Barnett sample: (1) Pure OM – this OM does not contain any minerals, and its occurrence is sparse. OM grains are in general oriented parallel to bedding and compacted (Figure 4.6). Pure OM particles range from 20 to 30 μm in length. (2) OM-mineral admixtures – this is the most abundant type of organic matter in the Barnett sample (Figure 4.6). Admixtures comprise organic matter, minerals, and clay mineral aggregates, and are parallel to bedding. Admixture of minerals can be significant (Figure 4.6). (3) Stringy/Flaky OM – this type of OM is the second most abundant type (Figure 4.6). OM particles are elongate and lamellar and have fairly well-defined boundaries. Although they are stringy and flaky in 2D, they can be platy in 3D. They are also parallel or subparallel to bedding but do not encase as much mineral and clay mineral matter as OM-mineral admixtures. Pyrite is the most common mineral associated with this type of OM. Stringy/Flaky OM is roughly 50 to 200 μm long and 10 to 20 μm wide after compaction. (4) Particulate OM with discrete shape and well-defined boundaries – these OM fragments are seldom compacted and randomly dispersed in the matrix (Figure 4.6). They are usually uncommon (<5 vol. % of the total OM) based on visual estimates, and their shape and size vary. They are interpreted to be part of plants, marine algae, marine phytoplankton, or the altered/oxidized remains of these organisms.

Because reflectance and fluorescence are not observable with SEM petrography, maceral type identification is challenging. After comparing observations of organic

matter in the Barnett mudrock from SEM and optical microscopy, based on size, abundance, morphology, and mineral associations, we interpret pure OM (SEM organic matter category 1) to be telalginite macerals; OM-mineral admixtures and stringy/flaky OM (SEM categories 2 and 3) to be AOM or bituminite; particulate OM (SEM category 4) to be inertinite macerals. Although both OM-mineral admixtures and stringy/flaky OM represents AOM (or bituminite), OM-mineral admixtures (SEM category 2) demonstrate a greater admixture of mineral matter than does the stringy/flaky OM (SEM category 3).

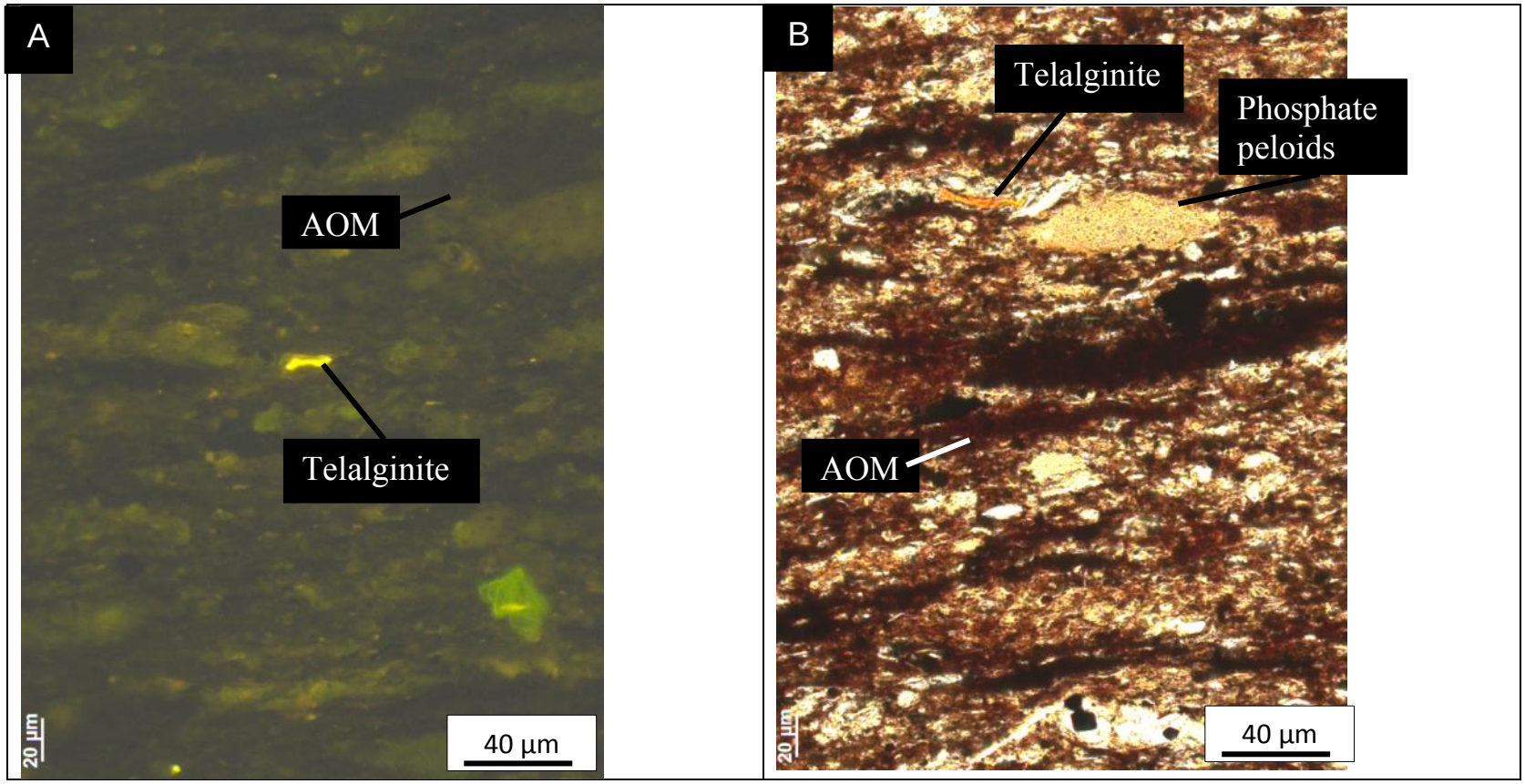
A
AOM
Telalginite
20 µm
40 µm
B
Telalginite
Phosphate peloids
AOM
20 µm
40 µm

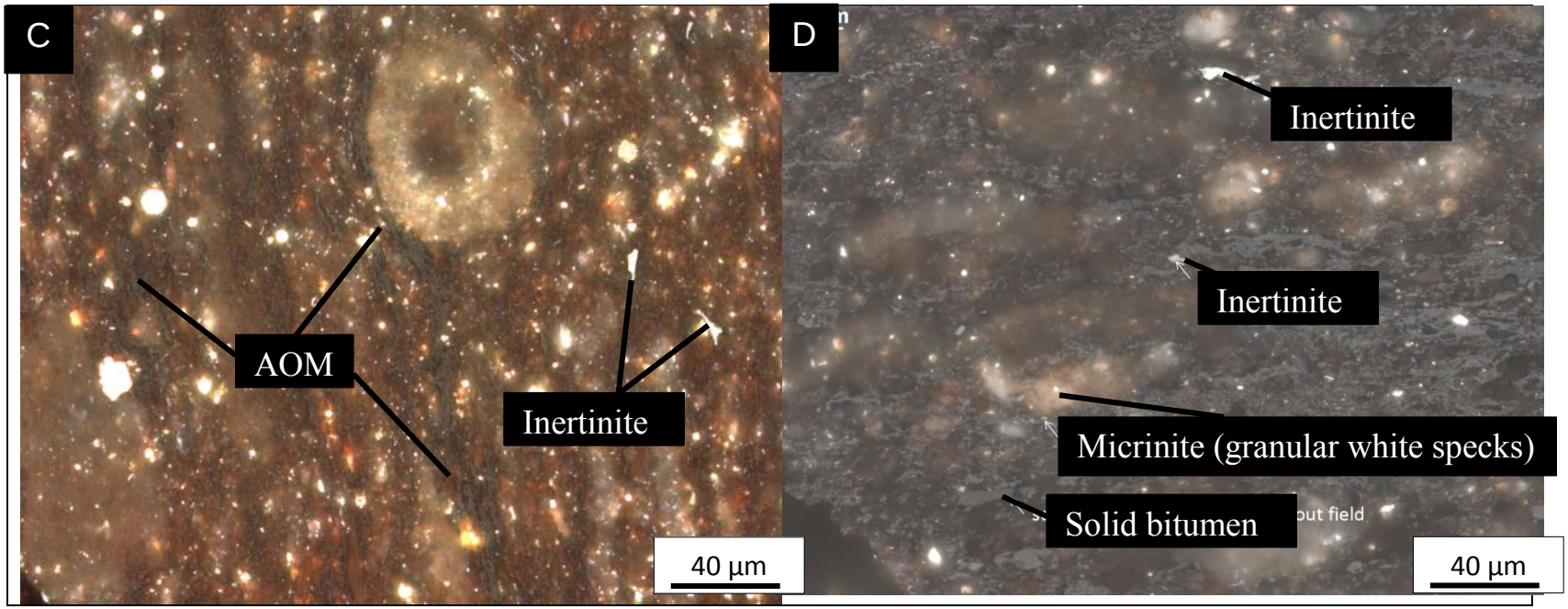

Figure 4.5: Optical photomicrographs under oil immersion showing types of macerals identified from polished thin-sections and pellets of the Barnett siliceous mudstone. (A) Scattered fluorescent telalginite and faintly fluorescent amorphous organic matter (AOM) were identified under epi-fluorescence. AOM is the dominant organic component in the Barnett mudstone. (B) Telalginite and AOM in transmitted light. (C) AOM and inertinite identified in incident white light. (D) Micrinite associated with low gray reflecting solid bitumen under incident white light. The presence of the micrinite indicates early conversion of the amorphous kerogen to petroleum.

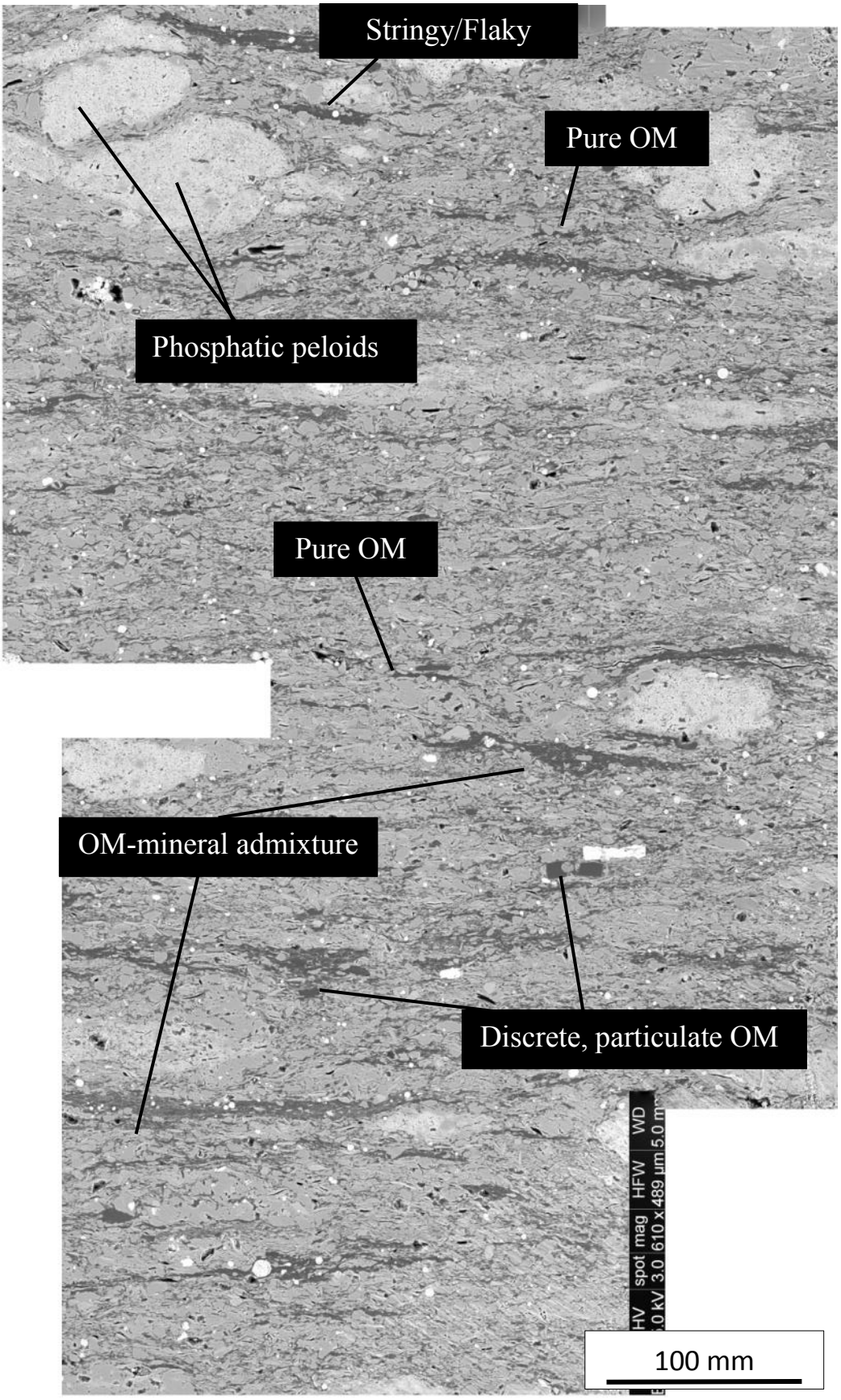

Figure 4.6: SEM image of the Barnett siliceous mudstone sample. Ar-ion milled surface showing lamination, phosphatic peloids, and four distinct types of OM (1) pure OM (2) stringy/flaky OM (3) OM-mineral admixture (4) discrete and particulate OM. OM: organic matter.

4.4.2.2 Woodford Chert and Siliceous Mudstone

The Woodford siliceous mudstone sample (TOC = 16.7 wt.%) is richer in organic matter than the Woodford chert sample (TOC = 6.2 wt.%) (Table 4.2). The Woodford chert contains solid bitumen with reflectance of 0.40 $\%R_o$ (30 measurements, standard deviation = 0.07), and the Rock-Eval T_{max} temperature is approximately 432°C or less (Table 4.2). The Woodford siliceous mudstone sample contains solid bitumen reflectance of 0.38 $\%R_o$ (30 measurements, standard deviation = 0.07), and the Rock-Eval T_{max} temperature is approximately 425°C or less (Table 4.2). Both solid bitumen reflectance and Rock-Eval data show that the Woodford chert and siliceous mudstone facies are immature.

Organic matter in both Woodford siliceous mudstone and chert is amorphous or in the form of *Tasmanites* microfossils (Figure 4.2). *Tasmanites* is a unicellular green algal cyst that generally is preserved as elliptical discs compressed along the bedding plane; some can be infilled by recrystallized quartz, calcite, or pyrite before compaction preserving the original spherical shape (Schieber, 1996; Loucks and Ruppel, 2007; Slatt and O'Brien, 2011; Fishman et al., 2012; Hart et al., 2013; Hackley and Kus, 2015). The Woodford siliceous mudstone sample contains abundant thick-walled *Tasmanites* and *Leiosphaeridia* (unknown spherical alga) that are flattened into the bedding planes (Figure 4.7A). Some of the *Tasmanites* have been partially bituminized as revealed by a decrease in fluorescence intensity, a shift to more reddish color in fluorescence and the development of a gray reflecting surface in reflected light (Figure 4.7A, B). The matrix

contains abundant dispersed fluorescent AOM (Figure 4.7A, B). Some scattered inertinite is present and very fine grained (Figure 4.7B).

The Woodford chert facies also contains abundant *Tasmanites* and *Leiosphaeridia* (Figure 4.7C). Other petrographers also have identified telalginite in the Woodford as *Foerstia* (Cardott and Chaplin, 1993). The variations in telalginite morphology may represent different life-cycle phases of one species, i.e., active vs. resting (spore) phases, rather than different species. Maturity is low as suggested by the high-intensity green fluorescence (short wavelength) response (Bertrand et al., 1985; Pradier et al., 1991). Qualitatively, the OM in chert is more oxidized than in the mudstone sample as is evident through secondary mineralization (oxides) (Figure 4.7D).

Based on SEM petrography, the Woodford sample contains three types of kerogen: (1) *Tasmanites* OM – the most abundant type of organic matter, is characterized by its thin- to thick-wall, in some cases with discrete shape or encasing pyrite or quartz grains (Figure 4.8A, B). The size of *Tasmanites* ranges from approximately 50 to 200 microns. (2) Stringy and dispersed OM – this type of OM has no well-defined boundaries and is generally admixed with minerals in the matrix (Figure 4.8B). The abundance of minerals is less than in the OM-mineral admixtures and stringy/flaky OM categories observed by SEM in the Barnett mudrocks. (3) Particulate and discrete OM – this OM has well-defined boundaries, discrete shapes and resists compaction. This OM is randomly dispersed in the matrix and usually low in abundance (<5 vol. % of the OM) (Figure 4.8A).

Tasmanites OM is easily identified in both light and SEM microscopy. Based on size, abundance, morphology, and mineral associations, we interpret stringy, dispersed OM observed by SEM to be AOM (or bituminite), and particulate and discrete OM to be inertinite.

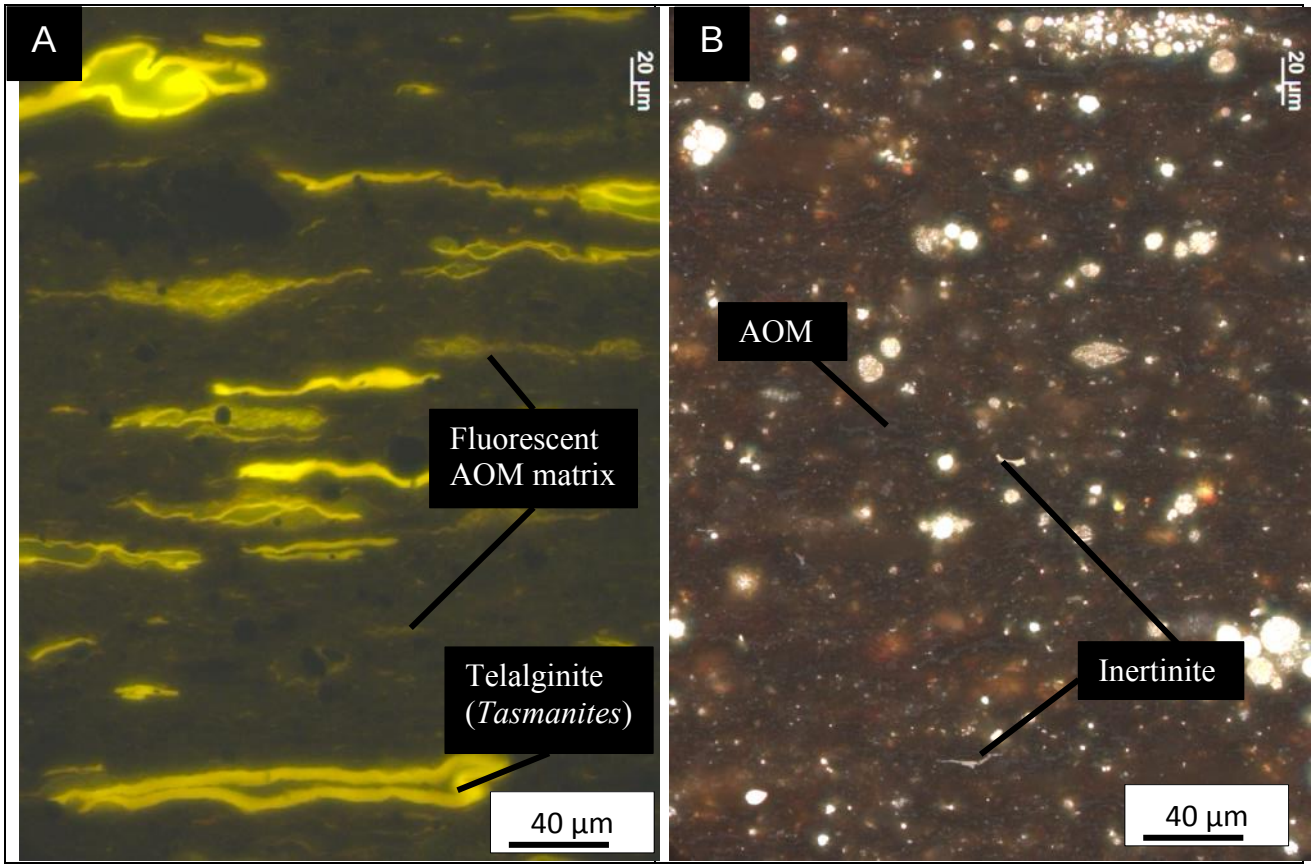

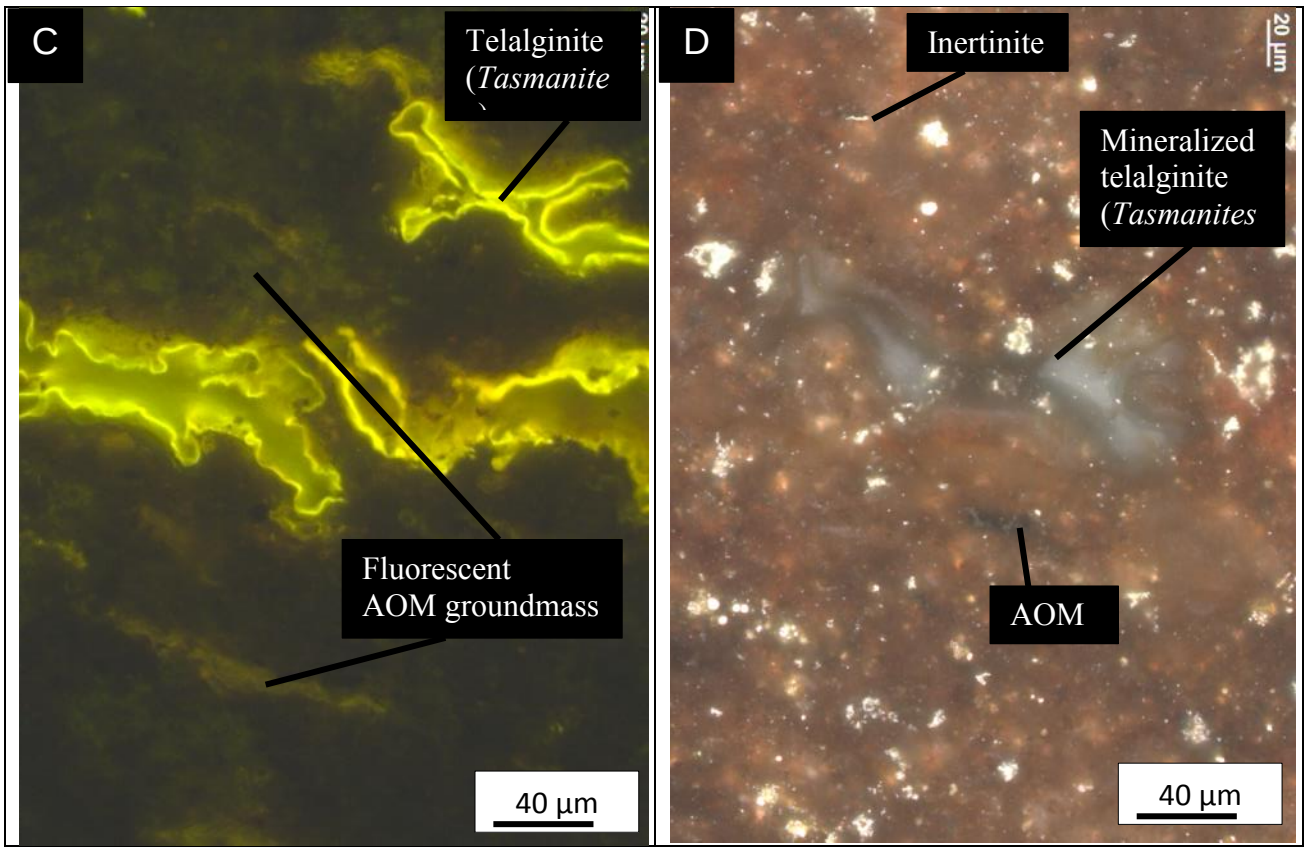

Figure 4.7: Optical photomicrographs under oil immersion showing types of macerals identified from polished thin-sections and pellets of the Woodford siliceous mudstone and chert samples. (A) Woodford siliceous mudstone: thick-walled Tasmanites and Leiosphaeridia (unknown spherical alga) flattened in the bedding planes. The matrix contains abundant dispersed fluorescent AOM. (B) Woodford siliceous mudstone: AOM and inertinite identified in incident white light, same field as (A). (C) Woodford chert: abundant Tasmanites and Leiosphaeridia (unknown spherical alga). High-intensity green fluorescence response suggests low maturity. (D) Woodford chert: Mineralized Tasmanites, AOM and inertinite identified in incident white light, same field as (C).

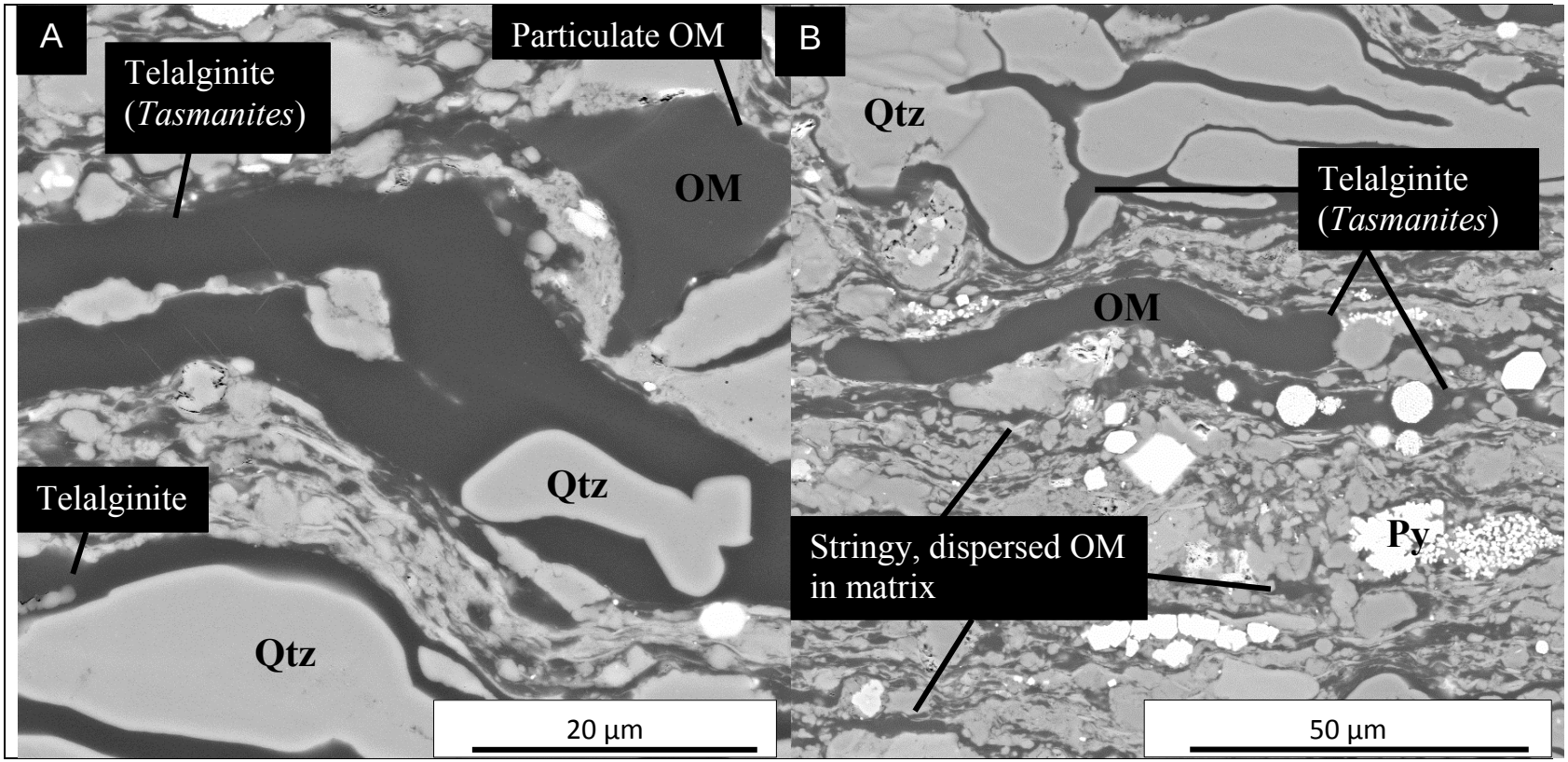

Figure 4.8: SEM images of the immature Woodford siliceous mudstone. Ar-ion milled surface showing lamination, phosphatic peloids, and three distinct types of kerogen (1) *Tasmanites* microfossil remains. (2) Stringy, dispersed OM (3) Particulate and discrete OM. Qtz: quartz; Py: pyrite. (A) Compressed *Tasmanites* microfossil with quartz encased within and adjacent particulate, discrete OM. (B) Compressed *Tasmanites* microfossil. Some are associated with pyrite framboids. Some have quartz are encased within. Matrix is composed of clay minerals, clay-sized quartz, and stringy, dispersed organic matter.

4.4.3 Geochemical Properties and Stages of Petroleum Generation

4.4.3.1 Barnett and Woodford Mudstones

The Barnett and Woodford mudrocks show distinct geochemical properties in terms of total organic content (TOC), Rock-Eval S_1, S_2, T_{max}, hydrogen index (HI), and oxygen index (OI) values (Table 4.2). The Woodford siliceous mudstone sample contains the highest amount of TOC (16.7 wt.%). As discussed above, both Barnett and Woodford mudrock samples are immature with T_{max} values of approximately 430°C (~ 0.6%R_o) (Table 4.2). Lewan (1983, 1987) also recognized the immature character of the Woodford Shale from the same outcrop location. The Barnett and Woodford organic-rich siliceous mudstone samples show higher Rock-Eval S_1 and S_2 but lower T_{max} and HI values when compared to less organic-rich Woodford chert (Table 4.2). During the gold tube experiments, all samples showed decreases in the amount of TOC, S_2, and HI values and increases in T_{max} values (Tables 4.3 to 4.5). Rock-Eval and TOC data from the Boquillas (Eagle-Ford equivalent) organic-lean mudstone (TOC = 1.5 wt.%) is also plotted with the Barnett and Woodford for comparison (Figure 4.9).

Stages and timing of organic matter conversion and petroleum generation in the Barnett and Woodford mudrock samples were identified by the yield of generated gas (C_1-C_5), light hydrocarbons (C_7-C_{14}), hydrocarbons (C_{14+}), extractable organic matter (EOM), and SARA fractions (saturate, aromatic, NSO compounds, and asphaltene) with increasing experimental temperatures (Figure 4.10; Tables 4.6 to 4.8). In general, the selected experimental temperatures simulate the generation of bitumen, early oil, oil

window, and the very beginning of wet gas generation (Figure 4.10). However, between Barnett and Woodford mudrock samples there are differences in the amount of generated oil, gas, and SARA fractions, as well as differences in the rate of conversion. The Barnett siliceous mudstone sample generated slightly more methane to pentane compared to the Woodford chert and siliceous mudstone samples from the middle to early oil cracking to wet gas stage. The Woodford chert sample showed the greatest petroleum generation potential (extractable organic matter) compared to the other samples at the beginning of the oil window (Figure 4.10).

Five oil and gas generation stages were defined based on yields of gas, light oil, EOM, and SARA fractions (Figure 4.10). They are (1) bitumen or polar (resins and asphaltenes) generation, (2) early oil generation, (3) oil window and associated gas generation, (4) end of oil window generation, and (5) early oil cracking and associated wet gas generation. In the Barnett and Woodford siliceous mudstone samples, gradual increases in extractable organic matter (EOM) from 130 to 333°C runs indicate that the Barnett and Woodford went through the kerogen to bitumen transformation. Comparison of EOM versus experiment temperature shows that above 333°C, EOM (SARA components) gradually decreased in the higher temperature experiments (Figure 4.10). The amount of light oil (C_{7-14}) gradually increased to a maximum at 400°C at the end of oil window. This corresponds to bitumen gradually being transformed into oil. From 400°C to 425°C, light oil began to decrease and gaseous hydrocarbon (C_{1-3}) continued to increase. This corresponds to the early oil cracking to wet-gas stage (Figure 4.10). The saturate fraction of the Barnett sample and saturate and aromatic components of the

Sample ID	Experiment temperature stage (°C)	Leco TOC (wt.%)	Rock-Eval-2 S_1 (mg HC/g)	Rock-Eval-2 S_2 (mg HC/g)	Rock-Eval-2 T_{max} (°C)	Hydrogen Index	Oxygen Index
BS-1	Outcrop	9.70	1.14	53.72	421	554	15
BS-10	130	10.60	0.48	56.93	420	537	13
BS-3	300	10.80	6.94	47.18	428	437	9
BS-6	310	10.90	10.39	42.55	431	390	9
BS-8	333	9.09	11.69	20.37	437	224	11
BS-12	367	7.23	0.09	2.54	456	35	4
BS-14	400	7.48	0.20	1.21	549	16	4
BS-2	425	7.76	4.63	1.49	340	19	5

Table 4.3: Geochemical data from Barnett siliceous mudstone facies samples from laboratory pyrolysis experiments.

Sample ID	Experiment temperature stage (°C)	Leco TOC (wt.%)	Rock-Eval-2 S_1 (mg HC/g)	Rock-Eval-2 S_2 (mg HC/g)	Rock-Eval-2 T_{max} (°C)	Hydrogen Index	Oxygen Index
WM-1	Outcrop	16.70	1.93	89.74	425	537	4
WM -10	130	15.40	2.04	90.75	420	589	3
WM -7	300	13.60	9.27	69.16	431	509	3
WM -2	310	13.20	10.89	60.11	435	455	5
WM -4	333	12.30	20.52	38.15	428	310	3
WM -12	367	10.30	25.50	12.84	392	125	3
WM -14	400	10.60	12.49	5.80	391	55	3
WM -6	425	9.99	8.48	2.32	387	23	3

Table 4.4: Geochemical data from Woodford siliceous mudstone facies samples from laboratory pyrolysis experiments.

Sample ID	Experiment temperature stage (°C)	Leco TOC (wt.%)	Rock-Eval-2 S_1 (mg HC/g)	Rock-Eval-2 S_2 (mg HC/g)	Rock-Eval-2 T_{max} (°C)	Hydrogen Index	Oxygen Index
WF-1	Outcrop	6.22	0.89	38.04	432	612	6
WF -10	130	3.99	0.50	26.55	426	665	3
WF -4	300	3.40	0.24	19.27	430	567	4
WF -6	310	3.26	0.11	17.02	435	522	3
WF -7	333	3.73	7.68	13.37	433	358	3
WF -12	367	2.41	0.13	1.03	447	43	4
WF -13	400	3.60	0.22	0.44	445	12	3
WF -15	425	2.50	0.39	0.35	434	14	3

Table 4.5: Geochemical data from Woodford chert facies samples from laboratory pyrolysis experiments.

Heating Temperature (°C [°F])	C_1-C_3 (mg/g TOC)	C_4-C_5 (mg/g TOC)	C_7-C_{14} (mg/g TOC)	EOM (mg/g TOC)	SAT (mg/g TOC)	ARO (mg/g TOC)	NSO (mg/g TOC)	Asphaltene (mg/g TOC)	CO_2 (mg/g TOC)	H_2S (mg/g TOC)
130 (266)	0.01	0.00	0.84	34.67	3.80	9.27	12.01	3.84	0.43	0.00
300 (572)	6.69	1.22	14.01	217.03	11.01	49.75	62.08	78.92	94.22	2.17
310 (590)	9.84	1.44	22.23	314.37	22.38	73.75	82.29	114.29	66.49	0.45
333 (631.4)	24.24	6.34	34.60	341.83	30.60	95.20	92.96	106.56	68.48	3.02
367 (692.6)	91.17	24.83	50.60	197.85	20.61	70.28	39.46	61.32	146.91	16.09
400 (752)	175.79	39.20	52.17	62.28	28.84	28.03	16.77	13.97	186.37	29.40
425 (797)	244.07	39.16	40.65	40.10	6.07	22.03	11.63	3.64	227.25	51.99

Abbreviations: ARO = aromatic; C_1-C_3 = methane, ethane, and propane; C_4-C_5 = butane and pentane; C_7-C_{14} = light oil; EOM = extractable organic matter; NSO = nitrogen, sulfur, oxygen, and heavy metals; SAT = saturate

Table 4.6: Yields of generated gas and oil components from Barnett siliceous mudrocks after each experimental run.

Heating Temperature (°C [°F])	C_1-C_3 (mg/g TOC)	C_4-C_5 (mg/g TOC)	C_7-C_{14} (mg/g TOC)	EOM (mg/g TOC)	SAT (mg/g TOC)	ARO (mg/g TOC)	NSO (mg/g TOC)	Asphaltene (mg/g TOC)	CO_2 (mg/g TOC)	H_2S (mg/g TOC)
130 (266)	0.01	0.00	0.21	14.95	N/A	N/A	N/A	N/A	0.17	0.00
300 (572)	5.47	0.43	11.16	176.47	15.14	51.29	40.77	63.41	25.05	0.00
310 (590)	10.81	1.59	18.83	288.89	14.18	75.32	66.14	123.79	32.24	0.00
333 (631.4)	33.55	9.45	26.12	408.09	24.79	122.60	75.32	307.97	30.32	0.01
367 (692.6)	84.06	20.32	37.72	252.82	24.66	94.89	41.84	83.68	69.13	0.02
400 (752)	156.35	33.37	38.75	93.12	5.57	35.41	11.35	39.36	67.01	0.06
425 (797)	201.20	30.92	15.78	54.93	6.91	28.04	12.63	5.47	90.96	0.09

Abbreviations: ARO = aromatic; C_1-C_3 = methane, ethane, and propane; C_4-C_5 = butane and pentane; C_7-C_{14} = light oil; EOM = extractable organic matter; NSO = nitrogen, sulfur, oxygen, and heavy metals; SAT = saturate

Table 4.7: Yields of generated gas and oil components from Woodford siliceous mudrocks after each experimental run.

Heating Temperature (°C [°F])	C_1-C_3 (mg/g TOC)	C_4-C_5 (mg/g TOC)	C_7-C_{14} (mg/g TOC)	EOM (mg/g TOC)	SAT (mg/g TOC)	ARO (mg/g TOC)	NSO (mg/g TOC)	Asphaltene (mg/g TOC)	CO_2 (mg/g TOC)	H_2S (mg/g TOC)
130 (266)	0.01	0.00	1.56	20.51	N/A	N/A	N/A	N/A	1.40	0.00
300 (572)	1.25	0.07	5.20	124.59	9.37	35.30	31.67	40.89	6.50	0.00
310 (590)	1.75	0.07	8.07	240.89	17.00	67.16	53.48	94.00	6.00	0.00
333 (631.4)	36.81	12.73	39.06	709.92	50.50	210.02	123.99	271.67	29.60	0.00
367 (692.6)	66.30	16.34	45.88	219.95	21.91	70.61	30.98	51.12	44.20	0.00
400 (752)	111.28	32.03	62.81	66.20	4.58	33.49	13.74	14.10	53.60	0.10
425 (797)	195.06	31.97	45.74	42.21	7.02	21.39	9.93	5.07	69.80	0.20

Abbreviations: ARO = aromatic; C_1-C_3 = methane, ethane, and propane; C_4-C_5 = butane and pentane; C_7-C_{14} = light oil; EOM = extractable organic matter; NSO = nitrogen, sulfur, oxygen, and heavy metals; SAT = saturate

Table 4.8: Yields of generated gas and oil components from Woodford chert after each experimental run.

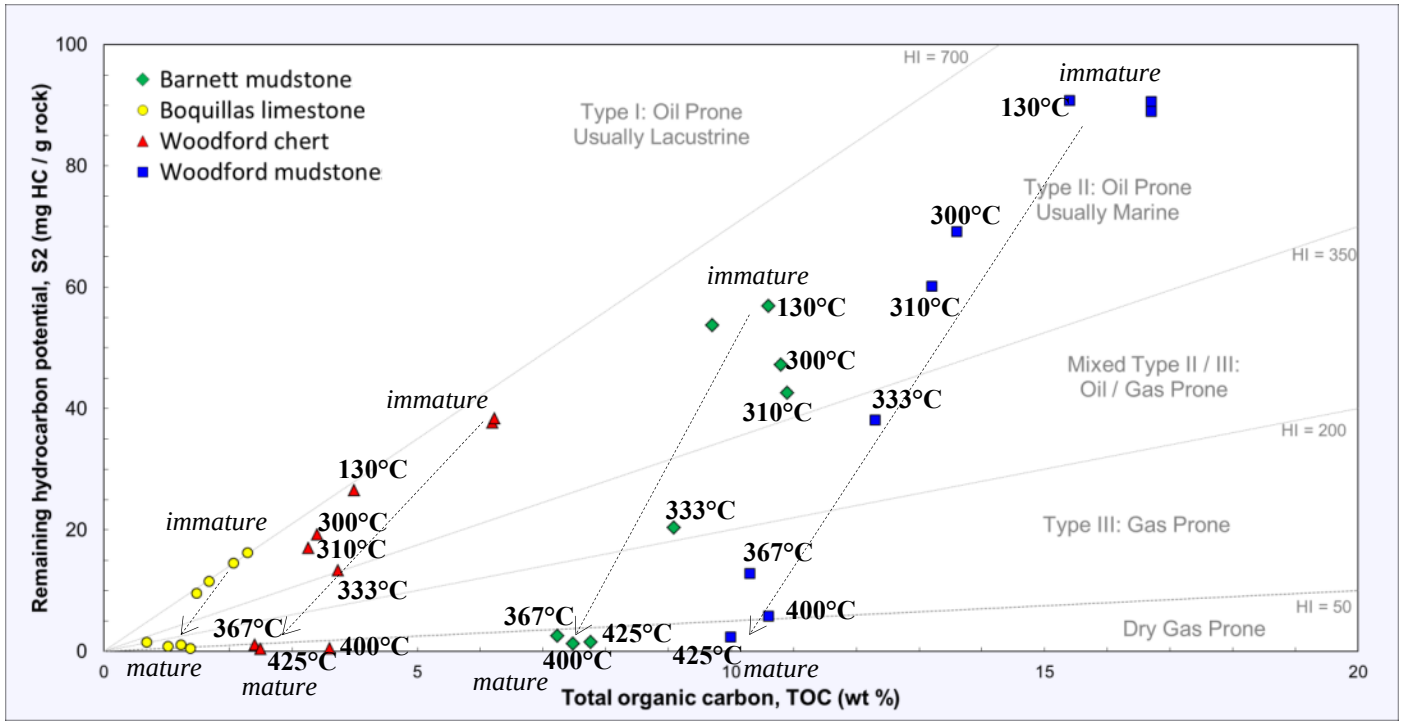

Figure 4.9: Plot of Rock-Eval S_2 versus TOC of the Barnett, Boquillas, and Woodford mudrock samples showing original types of OM (Type II marine source) and decreases in HI and TOC content in all samples with increased thermal maturation. Dash lines and arrows represent samples from immature to mature during gold tube pyrolysis (Ko et al., 2016).

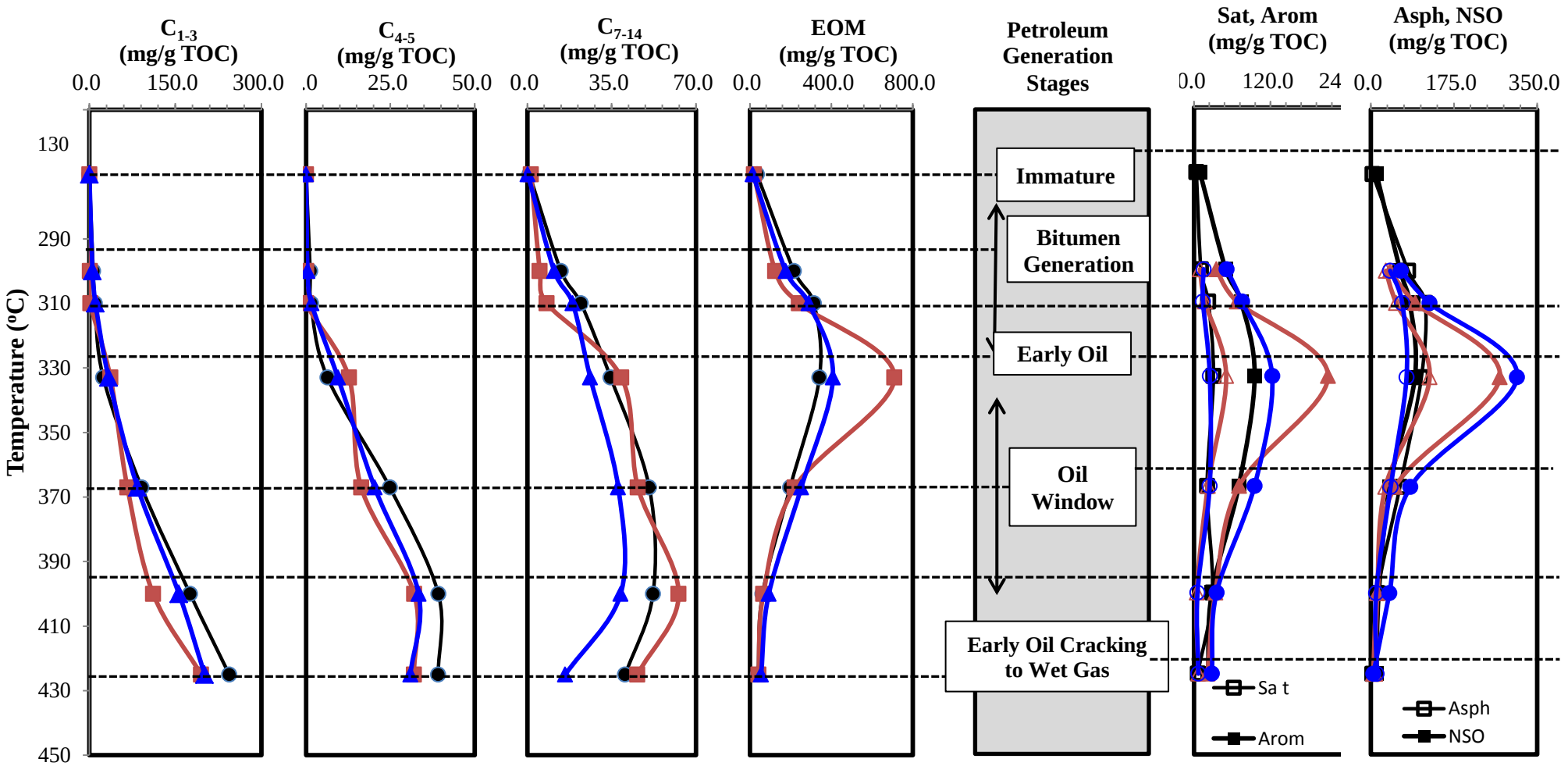
C1-3 (mg/g TOC)
0.0
150.0
300.0
C4-5 (mg/g TOC)
.0
25.0
50.0
C7-14 (mg/g TOC)
0.0
35.0
70.0
EOM (mg/g TOC)
0.0
400.0
800.0
Petroleum Generation Stages
Sat, Arom (mg/g TOC)
0.0
120.0
24
Asph, NSO (mg/g TOC)
0.0
175.0
350.0
Temperature (°C)
130
290
310
330
350
370
390
410
430
450
Immature
Bitumen Generation
Early Oil
Oil Window
Early Oil Cracking to Wet Gas
Sa t
Arom
Asph
NSO

Figure 4.10: Plots of experimental temperatures (130, 300, 310, 333, 367, 400, 425°C) against generated hydrocarbon components (gaseous and liquid petroleum). Five oil- and gas-generation stages are defined by trends from produced gas (C_1-C_3 and C_4-C_5), liquids (C_7-C_{14}, C_{14+}), EOM (bitumen), and SARA fractions. Black (Barnett siliceous mudstone), blue (Woodford siliceous mudstone), and red (Woodford chert) indicate phase abundance at different temperatures. sat: saturate (open squares); arom: aromatic (solid squares); NSO: nitrogen, sulfur, oxygen, and heavy metals (solid squares); asph: asphaltene (open squares).

Boquillas (Eagle Ford) sample exhibited similar trends; those of the Woodford chert and siliceous mudstone samples, however, did not (see Fig. 9 in Ko et al., 2016).

4.4.4 Original Pore Networks

4.4.4.1 Barnett Mudstone

The original pore network in the immature Barnett siliceous mudstone sample is associated with minerals especially clay minerals. The majority of these mineral pores are elongated intraparticle pores between clay-mineral platelets, commonly a few microns in length (Figure 4.11A). Interparticle pores are less abundant and relatively small, between minerals and OM (Figure 4.11B). Other less common intraparticle pores are associated with phosphatic peloids (Figure 4.11C). Other uncommon pores include intra-pyrite-framboid OM pores (Figure 4.11D), primary OM pores (Figure 4.11E), and convoluted OM pores (Figure 4.11F). The convoluted OM pores is related to the deformation of OM after compaction, between folded, twisted, or coiled kerogen that is clearly particulate (Ko et al., 2016). Pore classification and the definition of pore type as proposed by Loucks et al. (2012) and Ko et al. (2016, 2017) are used in this study.

4.4.4.2 Woodford Mudstone

The original pore network in the immature Woodford chert is predominantly composed of interparticle pores between quartz grains, between quartz and clay minerals (mainly illite), and intra-clay-platelet (intraparticle) pores. The original pore network in the immature Woodford siliceous mudstone sample is predominantly associated with intraparticle pores, especially from grain dissolution and clay mineral platelets (Figure

4.12A). Many intraparticle pores appear to be related to dolomite-rim dissolution (Figure 4.12B). Other pore types include convoluted OM pores associated with *Tasmanties* (Figure 4.12C) and primary (inherited) OM pores in kerogen (Figure 4.12D).

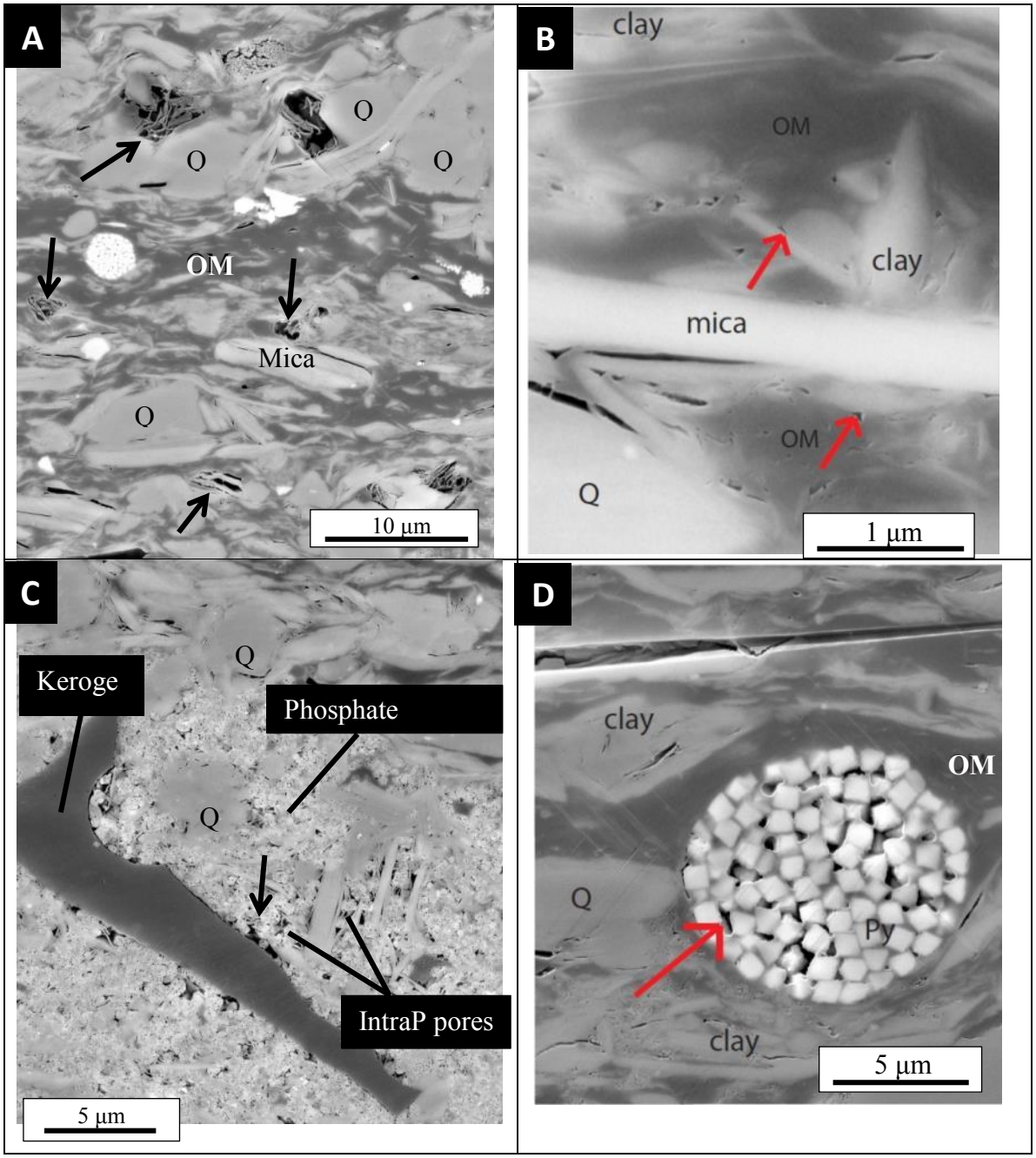

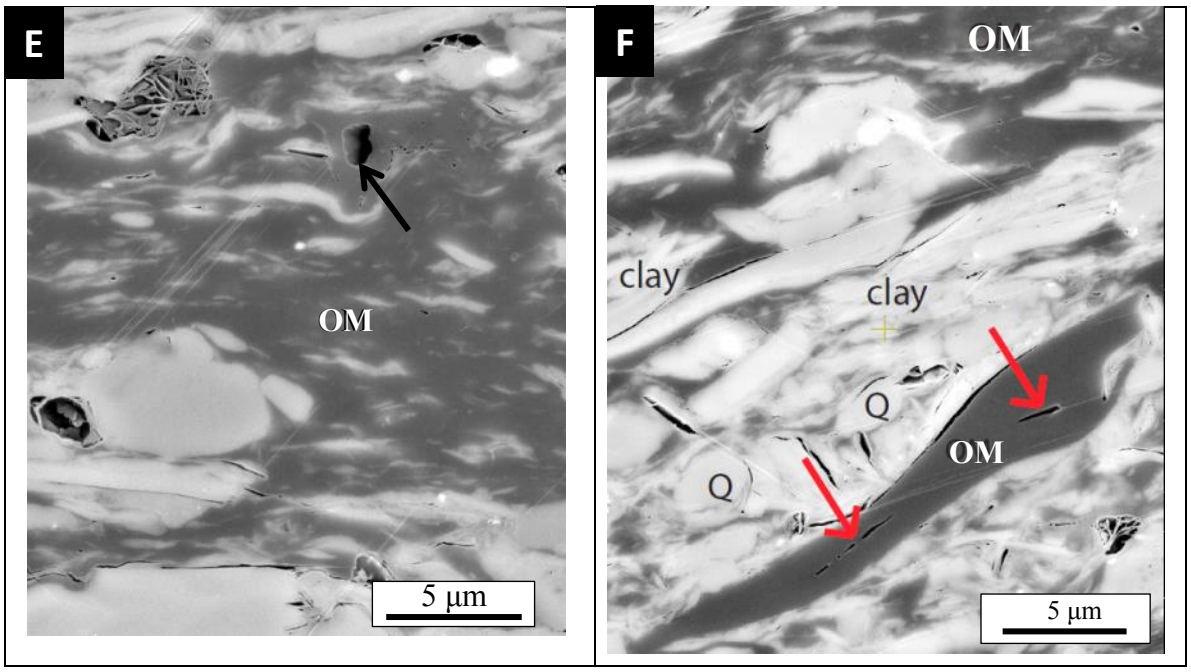

Figure 4.11: SEM images showing types of pores (arrows) in the immature Barnett mudstone. (A) intra clay-platelet pore (black arrow); (B) interparticle (interP) pore between organic matter and mineral grains (red arrows); (C) intra-apatite (intraP) pore (black arrow); (D) intra framboid pore (red arrow); (E) primary OM pore (black arrow); (F) convoluted OM pore (red arrows). Q: quartz; clay: clay minerals.

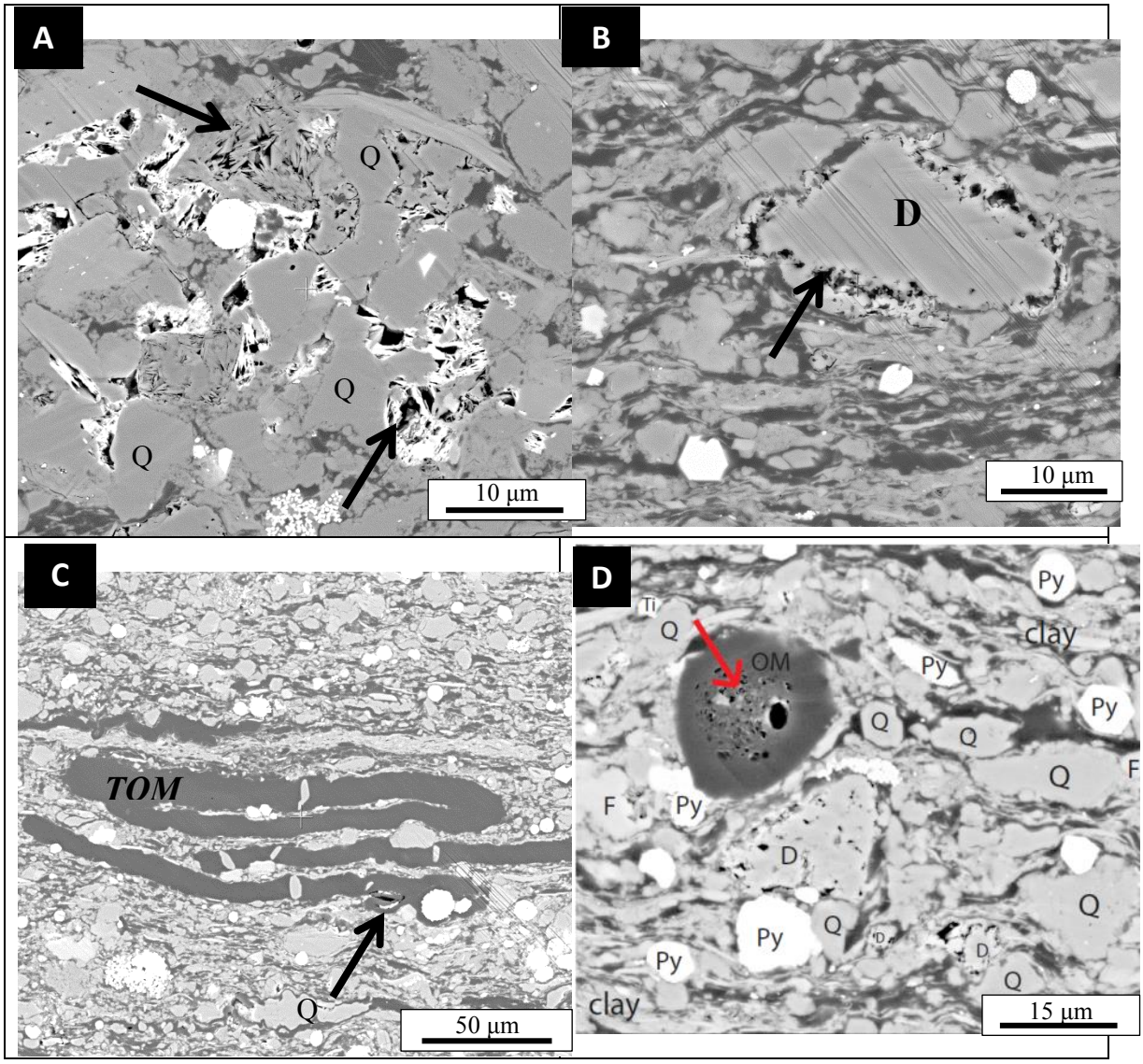

Figure 4.12: SEM images showing types of pores (arrows) in the immature Woodford mudstone. (A) intra-clay-mineral platelet pore; (B) intraparticle (intraP) pore from dolomite dissolution; (C) Convoluted OM pore; (D) primary OM pore. Q: quartz; F: feldspar; D: dolomite; Py: pyrite; clay: clay minerals; TOM: *Tasmanites* OM.

4.4.5 Pore and Pore Network Evolution

As with the previously studied Eagle Ford Group calcareous mudrock sample (Ko et al., 2016), Barnett and Woodford pores and pore networks also evolved with OM

conversion during thermal maturation. Migration of pre-oil solid bitumen into the original mineral pore network was observed as a result of the kerogen being transformed into petroleum (bitumen). The migration of pre-oil solid bitumen into the original mineral-pore network in the Barnett and Woodford samples implies that mineral pores were at least partly interconnected.

4.4.5.1 Barnett Mudstone

At the early bitumen generation stage (after 300°C/72 hrs of heating), bubble-shaped OM-hosted pores were common in the OM-mineral admixtures **(**AOM or bituminite) in the matrix (Figure 4.13A). A string of bubble OM pores was also developed in the pure OM (telalginite) (Figure 4.13B). Some shrinkage of kerogen was developed between interfaces of OM and minerals (Figure 4.13A). We believe the shrinkage pores were formed when the sample was quickly quenched as the experiment temperature was reduced to room temperature and those pores are unlikely to have been developed in the subsurface. At the peak bitumen generation stage (after 310°C/72 hrs of heating), the abundance and size of the OM bubble pores increased in telalginite, possibly related to the greater amount of bitumen generated (Figures 4.10 and 4.14). Most original interparticle and intraparticle mineral pores disappeared and became filled with petroleum (pre-oil solid bitumen) at 310°C/72 hrs of heating (Figure 4.14). Observed pre-oil solid bitumen migration into the phosphatic peloids implies that the phosphatic peloids have some interconnected pore network and act like a conduit for fluid movement

(Figure 4.15). No pores were found in the particulate OM under SEM (inertinite maceral).

At the beginning of the oil window (after 333°C/72 hrs of heating), the continuous conversion of relatively viscous bitumen to less viscous oil (rich in saturate and aromatic components) caused a significant volume loss resulting in the formation of void spaces and pore development, fluid migration, and post-oil solid bitumen and pyrobitumen precipitation. At the beginning of oil generation, the predominant pore types and pore network composed modified mineral pores containing relic OM (Figure 4.16). The modified mineral pores are resulted from generated, expelled, and migrated petroleum pervading original mineral pores (Ko et al., 2016). The relic OM can be residual oil or solid bitumen. These pores should originally be filled with petroleum. During post experimental and sample preparation processes under vacuum conditions, generated petroleum had migrated or the originally retained petroleum had escaped from the pore spaces. Some modified mineral pores are characterized by isopachous organic matter rims (Figure 4.16C, Ko et al., 2016). Their sizes and shapes are determined by the surrounding mineral framework grains. The particulate OM showed no evidence of pore development.

At the middle oil window stage (after 367°C/72 hrs of heating), the abundance of modified mineral pores was significantly increased because of continued organic matter conversion (Figure 4.17C). Spongy OM-hosted pores started to appear in both OM-mineral admixtures and pure organic matter patches (likely post-oil solid bitumen) (Figure 4.17A, D). The particulate OM still showed no evidence of pore development

(Figure 4.17B). At the stage of early oil cracking and into the wet gas (after 400 and 425°C/72 hrs of heating), the dominant pore types, modified mineral pores and OM spongy pores, were similar to those observed in the middle oil window although their abundances and volume are greater (Figure 4.18A, B). Little change in dominant pore types above 400°C/72 hrs of heating is supported by geochemical analyses (Figure 4.10), which showed no significant change in generated gas or liquid. Little or no pore development was observed in any particulate OM (inertinite maceral) under SEM throughout the experiment series. This implies that inertinite maceral (terrestrial kerogen) does not convert to petroleum, changing little or none during maturation into the wet gas window in this study, and therefore does not contribute much to total pore volume in the mudstone. Our experiments showed that kerogen and maceral particles show variable pore development, resulting in inhomogeneity of pore types, caused by differences in generation kinetics of maceral particles during thermal maturation.

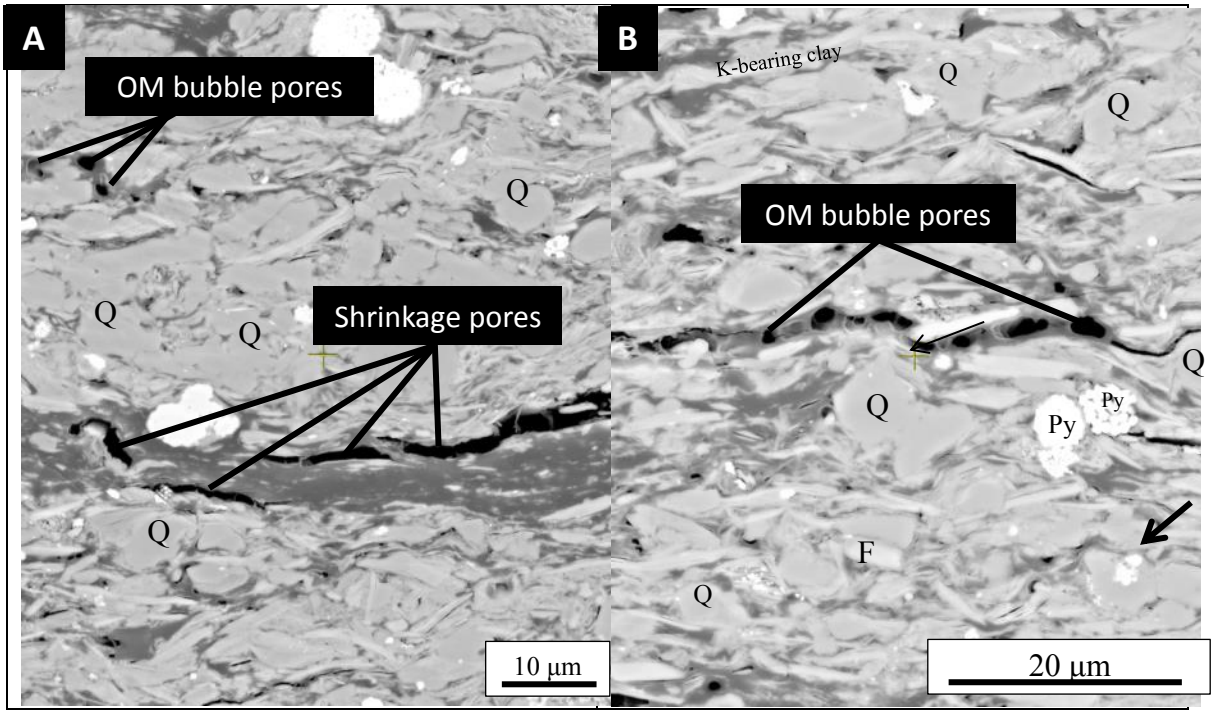

Figure 4.13: SEM images showing shrinkage pores and development of OM bubble pores in the Barnett mudrock sample at the early bitumen generation stage. (A) Shrinkage pores, which are experimental artifacts, developed at contact between elongated kerogen and mineral grains. OM bubble pores developed within dispersed and compacted organic matter. (B) OM bubble pores (black arrows) developed within pure organic matter (telalginite). F: feldspar; Q: quartz; Ph: phosphate; Py: pyrite; Ti: titanium oxide.

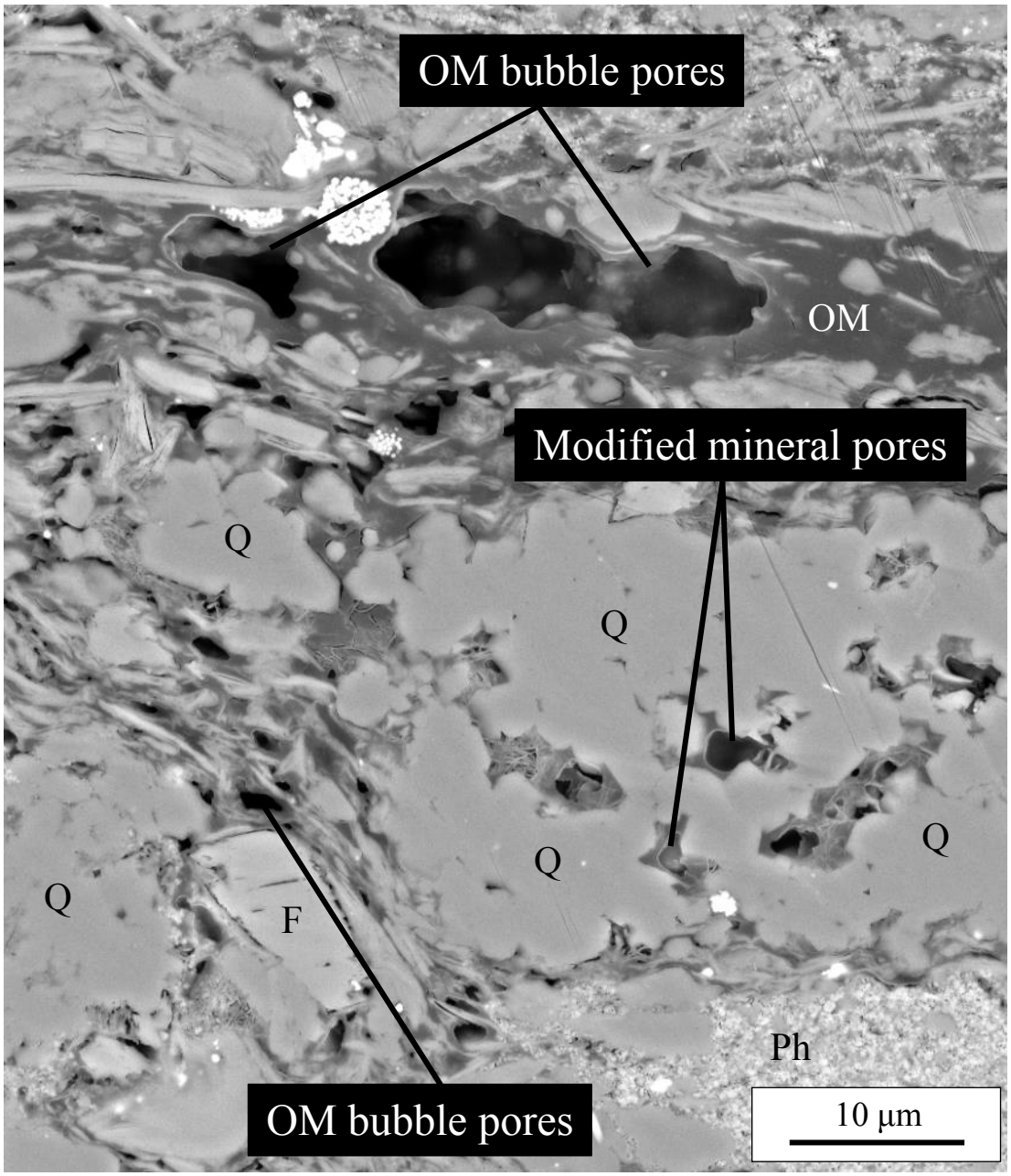

Figure 4.14: SEM image showing development of bubble OM pores in the AOM or bituminite in the Barnett siliceous mudstone sample because of volume loss at the peak bitumen generation stage. Migration of petroleum (pre-oil solid bitumen) into the surrounding primary mineral pores forming modified mineral pores with relic OM. The Barnett mudrock has abundant quartz cement, forming a rigid framework. Feldspar is slightly dissolved. F: feldspar; Q: quartz; Ph: phosphate.

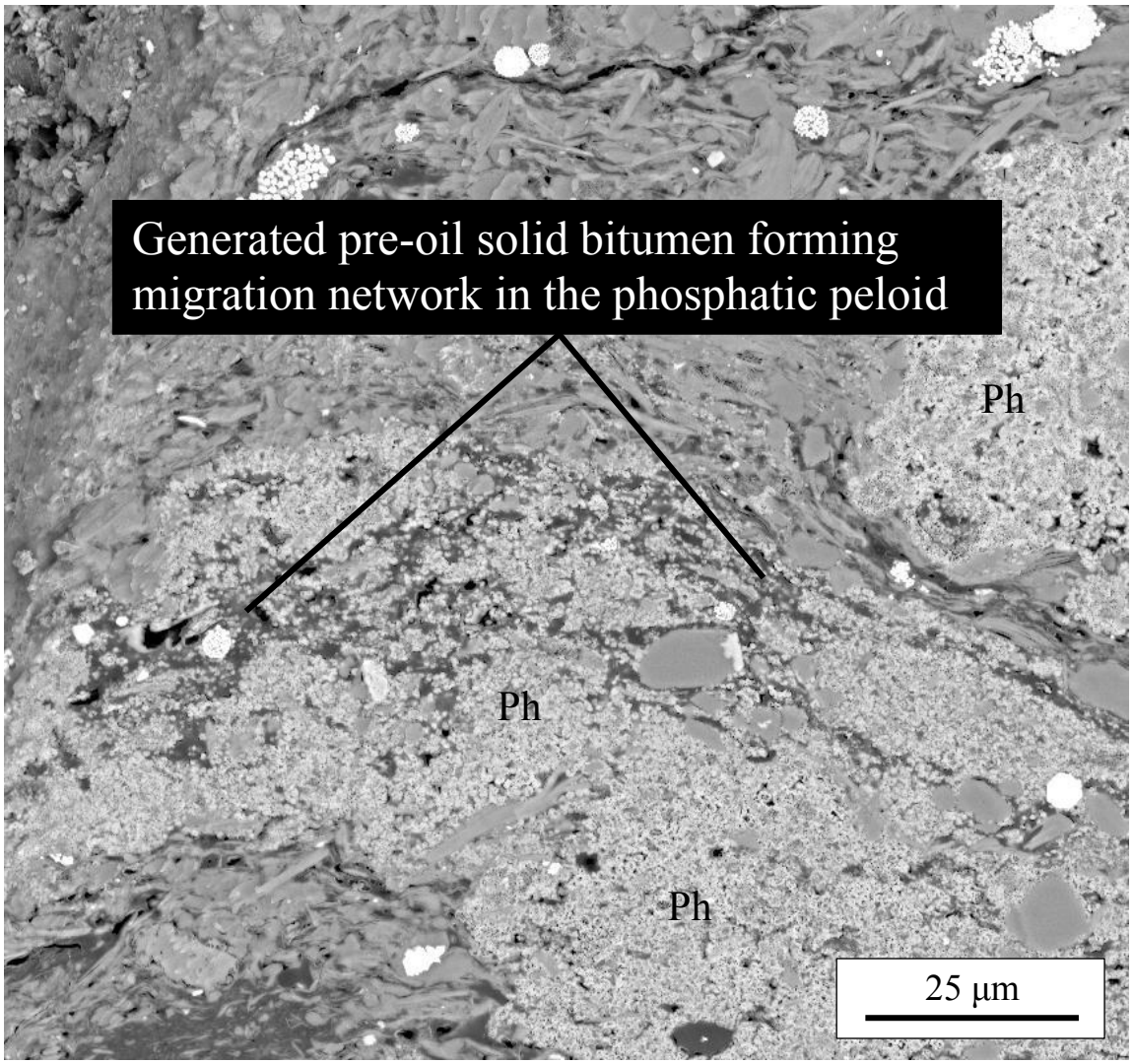

Figure 4.15: SEM image showing original intra-phosphate pore networks in the phosphatic peloid in the Barnett sample as possible migration pathways for generated petroleum (pre-oil solid bitumen) at the peak bitumen generation stage. Ph: phosphate.

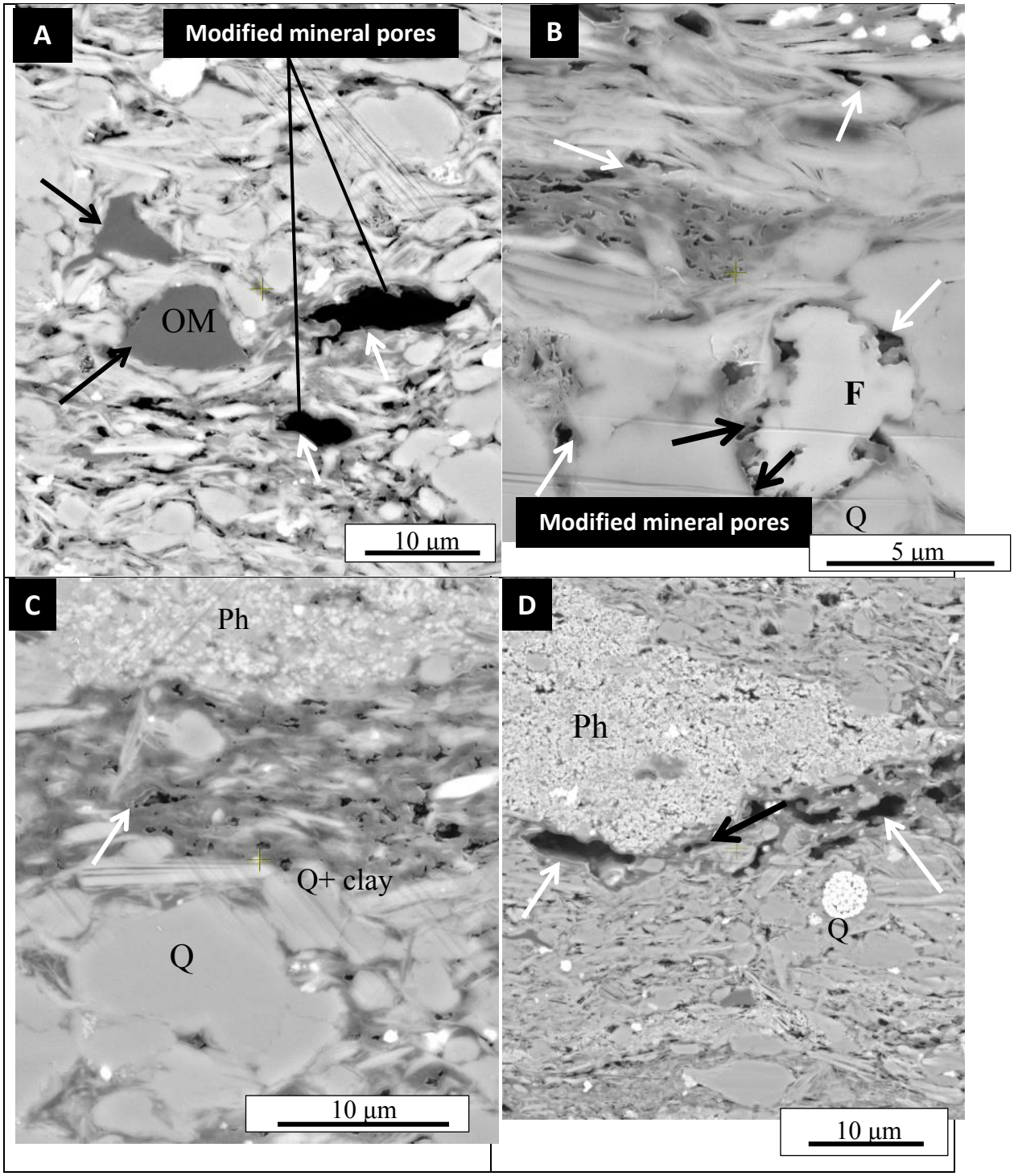
A
Modified mineral pores
OM
10 μm
B
F
Modified mineral pores
Q
5 μm
C
Ph
Q+ clay
Q
10 μm
D
Ph
Q
10 μm

Figure 4.16: SEM images showing modified mineral pores as dominant pore types in the Barnett sample at the beginning of the oil window. (A) Macerals with different conversion capability. Particulate macerals (black arrows: possibly inertinite) have little to no conversion capability. OM-mineral admixture (white arrows) has converted to petroleum and formed modified mineral pores; (B) Modified mineral pores within dissolved feldspar and between clay-mineral platelets; (C) Some OM-mineral admixture shows less conversion and develop fewer pores (white arrows); (D) Stringy/flaky OM shows significant conversion (white arrows), forming pores within the original maceral. Q: quartz; F: feldspar; Ph: phosphate.

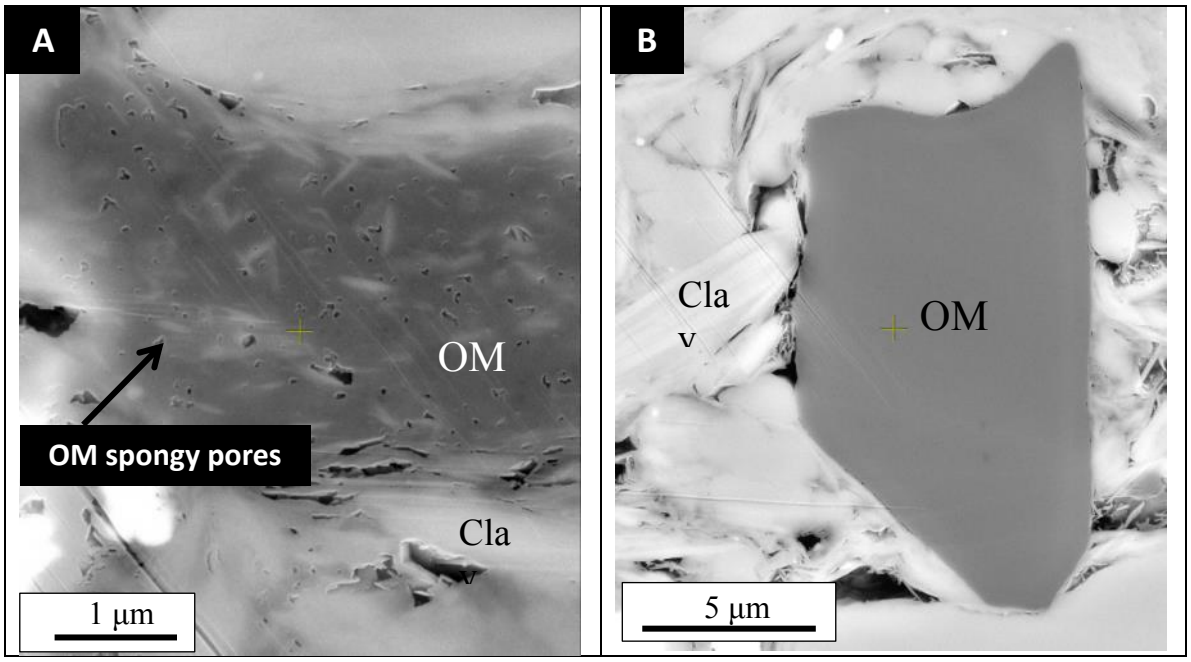

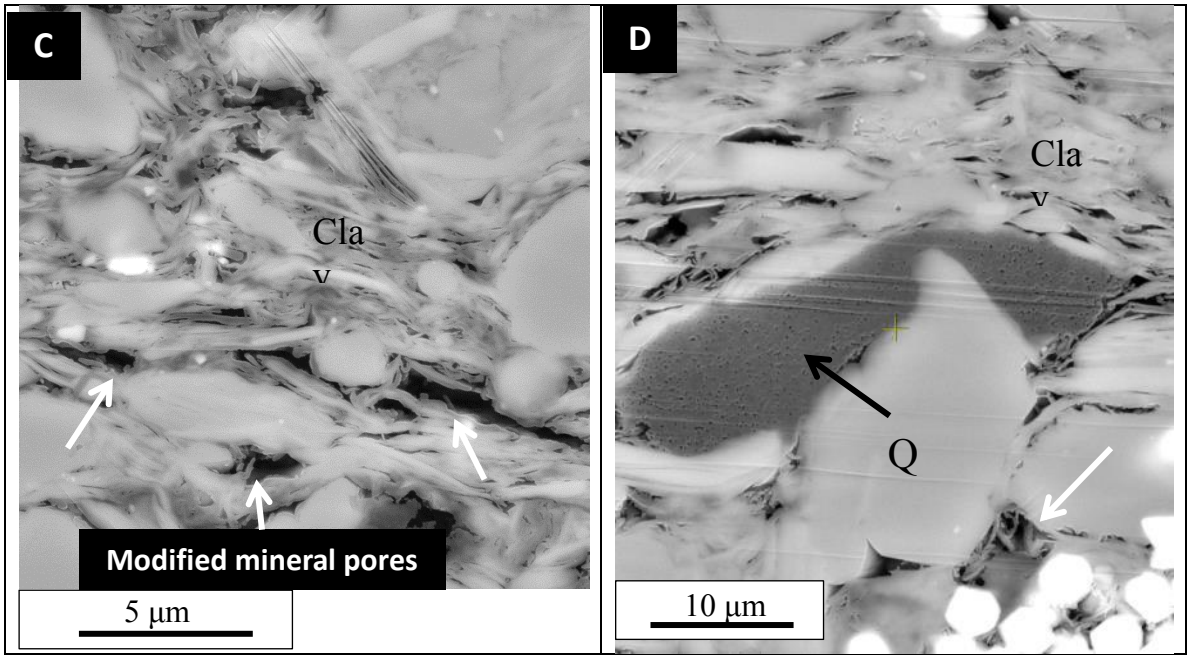

Figure 4.17: SEM images showing modified mineral pores (black arrows) and OM spongy pores (white arrows) as dominant pore types in the Barnett siliceous mudstone sample at the middle of the oil-window generation stage. (A) OM spongy pores in the OM-mineral admixtures. (B) Abundant modified mineral pores ranged from nanometers to micrometers in the groundmass of the Barnett mudrock. (C) Particulate OM with no visible pores. (D) OM spongy pores (black arrow) in pure OM. Q: quartz; Clay: clay minerals.

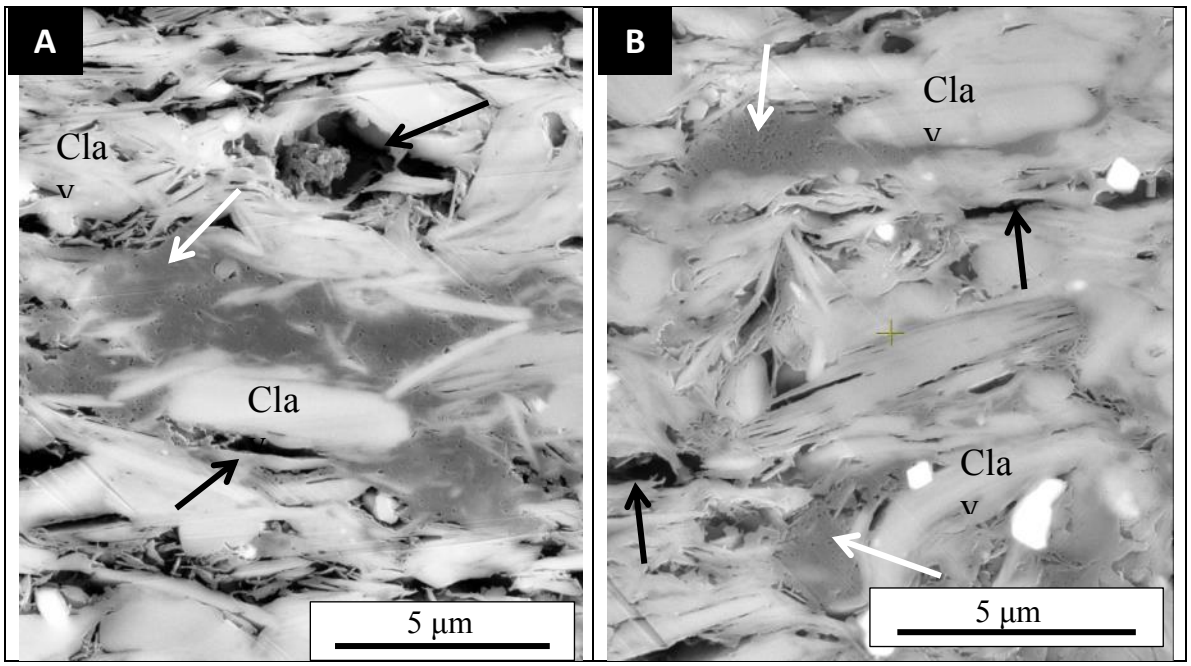

Figure 4.18: SEM images showing modified mineral pores (black arrows) and OM spongy pores (white arrows) in the Barnett samples as dominant pore types in the late oil window and the early wet gas window. Dominant pore types do not change and are similar to pores in the middle oil window. This is confirmed by the geochemical analyses in Fig. 9 which show that during these two stages, no significant change in generated gas and liquid is observed. Clay: clay minerals.

4.4.5.2 Woodford Mudstone

As with the Barnett mudstone, at the early bitumen generation stage (after 300°C/72 hours of heating), shrinkage was observed especially between *Tasmanites* and surrounding mineral grains (Figure 4.19). During the stage of main bitumen generation (310°C/72 hrs), a few OM bubble pores were formed in stringy, dispersed OM; however, OM bubble pores were not as abundant as those observed at this stage in the Barnett sample (Figure 4.20A). Simultaneously, migration of petroleum (pre-oil solid bitumen) into the original intraparticle mineral pores in the dissolved dolomite rim was observed.

Intriguingly, no pores were developed in *Tasmanites* OM (unicellular green algae) (Figure 4.20 B, D). The unchanged *Tasmanites* OM implies that even though from Rock-Eval analysis, bulk organic matter in the Woodford is mainly marine Type II as in the Barnett, the telalginite macerals in the two mudrocks have different geochemical characteristics and transformation rates and ratios during thermal maturation. Importantly, the variable transformation ratios of the two different telalginite macerals can significantly impact pore development and the amount of fluid generated. At the end of bitumen and early oil generation (after 333°C/72 hours of heating), *Tasmanites* OM was fully converted to mobile petroleum, leaving a large void space ranging from tens to hundreds micrometers (Figure 4.21). The dominant pore types in the Woodford siliceous mudstone are the modified mineral pores with relic OM (Figure 4.21). However, some petroleum is still present in matrix pores (Figure 4.21A). It could be that the petroleum that is still trapped within the mineral pores was too viscous to escape even under experimental vacuum conditions. At the middle oil window stage (after 367°C/72 hours of heating), the abundance of modified mineral pores had increased slightly. Much petroleum was still retained in the modified mineral pores (Figure 4.22A, C). It is not until the cracking of oil to the wet-gas stage (after 425°C/72 hrs of heating) that most fluids were entirely expelled, resulting in significant increase in the abundance and size of modified mineral pores (Figure 4.23). It is worth noticing that the OM spongy pores were uncommon and difficult to observe in the Woodford sample at the end of the oil window and at the cracking of early oil to the wet-gas stage.

minerals

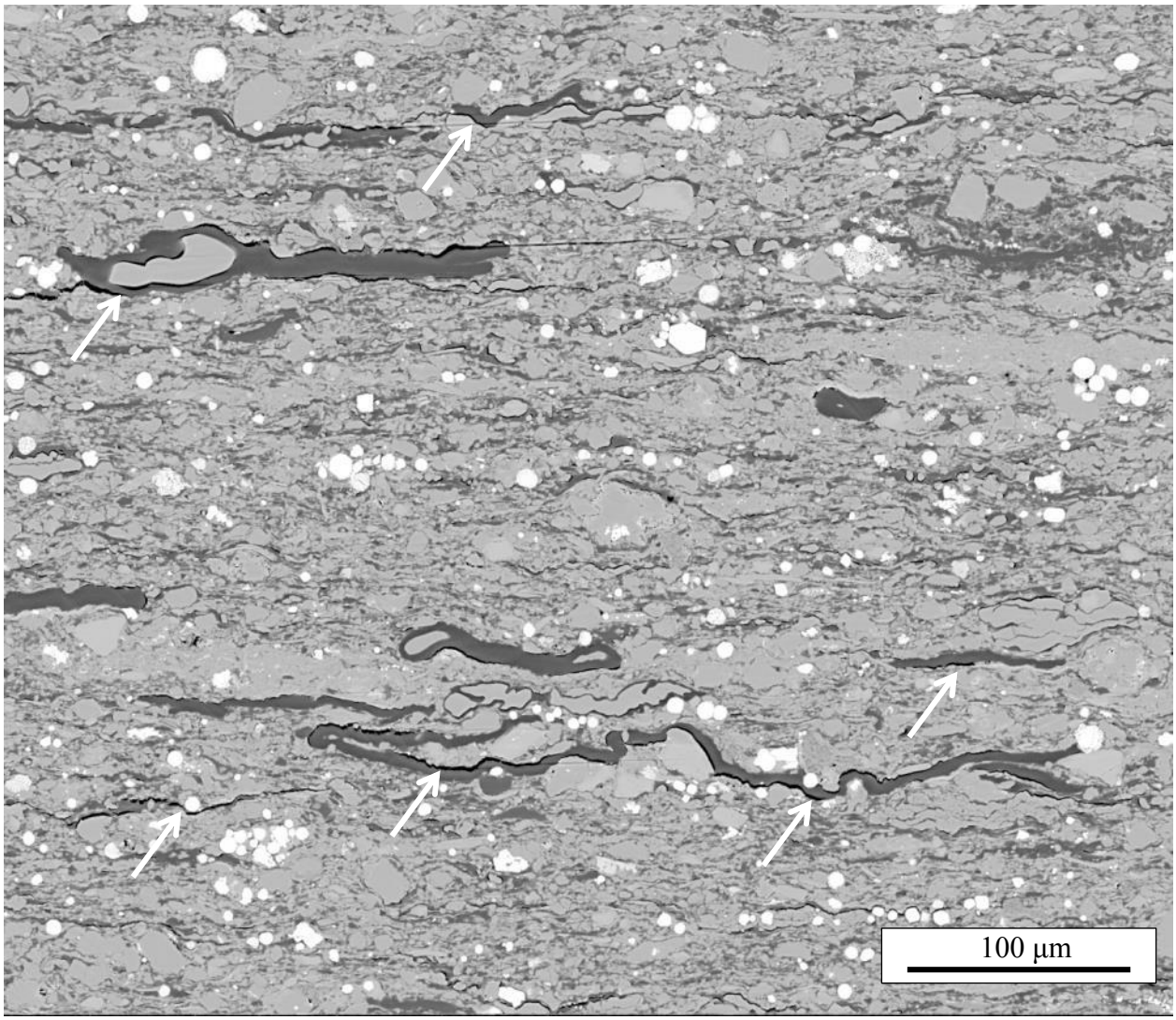

Figure 4.19: SEM image of the Woodford siliceous mudstone sample at early bitumen generation stage. Shrinkage pores (white arrows) are artifacts, between *Tasmanites* kerogen particles and minerals.

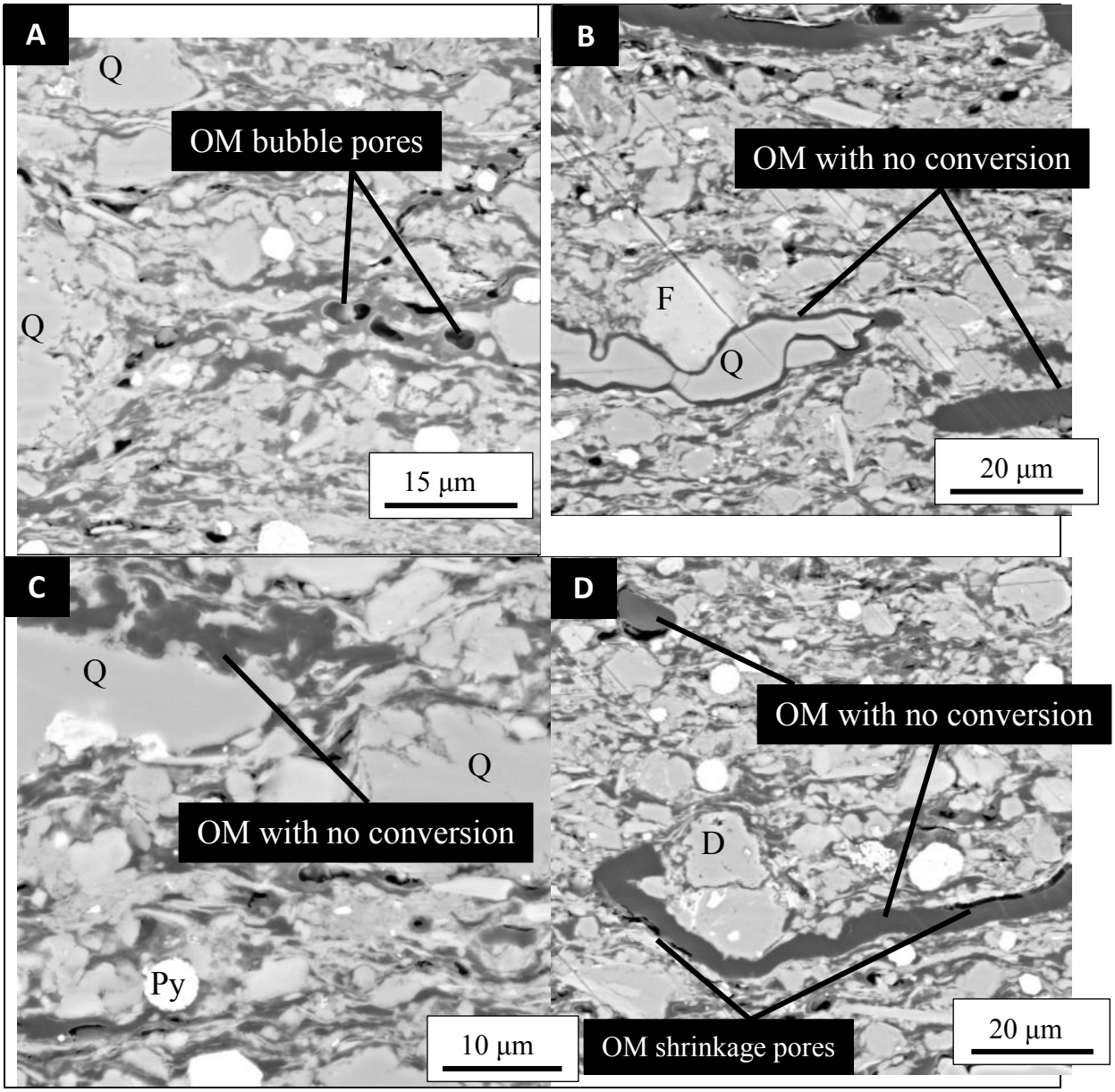

Figure 4.20: SEM images of the Woodford organic-rich siliceous mudstone sample at the bitumen generation stage. (A) Stringy,dispersed OM has gone through kerogen to bitumen conversion, forming bubble OM pores in the matrix. (B) *Tasmanites* are intact and have not gone through any conversion. Therefore, no pores were developed. (C) Unknown type of kerogen also has not gone through any conversion. (D) Both particulate OM and broken pieces of *Tasmanites* show no conversion. Some artifact shrinkage was observed. D: dolomite; F: feldspar; Py: pyrite; Q: quartz.

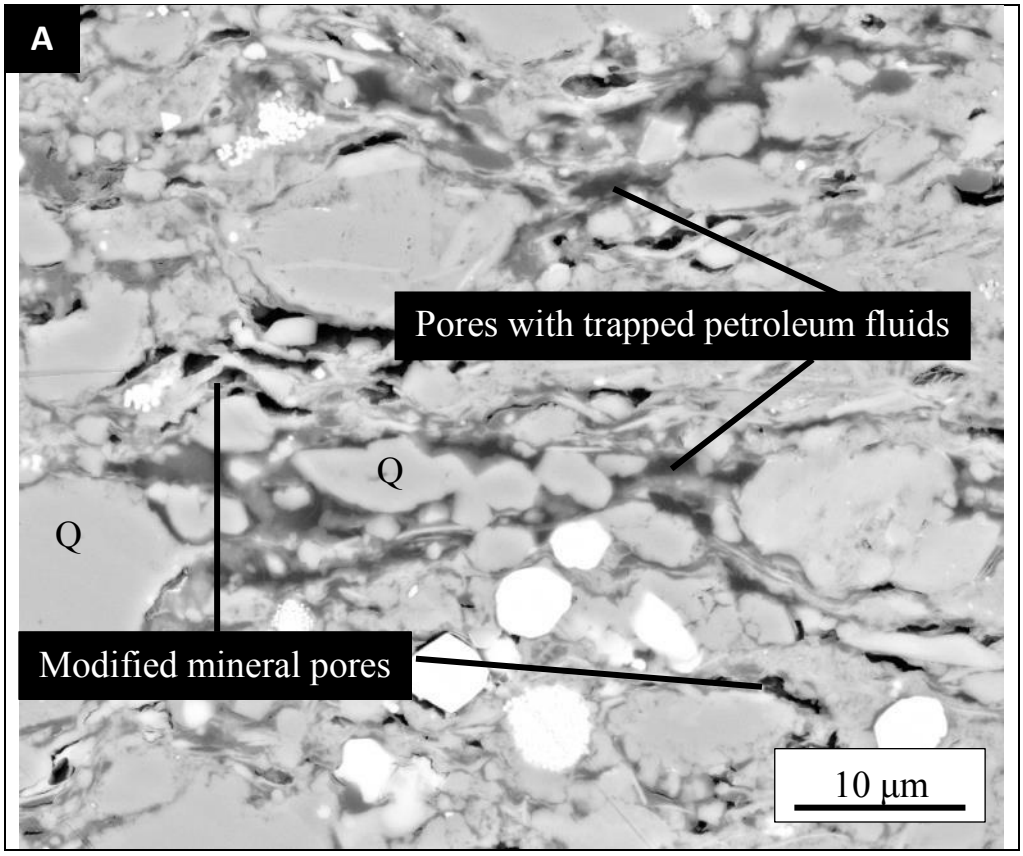
A
Pores with trapped petroleum fluids
Q
Q
Modified mineral pores
10 µm

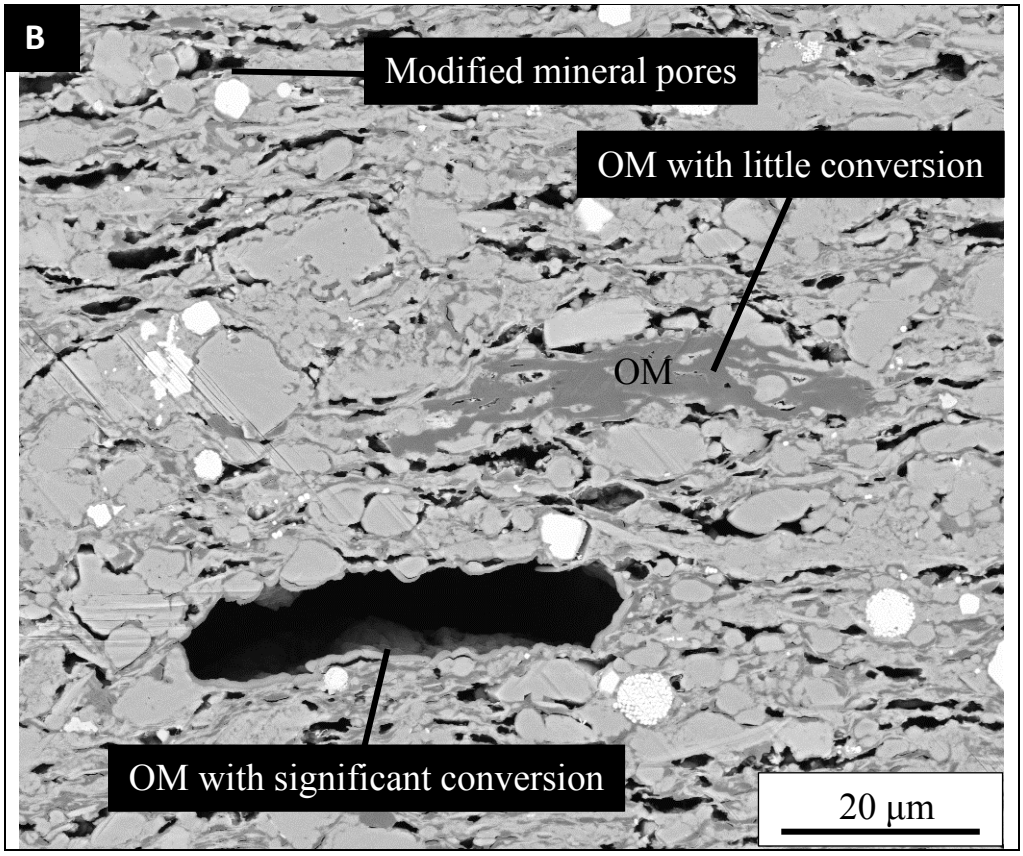

Figure 4.21: SEM images of the Woodford organic-rich siliceous mudstone sample at the end of bitumen and early oil generation stage. (A) Modified mineral pores (black arrows). (B) Differences in OM conversion and modified mineral pores. Q: quartz.

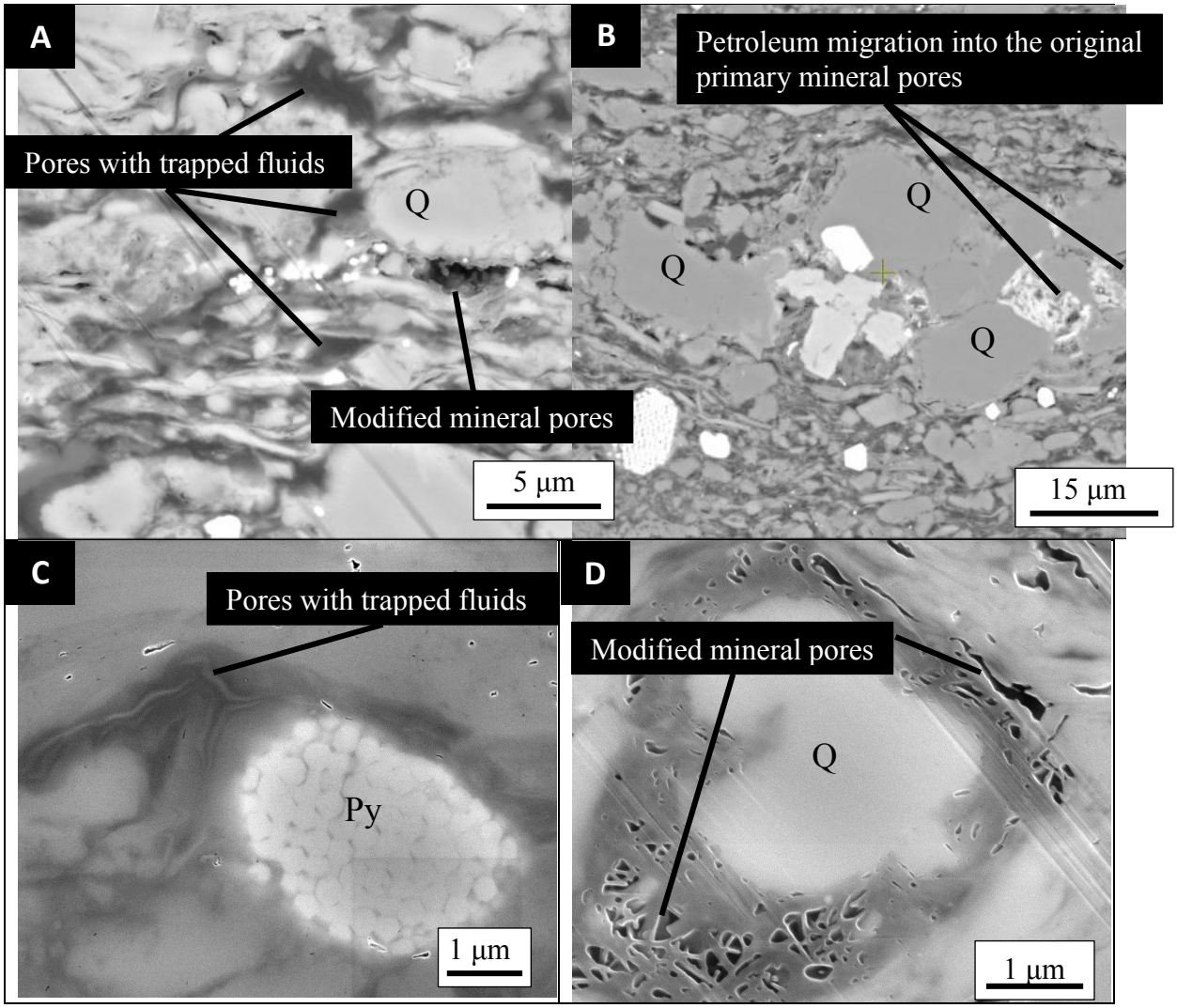

Figure 4.22: SEM images from the Woodford organic-rich siliceous mudstone sample in the oil window generation stage. (A) Most pore spaces are still filled with generated hydrocarbon fluids. Some fluids escaped during sample preparation processes, forming modified mineral pores with relic OM. (B) Evidence of petroleum (pre-oil bitumen) migration into the original mineral pores (Fig. 11A shows the original mineral pores). (C) Trapped HC fluids under SEM. (D) Modified intraparticle mineral pores in clay minerals. Q: quartz; Py: pyrite.

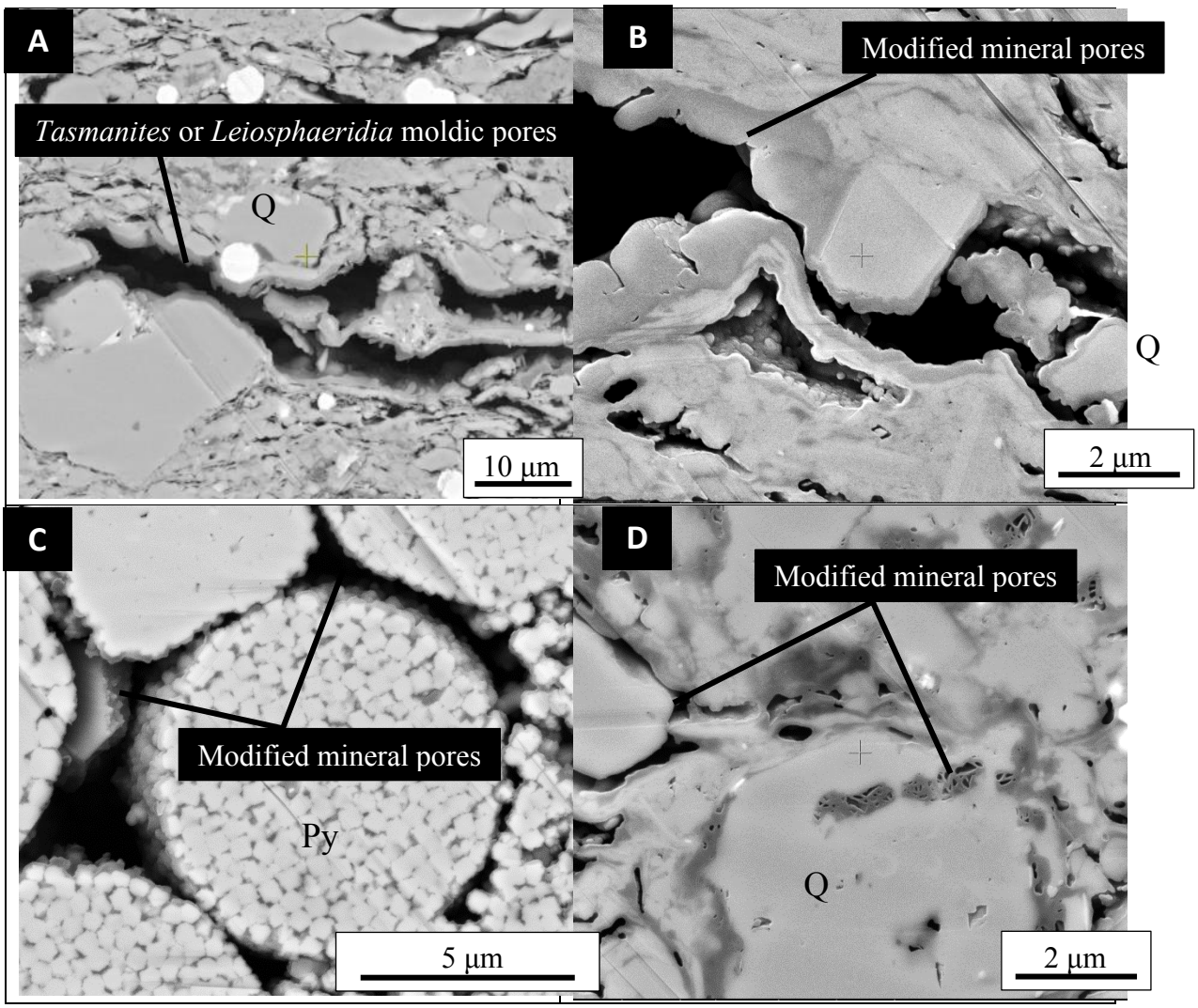

Figure 4.23: SEM images showing modified mineral pores as the most abundant pore types in the Woodford organic-rich siliceous mudstone sample at the end of the oil window and in the early wet gas generation stage. (A) *Tasmanites* or *Leiosphaeridia* moldic pores. (B) Original kerogen has gone through significant conversion and has become modified mineral pores. (C) Modified mineral pores between pyrite framboids. (D) Modified mineral pores between mineral grains and clay minerals. Q: quartz; Py: pyrite.

4.5 DISCUSSION

4.5.1 Effect of Organic-Matter Maceral Types on Pore Evolution

Many petrographic and geochemical schemes such as morphology, texture, maceral and palynomorph composition, and bulk geochemical composition can be used to classify organic matter type (Walters, 2007). In this study, we attempted to integrate SEM petrography with organic petrography based on observation and description of texture, mineral-mixing, and morphological characters made by organic petrologists. To further differentiate OM facies, "organic matter type, its source, and depositional environment" need to be taken into account (Tyson, 1995). The kerogen type classification (Type I, II, IIS, III, or IV) based on a pseudo-Van Krevelen diagram derived from hydrogen and oxygen indices is commonly used, representing bulk geochemical results. Petrographic study identifies individual components of OM (macerals) and can provide confirmation of bulk geochemical data and linkage between geochemical and sedimentological data. Using organic petrography can also separate assessment of OM source, mixing, preservation, and maturation. This study reflects the under-appreciation of applying organic petrography to the study of maceral and palynomorph assemblages for OM facies identification and their associated pore evolution in mudstones.

Algae such as *Gloeocapsomorpha* (thought to be either a cyanobacterium or related to *Botryococcus*; Derenne et al., 1992, Fowler et al., 2004), *Botryococcus* (green microalgae, Derenne et al., 1992) and *Tasmanites* (Revill et al., 1994) have unusual lipid biochemistry (high hydrogen content) and are commonly found in organic-rich

mudstones (Volkman et al., 2015). Although they live and are commonly deposited in marine settings, these algae have relatively high hydrogen content, aliphatic molecules, and are geochemically more similar to Type I than Type II kerogen (see Walters, 2007, Figure 7). Depending on the amount, type, and mixing of these algae in marine mudstones, it is difficult to identify their occurrence by using only the bulk geochemical analysis. Therefore, applying organic petrography to identify their existence and occurrence is a necessary step in order to accurately predict the amount of petroleum generated and associated pore-evolution model. Petrography analysis, like any other type of method, has its limitation as well; for example, it cannot be done after the samples have matured through the peak oil window as the telalginite maceral converts to petroleum.

The differences observed in pore evolution in the Barnett and Woodford siliceous mudstone samples through laboratory pyrolysis simulation in fact correspond to one of the key differences between marine (Type II) and lacustrine (Type I) source rock, relating to petroleum generation kinetics (Katz and Lin, 2014). The activation energy distribution between marine and lacustrine kerogen is different, with lacustrine (Type I) source rocks having a much narrower distribution of activation energy than marine (Type II) source rocks (Tissot et al., 1987; Sundararaman et al., 1988; Pepper and Corvi, 1995). The narrow activation energy distribution of Type I kerogen means that the main stage of petroleum generation from Type I kerogen is short (Katz and Lin, 2014). Another important aspect of activation energy distribution is that in general, the mean activation

energy of Type I kerogen is higher than Type II kerogen, requiring a higher level of thermal maturity to generate petroleum (Katz and Lin, 2014).

Pore evolution in *Tasmanites* OM matches exactly with these two pronounced differences in OM conversion and petroleum generation of Type I kerogen — pores developed from *Tasmanites* OM formed later in the oil window and developed much more quickly than in the Barnett and Eagle Ford mudstones. No pore was ever observed in the *Tasmanites* before in the literature. The *Tasmanites* has no pores at all from immature to bitumen maturation stage, and then it converts almost completely to petroleum leaving a void where it was at the beginning of the oil window maturation. Although the OM in the Woodford has a Type I geochemical signature, these OM are clearly marine facies. Abundant marine-derived bituminite or AOM is also observed in the Woodford mudrock. Sources of these bituminite or AOM can be marine snow (organic-mineral aggregates), fecal pellets, and microbial mats (cyanobacteria and thiobacteria) (Tyson, 1995).

Mastalerz et al. (2012) stated that "the relative proportions of individual macerals can significantly impact the geochemical characteristics of the organic matter." We found that pore evolution and pore heterogeneity in mudrocks are affected by mixing of different maceral types and their resulted geochemical properties as well. The stringy/flaky OM (AOM or bituminite) in the Barnett sample had better conversion potential than the OM-mineral admixtures (AOM or bituminite). The differences in OM conversion can be related to different preservation state of AOM (or bituminite) and the character of the mineral mixing from which it is liberated (Tyson, 1995). If the AOM (or

bituminite) has abundant mineral mixing or is degraded, it becomes increasingly heterogeneous and dull when viewed under fluorescence (Tyson, 1995). As a result, the conversion is not as good as the AOM with less mineral mixing and degradation. The conversion of inertinite, AOM, and *Tasmanites* in the Woodford were different. As previously discussed, the transformation of *Tasmanites* organic matter to petroleum did not occur until early oil maturation window, where it occurred almost instantaneously, undergoing complete transformation to petroleum without development of internal pores and leaving only void space. The particulate and less compacted OM (inertinite) shows no pore development as viewed in the SEM. Other techniques such as higher-resolution transmitted electron microscopy (TEM) or atomic force microscopy (AFM) instruments are required to further validate this observation.

4.5.2 Effect of Mineralogy and TOC on Pore Development

Although the Barnett and Woodford "siliceous" mudstones have different mineralogy than the Eagle Ford "calcareous" mudstones (Pommer and Milliken, 2015; Ko et al., 2016), we did not find that mineralogy has a significant effect on pore evolution. Even though the Barnett (25 to 40% clay minerals: illite, interlayered I/S, chlorite, and kaolinite) and Woodford (20 to 35% clay minerals: illite and kaolinite) have higher clay mineral content than the Eagle Ford limestone (< 5%: kaolinite and chlorite) and Eagle Ford marl (8 to 22% clay minerals: illite, interlayered I/S, chlorite, and kaolinite), the abundance and type of clay mineral does not seem to show any significant catalytic or sorption effect on generated petroleum and thus pore evolution. This might be

related to the relatively low smectite content in these three major mudrock units. We expect to see differences in fluid retention and pore development in mudrocks with high smectite content (e.g., Hetényi, 1995; Lewan et al., 2014).

The Woodford siliceous mudstone sample has the highest TOC content among our samples and is characterized by its abundant fluorescent *Leiosphaeridia* and *Tasmanites* macerals that requires relatively high levels of thermal maturity to convert. This may explain the delay of pore development and the significant retention of petroleum in the pore network during the entire oil window maturation stage, causing generated HC fluids to be trapped longer in the pore spaces than in the Barnett and Eagle Ford samples (Figures 4.21A and 4.22). Results from our experimental study imply that the relatively high TOC content (with delayed OM conversion in the *Leiosphaeridia* and *Tasmanites*) promotes hydrocarbon fluids to be retained longer in the pore spaces of the rock.

4.5.3 Pore-Connectivity Implications

Migration of petroleum (pre-oil solid bitumen) into the initial primary mineral pore network was observed in both Barnett and Woodford mudrock samples. When the Barnett samples reached bitumen generation, the majority of the primary intra-clay mineral platelets were filled with OM (Figure 4.14). Also, the pre-oil solid bitumen network was observed within some phosphatic peloids (Figure 4.15). The initial mineral pore network of the Woodford mudstone is predominantly composed of intraparticle pores from dissolution of dolomite and feldspar and within clay- mineral platelets. As

with the Barnett, these mineral pores later disappeared and were replaced by migrated petroleum (Figure 4.22B). The migration of petroleum implies that the pores (not only interparticle but also intraparticle) are at least partially interconnected in these mudrocks during thermal maturation and petroleum generation from bitumen to wet gas stages. Therefore, it is likely that the modified mineral pores form an effective pore network, especially when the amount of post-oil solid bitumen (or pyrobitumen) is minor. Cardott et al. (2015) and Wood et al. (2015) suggested that the connected pore network formed by post-oil solid bitumen (pyrobitumen) precipitation was indicative of primary migration pathways. We think a pyrobitumen network is most likely formed towards the end of oil window, wet gas and condensate, and dry gas window stages of thermal maturity but not likely in the immature and bitumen generation stages, forming a connected primary migration pathway.

4.5.4 Comparison of Pore-Evolution Models

Both the Barnett and Woodford siliceous mudstones in this study were deposited in a deep-marine environment (Cardott and Chaplin, 1993; Loucks and Ruppel, 2007), and based on organic petrography and Rock-Eval data, they both contain predominantly marine Type II kerogen with minor terrestrial Type III kerogen. Under similar temperature and pressure conditions (thermal maturation), the evolution of OM pores in the Barnett and Woodford mudstones should be similar; however they are not. Figures 4.24 and 4.25 present general pore- evolution models for the Barnett and Woodford mudstones, respectively. The pore evolution history observed for the Barnett is similar to

Barnett siliceous mudstone facies

(I) Immature

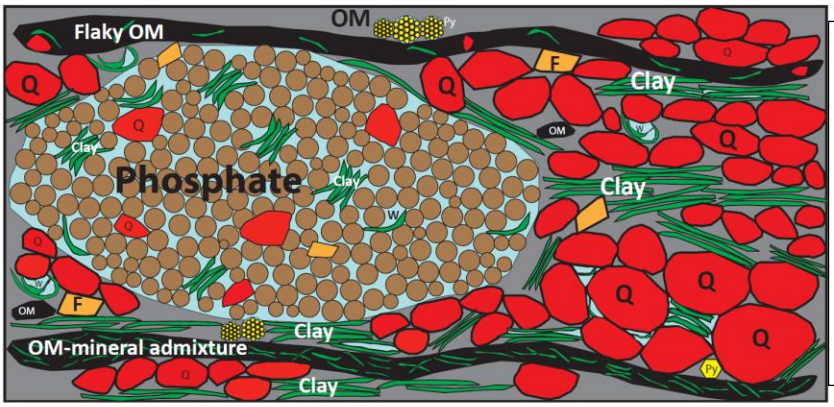

Original pore network (light blue) in the immature Barnett mudstone is predominantly composed of intraparticle pores between clay-mineral platelet, and within phosphate peloids

(II) Peak bitumen

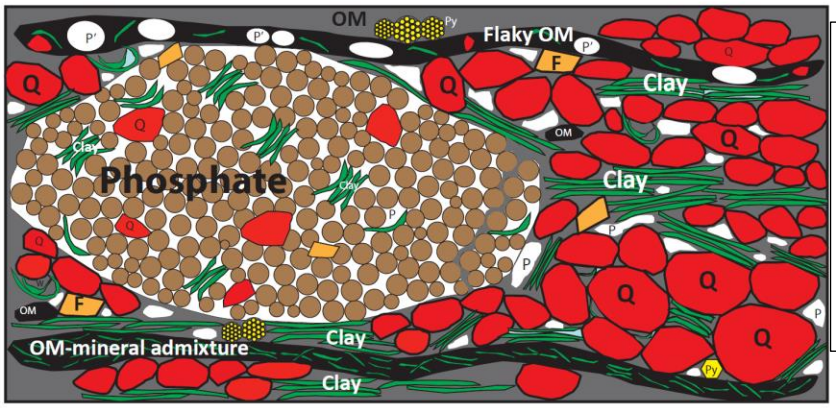

Bubble-shaped pores (white) started to develop in the stringy/flaky OM and in the matrix OM, both are bituminite (or AOM). Migrated pre-oil solid bitumen was observed within phosphate peloids.

(III) Early oil

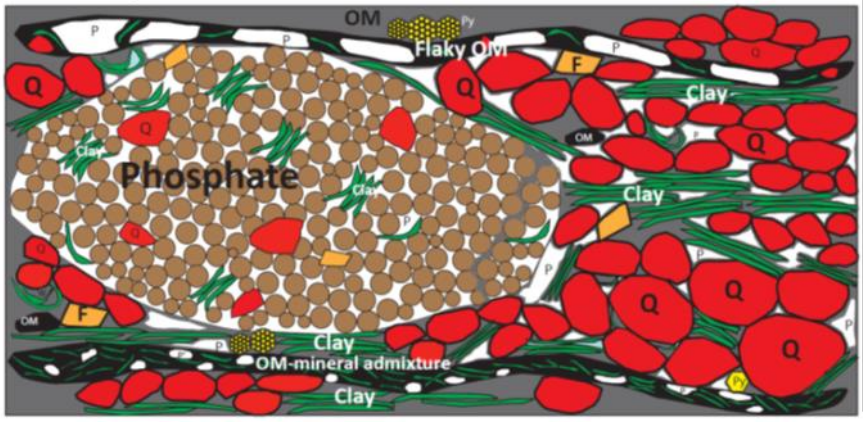

Pores (white) continued to develop in the stringy/flaky OM and in the matrix OM, both are bituminite (or AOM). Stringy/flaky OM (upper) shows more OM pore development than OM-mineral admixture (lower).

(IV) Oil window

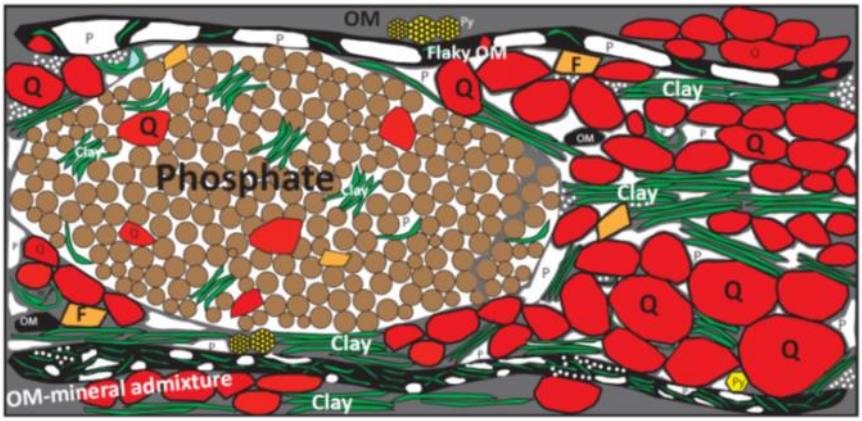

Pores (white) continued to develop in the stringy/flaky OM, OM-mineral admixture and in the matrix OM, all are bituminite (or AOM). OM-hosted spongy pores were developed in the matrix OM, bituminite (or AOM).

(V) Early cracking of oil to wet gas

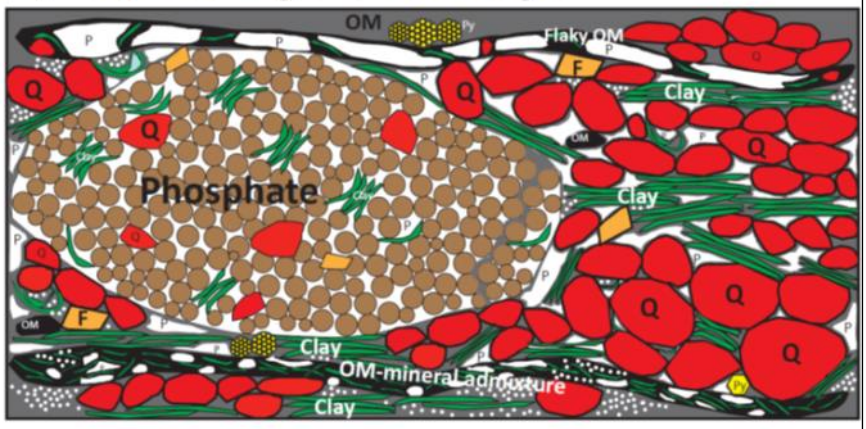

Pores (white) continued to develop in the stringy/flaky OM, OM-mineral admixture and in the matrix OM, all are bituminite (or AOM). The abundance of OM-hosted spongy pores increased in the matrix OM and within OM-mineral admixture, both are bituminite (or AOM).

Figure 4.24: A generalized model for the formation and evolution of OM and mineral pores observed in the Barnett siliceous mudstone facies sample. (I) Immature: the mudstone is significantly compacted and composed of much ductile organic matter and clay mineral. Pores are filled with connate water. The primary pore network consists of mostly intraparticle and a few interparticle pores. (II) Peak bitumen: stringy/flaky OM and the OM in the matrix have gradually converted to pre-oil bitumen, creating pore spaces (OM-hosted bubble-shaped pores). Bitumen migration (in phosphate peloid: black arrows) is observed. (III) Early oil: More conversion of kerogen to pre-oil bitumen and some conversion of pre-oil bitumen to oil occurred, creating more pore spaces. Some pores are hosted by minerals (modified mineral pores with relic OM) and some are hosted by OM (OM-hosted bubble pores). (IV) Oil window: most pre-oil bitumen has converted to hydrocarbons. Some nanometer-sized OM-hosted spongy pores began to appear in the post-oil solid bitumen or pyrobitumen. Most pores are hosted by minerals (modified mineral pores with relic OM). (V) Early cracking of oil to wet gas: Similar to stage (IV) but with increased amount of OM-hosted spongy pores. Clay: clay minerals (green); F: feldspar (orange); P: modified mineral pores (white); P': bubble pores (white); Q: quartz (red); W: water (blue); distinct kerogen piece (black); amorphous kerogen (grey).

Woodford siliceous mudstone

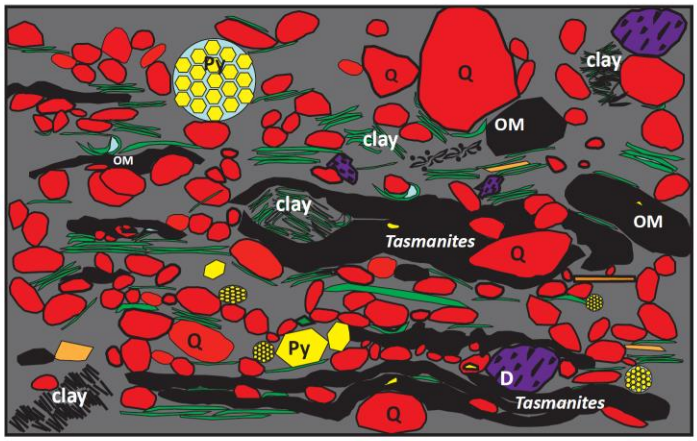

(I) Immature
130°C/72 hours

Original pore network (light blue) in the immature Woodford mudstone is predominantly composed of intraparticle pores between clay-mineral platelet, from dissolution of dolomite rims, and within pyrite framboids

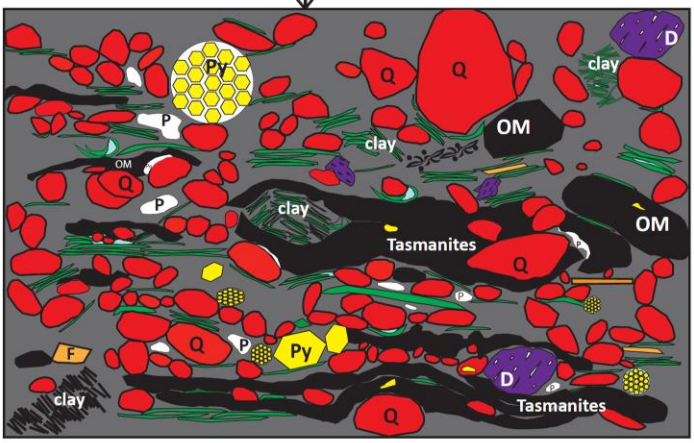

(II) Early bitumen
300°C/72 hours

Bubble-shaped pores (white) started to develop in the matrix OM, bituminite (or AOM). Some of the original intraparticle pores are filled with migrated pre-oil solid bitumen.

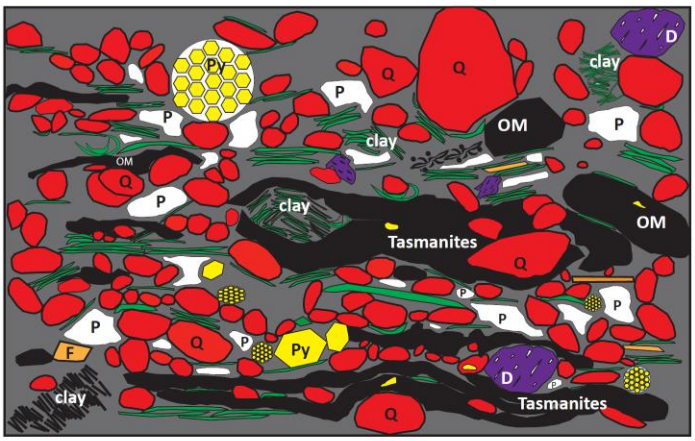

(III) Peak bitumen
310°C/72 hours

Increasing numbers of OM bubble pores were developed in the matrix OM, bituminite (or AOM). Increasing amount of original intraparticle pores are filled with migrated pre-oil solid bitumen.

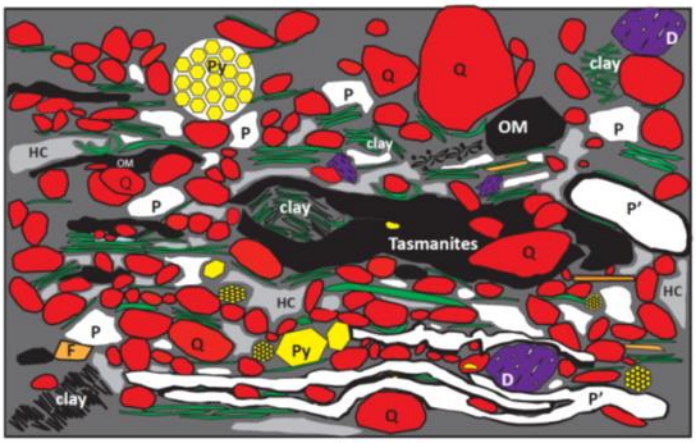

(IV) Early oil
333°C/72 hours

Leiosphaeridia and *Tasmanites* started to transfer to petroleum, leaving large moldic pores (white). This implies that the transformation from kerogen to petroleum in these telalginite particles is exceptional (more than 50%). Pores were developed in bituminite (or AOM) but some were still filled with petroleum (light grey)

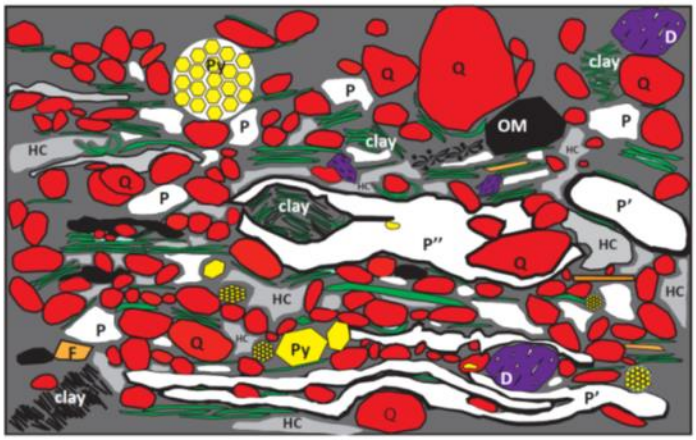

(V) Oil window
367°C/72 hours

Leiosphaeridia and *Tasmanites* continued to transfer to petroleum, leaving large moldic pores (white). At this stage, the majority of *Leiosphaeridia* and *Tasmanites have been fully converted. Many* pores in bituminite (or AOM) were filled with petroleum (light grey)

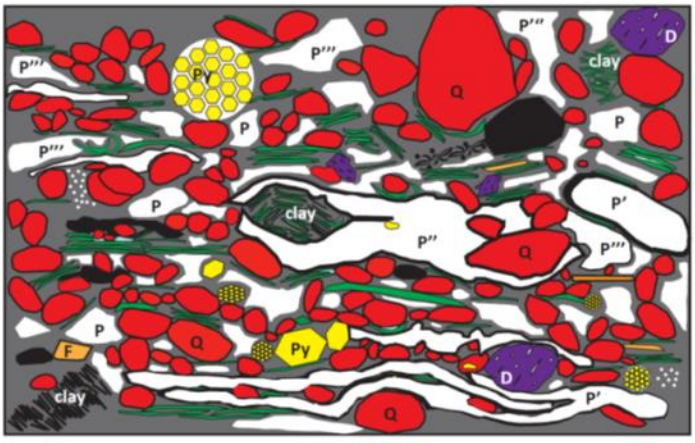

(VI) Cracking of oil to wet gas
425°C/72 hours

Pores in bituminite (or AOM) were no longer with petroleum. Some spongy-shape pores were developed in the matrix OM, bituminite (or AOM).

Figure 4.25: A generalized model for the formation and evolution of OM and mineral pores observed in the Woodford siliceous mudstone. (I) Immature: the mudstone is significantly compacted because it contains much ductile materials like organic matter and clay minerals. Pores are filled with connate water. The primary pore network consists of mostly intraparticle pores. Few interparticle pores. (II) Early bitumen: few OM in the matrix has gradually converted to pre-oil bitumen, creating some pore spaces (OM-hosted bubble-shaped pores). (III) Peak bitumen: A few OM in the matrix has gradually converted to pre-oil bitumen, creating pore spaces (OM-hosted bubble pores and modified mineral pores). (IV) Early oil: Some *Leiosphaeridia* and *Tasmanites* (telalginite) started to convert to hydrocarbon. More pores were developed in the matrix, and some were filled with HCs. (V) Oil window: Fully conversion of *Leiosphaeridia* and *Tasmanites* (telalginite) OM to HCs, creating abundant pore spaces. There are still much HCs retained in the pores. (VI) Early cracking of oil to wet gas: Most HCs in the matrix were expelled, leaving abundant pores. Clay: clay minerals (green); D: dolomite (purple); P: pores (white); Q: quartz (red); W: water (blue); trapped fluid (HC: light grey); distinct kerogen piece (black); amorphous kerogen (grey).

that reported by Ko et al. (2016) for Eagle Ford Group calcareous mudrocks. During organic matter conversion, the predominant pore types evolve from (1) primary mineral pores (immature) (Figure 4.11), to (2) less common OM bubble pores (early bitumen) (Figure 4.13B), to (3) co-dominant OM bubble pores and modified mineral pores with relic OM (early oil window) (Figures 4.14 and 4.16), to (4) predominant modified mineral pores (middle oil window) (Figure 4.17), and finally to (5) modified mineral pores and OM spongy OM pores (end of oil window and early oil cracking to wet gas) (Figure 4.18). The abundance of modified mineral pores and OM spongy pores increases from the middle of oil window to early oil cracking to wet-gas stage (Figures 4.17 and 4.18). In the subsurface, the modified mineral pores would be filled with petroleum.

The Woodford siliceous mudstone sample has a different pore-evolution history compared to the Barnett and the Eagle Ford (Ko et al., 2016) (Figure 4.25). First, the Woodford mudstone is characterized by *Tasmanites* (telalginite) OM that did not undergo transformation to petroleum (pre-oil bitumen) until the oil window. When conversion of *Tasmanites* OM occurred, it happened quickly, expulsion was sudden, and transformation efficiency of *Tasmanites* OM was excellent (more than 80%) (Figures 4.21B, 4.23A, and 4.25). Our study is the first to demonstrate this observation, which may relate to it having dominantly aliphatic molecules. This type of maceral makes generation potential and conversion behavior similar to Type I kerogen (Tissot, 1974; Mukhopadhyay, 1984; Vigran, 2008). The rest of the macerals and AOM (bituminite) in the Woodford samples behaved similarly to the Barnett and Eagle Ford mudrock samples relative to pore evolution. The onset of pore development began at the beginning of the bitumen generation window; pores evolve gradually with petroleum generation, and the OM transformation ratio is generally less than 50%. Second, the occurrence and abundance of modified mineral pores throughout the entire oil-window phase of maturation was less than those in the Barnett and Eagle Ford mudrock samples. Instead, a great amount of hydrocarbon fluid was retained within the pore spaces of the Woodford siliceous mudstone sample and not expelled even after post experimental procedures and sample preparation processes. Third, fewer OM spongy pores were found in the Woodford sample even during the cracking of oil to wet-gas generation stage when compared with Barnett and Eagle Ford samples. This could be related to the fact that the Woodford samples had not generated significant amounts of gas during gold tube pyrolysis as had

the Barnett and Eagle Ford (Figure 4.10). It is possible that gas generation and pyrobitumen precipitation occurred much later in the Woodford mudrocks, before OM spongy pores had begun to form.

The evolution of pores and their abundance corresponds to the amount of petroleum (bitumen, oil, and gas) generated (Figure 4.10 and Table 4.6). For example, during early to middle oil window maturation when most of kerogen and pre-oil bitumen have converted to oil (Curiale, 1986; Mastalerz and Glikson, 2000), the volume loss from solid kerogen is the largest, resulting in significant increases in pore space. At the same time, the rock contains the most abundant amount of accumulated oil, resulting in the greatest abundance of modified mineral pores. When the rock enters the middle to late oil window maturation, post-oil solid bitumen and pyrobitumen starts to form and occludes parts of the pore spaces. Simultaneously, gas generation increases, forming OM spongy pores in the post-oil solid bitumen (or pyrobitumen) (Figure 4.10). Bernard et al. (2012) suggested that the residual organic matter that hosts nanometer-sized OM pores (OM spongy pores in our definition) might be pyrobitumen (post-oil solid bitumen). Theoretically, pyrobitumen or post-oil solid bitumen increases from oil window to gas window which corresponds to our observation that the abundance of OM spongy pores increases from the middle of the oil window to the early oil cracking to wet gas stage in the Barnett. We could not identify the exact form of organic matter that hosts spongy pores without using scanning transmission x-ray microscopy (STXM) to unveil the bonding of carbon in organic compounds at microscopic scale (Bernard et al., 2012a, b; Romero-Sarmiento et al., 2014).

4.6 CONCLUSIONS

Laboratory gold-tube pyrolysis, scanning electron microscopy (SEM) and thin-section petrography, organic petrography, mineralogical identification, and stepwise geochemical characterization of Barnett and Woodford siliceous mudstones suggest that variations in mineralogy (siliceous vs. calcareous) does not have catalytic or sorption effects on pore evolution, nor did variations in the types of clay minerals show any significant catalytic or sorption effect on generated petroleum and thus pore development and evolution.

OM maceral types, identified using both SEM (platy OM, particulate OM, organic-mineral admixtures, *Tasmanites*) and organic petrology [telalginite, vitrinite, inertinite, amorphous organic matter (AOM), *Leiosphaeridia*, and *Tasmanites*], do affect the evolution of OM pores related to differences in generation kinetics and activation energy distributions between *Tasmanites* and AOM and other types of macerals. In this study, we integrated SEM petrography with organic petrography based on observation and description of size, abundance, mineral-mixing, and morphological characteristics and interpreted SEM observations of pure OM to be telalginite macerals; OM-mineral admixtures and stringy/flaky OM to be AOM or bituminite; and particulate OM to be inertinite macerals. Although both OM-mineral admixtures and stringy/flaky OM represents AOM (or bituminite), OM-mineral admixtures demonstrate a greater admixture of mineral matter than the stringy/flaky OM does. Applying organic petrography to identify the existence and occurrence of macerals especially algae such as *Botryococcus* and *Tasmanites* is a necessary step in order to accurately predict the

amount of petroleum generated and associated pore-evolution models in organic-rich mudstones.

Our results show that OM-rich Woodford rocks exhibit a markedly different pore evolution from Barnett and Eagle Ford mudstones because of the differences in maceral types, especially the abundance of *Tasmanites*. The pore-evolution history observed for the Barnett sample is similar to that reported by Ko et al. (2016) for Eagle Ford Group calcareous mudrocks. At higher levels of thermal maturation, the volume of primary mineral pores decreases and the pore volume composed of modified mineral pores and OM pores increase. During organic matter conversion, the predominant pore types change from (1) primary mineral pores (immature), to (2) less common OM bubble pores (early bitumen), to (3) co-dominant OM bubble pores and modified mineral pores with relic OM (early oil window), to (4) predominant modified mineral pores (middle oil window), and finally to (5) modified mineral pores and OM spongy OM pores (end of oil window and early oil cracking to wet gas). The abundance of modified mineral pores and OM spongy pores increases from the middle of the oil window to the early oil cracking to wet- gas stage. In the subsurface, the modified mineral pores would be filled with petroleum.

The Woodford siliceous mudstone has a different pore-evolution model. During organic matter conversion, the predominant pore types change from (1) OM-hosted bubble-shaped pores (early bitumen), to (2) few OM-hosted bubble pores and modified mineral pores (peak bitumen), to (3) increased abundance of OM-hosted bubble pores and modified mineral pores (early oil: *Tasmanites* has started to convert to petroleum), to

(4) predominant modified mineral pores (oil window: fully conversion of *Tasmanites* OM to petroleum, creating abundant pore space but with petroleum retained in the pores as solid bitumen), and finally to (VI) most abundant modified mineral pores (early cracking of oil to wet gas: most petroleum in the matrix has been expelled, leaving abundant pores). Unlike the Barnett siliceous and Eagle Ford calcareous facies, the spongy OM pores are rare.

Migration of generated petroleum (pre-oil solid bitumen) into initial primary mineral pores and pore networks was observed in both Barnett and Woodford mudrocks. The abundance of modified mineral pores in the OM-rich Barnett and Woodford implies that these pores were partially interconnected by pore-scale petroleum migration.

No pores were ever observed in *Tasmanites*. Petroleum generation and pore development from *Tasmanites* is similar to lacustrine (Type I) kerogen which has a narrower activation energy distribution and the higher mean activation energy than marine (Type II) kerogen. These two differences result in *Tasmanites* having a later and shorter OM conversion and petroleum generation history in the Woodford siliceous mudstone, resulting in a different pore-development history and possibly a different expulsion model compared to Barnett and Eagle Ford mudstones. Because the Woodford has the highest TOC content among the samples, generated petroleum are retained longer in the pore space of the rock.

ACKNOWLEDGEMENTS

The Woodford outcrop samples for this study were kindly provided by Dr. Geoffrey S. Ellis in the Central Energy Resources Team at the U.S. Geological Survey, Denver, Colorado. The authors would like to thank Lanzhou University, China, for carrying out the pyrolysis experiments with the support of the Major State Basic Research Development Program of China (Grant number: 2012CB214701). Authors would also like to thank Patrick Smith for providing CL training and imaging. Dr. Kitty Milliken, Dr. Terri Olson, Dr. Robert Reed, and Dr. Joan Spaw provided insightful discussions, suggestions, and inspiration during the manuscript preparation. We also would like to thank the Bureau of Economic Geology Mudrock System Research Laboratory (MSRL) sponsors who supported this research: Anadarko, Apache, BHP Billiton, BP, Cenovus, Centrica, Chesapeake, Chevron, Cima, Cimarex, Concho, ConocoPhillips, Cypress, Devon, Encana, Eni, EOG, EXCO, ExxonMobil, FEI, Hess, Husky, IMP, Kerogen, Marathon, Murphy, Newfield, Oxy, Penn Virginia, Penn West, Pioneer, QEP, Samson, Shell, Statoil, Talisman, Texas American Resources, The Unconventionals, U.S. EnerCorp, Valence, and YPF. Publication was authorized by the Director, Bureau of Economic Geology, Jackson School of Geosciences, The University of Texas at Austin.

REFERENCES

ASTM D2797, 2016a, Standard practice for preparing coal samples for microscopical analysis by reflected light: Annual book of ASTM standards, Petroleum products, lubricants, and fossil fuels; Gaseous fuels; coal and coke, sec. 5, v. 5.06: ASTM International, West Conshohocken, PA, 542–546, http://www.astm.org/Standards/D2797.htm.

ASTM D7708, 2016b, Standard test method for microscopical determination of the reflectance of vitrinite dispersed in sedimentary rocks: Annual book of ASTM standards, Petroleum products, lubricants, and fossil fuels; Gaseous fuels; coal and coke, sec. 5, v. 5.06: ASTM International, West Conshohocken, PA, 923–932, http://www.astm.org/Standards/D7708.htm

Aufill, M., 2007, High resolution magnetic susceptibility of the Oklahoma Woodford Shale and relationships to variations in outcrop spectral gamma-ray response: MS thesis, Oklahoma State University, Stillwater, Oklahoma, 165 p.

Bernard, S., B. Horsfield, H.-M. Schulz, R. Wirth, A. Schreiber, and N. Sherwood, 2012a, Geochemical evolution of organic-rich shales with increasing maturity: A STXM and TEM study of the Posidonia Shale (Lower Toarcian, northern Germany): Marine and Petroleum Geology, v. 31, p. 70–89, doi: 10.1016/j.marpetgeo.2011.05.010.

Bernard, S., R. Wirth, A, Schreiber, H.-M. Schulz, and B. Horsfield, 2012b, Formation of nanoporous pyrobitumen residues during maturation of the Barnett Shale (Fort Worth Basin): International Journal of Coal Geology, v. 103, p. 3–11, doi: 10.1016/j.coal.2012.04.010.

Bernard, S., and B. Horsfield, 2014, Thermal maturation of gas shale systems: Annual Review of Earth and Planetary Sciences, v. 42, p. 635–651, doi: 10.1146/annurev-earth-060313-054850.

Bertrand, P. J.-L. Pittion, and C. Bernaud, 1986, Fluorescence of sedimentary organic matter in relation to its chemical composition, Organic Geochemistry, v. 10, p. 641–647, doi: 10.1016/0146-6380(86)90061-6.

Blakey, R., 2009, Paleogeography and geologic evolution of North America, Late Devonian (360 Ma), map: http://jan.ucc.nau.edu/~rcb7/namD360.jpg, accessed September 2016.

Bohacs, K. M., Q. R. Passey, M. Rudnicki, W. L. Esch, and O. R. Lazar, 2013, The spectrum of fine-grained reservoirs from ‘shale gas’ to ‘shale oil’/ tight liquids: essential attributes, key controls, practical characterization, International Petroleum Technology Conference, Society of Petroleum Engineers IPTC-16676-MS, Beijing, China, 26–28 March 2013.

Bowker, K. A., 2007, Barnett Shale gas production, Fort Worth Basin: Issues and discussion: AAPG Bulletin, v. 91, p. 523–533, doi:10.1306/06190606018.

Cardott, B. J., and J. R. Chaplin, 1993, Guidebook for selected stops in the Western Arbuckle Mountains, southern Oklahoma, Oklahoma Geological Survey Special Publication 93-3, 61 p.

Cardott, B. J., 2011, Four distinct Woodford Shale plays in Oklahoma—gas, condensate, oil, and biogenic methane: AAPG Hedberg Conference, http://www.searchanddiscovery.com/abstracts/pdf/2011/hedberg-texas/abstracts/ndx_cardott.pdf, accessed 1/23/2016.

Cardott, B. J., C. R. Landis, and M. E. Curtis, 2015, Post-oil solid bitumen network in the Woodford Shale, USA — A potential primary migration pathway: International Journal of Coal Geology, v. 139, p. 106–113, doi: 10.1016/j.coal.2014.08.012.

Comer, J. B., 2007, Lithologic characeristics and gas production potential of Woodford Shale in the southern midcontinent, abstract, GSA Annual Meeting, Denver, 28–31 October 2007.

Curiale, J. A., 1986, Origin of solid bitumens, with emphasis on biological marker results: Organic Geochemistry, v. 10, p. 559–580.

Curtis, M. E., Cardott, B. J., Sondergeld, C. H. and Rai, C.S., 2012, Development of organic porosity in the Woodford Shale with increasing thermal maturity: International Journal of Coal Geology, v. 103, p. 26–31, doi: 10.1016/j.coal.2012.08.004.

Derenne, S., P. Metzger, C. Largeau, P. F. van Bergen, J. P. Gatellier, J. S. Sinninghe Damste, J. W. de Leeuw, C. Berkaloff, 1992, Similar morphological and chemical variations of *Gloeocapsomorpha prisca* in Ordovician sediments and cultured *Botryococcus braunii* as a response to changes in salinity: Organic Geochemistry, v. 19, 299–313.

Espitalié, J., M. Madec, and B. Tissot, 1980, Role of mineral matrix in kerogen pyrolysis: Influence on petroleum generation and migration: AAPG Bulletin, v. 64, p. 59–66.

Espitalié, J., K. Senga Makadi, and J. Trichet, 1984, Role of the mineral matrix during kerogen pyrolysis: Organic Geochemistry, v. 6, p. 365–382, doi: 10.1016/0146-6380(84)90059-7.

Fishman, N. S., P. C. Hackley, H. A. Lowers, R. J. Hill, S. O. Egenhoff, D. D. Eberl, and A. E. Blum, 2012, The nature of porosity in organic-rich mudstones of the Upper Jurassic Kimmeridge Clay Formation, North Sea, offshore United Kingdom: International Journal of Coal Geology, v. 103, p. 32–50, doi:10.1016/j.coal.2012.07.012.

Fishman, N. S., G. S. Ellis, S. T. Paxton, A. R. Boehlke, and S. O. Egenhoff, 2013, Gas storage in the Upper Devonian–Lower Mississippian Woodford Shale, Arbuckle Mountains, Oklahoma: How much of a role do chert beds play?, *in* J. Chatellier and D. Jarvie, eds., Critical assessment of shale resource plays: AAPG Memoir 103, p. 81–107, doi: 10:1306/13401726H53493.

Fowler, M. G., L. D. Stasiuk, M. Hearn, and M. Obermajer, 2004, Evidence for *Gloeocapsomorpha prisca* in Late Devonian source rocks from southern Alberta, Canada: Organic Geochemistry, v. 35, p. 425–441.

Goldstein, T. P., 1983, Geocatalytic reactions in formation and maturation of petroleum: AAPG Bulletin, v. 67, p. 152–159.

Hackley, P. C., and J. Kus, 2015, Thermal maturity of Tasmanites microfossils from confocal laser scanning fluorescence microscopy: Fuel, v. 142, p. 343–350.

Hackley, P. C., and B. J. Cardott, 2016, Application of organic petrography in North American shale petroleum systems: A review: International Journal of Coal Geology, v. 163, p. 8–51, doi: 10.1016/j.coal.2016.06.010.

Hackley, P. C., Fishman, N., Wu, T., and Baugher, G., 2016, Organic petrology of mudrocks from the lacustrine Lucaogou Formation, Santanghu Basin, northwest China: application to lake basin evolution: International Journal of Coal Geology, v 168, p. 20–34.

Hackley, P. C., and J. R. SanFilipo, 2016, Organic petrology and geochemistry of Eocene Suzak bituminous marl, north-central Afghanistan: depositional environment and source rock potential: Marine and Petroleum Geology, v. 73, p. 572–589, doi: 10.1016/j.marpetgeo.2016.02.029.

Ham, W. E., 1973, Regional geology of the Arbuckle Mountains, Oklahoma: The Geological Society of America, compiled by T. L. Rowland, 62p.

Hart, B. S., J. H. S. Macquaker, and K. G. Taylor, 2013. Mudstone ("shale") depositional and diagenetic processes: implications for seismic analyses of source-rock reservoirs: Interpretation, v. 1, B7–B26.

Hetényi, M., 1995, Simulated thermal maturation of type I and III kerogens in the presence, and absence, of calcite and montmorillonite: Organic Geochemistry, v. 23, p. 121–127, doi: 10.1016/0146-6380(94)00120-P.

Horsfield, B., and A. G. Douglas, 1980, The influence of minerals on the pyrolysis of kerogen: Geochimica et Cosmochimica Acta, v. 44, p. 1119–1131, doi: 10.1016/0016-7037(80)90066-6.

Huizinga, B. J., E. Tannenbaum, and I. R. Kaplan, 1987a, The role of minerals in the thermal alteration of organic matter: III. Generation of bitumen in laboratory experiments: Organic Geochemistry, v. 11, p. 591–604.

Huizinga, B. J., E. Tannenbaum, and I. R. Kaplan, 1987b, The role of minerals in the thermal alteration of organic matter: IV. Generation of n-alkanes, acyclic isoprenoids, and alkenes in laboratory experiments: Geochimica et Cosmochimica Acta, v. 51, p. 1083– 1097.

Johns, W. D., 1979, Clay mineral catalysis and petroleum generation: Annual Review Earth Planetary Science, v. 7, p. 183–198.

Katz, B., and F. Lin, 2014, Lacustrine basin unconventional resource plays: Key differences: Marine and Petroleum Geology, v. 56, p. 255–265, doi: 10.1016/j.marpetgeo.2014.02.013.

Kirkland, D. W., R. E. Denison, D. M. Summers, and J. R. Gormly, 1992, Geology and organic geochemistry of the Woodford Shale in the Criner Hills and western Arbuckle Mountains, *in* K. S. Johnson and B. J. Cardott, eds., Source rocks in the southern Midcontinent, 1990 symposium: Oklahoma Geological Survey Circular 93, p. 38–69.

Ko, L. T., R. G. Loucks, T. Zhang, S. C. Ruppel, D. Shao, 2016, Pore and pore network evolution of Upper Cretaceous Boquillas (Eagle Ford-equivalent) mudrocks: Results from gold-tube pyrolysis experiments: AAPG Bulletin, v. 100, p. 1693–1722. doi: 10.1306/04151615092.

Ko, L. T., R. G. Loucks, S. C. Ruppel, T. Zhang, S. Peng, 2017, Origin and characterization of Eagle Ford pore networks in the south Texas Upper Cretaceous shelf: AAPG Bulletin, v. 101, p. 387–418, doi: 10.1306/08051616035.

Krystyniak, A. M., 2005, Outcrop-based gamma-ray characterization of the Woodford Shale of south-central Oklahoma: MS thesis, Oklahoma State University, Stillwater, Oklahoma, 145 p.

Lambert, M. W., 1993, Internal stratigraphy and organic facies of the Devonian-Mississippian Chattanooga (Woodford) Shale in Oklahoma and Kansas: Source rocks in a sequence stratigraphic framework: Chapter 11, AAPG Studies in Geology, v. 37, p. 163-176.

Lao, Y., J. Korth, J. Ellis, and P. T. Crisp, 1989, Heterogeneous reactions of 1-pristene catalyzed by clays under simulated geological conditions: Organic Geochemistry, v. 14, p. 375–379.

Lewan, M. D., 1983, Effects of thermal maturation on stable organic carbon isotopes as determined by hydrous pyrolysis of Woodford Shale: Geochimica et Cosmochimica Acta, v. 47, p. 1471–1479, doi: 10.1016/0016-7037(83)90306-X.

Lewan, M. D., 1987, Petrographic study of primary petroleum migration in the Woodford Shale and related rock units, in Doligez, B., ed., Migration of hydrocarbons in sedimentary basins: Paris, Editions Technip, p. 113–130.

Lewan, M. D., M. P. Dolan, and J. B. Curtis, 2014, Effects of smectite on the oil-expulsion efficiency of the Kreyenhagen Shale, San Joaquin Basin, California based on hydrous-pyrolysis experiments: AAPG Bulletin, v. 98, p. 1091–1109, doi: 10.1306/10091313059.

Löhr, S. C., E. T. Baruch, P. A. Hall, and M. J. Kennedy, 2015, Is organic pore development in gas shales influenced by the primary porosity and structure of thermally immature organic matter?: Organic Geochemistry, v. 87, p. 119–132, doi: 10.1016/j.orggeochem.2015.07.010.

Loucks, R. G., and S. C. Ruppel, 2007, Mississippian Barnett Shale: lithofacies and depositional setting of a deep-water shale-gas succession in the Fort Worth Basin, Texas: AAPG Bulletin, v. 91, p. 579–601, doi:10.1306/11020606059.

Loucks, R. G., R. M. Reed, S. C. Ruppel, and D. M. Jarvie, 2009, Morphology, genesis, and distribution of nanometer-scale pores in silieous mudstones of the Mississippian Barnett Shale: Journal of Sedimentary Research, v. 79, p. 848–861, doi: 10.2110/jsr.2009.09.

Loucks, R. G., R. M. Reed, S. C. Ruppel, and U. Hammes, 2012, Spectrum of pore types and networks in mudrocks and a descriptive classification for matrix-related mudrock pores: AAPG Bulletin, v. 96, p. 1071–1098, doi:10.1306/08171111061.

Loucks, R. G., and R. M. Reed, 2014, Scanning-electron-microscope petrographic evidence for distinguishing organic-matter pores associated with depositional organic matter versus migrated organic matter in mudrocks: GCAGS Journal, v. 3, p. 51–60.

Mastalerz, M., and M. Glikson, 2000, In-situ analysis of solid bitumen in coal: examples from the Bowen Basin and the Illinois Basin: International Journal of Coal Geology, v. 42, p. 207–220, doi: 10.1016/S0166-5162(99)00040-3.

Mastalerz, M., Schimmelmann, A., Lis, G. P., Drobniak, A., Stankiewicz, A., 2012, Influence of maceral composition on geochemical characteristics of immature shale kerogen: Insight from density fraction analysis: International Journal of Coal Geology, v. 103, p. 60–9, doi: 10.1016/j.coal.2012.07.011.

Mastalerz, M., Schimmelmann, A., Drobniak, A. and Chen, Y., 2013, Porosity of Devonian and Mississippian New Albany Shale across a maturation gradient: Insights from organic petrology, gas adsorption, and mercury intrusion: AAPG Bulletin, v. 97, p. 1621–1643, doi:10.1306/04011312194.

Meckel. L. D., D. G. Smith, and L. A. Wells, 1992, Ouachita foredeep basins: Regional paleogeography and habit of hydrocarbons: Foreland basins and foldbelts: Chapter 15, AAPG Memoir 55, Tulsa, Oklahoma, p. 427–444.

Meissner, F. E, 1978, Petroleum geology of the Bakken Formation, Williston basin. North Dakota and Montana, in The economic geology of the Williston basin: Montana Geological Society 24th Annual Conference; 1978 Williston Basin Symposium, p. 207–227.

Milliken, K. L. and S. E. Laubach, 2000, Brittle deformation in sandstone diagenesis as revealed by scanned cathodoluminescence imaging with application to characterization of fractured reservoirs, in: M. Pagel, V.B., P. Blanc, and D. Ohnenstetter (Ed.), Cathodoluminescence in Geosciences, Springer Berlin Heidelberg, pp. 225-243.

Milliken, K. L., W. L. Esch, R. M. Reed, and T. Zhang, 2012, Grain assemblages and strong diagenetic overprinting in siliceous mudrocks, Barnett Shale (Mississippian), Fort Worth Basin, Texas: AAPG Bulletin, v. 96, p. 1553–1578.

Milliken, K. L., M. Rudnicki, D. N. Awwiller, and T. Zhang, 2013, Organic matter-hosted pore system, Marcellus Formation (Devonian), Pennsylvania: AAPG Bulletin, v. 97, p. 177–200.

Montgomery, S. L., D. M. Jarvie, K. A. Bowker, and R. M. Pollastro, 2005, Mississippian Barnett Shale, Fort Worth Basin, northcentral Texas: Gas-shale play with multi-trillion cubic foot potential: AAPG Bulletin, v. 89, no. 2, p. 155– 175, doi:10.1306/09170404042.

Mukhopadhyay, P. K., and J. R. Gormly 1984, Hydrocarbon potential of two types of resinite: Organic Geochemistry, v. 6, p. 439–454.

Nicholas, R. L., and R. A. Rozendal, 1975, Subsurface positive elements within Ouachita foldbelt in Texas and their relation to Paleozoic cratonic margin: AAPG Bulletin, v. 59, p. 193– 216.

Pan, C., A. Geng, N. Zhong, and J. Liu, 2010, Kerogen pyrolysis in the presence and absence of water and minerals: Steranes and triterpenoids: Fuel, v. 89, p. 336–345, do:10.1016/j.fuel.2009.06.032.

Paxton, S. T., and B. J. Cardott, 2008, Oklahoma gas shales, field trip guidebook: Oklahoma Geological Survey Open File Report 2-2008, 87 p.

Pepper, A. S., and P. J. Corvi, 1995, Simple kinetic models of petroleum formation. Part 1: oil and gas generation from kerogen: Marine and Petroleum Geology, v. 12, p. 291–319.

Pollastro, R. M., D. M. Jarvie, R. J. Hill, and C. W. Adams, 2007, Geologic framework of the Mississippian Barnett Shale, Barnett–Paleozoic total petroleum system, Bend arch–Forth Worth Basin, Texas: AAPG Bulletin, v. 91, p. 405–436, doi:10.1306/10300606008.

Pommer, M. E., and K. L. Milliken, 2015,. Pore types and pore-size distributions across thermal maturity, Eagle Ford Formation, southern Texas, AAPG Bulletin, v. 99, p. 1713–1744, doi: 10.1306/03051514151.

Pradier, B., B. Bertrand, L. Martinez, and F. Laggoun-Defarge, 1991, Fluorescence of organic matter and thermal maturity assessment: Organic Geochemistry, v. 17, p. 511–524.

Redmond, L., 2016, Lithofacies, depositional environments, and depositional model of the Mississippian Barnett Formation in the southern Fort Worth Basin, Master's Thesis, University of Texas at Austin, Austin, Texas, 162 p.

Revill, A. T., J. K. Volkman, T. O'Leary, R. E. Summons, C. J. Boreham, M. R. Banks, and K. Denwer, 1994, Hydrocarbon biomarkers, thermal maturity, and depositional setting of tasmanite oil shales from Tasmania, Australia: Geochimica et Cosmochimica Acta, v. 58, p. 3803–3822.

Romero-Sarmiento, M.-F., Rouzaud, J.-N., Bernard S., Deldicque D., Thomas M., Littke R., 2014, Evolution of Barnett Shale organic carbon structure and nanostructure with increasing maturation: Organic Geochemistry, v. 71, p. 7–16.

Schieber, J., 1996, Early diagenetic silica deposition in algal cysts and spores: A source of sand in black shales?: AAPG Bulletin, v. 66, 175–183.

Schieber, J., 2010, Common themes in the formation and preservation of intrinsic porosity in shales and mudstones — Illustrated with examples across the Phanerozoic: Society of Petroleum Engineers (SPE) Unconventional Gas Conference, Pittsburgh, USA, February 23–25, 2010, Paper # SPE 132370.

Slatt, R. M., and N. R. O'Brien, 2011, Pore types in the Barnett and Woodford gas shales: Contribution to understanding gas storage and migration pathways in fine-grained rocks: AAPG Bulletin, v. 95, p. 2017–2030.

Sundararaman, P., S. C. Teerman, R. G. Mann, and B. Mertani, 1988, Activation energy distribution: a key parameter in basin modeling and a geochemical technique for studying maturation and organic facies, Proc. 17th Annu. Indones. Pet. Assoc. 1, p. 169–185.

Tannenbaum, E., and I. R. Kaplan, 1985, Role of minerals in the thermal alteration organic matter—I: Generation of gases and condensates under dry condition Geochimica et Cosmochimica Acta, v. 49, p. 2589–2604, doi:10.1016/0016-7037(85)90128-0.

Tannenbaum, E., B. J. Huizinga, and I. R. Kaplan, 1986, Role of minerals in thermal alteration of organic matter—II: A material balance: AAPG Bulletin, v. 70, p. 1156–1165.

Taylor, G. H., and S. Y. Liu, 1989, Micrinite — its nature, origin, and significance: International Journal of Coal Geology, v. 14, p. 29–46, doi: 10.1016/0166-5162(89)90077-3.

Tissot, B. P., B. Durand, J. Espitalie, and A. Combaz, 1974, Influence of nature and diagenesis of organic matter in formation of petroleum: AAPG Bulletin, v. 58, p. 499–506.

Tissot, B. P., R. Pelet, Ph. Ungerer, 1987, Thermal history of sedimentary basins, maturation indices, and kinetics of oil and gas generation: AAPG Bulletin, v. 71, 1445–1466.

Thompson, D. M., 1988, Fort Worth basin, in L. L. Sloss, ed., The geology of North America: Geological Society of America, v. D-2, p. 346– 352.

Tyson, R. V., 1995, Sedimentary organic matter: organic facies and palynofacies, Chapman & Hall, Univ. California, 615 p.

Vigran, J. O., A. Mork, A. W. Forsberg, H. M. Weiss, and W. Weitschat, 2008, *Tasmanites* algae—contributors to the Middle Triassic hydrocarbon source rocks of Svalbard and the Barents Shelf: Polar Research, v. 27, p. 360–371.

Volkman, J. K., Z. Zhang, X. Xie, J. Qin, and T. Borjigin, 2015, Biomarker evidence for *Botryococcus* and a methane cycle in the Eocene Huadian oil shale, NE China: Organic Geochemistry, v. 78, p. 121–134.

Walters, C. C., 2007, The origin of petroleum, in book: Practical Advances in Petroleum Processing, Chapter 2, pp.79–101, doi: 10.1007/978-0-387-25789-1_2

Wei, Z., J. M. Moldowan, J. Dahl, T. P. Goldstein, and D. M. Jarvie, 2006a, The catalytic effects of minerals on the formation of diamondoids from kerogen macromolecules: Organic Geochemistry, v. 37, p. 1421–1436, doi:10.1016/j.orggeochem.2006.07.006.

Wei, Z., J. M. Moldowan, and A. Paytan, 2006b, Diamondoids and molecular biomarkers generated from modern sediments in the absence and presence of minerals during hydrous pyrolysis: Organic Geochemistry, v. 37, p. 891–911, doi:10.1016/j.orggeochem.2006.04.008.

Wood, S. G., 2013, Lithofacies, depositional environments, and sequence stratigraphy of the Pennsylvanian (Morrowan-Atokan) Marble Falls Formation, central Texas, Master's Thesis, University of Texas at Austin, Austin, Texas, 276 p.

Wood, J. M., H. Sanei, M. E. Curtis, and C. R. Clarkson, 2015, Solid bitumen as a determinant of reservoir quality in an unconventional tight gas siltstone play: International Journal of Coal Geology, v. 150–151, p. 287–295, doi: 10.1016/j.coal.2015.03.015.

Chapter 5: Controls on Pore Types and Pore-Size Distribution in the Upper Triassic Yanchang Formation, Ordos Basin, China: Implications for Models of Lacustrine Mudrocks[4]

ABSTRACT

The main objectives of this study are to (1) determine if pore-evolution models developed from marine mudrocks can be directly applied to lacustrine mudrocks, (2) investigate which factors control different pore types and sizes of organic matter (OM)-rich argillaceous mudstones of the Chang 7 Member of the Upper Triassic Yanchang Formation, and (3) describe the variety of texture, fabric, mineralogy, and thermal maturity of the Chang 7 mudstones. Lacustrine mudstones from nine cored wells along depositional dip in the southeastern Ordos Basin, China, were investigated. Helium porosimetry, nitrogen adsorption, and field-emission scanning electron microscopy of Ar-ion milled samples were applied. Measured average total porosity of samples from a proximal to distal transect (ϕ = 5.0%) is higher than those from the two adjacent cored wells (ϕ = 2.3%). This difference in porosity partly caused by differences in clay mineral content implies that in the fluvial-deltaic-lacustrine depositional environment, reservoir quality can vary significantly in a short distance.

Because of the uneven distribution of the sample set from the proximal to the distal parts of the basin, this study mainly discusses variations in the proximal setting. Results from nitrogen-gas adsorption experiments show that there are four distinct

[4]The full content of this chapter is published in *Interpretation* in 2017.

patterns of pore-size distribution (PSD) within the Chang 7 Member of the Yanchang Formation with no particular correlation to mineralogical composition or thermal maturity. The pore network within Chang 7 mudstones is dominated by OM–hosted pores, with a lesser abundance of interparticle and intraparticle pores. The size distribution of mineral-hosted pores within these mudstones is closely related to rock texture (sorting and grain size) and fabric. Mudstones with well-sorted grains and a higher percentage of coarser grains have more abundant mineral pores. The sizes of OM-hosted pores in these compaction-dominated lacustrine mudstones are 1 to 2 orders of magnitude smaller than those in marine mudstones that display abundant early cementation.

5.1 INTRODUCTION

The success of shale gas and oil exploration in continental lacustrine sediments in China has necessitated a detailed characterization of lacustrine mudrocks and attracted interest in understanding the heterogeneity of lacustrine shale reservoirs as a means of defining the "sweet spots" in lacustrine basins (e.g., Zhao et al., 2005). Lacustrine basins are characterized by relatively uniform subsidence rates and sedimentation. The rise and fall of lake levels is one of the major controls on facies distribution, organic matter preservation, and depositional environment. During maximum lake level rise, organic matter (OM)-rich sediments are deposited most extensively and are best developed near the center of the lake (Zhao et al., 2010). The Upper Triassic Yanchang Formation was deposited in the Ordos Basin, which is one of the largest lacustrine basins in China. Mudstones, siltstones, and sandstones deposited in lakes within the Ordos Basin fed by fluvial–deltaic complexes have been recognized as hybrid unconventional resource plays

in the Ordos Basin (e.g., Wang et al., 2015a; Zhao et al., 2015) (Figure 5.1). The Yanchang Formation ranges from 800 to 1,000 m thick in the northern Ordos Basin and is divided into ten lithological intervals, basal Chang 10 Member to uppermost Chang 1 Member, on the basis of lithological variations of mudstones, siltstones, and sandstones (Zou et al., 2010; Zhao et al., 2015). The Chang 7 Member represents the greatest lake expansion during the Upper Triassic, covering up to 60% of the lake area (roughly 8 x10^4 km^2), and depositing dominantly Type I kerogen (Zhao et al., 2010). The Chang 7 Member, which ranges from 80 to 130 m thick, is the thickest and the most organic-rich mudstone interval and has been identified as the main source rock of the Yanchang Formation (Wang, 2012; Yao et al., 2013; Wang et al., 2015a; Yuan et al., 2015; Zhao et al., 2015; Pan et al., 2016). Reported total organic carbon (TOC) content and T_{max} in both the immature and mature Chang 7 Member varies widely, ranging from 0.29 to 23.90 wt.%, and 424 to 475°C, respectively. The average TOC value is 5.65 wt.%, and average T_{max} value is 447°C (e.g., Guo et al., 2014; Han et al., 2014; Zhang et al., 2015; Cao et al., 2016; Li et al., 2016; Pan et al., 2016; Loucks et al., 2017). The documented hydrogen index (HI) values range from 29 to 454 mg/ gTOC for Chang 7 mudstones in oil window maturity, implying some Chang 7 samples might have Type I or mixed Type I/II kerogen in origin (e.g., Pan et al., 2016).

Several studies have characterized the pore size and structure of lacustrine Yanchang mudstones in the Ordos Basin (e.g., Li et al., 2016; Jiang et al., 2016; Yu et al., 2016). Jiang et al. (2016) characterized pore volume and pore-size distribution (PSD) using combined high-pressure mercury intrusion (MICP), low-pressure nitrogen (N_2), and carbon dioxide (CO_2) physisorption techniques, showing that mesopores (2−50 nm) were more dominant than micropores (<2 nm) and macropores (> 50 nm), and PSD ranges mainly from 0.3 to 60 nm. They proposed that clay mineral content and thermal maturity

are major controls on pore architecture. Yu et al., (2016) characterized pores on the basis of silty versus clayey laminae and concluded that silt laminae were dominated by macropores while clayey laminae were dominated by mesopores, using the same methods as Jiang et al. (2016). They also used scanning electron microscopy (SEM) images to identify predominated pore types – interparticle pores dominated in silty laminae whereas intraparticle and interparticle pores dominated in clayey laminae. Average measured porosity was higher in silty laminae (ϕ = 5.40%) than in clayey laminae (ϕ = 3.67%). Li et al. (2016) investigated the effect of extractable and solid organic matter (EOM and SOM) on porosity and the PSD of lacustrine shales, demonstrating that pores were occupied or blocked by EOM with varying extent and that SOM reduced total porosity. They also proposed that the generated hydrocarbons and associated fluid pressure in macropores protected them from collapsing due to compaction. All three studies have significantly improved our understanding of pore structure and characteristics in lacustrine mudstones and explain the possible key controls of porosity and PSD. However, there is an absence of published work providing a detailed and more in-depth integration of direct SEM imaging and indirect measuring techniques (MICP, N_2 and methane (CH_4) adsorption). Also absent are studies that compare and contrast the differences in texture, mineralogy, and pore systems of marine and lacustrine mudstones, especially when they have similar levels of thermal maturation.

In this study, samples were collected from the OM)-rich, argillaceous mudstone facies of Chang 7 Member in proximal (delta plain) and distal (near lake-center basin) areas of the southeastern Ordos Basin (Li et al., 1995; Ruppel and Rowe, 2017) (Figure 5.1). The main objectives of this study are to (1) describe the texture, fabric, mineralogy, and thermal maturity of the Chang 7 mudstone samples along a proximal to distal transect, (2) examine the causes of porosity and pore-size variations in the Chang 7

mudstones, and (3) assess the differences in porosity evolution between marine and lacustrine mudrocks.

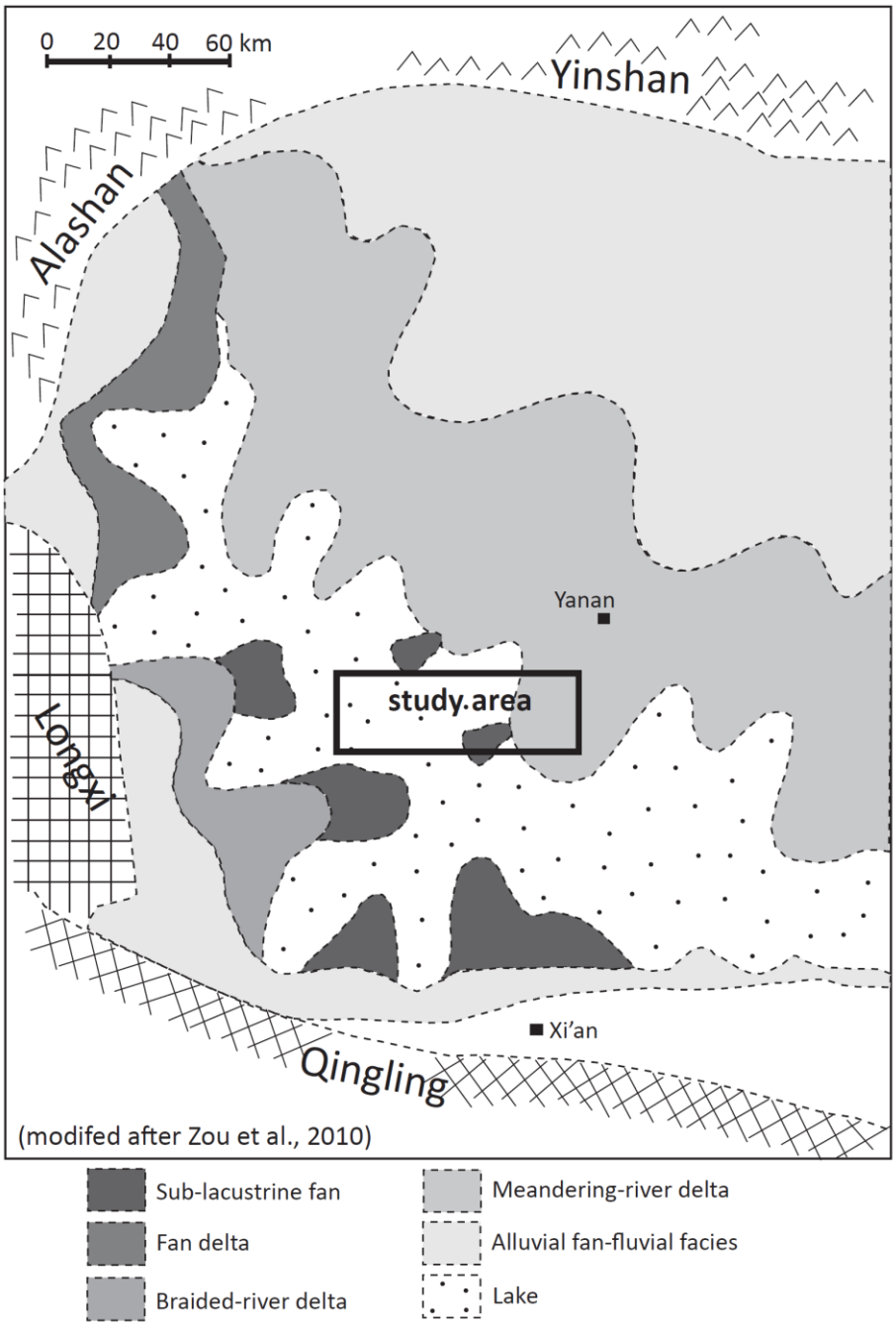

Figure 5.1: Paleogeographic map of the Ordos Lake during Upper Triassic, showing general facies distribution of the Chang 7 unit of the Yanchang Formation.

5.2 GEOLOGICAL SETTING

The Ordos Basin, one of the "walled sedimentary basins" in the North China block, is surrounded by active tectonic elements and characterized by little internal deformation (Carroll et al., 2010). The basin sits on Archean and Proterozoic basement overlain by Cambrian and Ordovician shallow-marine carbonates (Yang et al., 1986). Carboniferous shallow-marine limestone strata and siliciclastic fluvial–deltaic strata directly overlie the Ordovician section and are bounded by a regional unconformity (Yang et al., 1992; Liu et al., 1997). Carboniferous strata are overlain by Permian fluvial, deltaic, and lacustrine deposits (Li et al., 1995; Liu, 1998). Triassic and Jurassic sections also consist mainly of fluvial, deltaic, and lacustrine deposits (Li et al., 1995; Liu, 1998). Cretaceous strata are fluvial and eolian redbeds (Li et al., 1995).

The Ordos Basin has experienced three major tectonic stages: cratonic basin with divergent margins from the Cambrian to the Early Ordovician, cratonic basin with convergent margins from the Middle Ordovician to the Middle Triassic, and an intraplate remnant cratonic basin from the Late Triassic to the Early Cretaceous (Yang et al., 2005; Carroll et al., 2010). Two main petroleum systems are present in the Ordos Basin: the Ordovician and Permian gas system and the Triassic oil system (Yang et al., 2005). Internal drainage began in the Ordos Basin in the Middle to Late Triassic (Yang et al., 2005). During the Late Triassic, the northern deltas and southwestern fan deltas started to develop (Figure 5.1, Zou et al., 2010). The Upper Triassic Yanchang Formation records at least four third-order transgressive–regressive cycles with changing lake levels and two larger lacustrine–deltaic cycles (Figure 5.2; Zou et al., 2010; Zhao et al, 2015).

Member boundaries of the ten lithological intervals have distinct wireline-log responses, which are useful for subsurface correlations (Figure 5.2). Lake-deepening events, represented by organic-rich mudstones overlying organic-poor sandstones and

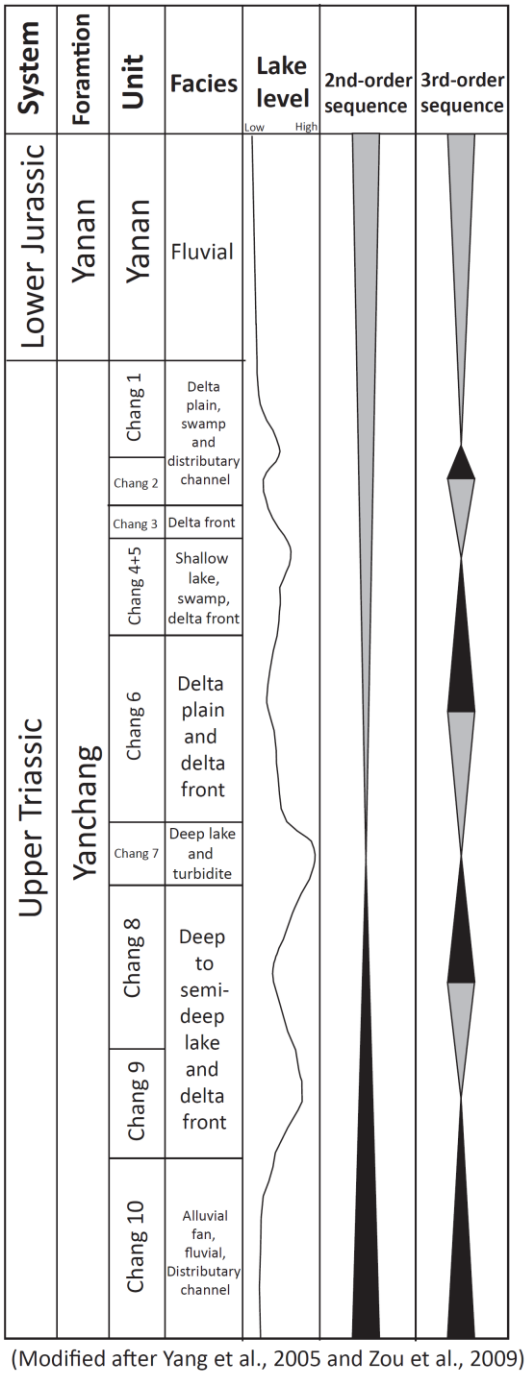

Figure 5.2: Stratigraphic column and subdivision of the Upper Triassic Yanchang Formation, Ordos Basin, China, showing facies change and stacking pattern, lake level variation, and sequence stratigraphic divisions.

events, recognized as organic-rich mudstones overlying organic-poor sandstones and siltstones, have been recognized in the upper Chang 9, middle Chang 8, lower Chang 7, middle Chang 4 and 5, and Chang 1 lacustrine mudstones (Figure 5.2, Zou et al., 2010; Tang et al., 2014; Yuan et al., 2015; Zhao et al., 2015; Ruppel and Rowe, 2017). The Chang 7 Member records the widest lake expansion and resulted in the most prolific source rocks deposition (Zou et al., 2010; Tang et al., 2014; Yuan et al., 2015; Zhao et al., 2015; Ruppel and Rowe, 2017). The Chang 4 and 5, Chang 8, and Chang 9 Members were also deposited during the lake expansion, which is indicated by the dominant thick intervals of organic-rich mudstones; the other intervals are primarily composed of sandstone and siltstone interbedded with mudstone (Zou et al., 2010; Zhao et al., 2015).

5.3 DATA AND METHODS

Nine Yanchang OM-rich mudstone samples were collected from varied depths (407 m to 2,297.1 m) along a proximal to distal section of the lake basin (Figure 5.3). One sample per mudstone facies per well was collected, based on macroscopic core study that allowed classification of facies by grain size and color. Eight samples are from the Chang 7 Member, and one sample is from the Chang 9 Member of the Yanchang Formation. The locality of this regional sample set is both in close proximity to and distant from the YCYV1112 and YCYV1133 vertical cores that span from the Chang 7 to Chang 9 Members (Loucks, et al., 2017). Eight samples are from the proximal area, and one sample is from the distal area near the center of the lake. The uneven distribution of samples from the proximal to the distal area renders this sample set as not representative of regional variation. Rather, sample locations are limited to a fairly small area.

Mineralogical and geochemical analyses such as thin-section descriptions (Milliken et al., 2017), X-ray diffraction analyses (XRD; completed by K-T GeoServices, Gunnison, Colorado), Rock-Eval pyrolysis (completed by GeoMark, Houston, Texas), LECO TOC (completed by GeoMark, Houston, Texas), organic petrology (Hackley et al., 2017; maceral identification and bitumen reflectance measurements per ASTM D7708 (ASTM, 2015)), and biomarker analyses (Sun et al., 2017) were completed on these nine samples. Nitrogen-gas adsorption (Zhang et al., 2017), helium-gas porosity measurement (completed by Peng, this study), and field emission scanning electron microscopy (FE-SEM) analysis of argon (Ar)-ion-milled samples (this study) were completed to characterize pore-size distribution (PSD) and to determine porosity and pore types.

Vitrinite reflectance equivalent values were determined by solid bitumen reflectance (BR_o) measurement because vitrinite is sparse, absent, or difficult to identify with confidence. BR_o is interpreted to be a good proxy for vitrinite reflectance in the peak oil window based on previous studies (Jacob, 1989; Landis and Castano, 1994). Vitrinite reflectance equivalent values were also determined by methylphenanthrene indexes (MPI-1) in aromatic fractions of the biomarker (Radke et al., 1982). Both are interpreted to be good proxies for vitrinite reflectance in the peak oil window. However, caution needs to be exercised while using these data. Results should be subject to interpretation by an experienced petrographer and the conversion applied to obtain vitrinite reflectance as an empirical conversion should be treated with caution (Hackley et al., 2015).

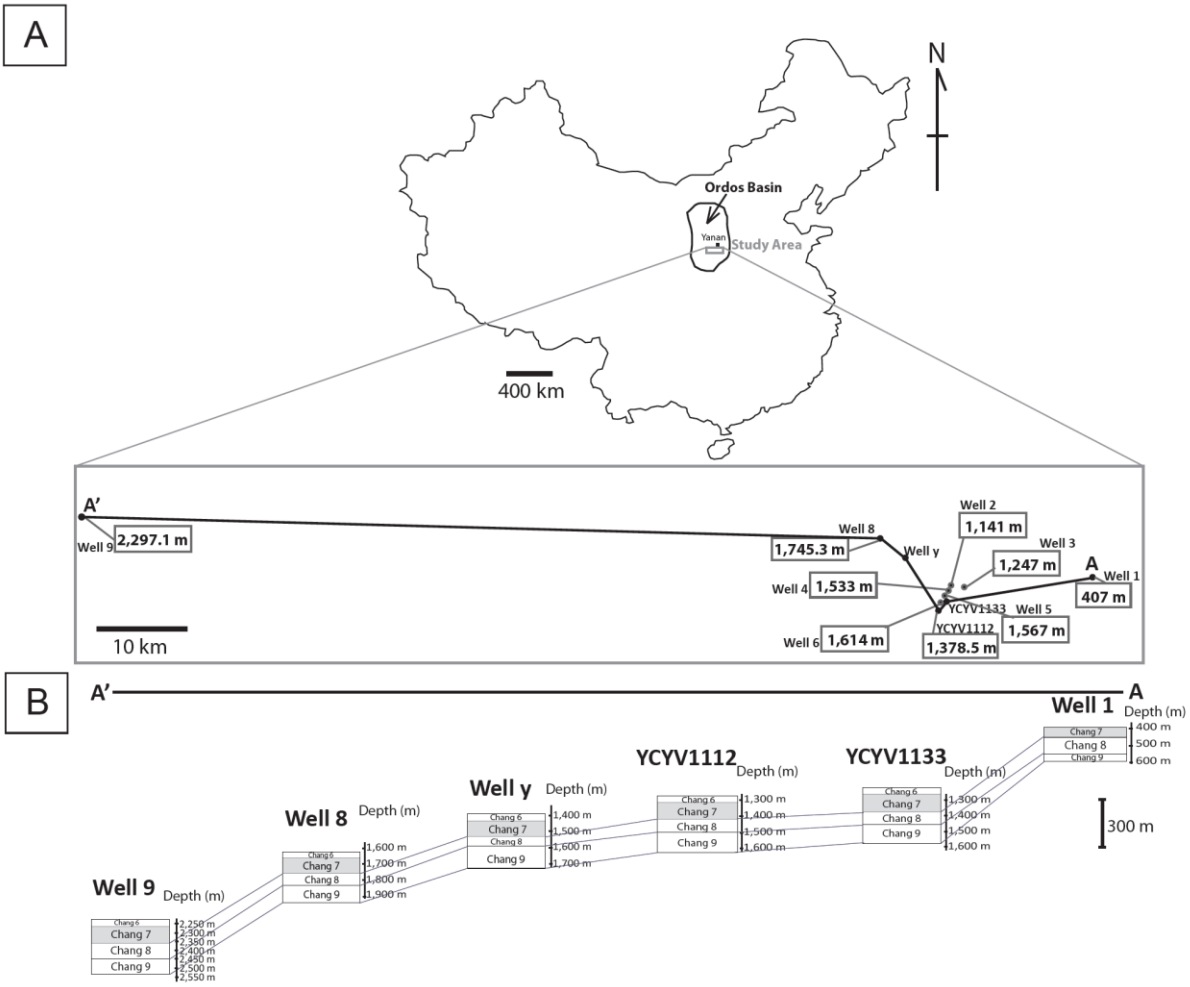

Figure 5.3: Location of study area in the Ordos Basin, China and Yanchang wells sampled. Well 1 (east) is the most proximal and Well 9 (west) is the most distal. (A) Cross section of line A-A' in (B) illustrating a dip-direction profile from Well 1 to Well 9. Subsurface correlation of Yanchang members is provided by the Yanchang Petroleum Group. YCYV 1112 is a representative well from Loucks et al., 2017.

5.3.1 FE-SEM Analyses and X-Ray Mapping

To determine texture, fabric, pore types, and pore-size distribution, a flat surface was prepared for FE-SEM analysis by Ar-ion-beam cross sectional milling using a Leica EM TIC020 Triple Ion Beam Miller (Loucks et al., 2009). An aliquot of approximately 1 cm^3 cube sample was used for Ar-ion milling. Each sample was milled for 10 hr using an

accelerating voltage of 8 keV and a current of 2.8 mA. A thin (5 nm or less), conductive coating of iridium (Ir) was applied to each sample to reduce charging and improve SEM image quality. FE-SEM with an FEI Nova NanoSEM 430 microscope, was used to image pores, organic matter (OM), and mineral grains under an accelerating voltage of 5–10 keV and a working distance of 4–5 mm.

Backscattered electron (BSE), secondary electron (SE), and SE through-the-lens detector (TLD) images were collected systematically at four different magnifications: 5,000X, 14,000X, 60,000X, and 160,000X (Figure 5.4). TLD imaging was used for high-magnification (160,000X) examination. The ion-milled surface provides a typical half-moon shaped viewing area of approximately 0.5 cm by 0.5 mm (Figure 5.4). To describe and quantify the sample, five backscattered electron (BSE) and secondary electron (SE) photomicrographs were taken at equal intervals perpendicular to bedding along the milled surface at 5,000X (machine magnification) (Figure 5.4). For each 5,000X photomicrograph, two to three 14,000X SEM photomicrographs were taken perpendicular to bedding planes. For each 14,000X photomicrograph, two to three 60,000X SEM photomicrographs were taken perpendicular to bedding planes and two high-resolution 160,000X SEM photomicrographs were taken to image the detailed size and shape of OM pores. The detection limit of pore size under FE-SEM is 5 nm; therefore, pores smaller than 5 nm cannot be resolved. Additional imaging techniques such as low-voltage mode SEM, HIM (helium-ion microscopy), and TEM (transmitted electron microscopy) were applied to clearly characterize pore sizes from sub-nanometer to tens of nanometers (Smith et al., 2016).

Identification of mineral components of the thin sections and ion-milled surfaces was completed by X-ray energy-dispersive spectroscopy detectors (EDS) mapping. Two 30-mm^2 Bruker XFlash Detectors—a silicon-drift detector (SDD) and an energy-

dispersive X-ray detector—were used, under an accelerating voltage of 15 keV, a spot size of 3.0–3.5, a 50-μm aperture, and a total count time greater than 700 s. Surfaces of uncovered polished thin sections (produced by Spectrum Petrographics) were coated with 25 nm of carbon. To allow systematic comparisons of samples, X-ray maps of thin sections and Ar ion-milled surfaces were collected at routine magnifications of 1,000X and 3,000X (thin sections), and 5,000X, and 14,000X (Ar ion-milled surfaces).

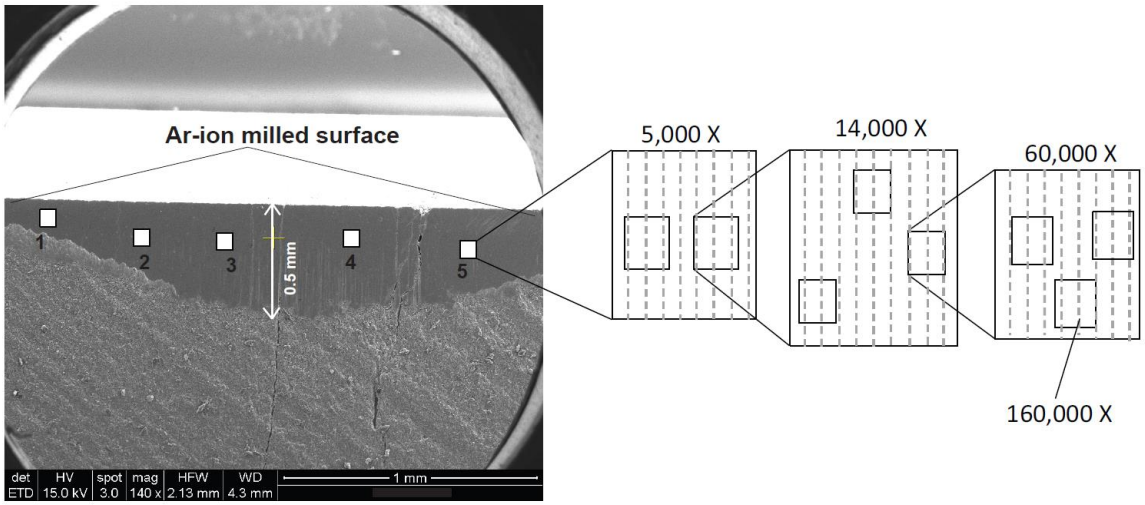

Figure 5.4: Example of Ar-ion milled surface of the Yanchang OM-rich argillaceous mudstone. The sampling method is shown by white squares. The image was taken at 5,000X, 14,00X, 60,000X, and 160X machine magnifications.

5.3.2 Particle-Size Analysis

Particle-size distribution for silt-grain populations was performed on BSE images and X-ray EDS maps. Grain outlines were interpreted and manually traced. Measuring particle sizes in a series of two-dimensional (2D) images was both time-consuming and labor-intensive. Because the surface view of the specimen was extremely limited on the ion-milled samples and there were not enough samples, the derived data representation of the specimen caused the greatest uncertainty. The best practice would have been to obtain high-resolution 2D mosaics of several mineral maps on a larger area and integrate the

results with three-dimensional (3D) data to provide a dataset using, for example, QENSCAN. Digitization and quantification were performed using JMicroVision image analysis program (Roduit, 2008). The pore-tracing method began with scale calibration and pixel determination in JMicrovision.

5.3.3 Nitrogen-Gas Adsorption Analysis

Nitrogen PSD analyses were performed using an Autosorb-iQ-MP instrument (Quantachrome Instruments) equipped with a vacuum pump capable of reaching 5E-7 Pa. Samples were crushed to 20–50 mesh size, and residual oil was removed by CH_2Cl_2 solvent extraction. At least 500 mg of the sample was placed into 6-mm-stem quartz sample cells and degassed for 12 hr at 110°C under vacuum. Nitrogen at 77 K was used as the probe gas for all experiments. Surface areas were calculated using the best linear range between 0.05 and 0.3 P/P_o of N_2 sorption, with a minimum of five points used in the Brunauer–Emmett–Teller (BET) surface-area analysis. PSDs were obtained using the density functional theory (DFT) method, which is available within the ASiQwin instrument software package (v. 2.02).

5.3.4 Helium Porosity Analysis

Porosity was measured with crushed samples having a mesh size of 20–50 (0.707 to 0.841 mm) using the Gas Research Institute (GRI) method (Luffel et al., 1993). The GRI method involves a helium expansion process from which initial and equilibrium pressures can be measured. With known volumes of the reference cell and sample cell, grain volume of the sample can be measured. Bulk volume of samples was measured using a 3D laser scanner (Peng and Loucks, 2016). With known bulk volume and grain volume of the sample, porosity can be calculated as 1 – bulk volume/grain volume. The advantage of using helium (He) gas to measure porosity is because helium has greater

access to the fine pores in mudstones than larger molecules like argon or methane. Using gases other than helium also requires corrections for sorption. An advantage of using helium instead of mercury injection is that it does not destroy the rock sample.

5.4 MINERALOGY AND LITHOLOGY

General core description and facies identification of the Yanchang Formation were completed by Kitty Milliken at the Bureau of Economic Geology. Lithofacies characterization was also completed using thin-section petrography, x-ray diffraction (XRD), Rock-Eval and LECO TOC analyses. Five major lithofacies were identified: ash, sandstone, argillaceous siltstone, OM-lean argillaceous mudstone, and OM-rich argillaceous mudstone. All samples used for this study are OM-rich argillaceous mudstones, which likely deposited in basinward position during lake level rise in prodelta and/or lake environments. These mudstones have little bioturbation, high OM content, and have parallel lamination. Several studies have documented the mineralogy of the Yanchang Formation (e.g., Wang, 2012; Guo et al., 2014; Yao et al., 2013; Rowe et al., 2015; Jiang et al., 2016). Quartz, feldspar, and clay minerals are major components; ankerite, siderite, and pyrite are diagenetic minerals; calcite is either detrital (as calcitic allochems) or diagenetic (Table 5.1). These OM-rich argillaceous mudstones are highly feldspathic, with total feldspar content exceeding total quartz in many samples. Most Chang 7 samples in the proximal area (Wells 1 to 8) consists of 30 to 40 wt% clay minerals, 23 to 33 wt% quartz, and 13 to 29 wt% feldspar (Table 5.1, Figure 5.5). These proximal samples contain abundant quartz and feldspar (> 50%) with little carbonate, different from the Chang 7 mudstone in the YCYV1112 well (Figure 5.5). The mineralogy of the sample from the Chang 7 Member in most distal Well 9 (which is closest to the lake center) has a distinct composition: 78 wt% quartz and 22 wt% clay

minerals, contrasting sharply with samples in the proximal area (Table 1). This sample lacks the abundant feldspars and micas that characterize the silt fraction in other samples. In this sample, half of the thin section is composed of a layer of volcanic ash. The other portion of the sample contains wavy-laminated mudstone suggestive of a microbial mat (Figure 5.6; Milliken et al., 2017).

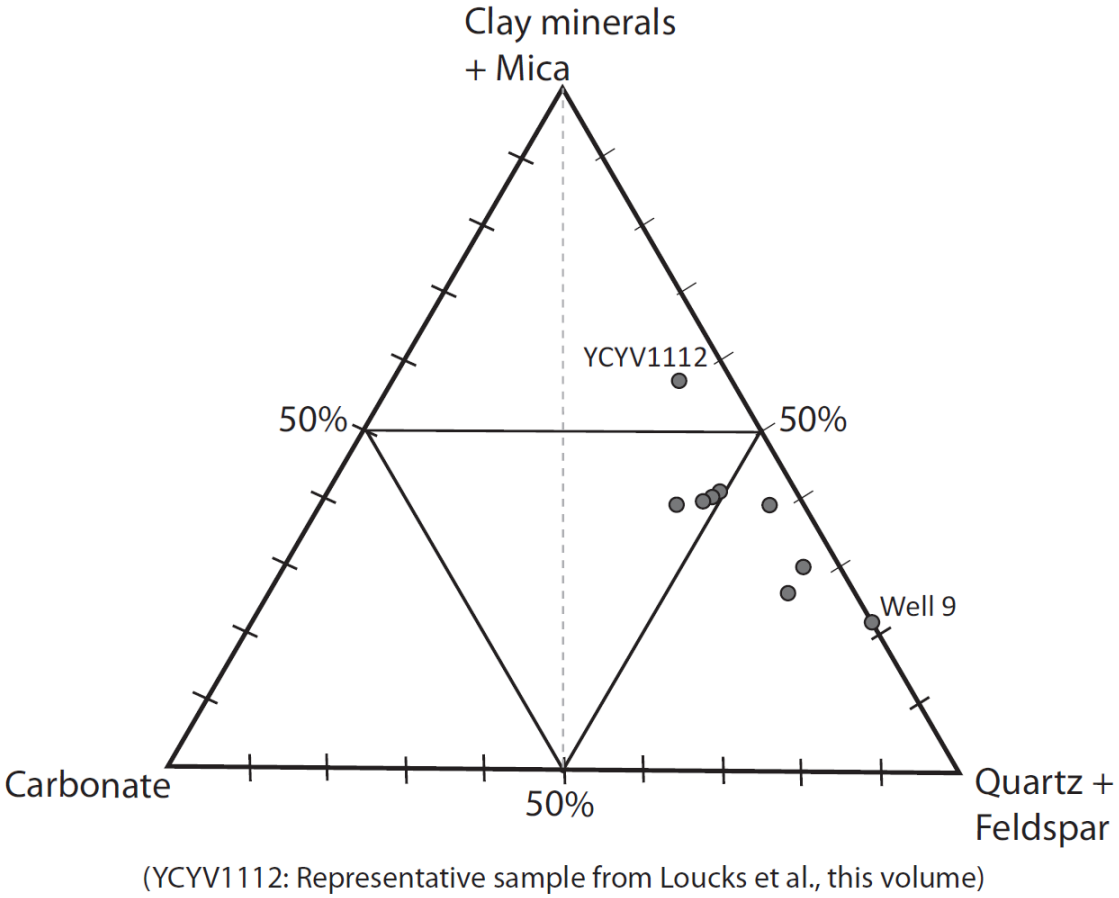

Figure 5.5: Mineralogy ternary diagram showing XRD analysis results of studied Yanchang OM-rich, argillaceous mudstone samples. Well 9 locates close to the center of lake basin and YCYV 1112 is a representative sample from Loucks et al. (2017).

Depth (m)	Well name	Quartz	K-Feldspar	Plagioclase	Calcite	Fe-Dolomite	Siderite	Pyrite	R3 M-L I/S (15%S)**	Illite&Mica	Kaolinite	Chlorite	Total clay mineral
407	Well 1	26.4	8.2	20.5	0.9	2.4	1.4	1	10	11.6	4.8	12.8	39.2
1141	Well 2	24.7	5.4	15.1	2	3.3	7.4	2.5	17.9	16.9	1.8	3	39.6
1247	Well 3	28.9	9.2	26.4	1.6	2.1	1.1	0.7	11.3	9.9	2.8	6	30
1378.5	YCYV1112	15.1	4.8	13.9	0.8	4.4	2.0	1.7	1.3	44.5	4.2	7.3	57.3
1533	Well 4	33.2	1.9	11.2	3.1	6.9	0	2.8	20.5	15.6	1.4	3.4	40.9
1567	Well 5	23	7.7	17	4.3	3.9	2.7	1	14.2	13.9	3.4	8.9	40.4
1614	Well 6	23	11	10.2	4.2	4.7	7.4	0.6	13	14.4	4.4	7.1	38.9
1745.3	Well 8	24.2	18.2	21	1.4	5.6	1.7	1.8	9.7	11.9	1.4	3.1	26.1
2297.1	Well 9	77.6	0	0	0	0	0	0.3	16.8	4.6	0.4	0.3	22.1

Table 5.1: XRD bulk mineralogy of Yanchang Formation samples. *R3 M-L I/S (15%S) represents interlayered illite and smectite.

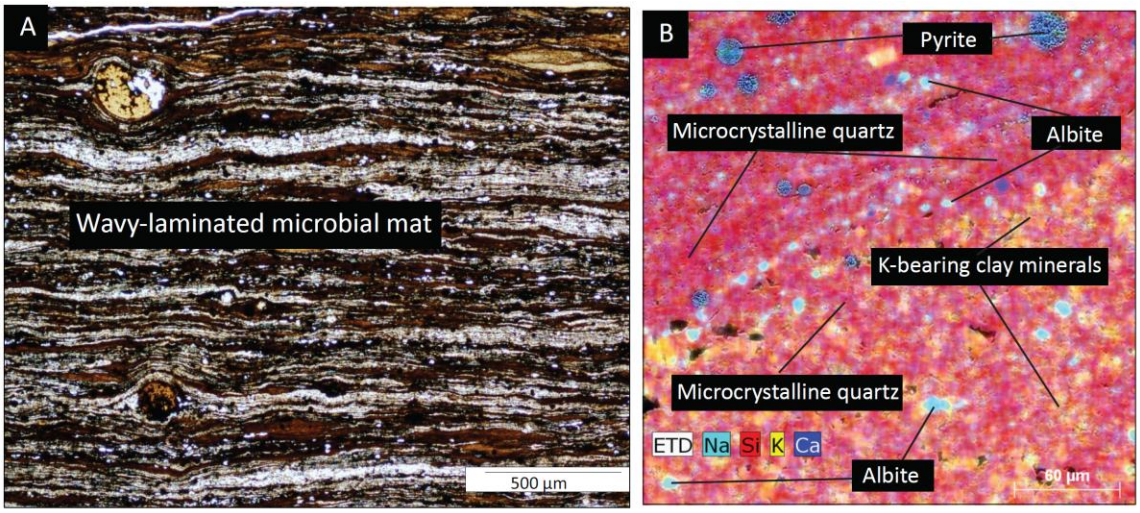

Figure 5.6: Thin-section photomicrograph and X-ray map of Chang 7 mudstones in Well 9 (distal lake center). (A) Thin-section photomicrograph showing wavy-laminated microbial mat. (B) SEM X-ray map showing mineralogical compositions of probable altered volcanic ash: microcrystalline quartz (78%), albite, pyrite framboids, and potassium-bearing clay minerals.

Ruppel and Rowe (2017) have also completed a detailed characterization of the depositional facies of the Yanchang Formation on the basis of core description, thin-section microscopy, and chemostratigraphy obtained from X-ray fluorescence (XRF) analyses on two continuous cored wells YCYV1112 and YCYV1133. Five major facies were defined and each facies infers its own depositional environment and setting: (1) feldspathic, quartzose, argillaceous arkose facies, (2) quartzose, feldspathic, argillaceous arkose facies, (3) OM-lean mudstone facies, (4) OM-rich argillaceous mudstone facies, and (5) volcanic ash facies. Each facies can be correlated to rock attributes and wireline log responses. According to their (Ruppel and Rowe, 2017) chemostratigraphy characterization, samples in this study are characterized by abundant argillaceous peloids, high TOC content (>3 wt%), and faint to well-developed laminations. The abundance of organic matter and clay minerals reflect low-energy deposition and low sediment accumulation rate, distant from clastic source input. This OM-rich argillaceous mudstone

facies is commonly found in the lower part of the Chang 7 Member, middle Chang 8 Member, and upper Chang 9 Member. Several authors (e.g. Ji et al., 2008; Yao et al., 2013; Yuan et al., 2015; Pan et al., 2016) further separate Chang 7 into three submembers (Chang 7-1, 7-2, and 7-2) based on wireline log signatures and lithologies: Chang 7-1 dominated by sandstone and siltstone; Chang 7-2 dominated by sandstone, siltstone, and mudstone; Chang 7-3 dominated by mudstone. Our samples were taken from mudstones in either the Chang 7-2 or Chang 7-3 submembers on the basis of the detailed stratigraphic correlation among studied wells provided by the Yanchang Petroleum Group.

Feldspar dissolution and albitization are common diagenetic processes that produce mineral-hosted pores in these lacustrine mudstones (Zhang et al., 2012; Wang et al., 2015a). It is worth noting that the sample in Well 8 has the highest K-feldspar (18.2 wt.%) and total feldspar (close to 40 wt%) contents compared to those of other samples. This unusually high concentration of feldspars requires further investigation and might relate to changes in sediment sources. Bulk mineralogy from Guo et al. (2014), Loucks et al. (2017), and Ruppel and Rowe (2017) shows that most Chang 7 to Chang 9 samples are relatively rich in clay minerals (40 to 80 wt.%) and contain less quartz (average of around 20 wt.%). The overall clay mineral-rich content has been interpreted to suggest that Yanchang mudstones are poor candidates for hydraulic fracturing (Wang, 2012; Ruppel and Rowe, 2017). However, sample sets from Jiang et al. (2016), Ruppel and Rowe (2017), and this study at least indicate that clay mineral-poor lithologies may be locally present in the more distal regions of the basin and more suitable for hydraulic fracturing. The heterogeneity of the mineralogy in the Yanchang Formation across the southeastern Ordos Basin has also been recognized by Wang et al. (2015a, b) and could be affected by differential sediment inputs from the two dominant source areas: a fluvial

deltaic system to the northeast and braided stream delta system to the southwest. Sediment influx from these two sources may not have been concurrent, thus producing complex facies stacking patterns in areas dominated by each system. If this is the case, correlation of regional deepening and shallowing cycles, as well as identification of mineralogical "sweet spots" for exploration, may be more difficult than has been concluded.

5.5 THERMAL MATURATION, ORGANIC MATTER, AND TOC CONTENT

Thermal maturation analyses from Rock-Eval pyrolysis, bitumen reflectance measurements, and biomarkers indicate that these samples are in the peak oil window maturation (equivalent vitrinite reflectance ranges from 0.78 to 1.1% R_o), similar to data reported by Wang (2012), Tang et al. (2014), Guo et al. (2014), Jiang et al. (2016), and Loucks et al. (2017) (Table 5.2; Figures 5.7 and 5.8). According to transmitted-light and incident-light organic petrology analysis, present-day observable organic matter in these mudstones is commonly solid bitumen with minor terrestrial organic matter (Hackley et al., 2017). The most proximal (shallowest) Chang 7 mudstone sample in Well 1 contains terrestrial kerogen in the form of fluorescent cutinite, a leaf exine. Some amorphous fluorescent kerogen possibly degraded algal material, is also present.

Because Chang 7 samples are within the oil window, some of the original kerogen has been converted to petroleum. The dominant organic matter is now predominantly extractable solid bitumen as indicated by a significant decrease in total organic carbon (TOC) content after solvent (CH_2Cl_2) extraction (Hackley et al., 2017). Rock-Eval pyrolysis and biomarker data indicate that most samples probably have mixed Type I/II

Depth (m)	Depth (ft)	Well name	OM Type	Member	BRo(m)*	MPI (Rc) *	He porosity	N2 porosity	Leco TOC (wt%)	Rock-Eval S1 (mg HC/g)	Rock-Eval S2 (mg HC/g)	Rock-Eval S3 (mg CO2/g)	Rock-Eval Tmax (°C)	HI
407	1335	Well 1	**Type III mixed**	Chang 7	0.79	0.78	5.68	4.1	14.70	3.54	43.84	0.84	442	298
1141	3743	Well 2	mixed	Chang 7	0.84	0.97	9.74	6.7	5.19	7.44	10.47	0.43	444	202
1247	4090.2	Well 3	mixed	Chang 7	N/A	0.92	2.66	3.5	4.08	2.26	7.45	0.55	454	183
1378.5	4522	YCYV1112	mixed	Chang 7	0.93	0.89	2.2	4.3	8.20	5.28	20.44	0.65	447	249
1533	5028	Well 4	mixed	Chang 9	N/A	1.02	1.69	7.5	4.48	3.84	9.22	0.63	453	206
1567	5140	Well 5	mixed	Chang 7	0.95	1.1	5.68	5.6	4.52	3.88	6.08	0.66	457	135
1614	5294	Well 6	mixed	Chang 7	N/A	1.06	2.83	4	4.94	2.24	7.58	0.95	450	153
1745.3	5725	Well 8	**Type I/II**	Chang 7	0.87	0.79	4.23	1.1	10.90	3.20	52.95	0.73	450	486
2297.1	7534	Well 9	**Type I/II**	Chang 7	0.95	1.04	7.24	4.8	3.71	1.92	7.60	0.58	459	205

Table 5.2: Geochemical properties and total porosity of Yanchang Formation samples. *BRo(m) is measured solid bitumen reflectance, and *MPI(Rc) is calculated thermal maturity equivalent from aromatic biomarkers (methylphenanthrene index).

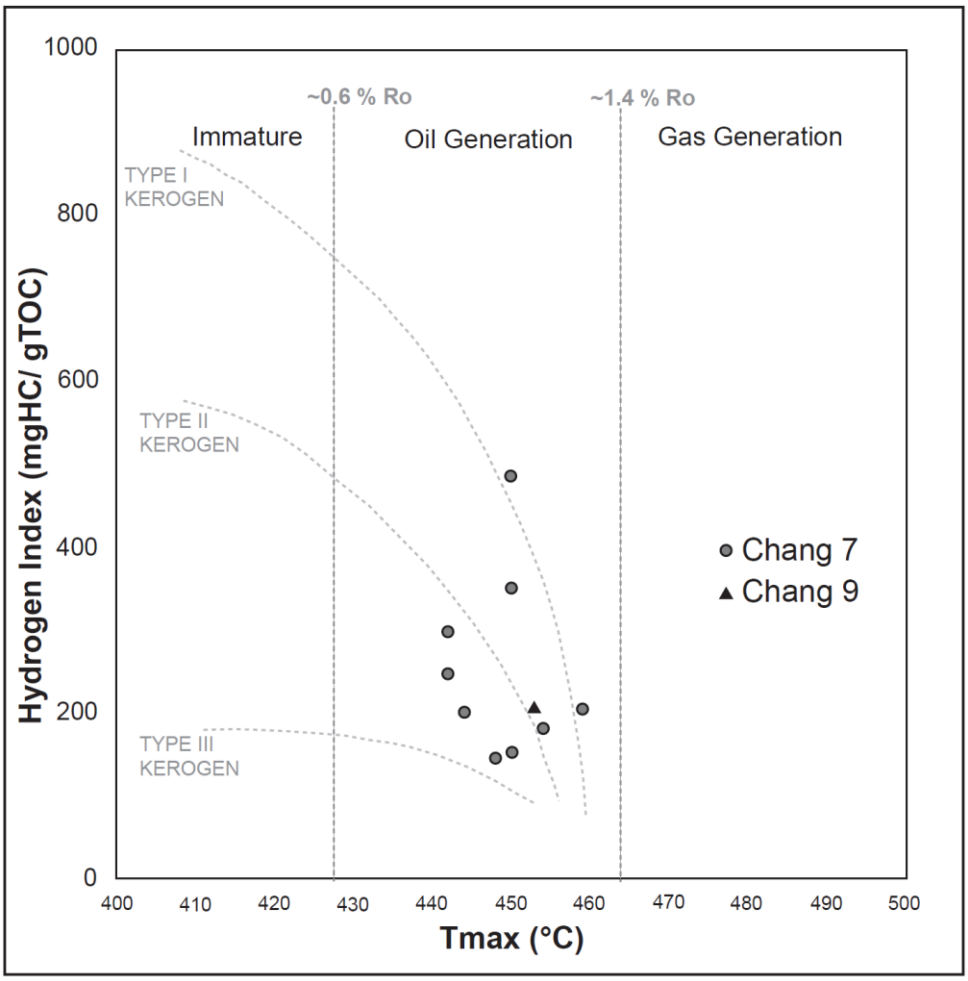

Figure 5.7: Plot of hydrogen index (mgHC/gTOC) versus T_{max} (°C) from Rock-Eval pyrolysis illustrating oil window thermal maturation of Yanchang OM-rich, argillaceous mudstone samples. Chang 7 Member (circles); Chang 9 Member (triangles).

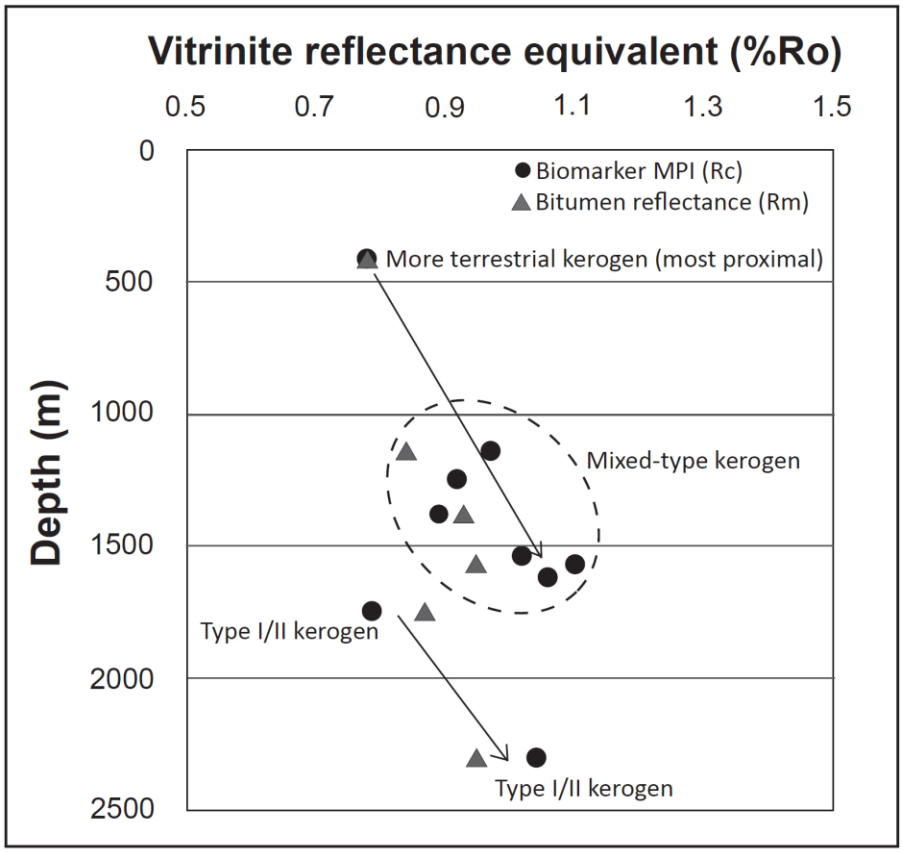

Figure 5.8: Plot of estimated equivalent vitrinite reflectance (%Ro) versus sample depth (m). Measured bitumen reflectance (Rm, triangles) and calculated vitrinite reflectance equivalent from aromatic biomarkers methylphenanthrene (Rc, circles) exhibit similar maturity values. Two possible maturation trends are proposed and shown by black arrows.

(lacustrine/marine) and Type III/IV terrestrial and inert kerogen. The two most distal samples (Wells 8 and 9) appear to be more dominated by Type I/II kerogen, and the most proximal sample (Well 1) possibly has slightly more terrestrial kerogen (Table 5.2; Sun et al., 2017). Ruppel and Rowe (2017) suggested, on the basis of relations between isotope data and facies, that the more distal OM-rich facies contained dominantly Type I/II kerogens whereas the more sandstone- and siltstone-rich facies contained Type III

kerogen. Tang et al. (2014), using relative maceral composition, identified Type II kerogen as the dominant organic matter composition, with minor amounts of Type I and Type III kerogen in the Chang 7 Member. Palynofacies and geochemical analyses by Zhang et al. (2015) indicate that the Chang 7 is rich in amorphous organic matter (AOM) and phytoclasts, and the amount of AOM can be correlated with the hydrogen index (HI). They also suggest abundant Type I and II kerogen in the Chang 7 and Chang 9. Pan et al. (2016) identified alginite (Type I kerogen) at the base of Change 7 Member (Chang 7-3).

The TOC content of the OM-rich mudstone samples ranges from 3.71 to 14.70 wt.%, with a median TOC value of 4.94 wt.% (Table 5.2; Figure 5.9). This wide range of TOC and median TOC values are similar to what is reported in the literature (Figure 5.10; Guo et al., 2014; Han et al., 2014; Zhang et al., 2015; Cao et al., 2016; Li et al., 2016; Pan et al., 2016; Loucks et al., 2017). The majority of the samples with mixed kerogen type samples have similar TOC contents (4.08 to 5.19 wt.%) and thermal maturities (0.92 to 1.10 $\%R_o$) (Figures 5.8 and 5.9). Samples from Well 1 and Well 8 have slightly lower thermal maturities and higher TOC content than do the rest of the mudstone samples. Two maturity trends in Yanchang lacustrine mudstones are possible because of changes in kerogen types from proximal to distal regions (Figures 5.8 and 5.9; Yuan et al., 2015; Sun et al., 2017). For the transition from dominant Type III terrestrial kerogen to mixed Type II/III kerogen from proximal to distal areas, we propose that Type III kerogen was episodically shed from landward areas during times of increased terrigenous clastic sediment influx, and Type II/III mixed kerogen dominated in distal areas when sediment influx was lower. For the transition from mixed Type II/III kerogen to mixed Type I/II kerogen, Ji et al. (2008, 2010) first identified algal fossil remains of *Leiosphaeridia* and *Botryococcus* (Type I kerogen) in the Chang 7 Member southwest of our study area, suggesting that the salinity of the fresh-water Ordos Lake fluctuated between fresh and

brackish. Because lake expansion was associated with maximum flooding and a warm and humid climate during the deposition of the Chang 7 (Ji et al., 2008, 2010), organic matter types probably varied across the basin, producing heterogeneity in kerogen availability, type, and quality.

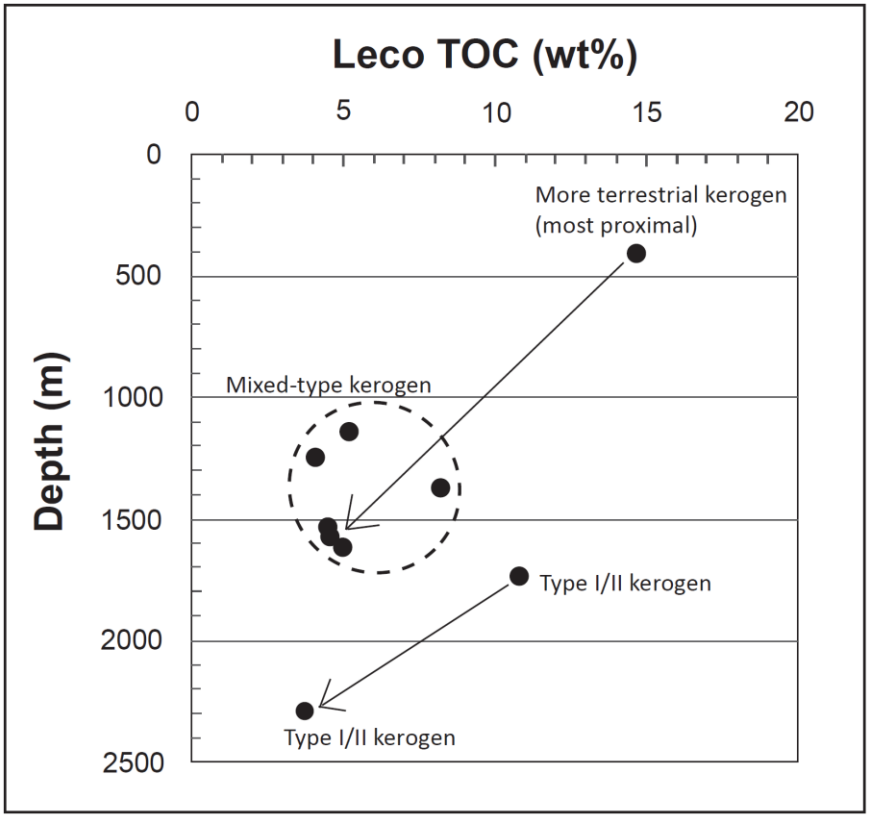

Figure 5.9: Plot of TOC (wt%) versus sample depth (m). The TOC trend is opposite from maturity trend shown in Figure 5.4. TOC decreases with increased maturity.

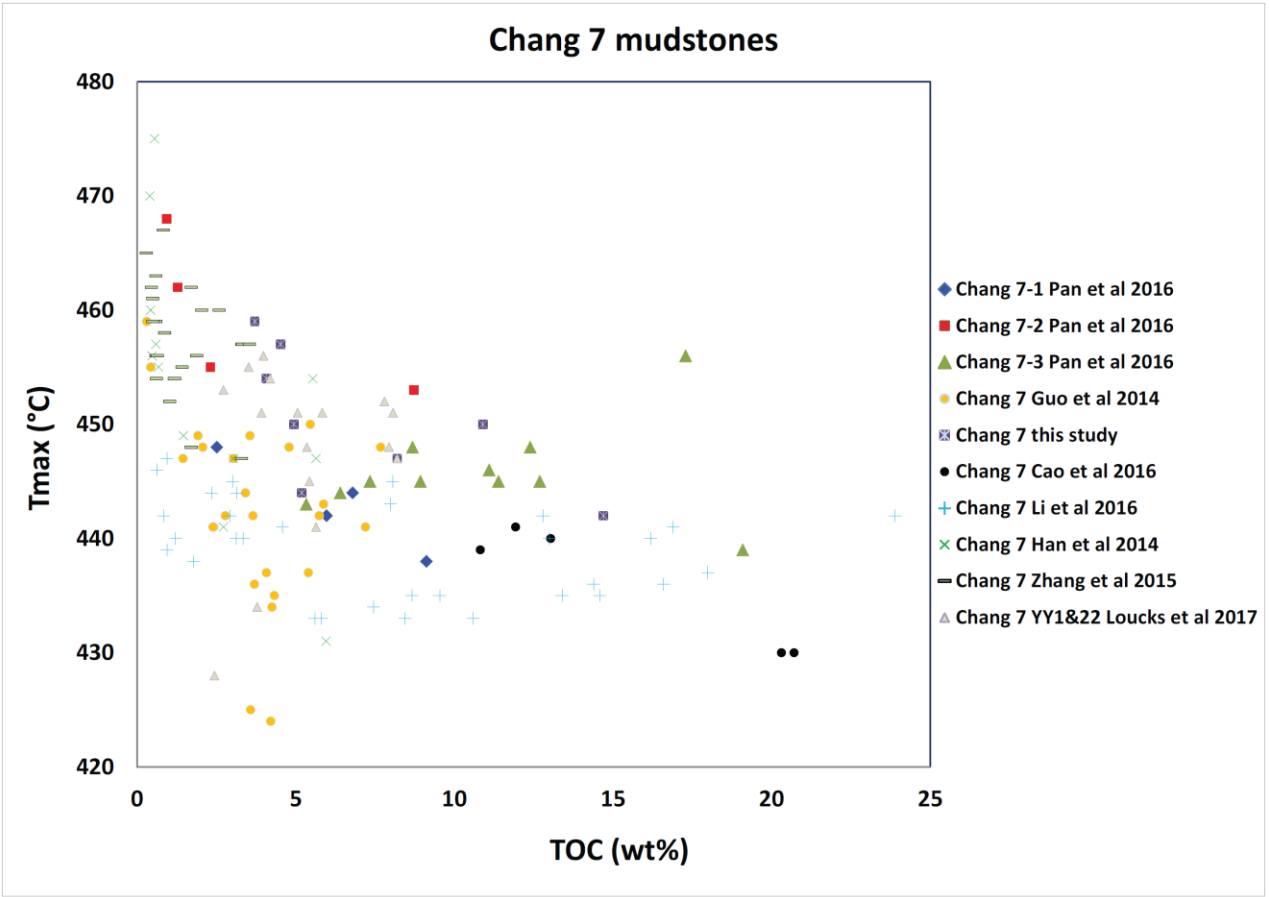

Figure 5.10: Plot of reported TOC (wt%) versus T_{max} (°C) of Chang 7 Member from six previous studies, this study, and Loucks et al. (2017). Only Pan et al. (2016) documents subdivided Chang 7-1, 7-2, and 7-3 units. The rest reports Chang 7 as one section.

5.6 PORE TYPES AND PORE-SIZE DISTRIBUTION

5.6.1 Pore Types

Primary interparticle and intraparticle pores, OM-hosted pores, and modified mineral-hosted pores within relic organic matter are observed within these OM-rich argillaceous mudstone facies (pore classification by Loucks et al., 2012 and Ko et al., 2016 a, b). We differentiated modified mineral-hosted pores from primary interparticle and intraparticle pores to ensure that they were not misinterpreted and misidentified as OM-hosted pores (Ko et al., 2016b). The modified mineral-hosted pores were also recognized and named "OM-mineral interface pores" by Pommer and Milliken (2015). Modified mineral-hosted pores are variations of primary mineral-hosted pores, although the pores contain a residual OM rim. They can result from three different processes: (1) Oil and gas can leave the original mineral-hosted pore, generally during sample preparation at various conditions. A rim of residual oil is formed when the heavy-component of the oil is adsorbed on the mineral surface. The shape and size of these pores are related to the pore formed by the surrounding framework grains or the original mineral-hosted pores (Figure 5.11A). (2) Pores can also form from petroleum (bitumen) migration and trapping of connate water on the edge and/or tip of minerals (Figure 5.11B). In other words, the migrated bitumen has only partially filled the pore space. (3) Incipient gas generation can create gas bubbles that nucleate on mineral surfaces prior to petroleum (bitumen) migration. These pores are characterized by being in contact with both mineral matter and organic matter. The occurrence and shape of these pores could be controlled by the wettability of the mineral surface and/or early gas generation and nucleation. Generally, the modified mineral pores are a few micrometers to tens of micrometers in diameter, some falling in the nanometer scale. Most of the pore shapes are

irregular, but some are rounded. The pore itself is not completely surrounded by solid bitumen, as a true OM-hosted pore would be.

OM-hosted bubble pores can only be observed in samples from Wells 2 and 5 (Table 5.3; Figure 5.11D). OM-hosted spongy pores — defined as pores with rounded, subrounded, or subangular shapes and diameters from 3 to 200 nm (based on observations of marine mudrocks) — are the most abundant pore type in these organic matter-rich lacustrine mudstones. However, sizes of OM-hosted spongy pores in lacustrine mudrocks in the present study appear to be one or two order of magnitude smaller than those found in marine mudrocks (e.g., Eagle Ford Formation) (Figure 5.12). OM devolatilization cracks were commonly observed adjacent to OM-hosted spongy pores (Figure 5.13). These OM devolatilization cracks and OM-hosted spongy pores were possibly developed in migrated post-oil solid bitumen and/or pyrobitumen (Curiale, 1986; Bernard et al., 2012; Loucks and Reed, 2014).

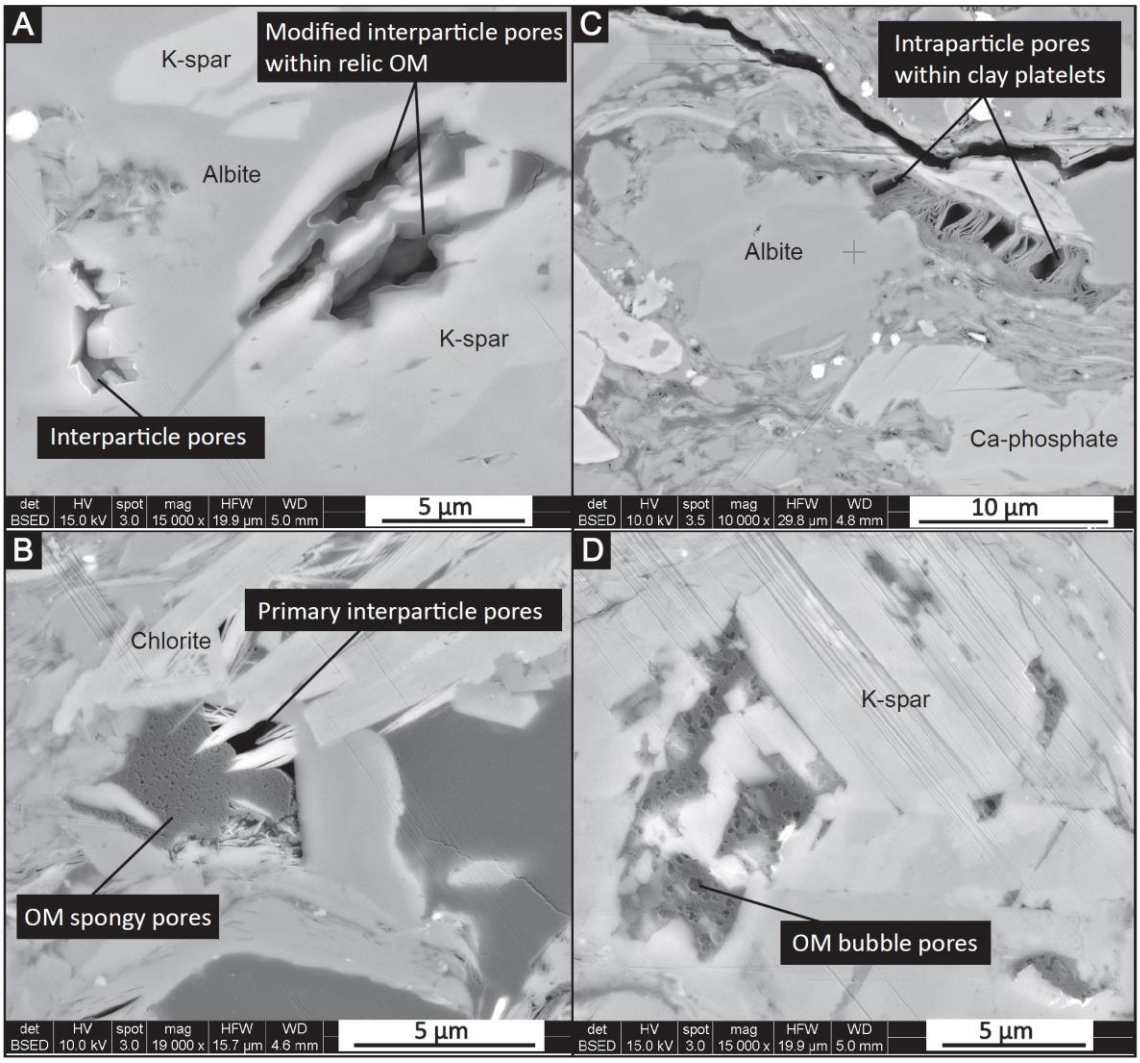

Figure 5.11: SEM photomicrograph images of pores in Yanchang Formation mudstones. (A) Interparticle pores and modified intraparticle pores in Well 1. (B) Modified interparticle pores and OM-hosted spongy pores in Well 3. (C) Intraparticle pores within clay platelets in Well 5. (D) OM-hosted bubble pores in Well 2. K-spar represents K-feldspar. Backscattered electron photomicrographs.

Well name	Depth (m)	Interparticle pore	Intraparticle pore	OM bubble pore	OM spongy pore	OM devolatilization crack	OM with no pore	Texture	Helium porosity (%)	N2 porosity (%)
Well 1	407	√	√ (abundant)				√	Silt-rich	5.68	4.1
Well 2	1141	√ (abundant)	√ (abundant)	√	√ (abundant)		√	Silt-rich (medium to coarse silt)	9.74	6.7
Well 3	1248	√	√		√ (abundant)	√	√	Silt and clay	2.66	3.5
YCYV1112	1378.5				√ (abundant)		√	Clay-rich	2.20	4.3
Well 4	1533				√ (some)	√	√	Silt-bearing, clay-rich	1.69	7.5
Well 5	1567	√	√	√	√ (abundant)	√	√	Silt-rich (coarse silt)	5.68	5.6
Well 6	1614				√ (abundant)	√	√	clay-rich	2.83	4.0
Well 8	1745.3				√ (some)	√	√	Silt-bearing, clay-rich	4.23	1.1
Well 9	2297.1				√ (abundant)	√	√	Silt rich (authigenic quartz and K-bearing clay minerals)	7.24	4.8

Table 5.3: Qualitative description of porosity, texture, pore types, and pore abundances in Yanchang Formation mudstones. Mudstone nomenclature from Macquaker and Adams (2003).

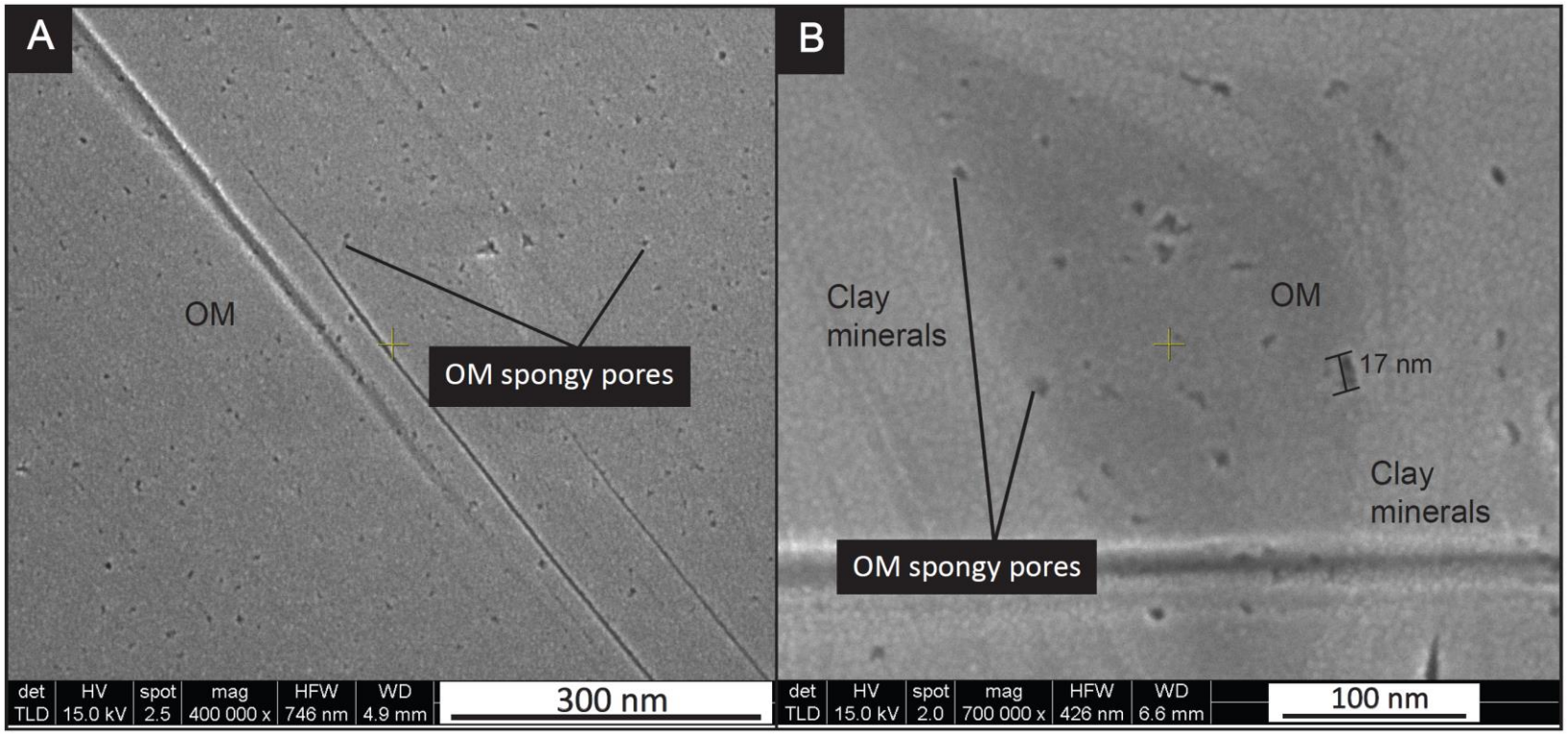

Figure 5.12: SEM photomicrograph images of OM-hosted spongy pores in Yanchang Formation mudstones. Sizes of these OM-hosted spongy pores are below 17 nm. (A) OM-hosted spongy pores in Well 6. (B) OM-hosted spongy pores mixed with clay minerals. The largest OM-hosted spongy pore is labeled (diameter = 17 nm). Backscattered electron photomicrographs.

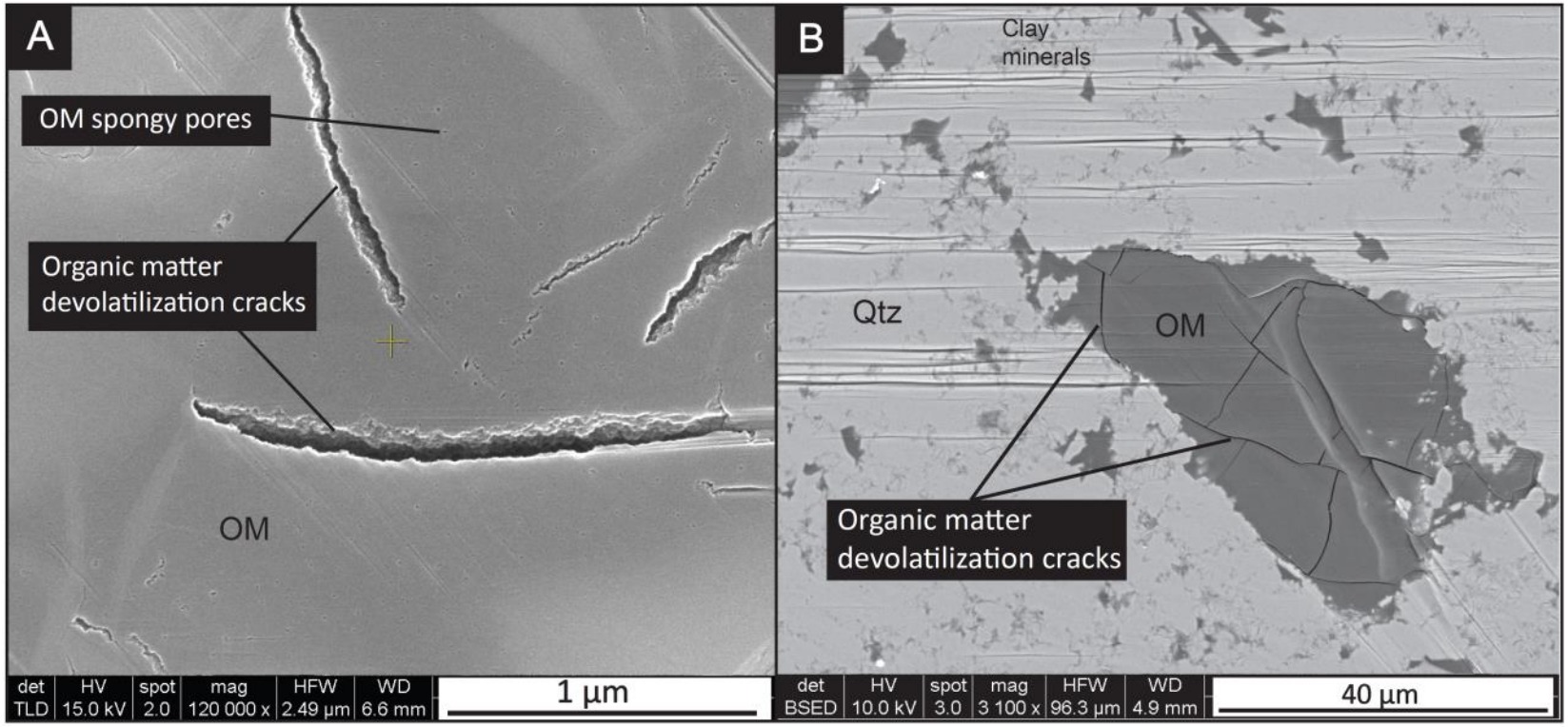

Figure 5.13: SEM photomicrograph images of artifact OM devolatilization cracks and OM spongy pores in Yanchang Formation mudstones. (A) Lengths of devolatilization cracks in organic matter are a few micrometers. (B) Devolatilization cracks are limited to organic matter. Qtz = quartz; OM = organic matter.

5.6.2 Pore-Size Distribution (PSD)

Results of nitrogen-gas adsorption analysis show that there are four distinct PSD's within the Chang 7 Member of the Yanchang Formation (Figure 5.14; Zhang et al., 2017). Samples were grouped on the basis of similarities in their relative pore volume with respect to pore-width distribution. The first PSD group contains a wide range of pore sizes, ranging from 3 to 130 nm, and consists of samples from relatively proximal areas from shallow depths (wells 1, 2, and 5) (Figure 5.14A). The total porosity of these samples is largely controlled by pore sizes larger than 17 nm. The second PSD group contains two subgroups of pore sizes: one ranging from 3 to 17 nm, and the second with pores greater than 17 nm (Figure 5.14B). Samples from depths of 1,247 m (well 3) and 2,297 m (well 9) are included in this category; their pore volumes are controlled equally by both smaller and larger pore sizes. The third PSD group exhibits a unimodal PSD, with the majority of pores smaller than 17 nm (Figure 5.14C). Samples from depths of 1,533 m (well 4) and 1,614 m (well 6) are included in this category. The fourth PSD group shows almost no pore development (Figure 5.14D). The sample at a depth of 1,745 m (well 8) characterizes this pore-size distribution.

Nitrogen adsorption only measures pore sizes from 0.3 to 200 nm. Pores larger than 200 nm were observed qualitatively by FE-SEM imaging. Pore types identified using FE-SEM under varying magnifications are summarized in Table 5.3. Under the examination of FE-SEM, it is evident that most pores larger than 15 to 20 nm are mineral-hosted pores, whereas pores smaller than 17 nm are commonly OM-hosted pores (Figure 5.14). Samples at wells 4, 6, 8, 9, and YCYV 1112 have only OM spongy pores. Therefore, the majority of pores can be measured by nitrogen adsorption. Many of the interparticle, intraparticle, and OM bubble pores are larger than 200 nm, so samples at

wells 1, 2, 3, and 5 had a group of larger pores that cannot be accessed by nitrogen adsorption. Samples from the most proximal areas are dominated by mineral-hosted pores (Figure 5.14A). Others contain predominately OM-hosted pores (Figure 5.14B), both mineral-hosted and OM-hosted pores (Figure 5.14C), and minor OM-hosted and mineral-hosted pores (Figure 5.14D). Combined FE-SEM imaging and N_2 adsorption measurement techniques suggest that the abundance of OM-hosted spongy pores control the unimodal PSD (Figure 5.14B), that mineral-hosted pores controls PSD for pores larger than 17 nm (Figure 5.14A), and that both OM-hosted and mineral-hosted pores contribute to PSD (Figure 5.14C).

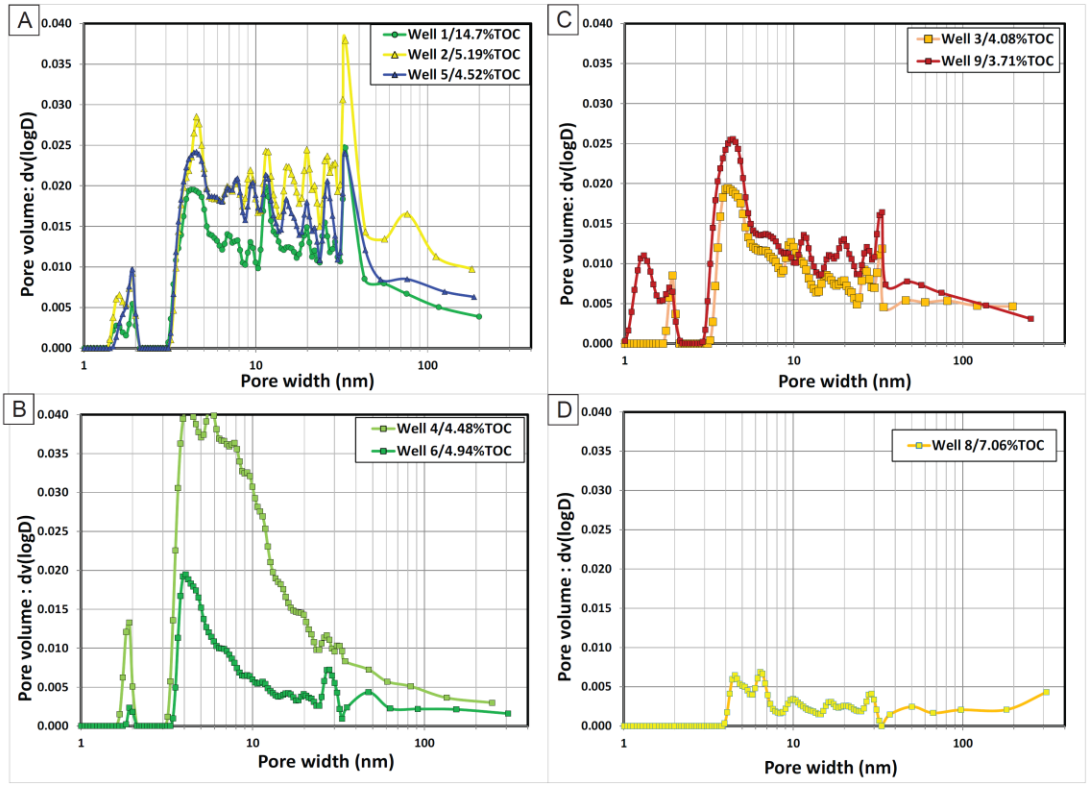

Figure 5.14 Plots of pore volume versus pore width (nm) showing four distinct patterns of pore-size distribution obtained from nitrogen gas adsorption measurements. Pore-size distributions from (A) Wells 1, 2, and 5, (B) Wells 3 and 9, (C) Wells 4 and 6, and (D) Well 8.

5.7 CONTROLS ON POROSITY, PORE TYPES, AND PORE-SIZE DISTRIBUTION

5.7.1 Controls on Total Porosity and OM Porosity

The total (bulk) porosity of the Yanchang mudstones was derived from both nitrogen adsorption and helium porosimetry. As mentioned earlier, nitrogen adsorption only measures pore sizes from 0.3 to 200 nm, whereas helium porosimetry measures the entire spectrum of pore sizes. We found a fairly poor correlation between nitrogen and helium porosity (correlation coefficient $R^2 = 0.0466$) in these Yanchang mudstones. The cause of this poor correlation is not clear. One possibility is that there are significant numbers of pores larger than 200 nm not taken into account using nitrogen adsorption. Plots of total porosity (derived from both nitrogen adsorption and helium porosimetry) against major mineralogical composition, TOC, HI, and thermal maturity are provided in Figure 5.15. In general, no correlation is apparent between helium porosity and any parameters. Some correlations can be found between nitrogen total porosity and mineralogy, and nitrogen total porosity and geochemical parameters. For example, a weakly positive correlation exists between nitrogen total porosity and clay mineral abundance (Figure 5.15A). This implies that some pores could be related to interparticle pores between mineral grains and clay minerals, and/or intraparticle pores between clay platelets. Also, a slightly negative correlation was found between nitrogen total porosity and Q+F+Py (quartz+feldspar+pyrite) abundance (Figure 5.15B). Quartz, feldspar, and pyrite are rigid-grain compositions in the Yanchang mudstone, and the majority of quartz and feldspar is detrital in origin. Because their abundance does not relate to porosity, it implies that quartz, feldspar, and pyrite abundance cannot help form a good rigid framework that inhibits mudstones from significant compaction.

A weakly positive correlation was found between nitrogen total porosity and calculated thermal maturity from the aromatic biomarker: methyl phenanthrene index (MPI), indicating porosity increases with increasing levels of thermal maturity (Figure 5.15C). Thermal maturity usually has a negative correlation with hydrogen index (HI). An immature mudstone has a higher HI value than a thermally mature mudstone. A negative correlation between OM porosity and hydrogen index (HI) also implies maturity controls on total porosity, especially OM porosity (Figure 5.15D). Table 3 shows that samples in wells YCYV 1112, 4, 6, 8, and 9 have only OM-hosted pores. Therefore, their total porosity is equal to OM porosity. A weakly negative correlation exists between nitrogen total porosity and TOC, and OM porosity and TOC (Figures 5.15E and 5.15F).

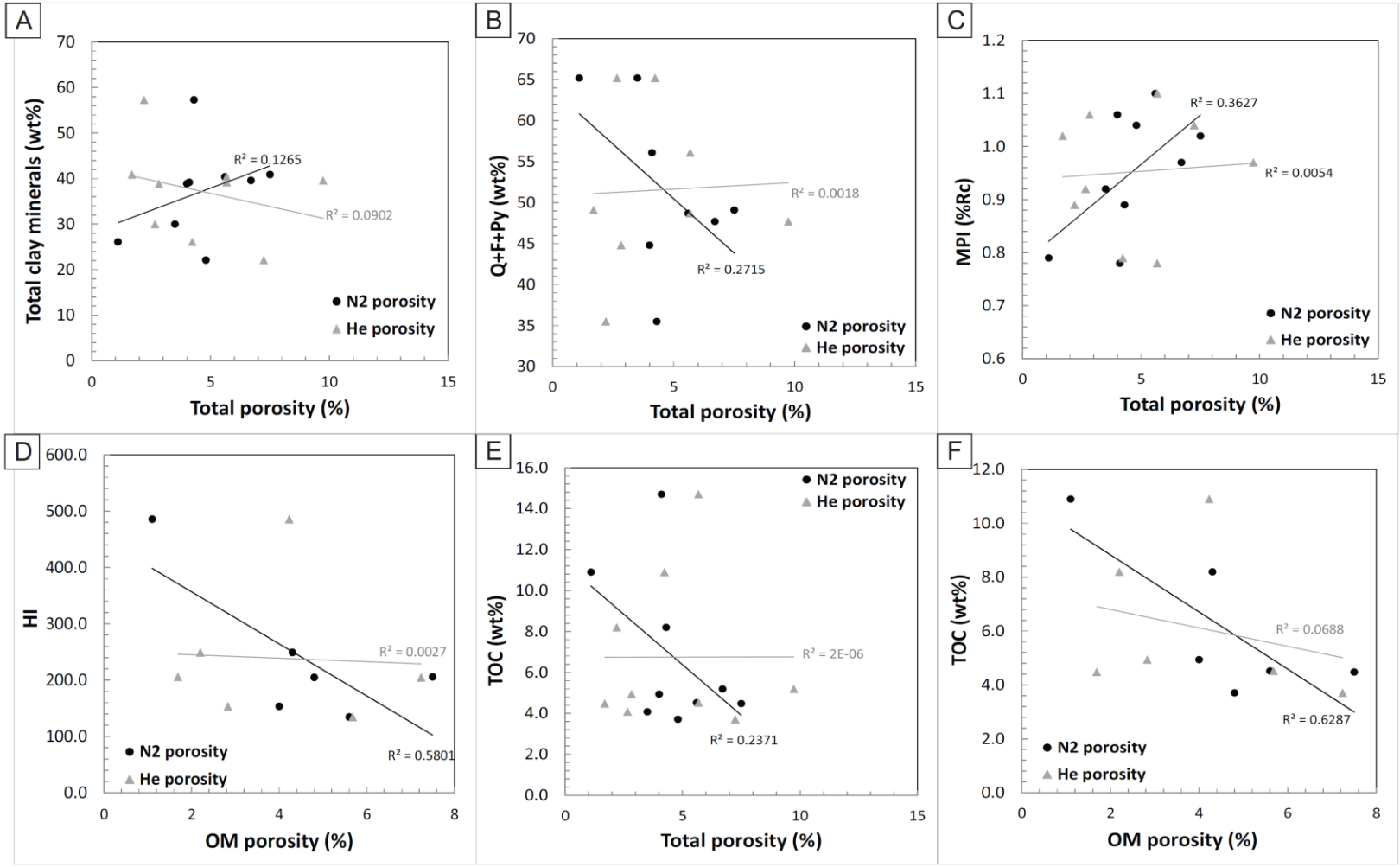
A
Total clay minerals (wt%)
Total porosity (%)
R² = 0.1265
R² = 0.0902
N2 porosity
He porosity
B
Q+F+Py (wt%)
Total porosity (%)
R² = 0.0018
R² = 0.2715
N2 porosity
He porosity
C
MPI (%Rc)
Total porosity (%)
R² = 0.3627
R² = 0.0054
N2 porosity
He porosity
D
HI
OM porosity (%)
R² = 0.0027
R² = 0.5801
N2 porosity
He porosity
E
TOC (wt%)
Total porosity (%)
R² = 2E-06
R² = 0.2371
N2 porosity
He porosity
F
TOC (wt%)
OM porosity (%)
R² = 0.0688
R² = 0.6287
N2 porosity
He porosity

Figure 5.15: Plots showing relationships between total porosity and major mineral abundance, total porosity and geochemical parameters, OM porosity and geochemical parameters. Total porosity is obtained by both helium porosimetry and nitrogen adsorption models. In general, no correlation is apparent between helium porosity and any parameters. (A) A weakly positive correlation exists between nitrogen porosity and clay mineral abundance. (B) A slightly negative correlation was found between nitrogen porosity and Q+F+Py (quartz+feldspar+pyrite) abundance. (C) A weakly positive correlation was found between nitrogen porosity and calculated thermal maturity from MPI (aromatic biomarker MPI: Methyl *Phenanthrene Index)*. (D) A negative correlation exists between OM porosity and hydrogen index (HI). (E) A weakly negative correlation exists between nitrogen porosity and TOC. (F) A negative correlation exists between OM porosity and TOC.

5.7.2 Silt Grain-Size Variation

Silt grain-size variation was obtained by digitizing silt grains from X-ray maps of thin sections and ion-milled sample surfaces. Silt sizes conventionally range from 4 to 62.5 μm. However, in this study, we adopted 2 μm as the particle analysis cutoff for the clay–silt boundary, as suggested by Williams et al. (2007). Silt grain sizes can be further subdivided into extremely fine (EF: 2 to 4 μm), very fine (VF: 4 to 8 μm), fine (F: 8 to 16 μm), medium (M: 16 to 31.5 μm), and coarse (C: 31.5 to 62.5 μm). Silt grain-size distribution of sampled Yanchang mudstones is expressed as the normalized percentage of silt grain sizes versus silt grain-size subdivisions, as shown in Figure 5.16. Except for grain-size information, these curves depict grain sorting. Silt grains in well 1 and well 2 are relatively well sorted compared to other samples because they have a relatively narrow standard deviation (Figure 5.16). Silt grains in well 8 are by comparison very poorly sorted because they have a broad grain-size distribution and the standard deviation of well 8 is the largest (Figures 5.16 and 5.17). Silt grains in wells 3 through 6 are moderately to poorly sorted (Figure 5.16). However, Wells 3 and 5 have a higher percentage of coarser silts than those of wells 4 and 6 (Figures 5.16 and 5.17).

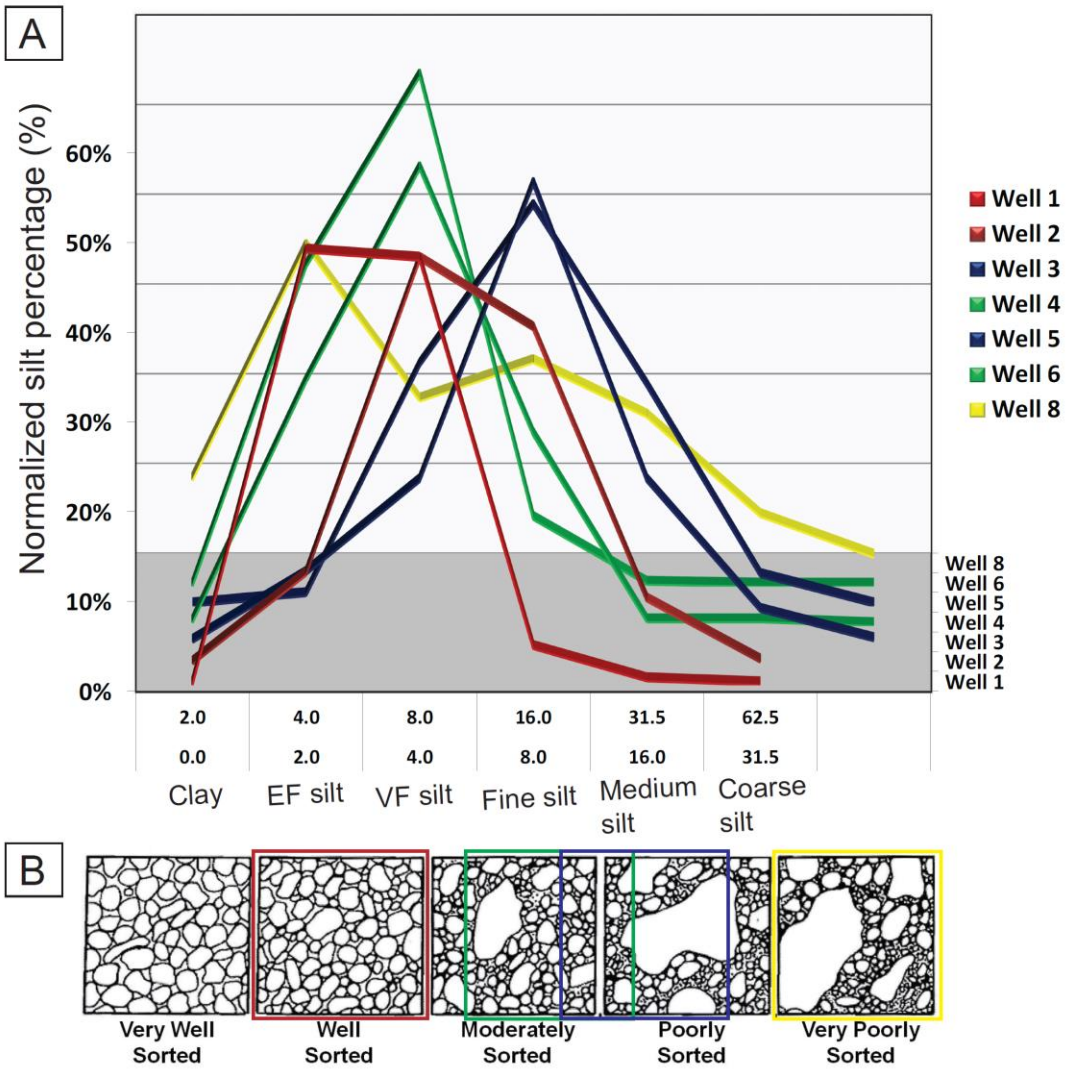

Figure 5.16: Plot of silt grain size distributions of the Yanchang OM-rich, argillaceous mudstone facies in wells from proximal (well 1) to distal (Well 8) area. (A) Plot of normalized silt percentage versus different silt sizes. Colored lines represent similar patterns of silt grain-size distribution: Wells 1 and 2 (red), Wells 3 and 5 (blue), Wells 4 and 6 (green), and Well 8 (yellow). If the mudstone has a higher percentage of coarser silt, the apex of the distribution curves gets closer to the right side of the graph. (B) Schematic diagram demonstrating the extent of sorting of grouped grain-size distribution patterns (source: https://www.geocaching.com/geocache/GC2H5H8_the-rainbow-sands-of-rodeo-beach?guid=1f6f2114-c0ae-474b-871d-459498b5eba7).

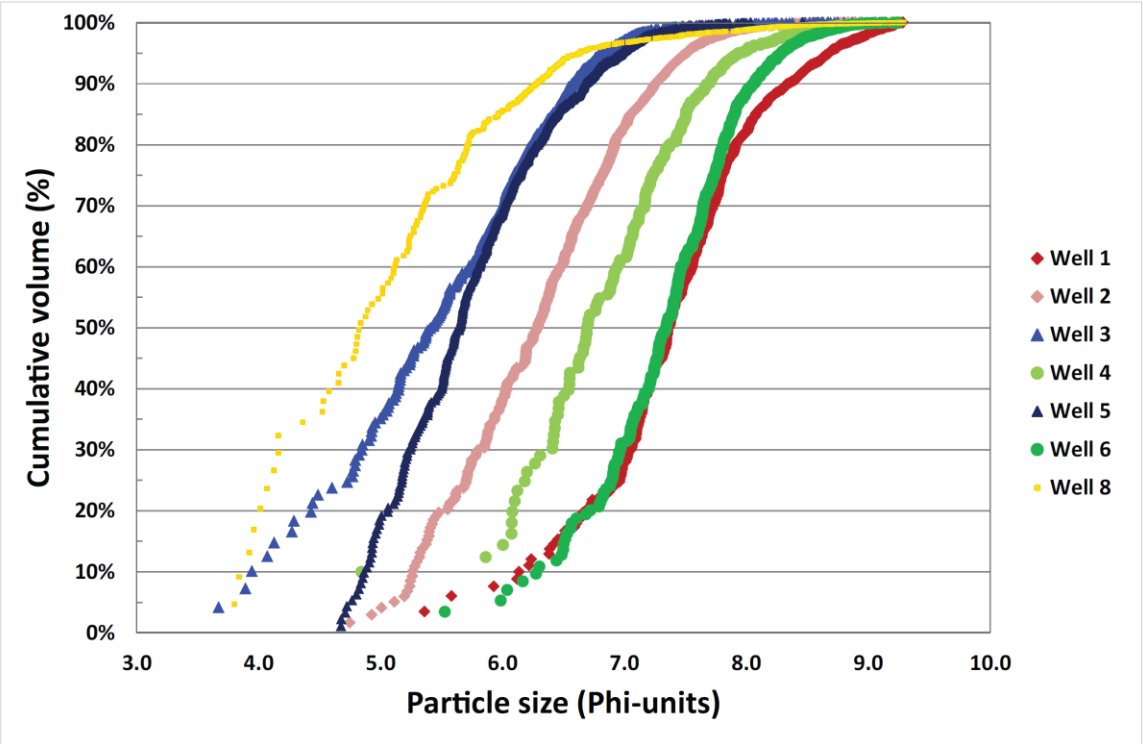

Figure 5.17: Variations in particle-size distribution within silt population. These seven samples represent important texture variations. Chang 7 OM-rich mudstone sample in Well 1 contains most clay-sized particles; samples in Wells 3 and 5 contain abundant silt and also silt of comparatively large size.

5.7.3 Controls on Distribution of Pore Sizes in Mineral Matter

Mineral-hosted pores described in this study (see also Loucks et al., 2017) include both primary mineral-hosted pores and modified mineral-hosted pores within relic organic matter, as defined in Ko et al. (2016a, b). In this study, we found that sorting and grain size affect the preservation and abundance of mineral-hosted pores. For example, grain-size and pore-size distributions in wells 1, 2, 3 and 5 (at depths of 407 m, 1,141m, 1,247m, and 1,567 m respectively) are compared in Figures 5.18A and 5.18B. In previous FE-SEM investigations, we have observed that mineral-hosted pores in general are larger than 17 nm, whereas OM-hosted pores are smaller than 17 nm. Observable OM-hosted pores range from 5 nm (limit of SEM resolution) to 17 nm. Figure 5.18B shows mineral-

hosted pore volume (porosity) is greater in the Chang 7 sample from well 2 than other samples from wells 1, 3, and 5. Among these four samples, well 2 does not have the highest percentage of coarser silt grains but has well-sorted silt grains (Figure 5.18A). This implies that sorting of silt grains could play a greater role for higher porosity in mudstones than the relative abundance of coarser silts. Thin-section petrography shows that Chang 7 OM-rich mudstone samples in wells 1, 2, and 5 are all faintly laminated with homogeneous fabric, but well 3 has distinct alternating clay- and silt- laminae and abundant scour surfaces. The significantly lower mineral pore volume of Chang 7 mudstone in well 3 may be due to its laminated nature even though it contains the coarsest silt grains among all studied samples (Figure 5.18).

Figures 5.19A and 5.19B show that the sample from well 8 is characterized by poor sorting and extremely fine-grained silt. Not surprisingly, this sample contains the fewest mineral-hosted pores, which is probably caused by extensive compaction. It should be noted that the total porosity values from helium porosimetry and nitrogen adsorption analyses are different in this sample. The helium porosity is 4.23 %, which is 3.13% more than the porosity value reported by nitrogen adsorption analysis. The inconsistency of reported porosity values can be interpreted by the sample having pores more than 200 nm, which is not measurable by nitrogen adsorption analysis. However, under the FE-SEM examination, pores larger than 200 nm were not observed. Although the validation of porosity values reported from different methods is beyond the scope of this study, efforts need to be made in the future for solid comparative results. Figures 5.20A and 5.20B show that the mudstone samples from wells 4 and 6 are moderately sorted but dominated by finer silt particles. The sample in well 4 has a slightly higher mineral-hosted pore volume than of the sample from well 6 (Figure 5.20B). However,

both samples contain lower mineral pores due to both moderate to poor sorting nature and finer grain sizes.

Differences in rock texture (sorting and grain size) have resulted in different compaction behavior in lacustrine mudstones. Mudstones with good sorting and more abundant coarse silt grains would preserve more mineral-hosted pores and facilitate fluid migration in mudrocks. Therefore, the abundance of mineral-hosted pores in these compaction-driven lacustrine mudrocks is predominantly affected by sorting, grain size, and rock fabric (Milliken et al., 2017). The preservation of pores is due to silt bridging which preserves larger mineral pores and inhibits clay-size particle alignment (Schneider et al., 2010; Day-Stirrat et al., 2012). The relatively large mineral pores between silt grains act as highly permeable pathways for fluid migration. Diagenetic effects such as grain dissolution and replacement were found in these Chang 7 mudstone samples, but the alteration is minor and should have little impact on grain-size distribution. In contrast, in mudrock systems that display abundant early cements (e.g., the Eagle Ford Formation), grain-size distribution can be significantly affected by both compaction and early cementation (Ko et al., 2016a, b).

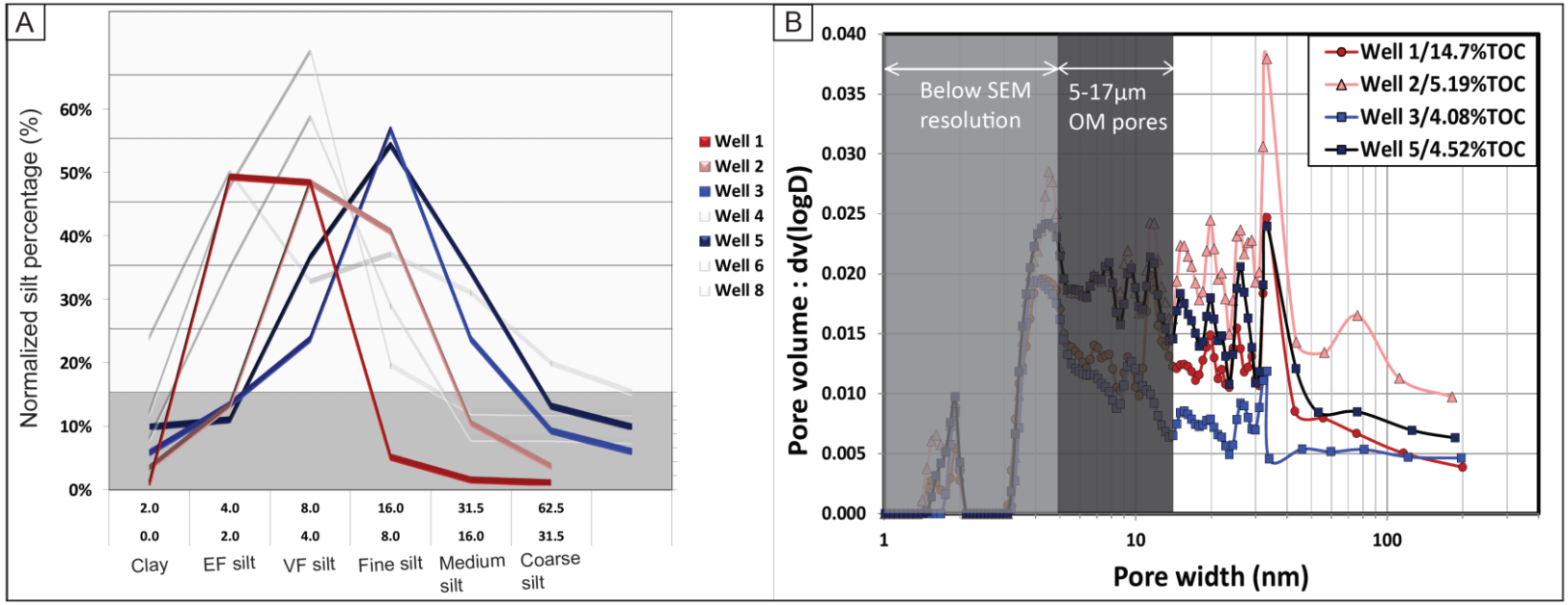

Figure 5.18: Plots of silt grain-size and mineral pore-size distributions of Yanchang Formation OM-rich mudstones in Wells 1 (red), 2 (pink), 3 (blue), and 5 (dark blue). (A) Silt grain-size distributions. (B) Mineral pore-size distributions. Pore size less than 5 nm cannot be resolved by SEM. Observable OM pore sizes ranged from 5 to 17 nm.

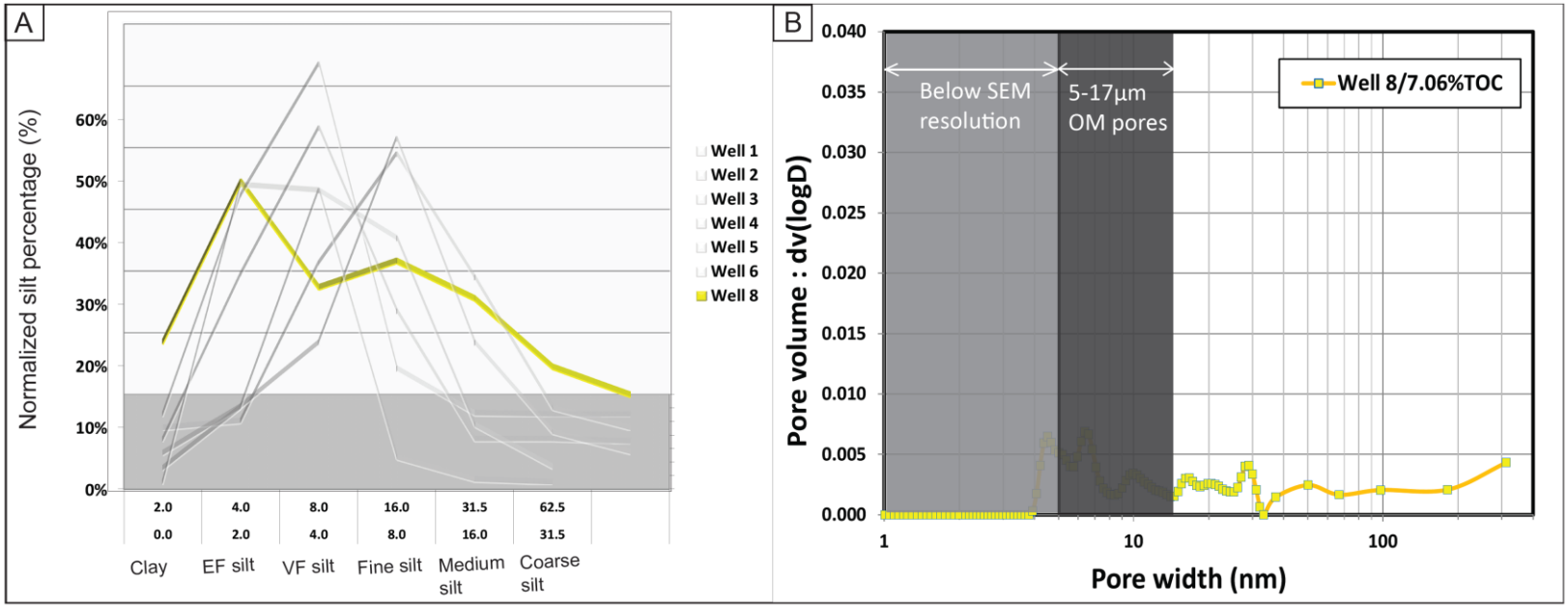

Figure 5.19: Plots of silt grain-size and mineral pore-size distributions of Yanchang Formation OM-rich mudstones in Well 8 (yellow). (A) Silt grain-size distributions. (B) Mineral pore-size distributions. Pore size less than 5 nm cannot be resolved by SEM. Observable OM pore sizes ranged from 5 to 17 nm.

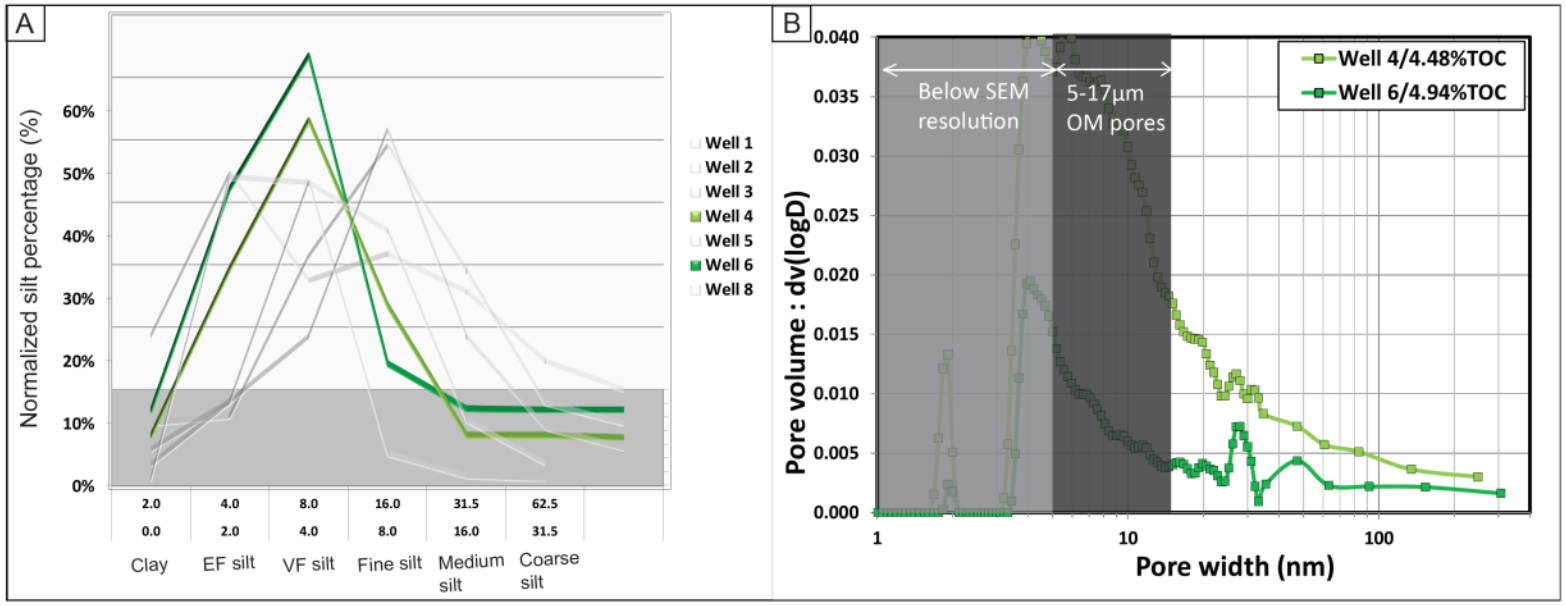

Figure 5.20: Plots of silt grain-size and mineral pore-size distributions of Yanchang Formation OM-rich mudstones in Wells 4 (light green) and 6 (green). (A) Silt grain-size distributions. (B) Mineral pore-size distributions. Pore size less than 5 nm cannot be resolved by SEM. Observable OM pore sizes ranged from 5 to 17 nm.

5.7.4 Controls on Distribution of Pore Sizes in Organic Matter

Sources and types of organic matter (first-order) and levels of thermal maturation (second-order) affect the development of OM-hosted pores in lacustrine mudrocks, much like they do in marine mudrocks (e.g. , Ko et al., 2016a, b). Formation of OM-hosted spongy pores during maturation is possibly related to thermal cracking in solid bitumen/pyrobitumen. These spongy pores start to form in the oil window and become the predominant pore type in the late oil/condensate window to gas window maturation in marine mudstones (Ko et al., 2016 a, b). The OM-hosted spongy pores are abundant in these lacustrine mudstones as well.

Although the majority of Yanchang mudstone samples are at middle to late oil window levels of maturation (equivalent vitrinite reflectance value of 0.9 to 1.1 $\%R_o$), two samples (from wells 1 and 8) are slightly less mature in the early oil window (0.78 $\%R_o$) (Figure 5.8) and do not contain observable OM-hosted pores. One of these samples (from well 1) was taken from the proximal area of the basin where input of Type III terrestrial kerogen is expected to have been greater (Sun et al., 2017; Ruppel and Rowe, 2017). The second sample (from well 8) was also taken from the proximal area but away from terrigenous source inputs where changes in kerogen type are likely to occur and the relative amount of Type I kerogen (algae-derived) content is likely to be higher (Sun et al., 2017; Ruppel and Rowe, 2017). Only primary mineral-hosted pores are found in the sample from the most proximal area of the basin (from well 1). OM-hosted pores were rarely observed in samples from well 1. Similarly, OM-hosted spongy pores were rarely observed in samples from well 8 (maturity: equivalent vitrinite reflectance value of 0.83 $\%R_o$). This might be explained by the fact that the mudstone sample from well 8 had the highest Rock-Eval S_2 value and the highest hydrogen index (HI) relative to the other

samples, indicating that it still retains much of its generation potential. It is possible that the well 8 sample, because it contains more Type I kerogen, would require higher activation energy to convert OM to petroleum (Tissot et al., 1987; Burwood, 1999; Katz and Lin, 2014). Therefore, only a few OM-hosted pores are developed because the OM is just undergoing early conversion. As previously pointed out, the sample from the mudstone in well 8 mudstone is poorly sorted and dominated by very fine silt grains, so the compaction effect is the most significant (Figures 5.19A and 5.19B). Even if some OM-hosted pores developed, they might not be preserved because of significant compaction.

Mudstones in the proximal area having similar sorting, silt content, texture, organic matter types, and thermal maturation contain similar pore types. Samples from wells 4 and 6 are silt-bearing, clay-rich mudstones and have similar mineralogical compositions and thermal maturities (vitrinite reflectance values were calculated using aromatic biomarker MPI-1; those values are 1.02 $\%R_o$ and 1.06 $\%R_o$ respectively), except that the sample from well 4 is from the Chang 9 Member and contains 10% more quartz than the well 6 sample (Table 5.1). The dominant pore type in these samples is the OM-hosted spongy pore with abundant artifact devolatilization cracks. Very few mineral-hosted pores were observed. Lengths of the devolatilization cracks ranged from hundreds of nanometers to tens of microns. We believe that both nitrogen-gas adsorption and helium-gas porosity measurements include the volume of these devolatilization cracks, which will cause inconsistency in total porosity values because the cracks are not present in the subsurface (Table 2). Development of these devolatilization cracks can result from the release of volatile elements in organic matter as well as from drops in temperature and pressure during coring from the burial depth to the surface (Kim et al., 2008; Loucks and Reed, 2014).

The sample from the most distal area of the basin (from well 9 at a depth of 2,297 m), positioned farther than other samples and is close the lake-center basinal environment, is silt rich yet lacks the abundant feldspars and micas that characterize the silt fraction in other samples (quartz content: 77.6%). Thin-section petrography shows that this sample contains an altered volcanic ash and a possible microbial mat (Figure 5.6). The ash could have been altered and replaced by authigenic microcrystalline quartz. OM-hosted spongy pores and OM devolatilization cracks are found ubiquitously in the migrated solid bitumen in the well 9 mudstone (Figure 5.13).

The representative Yanchang sample from wells YCYV1112 and YCYV1133 is compared with the studied samples (Loucks et al., 2017). Although locations of some wells in this study are in close proximity to those studied by Loucks et al. (2017), the sample from the YCYV1112 at a depth of 1,378.5 m has significantly higher clay-mineral content than the rest of the mudstone samples in this study (Table 5.2). This sample from the Chang 7 is described as slightly burrowed, peloidal, slightly silty, argillaceous mudstone. OM-hosted spongy pores are the only type of pore found. The location of these OM-hosted spongy pores is generally within less-compacted areas in the migrated solid bitumen (Loucks et al., 2017).

5.8 DISCUSSION

5.8.1 Controls on Total Porosity of OM-rich Mudstones

The total porosity in an OM-rich mudstone is composed of both mineral porosity (primary interparticle and intraparticle porosity + modified interparticle and intraparticle porosity) and OM porosity (primary kerogen porosity+ secondary OM bubble and spongy porosity). Figure 5.21 demonstrates a conceptual model of pore networks in a mature OM-rich mudstone. Mineral-hosted pores are a function of sediment sources, depositional

and diagenetic (compaction, cementation, dissolution, and replacement) processes. OM-hosted pores are a function of types of kerogen and maceral, and thermal maturation. If a mudstone is immature, the total pore network would be dominated by only mineral pores. Pore connectivity depends on effective pore networks which are likely comprised of interparticle mineral pores. If a mudstone is in oil window maturation, generated petroleum would expel, migrate, and interact with the mineral pore network, resulting in modified mineral pores (primary mineral pores with residual organic matter). According to the proposed pore network model, cross-plot of total porosity and major mineral composition does not necessarily correlate, either does total porosity and TOC or thermal maturity. We suggest correlating OM porosity with measured present-day TOC (TOC_m) when mudstones have similar types of kerogen and macerals. Correlation between mineral porosity and mineralogy will be better than correlation between total porosity and mineralogy. This helps explain why there are no apparent correlations between He porosity and any composition or any geochemical parameters (Figure 5.15). Because total (bulk) porosity of Yanchang mudstones was derived from nitrogen adsorption and measurements of helium porosimetry, it is difficult to investigate controls on total porosity in mudstones without direct observation and quantification using imaging techniques (e.g., SEM, HIM, TEM).

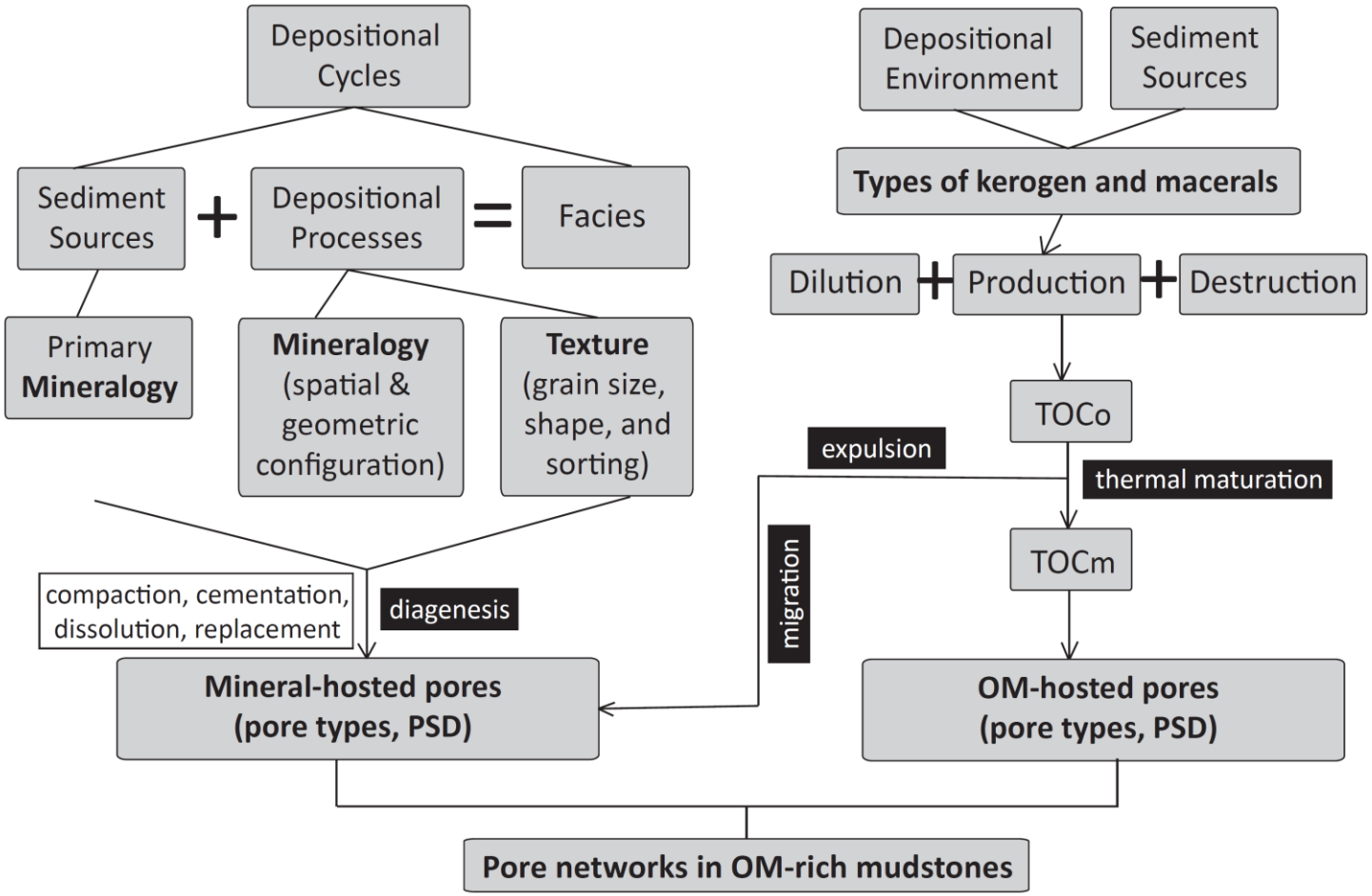

Figure 5.21: Conceptual models of the total pore network in mature OM-rich mudstones.

5.8.2 Implication for Pore-Evolution Models of Lacustrine Mudrocks

Pore types, abundance, and distribution in the Yanchang lacustrine mudrocks do not match well with pore-evolution models developed from Eagle Ford marine mudrocks (Pommer and Milliken, 2015; Ko et al., 2016a, b) even though the Yanchang lacustrine mudstones have similar levels of thermal maturity as those of the Eagle Ford marine mudstones (Figure 5.22). Ko et al. (2016a) studied and characterized the pore types and networks of the Eagle Ford mudrocks in Karnes County, Texas and concluded that modified mineral-hosted pores, OM-hosted bubble pores, and OM-hosted spongy pores are the dominant pore types in the late oil window (Figure 5.23). Pore types in the Eagle Ford mudrocks differ from those in the Yanchang lacustrine mudrocks (middle to late oil window), which have rare OM-hosted bubble pores, less modified mineral-hosted pores, and extremely abundant, but smaller, OM-hosted spongy pores (Table 3, Figure 23). The size and abundance of mineral pores are related to sorting (first-order) and grain size in the lacustrine mudstones (Figures 5.16 to 5.20). More mineral-hosted pores are found in samples with better sorting and a higher percentage of coarse silt and silt-framework fraction.

A lack of early cementation during diagenesis in Yanchang lacustrine mudrocks (Milliken et al., 2017) allowed for more compaction, possibly destroying interparticle pores and resulting in less abundant OM-hosted bubble pores than seen in the Eagle Ford marine mudrocks, which display abundant early cementation (Milliken et al, 2016). The relatively small sizes of OM-hosted spongy pores in pyrobitumen and/or post-oil solid bitumen in Yanchang mudstones (Curiale, 1986; Bernard et al., 2012; Loucks and Reed, 2014) might be the result of relatively high normal stress, as indicated by a lack of early cementation and significant compaction. A similar compaction model for reduction of

OM-hosted pores in Marcellus Formation mudrocks was proposed by Milliken et al. (2013), although in that study a possible control of organic matter type (kerogen, solid bitumen, or dead carbon) on the size and abundance of OM-hosted pores was not ruled out. The cause of smaller and less abundant OM-hosted bubble pores and smaller sizes of the OM-hosted spongy pores in pyrobitumen and/or post-oil solid bitumen is not yet clear. Two possibilities are proposed: (1) Kerogen and maceral sources (e.g., types of algae and bacteria) in the lake could be quite different from those in the marine environment. This might cause a difference in the size and abundance of the OM-hosted spongy pores. (2) There could be a compaction effect, whereby the sizes of pores are related to the equilibrium pressure outside (overburden pressure of sediments above) and inside (pore-fluid pressure of generated liquid and gas) the pore walls (Javadpour, personal communication, 2016). The sizes of OM-hosted pores and intraparticle clay-platelet pores will be affected by compaction much more than interparticle mineral-hosted pores because organic matter and clay minerals in general have weaker elastic parameters and mechanical properties (Sone and Zoback, 2013). Because organic matter and clay minerals are more easily compressed than mineral matter, the sizes of OM-hosted pores and intraparticle clay-platelet pores very possibly become smaller while the compaction effect is significant.

On the basis of the above observation and derived implication, a mineral and pore evolution model of lacustrine mudrocks is proposed (Figure 5.23). Because a lack of early cementation during diagenesis in Yanchang lacustrine mudrocks allowed for more compaction, primary mineral pores are not easily preserved and an effective pore network is not easily formed. During bitumen maturation, it is likely very difficult for viscous bitumen to migrate through the original mineral pore networks. Microfractures could possibly be formed if generation pressure is significantly higher than the rock strength.

Although bitumen starts to crack to oil and gas, solid bitumen and/or pyrobitumen begins to be formed and deposited as roadblocks, reducing porosity and permeability by filling pore spaces or closing pore throats, and making it more difficult for oil and gas to migrate in the pore network. The deposition of solid bitumen and/or pyrobitumen in turn might affect expulsion efficiency in various lithofacies. Oil and gas can be thermally cracked from solid bitumen and/or pyrobitumen, possibly forming OM-hosted spongy pores.

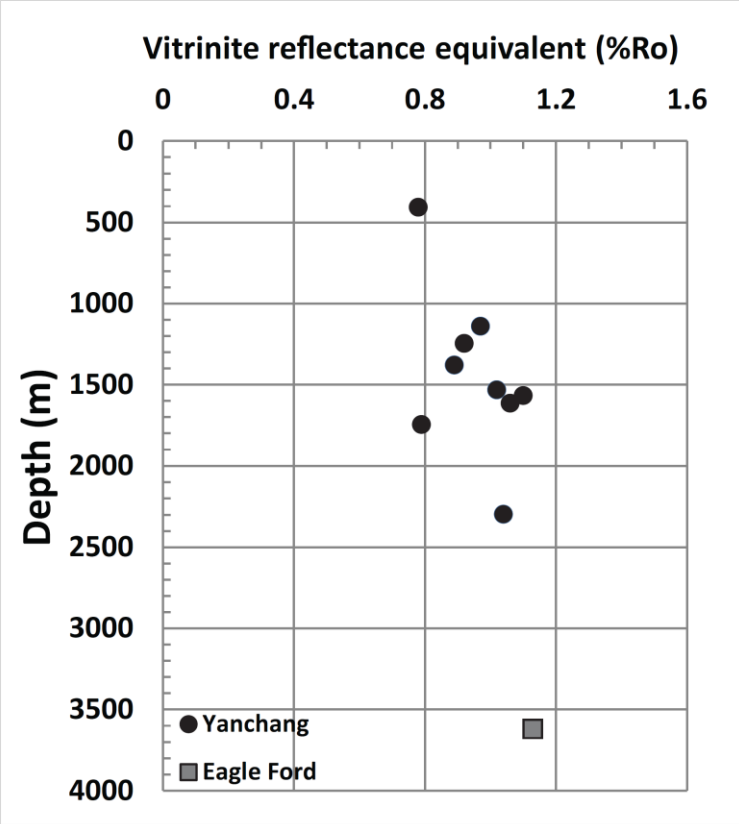

Figure 5.22: Plot of thermal maturity versus depths (m) of Yanchang and Eagle Ford mudstones. Yanchang samples in this study are in middle to late oil window maturation; representative Eagle Ford mudstones in Karnes County, Texas, are in late oil window maturation. Vitrinite reflectance equivalence was calculated from methylphenanthrene indexes (MPI-1) in aromatic fractions of the biomarker.

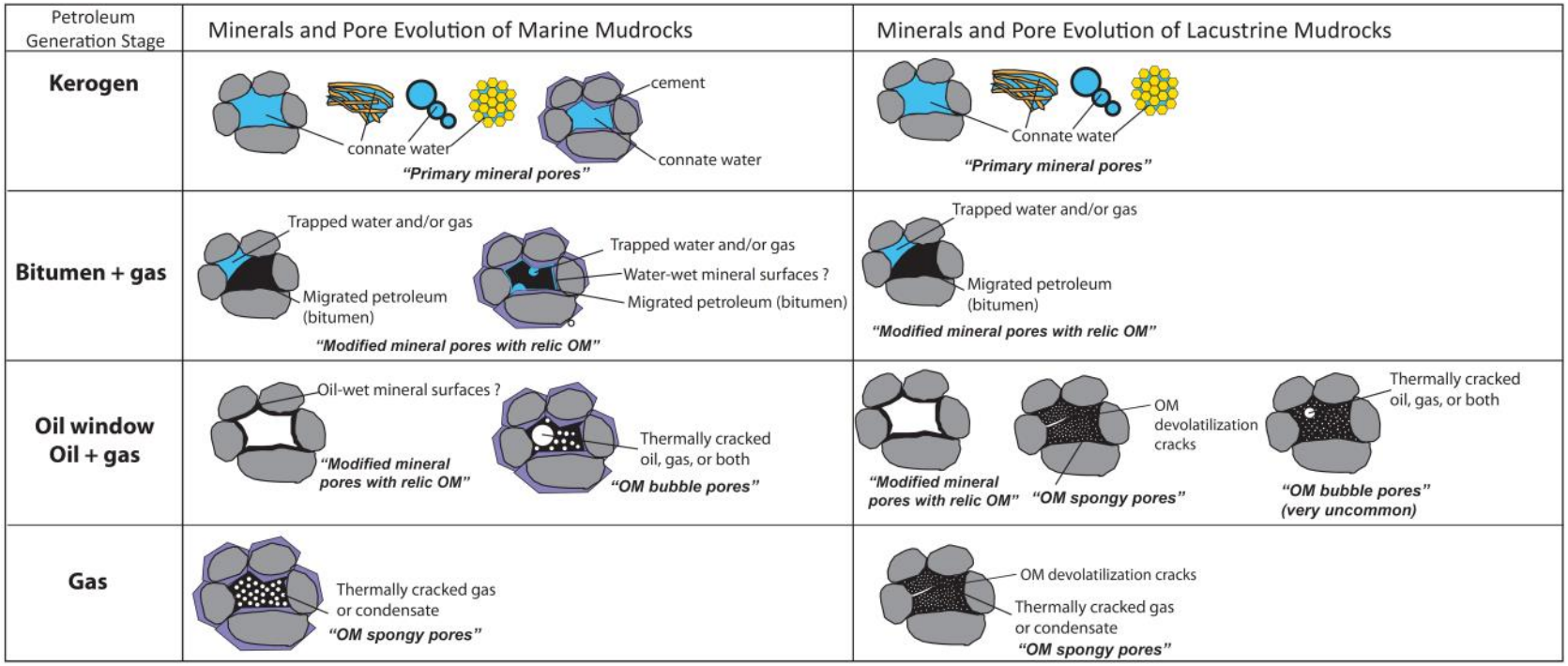

Figure 5.23: Schematic diagrams showing pore evolution of marine and lacustrine mudrocks based on data from Eagle Ford (Ko et al., 2016 a, b) and Yanchang as examples.

5.9 CONCLUSIONS

FE-SEM imaging aids in discriminating types of mineral- and OM-hosted pores, their relative sizes, and their contributions to total pore volume; and nitrogen adsorption measurement clarifies PSD's. Four distinct groups of PSDs can be defined from differences in types of kerogen, thermal maturation, silt-grain sorting, and relative abundance of coarse silt grains.

Silt-grain sorting (first order) and the relative abundance of coarse silt grains affect the preservation and abundance of mineral-hosted pores and mineral-hosted pore-size distribution in Yanchang OM-rich argillaceous mudstones, possibly through silt bridging.

Because of the small numbers of samples (nine) and the uneven distribution of the sample set from the proximal to distal areas of the Ordos Basin, conclusions need to be viewed with some degree of caution. This study mainly discusses variations in the proximal setting where most samples are located. Variations in types of organic matter from the proximal to distal areas of the basin affect the development of OM-hosted pores. The OM-hosted pores are abundant in samples with predominantly Type II/III kerogen. Samples that contained predominantly terrestrial Type III kerogen developed only rare OM-hosted pores at maturity levels of 0.79 $\%R_o$ (measured bitumen reflectance). At maturity levels of 0.79 $\%R_o$ (vitrinite reflectance values were calculated using aromatic biomarker MPI-1), mudstones containing Type I kerogen still retained a great amount of generation potential and developed only a minor amount of OM-hosted pores.

Pore types, abundance, and distribution in lacustrine mudrocks situated within the oil window are not a good match with pore-evolution models developed from Eagle Ford marine mudrocks in Texas. A lack of early cementation during compaction in Yanchang

lacustrine mudrocks results in less lithification and extensive compaction. It is possible that compaction results in sizes of OM-hosted spongy pores that are smaller than those in marine mudstones and also allows smaller and less-abundant OM-hosted bubble pores to form because pore sizes are related to the equilibrium pressure outside (overburden pressure of sediments above) and inside (pore-fluid pressure of generated liquid and gas) the pore walls. The sizes of OM-hosted pores in these compaction-dominated lacustrine mudstones are one to two orders of magnitude smaller than those in Eagle Ford marine mudstones that contain early cements.

Samples from the OM-rich, argillaceous mudstone facies of the Chang 7 Member of the Yanchang Formation in this study contain more and larger mineral-hosted pores and significantly less clay minerals, detrital quartz, and feldspar than samples from Chang 7 to Chang 9 in wells YCYV1112 and YCYV1133 (Loucks et al., 2017). Although the overall high clay mineral content is common in the Chang 7 mudstones and has been interpreted to suggest that Yanchang mudstones are poor candidates for hydraulic fracturing, sample sets from this study at least indicate that clay mineral-poor lithologies may be locally present in the more distal regions of the basin and may be suitable for hydraulic fracturing. The heterogeneity of the types of kerogen, thermal maturation, texture (sorting and grain sizes), fabric, mineralogy, and brittleness of rocks in the Yanchang Formation across the Ordos Basin have also been recognized and could be affected by differential sediment inputs from the two dominant source areas: a fluvial deltaic system to the northeast and braided stream a delta system to the southwest. Sediment influx from these two sources may not have been concurrent, thus producing complex facies stacking patterns in areas dominated by each system. If this is the case, correlation of regional deepening and shallowing cycles, as well as identification of

mineralogical “sweet spots” for exploration, may be more difficult than has been concluded.

ACKNOWLEDGMENTS

I would like to show the greatest appreciation to the Yanchang Petroleum Group for providing data and materials, as well as technical and financial support. X-ray diffraction analyses were provided by K-T GeoServices, Inc., of Gunnison, Colorado. I would like to thank Patrick Smith for providing Ar-ion milling and sample coating at the Bureau of Economic Geology SEM laboratory. I would also like to thank Dr. Xiangzeng Wang, Dr. Eric Potter, Dr. Hongliu Zheng, and Dr. Wei Wang for meetings and discussions, and Dr. Farzam Javadpour, Dr. Robert Reed, and Dr. Gregory Frebourg for suggestions and inspirations during the manuscript preparation.

REFERENCES

American Society for Testing and Materials (ASTM), 2015, Standard test method for microscopical determination of the reflectance of vitrinite dispersed in sedimentary rocks. Annual book of ASTM standards: petroleum products, lubricants, and fossil fuels; gaseous fuels; coal and coke, sec. 5, v. 5.06: ASTM International, West Conshohocken, Penn., http://www.astm.org/Standards/D7708.htm (accessed May 18, 2016).

Bernard, B., R. Wirth, A. Schreiber, H. Schultz, and B. Horsfield, 2012, Formation of nanoporous pyrobitumen residues during maturation of the Barnet Shale (Fort Worth Basin): International Journal of Coal Geology, v. 103, p. 3–11.

Burwood, R., 1999, Angola: source rock control for Lower Congo Coastal and Kwanza basin petroleum systems, *in*: N. R. Cameron, R. H. Bate, and V. S. Clure eds., The Oil and Gas Habitats of the South Atlantic, Geological Society (London), Special Publication v. 53, p. 181–194.

Cao, H., X. Shan, P. Sun, H. Chi, and S. Du, 2016, Geochemical characteristics of oil shale in the Triassic Chang7 subsection, southern Ordos basin, China, and palaeo-environment reconstruction: Journal of Mineralogy and Geochemistry, v. 193, p. 45–57.

Carroll, A. R., S. A. Graham, and M. E. Smith, 2010, Walled sedimentary basins of China: Basin Research, v. 22, p. 17–32, doi: 10.1111/j.1365-2117.2009.00458.x.

Curiale, J. A., 1986, Origin of solid bitumens, with emphasis on biological marker results: Organic Geochemistry, v. 10, p. 559–580.

Day-Stirrat, R. J., P. B. Flemings, Y. You, A. C. Aplin, and B. A. van der Pluijm, 2012, The fabric of consolidation in Gulf of Mexico mudstones: Marine Geology, v. 295–298, p. 77–85, doi: 10.1016/j.margeo.2011.12.003

Guo, H., W. Jia, P. Peng, Y. Lei, X. Luo, M. Cheng, X. Wang, L. Zhang, and C. Jiang, 2014, The composition and its impact on the methane sorption of lacustrine shales from the Upper Triassic Yanchang Formation, Ordos Basin, China: Marine and Petroleum Geology, v. 57, p. 509–520.

Hackley, P.C., Araujo, C.V., Borrego, A.G., Bouzinos, A., Cardott, B., Cook, A.C., Eble, C., Flores, D., Gentzis, T., Gonçalves, P.A., Mendonça Filho, J.G., Hámor-Vidó, M., Jelonek, I., Kommeren, K., Knowles, W., Kus, J., Mastalerz, M., Menezes, T.R., Newman, J., Oikonomopoulos, I.K., Pawlewicz, M., Pickel, W., Potter, J., Ranasinghe, P., Read, H., Reyes, J., Rodriguez, G.D.L.R., Fernandes de Souza, I.V.A., Suarez-Ruiz, I., Sýkorová, I., Valentine, B.J., 2015. Standardization of reflectance measurements in dispersed organic matter: results of an exercise to improve interlaboratory agreement: Marine and Petroleum Geology, v. 59, p. 22–34.

Hackley, P. C., L. Zhang, and T. Zhang, 2017, Organic petrology of peak oil maturity Triassic Yanchang Formation lacustrine mudrocks, Ordos Basin, China: Interpretation, v. 5, p. SF211–SF223.

Han, S., B. Horsfield, J. Zhang, Q. Chen, N. Mahlstedt, R. di Primio, and G. Xiao, 2014, Hydrocarbon generation kinetics of lacustrine Yanchang Shale in southeast Ordos Basin, North China: Energy & Fuels, v. 28, p. 5632–5639.

Ji., L.-M., F.-W. Meng, J. D. Schiffbauer, J.-L. Xu, K. Yuan, and J.-W. Shu, 2008, Correlation between highly abundant oil-prone leiosphaerid acritarchs and hydrocarbon source rocks from the Triassic Yanchang Formation, eastern Gansu Province, Northwestern China: Gondwana Research, v. 14, p. 554–560.

Ji, L.-M., K. Yan, F.-W. Meng, and M. Zhao, 2010, The oleaginous Botryococcus from the Triassic Yanchang Formation in Ordos Basin, northwestern China: Morphology and its paleoenvironmental significance: Journal of Asian Earth Sciences, v. 38, p. 175–185, doi: 10.1016/j.jseaes.2009.12.010

Jiang, F., D. Chen, Z. Wang, Z. Xu, J. Chen, L. Liu, Y. Huyan, and Y. Liu, 2016, Pore characteristic analysis of a lacustrine shale: A case study in the Ordos Basin, NW China: Marine and Petroleum Geology, v. 73, p. 554–571, doi: 10.1016/l.marpetgeo.2016.03.026

Katz, B. and F. Lin, 2014, Lacustrine basin unconventional resource plays: Key differences: Marine and Petroleum Geology, v. 56, p. 255-265.

Kim, B., S. Gupta, S. Lee, S. Kim, and V. Sahajwalla, 2008, Devolatilization and cracking characteristics of Australian lumpy coals: Energy & Fuels, v. 22, p. 514–522.

Ko, L. T., R. G. Loucks, S. C. Ruppel, T. Zhang, and S. Peng, 2017, Origin and characterization of Eagle Ford pore networks in the south Texas Upper Cretaceous shelf: AAPG Bulletin, v. 101, p. 387–418, doi: 10.1306/08051616035

Ko, L. T., R. G. Loucks, T. Zhang, S. C. Ruppel, and D. Shao, 2016b, Pore and pore network evolution of Upper Cretaceous Boquillas (Eagle-Ford equivalent) mudstones: Results from gold-tube pyrolysis experiments: AAPG Bulletin, v. 100, p. 1693–1722.

Li, S., S. Yang, and T. Jeryzkiewicz, 1995, Upper Triassic–Jurassic foreland sequences of the Ordos Basin in China, *in* S. L. Dorobek and G. M. Ross, eds., Stratigraphic evolution of foreland basins: SEPM Special Publication 52, p. 233–241.

Li, J., S. Zhou, Y. Li, Y. Ma, Y. Yang, C. Li, 2016, Effect of organic matter on pore structure of mature lacustrine organic-rich shale: A case study of the Triassic Yanchang Shale, Ordos Basin, China: Fuel, v. 185, p. 421–431.

Liu, B., Y. Wang, and X. Qian, 1997, Two Ordovician unconformities in north China: Their origins and relationships to regional carbonate-reservoir characteristics: Carbonates and Evaporites, v. 12, p. 177–184.

Liu, S., 1998, The coupling mechanism of basin and orogeny in the western Ordos Basin and adjacent regions of China: Journal of Asian Earth Sciences, v. 16, p. 369–383.

Loucks, R. G., and R. M. Reed, 2014, Scanning-electron-microscope petrographic evidence for distinguishing organic-matter pores associated with depositional organic matter versus migrated organic matter in mudrocks: GCAGS Journal, v. 3, p. 51–60.

Loucks, R. G., R. M. Reed, S. C. Ruppel, and U. Hammes, 2012, Spectrum of pore types and networks in mudrocks and a descriptive classification for matrix-related mudrock pores: AAPG Bulletin, v. 96, p. 1071–1098.

Loucks, R. G., R. M. Reed, S. C. Ruppel, and D. M. Jarvie, 2009, Morphology, genesis, and distribution of nanometer-scale pores in siliceous mudstones of the Mississippian Barnett Shale: Journal of Sedimentary Research, v. 79, p. 848–861.

Loucks, R. G., S. C. Ruppel, L. T. Ko, P. Smith, S. Peng, and T. Zhang, 2017, Pore types, pore-network analysis, and pore quantification of the lacustrine shale-hydrocarbon system in the Late Triassic Yanchang Formation in the southeastern Ordos Basin, China: Interpretation, v. 5, p. SF63–SF79.

Luffel, D. L., C. W. Hopkins, and P. D. Schettler Jr., 1993, Matrix permeability measurement of gas productive shales: SPE Annual Technical Conference and Exhibition, SPE No. 26633, p. 261–270.

Macquaker, J. H. S., and A. E. Adams, 2003, Maximizing information from fine-grained sedimentary rocks: An inclusive nomenclature for mudstones: Journal of Sedimentary Geology, v. 73, p. 735–744.

Mancini, E. A., R. M. Mink, J. W. Payton, and B. L. Bearden, 1987, Environments of deposition and petroleum geology of Tuscaloosa Group (Upper Cretaceous), south Carton and Pollard Fields, southwestern Alabama: AAPG Bulletin, v. 71, p. 1128–1142.

Milliken, K. L., M. Rudnicki, D. N. Awwiller, and T. Zhang, 2013, Organic matter-hosted pore system, Marcellus Formation (Devonian), Pennsylvania: AAPG Bulletin, v. 97, p. 177–200.

Milliken, K. L., S. M. Ergene, and A. Ozkan, 2016, Quartz types, authigenic and detrital, in the Upper Cretaceous Eagle Ford Formation, south Texas, USA: Sedimentary Geology, v. 339, p. 273–288.

Milliken, K. L., Y. Shen, L. T. Ko, and Q. Liang, 2017, Grain composition and diagenesis of organic-rich lacustrine tarls, Triassic Yanchang Formation, Ordos Basin, China: Interpretation, v. 5, p. SF189–SF210.

Pan, S., B. Horsfield, C. Zou, and Z. Yang, 2016, Upper Permian Junggar and Upper Triassic Ordos lacustrine source rocks in northwest and central China: Organic geochemistry, petroleum potential, and predicted organofacies: International Journal of Coal Geology, v. 158, p. 90–106.

Peng, S., and R. G. Loucks, 2016, Permeability measurements in mudrocks using gas-expansion methods on plug and crushed-rock samples: Marine and Petroleum Geology, v. 73, p. 299–310.

Pommer, M., and K. L. Milliken, 2015, Pore types and pore-size distributions across thermal maturity, Eagle Ford Formation, south Texas: AAPG Bulletin, v. 99, p. 1713–1744.

Roduit, N., 2008, JMICROVISION Version 1.2.7: Image analysis toolbox for measuring and quantifying components of high-definition images: http://www.jmicrovision.com (accessed November 3, 2015).

Rowe, H., X. Wang, B. Fan, T. Zhang, K. L. Milliken, Y. Shen, and J. Zhang, 2015, Chemostratigraphy of the Triassic Yanchang fluvio-lacustrine succession, Ordos Basin, Shaanxi Province, China: AAPG Annual Convention and Exhibition, Denver, Colo., abstract.

Ruppel, S. C., and H. Rowe, 2017, Facies, rock attributes, stratigraphy, and depositional environments of the Upper Triassic Yanchang Formation, Ordos Basin, China: Interpretation, v. 5, p. SF15–SF29.

Schneider, J. P. B. Flemings, R. J. Day-Stirrat, and J. T. Germaine, 2011, Insights into pore-scale controls on mudstone permeability through residimentation experiments: Geology, v. 9, p. 1011–1014.

Smith, P., L. T. Ko, and T. Zhang, 2016, High-resolution microscopic analysis of mineral and organic-matter components in the Upper Triassic Yanchang lacustrine shale deposits in southeastern Ordos Basin, China, 2016 SEPM-AAPG Hedberg Research Conference "Mudstone Diagenesis", October 16-19, Santa Fe New Mexico, USA.

Sone, H. and M. D. Zoback, 2013, Mechanical properties of shale-gas reservoir rocks – Part 1: static and dynamic elastic properties and anisotropy: Geophysics, v. 78, p. D381–D392.

Sun, S., Q. Liang, C. Jiang, D. Enriquez, T. Zhang, and P. C. Hackley, 2017, Liquid hydrocarbon characterization of lacustrine Yanchang Formation, Ordos basin: Organic matter source variation and maturity: Interpretation, v. 5, p. SF225–SF242.

Tang, X., J. Zhang, X. Wang, B. Yu, W. Ding, J. Xiong, Y. Yang, L. Wang, and C. Yang, 2014, Shale characteristics in the southeastern Ordos Basin, China: Implications for hydrocarbon accumulation conditions and the potential of continental shales: International Journal of Coal Geology, v. 128–129, p. 32–46.

Tissot, B. P., R. Pelet, and Ph. Ungerer, 1987, Thermal history of sedimentary basins, maturation indicies, and kinetics of oil and gas generation: AAPG Bulletin, v. 71, p. 1445–1466.

Wang, X., 2012, The exploration discovery and key technologies of continental shale gas, Yanchang Petroleum: http://www.uschinaogf.org/Forum12/pdf/21%20-%20Xiangzeng%20-%20Shaanxi%20Yanchang%20Petroleum-EN.pdf (accessed November 7, 2015).

Wang, X., L. Zhang, C. Jiang, and B. Fan, 2015a, Hydrocarbon storage space within lacustrine gas shale of the Triassic Yanchang Formation, Ordos Basin, China: Interpretation, v. 3, p. SJ15–SJ23.

Wang, Y., Y. Zhu, H. Wang, and G. Feng, 2015b, Nanoscale pore morphology and distribution of lacustrine shale reservoirs: Examples from the Upper Triassic Yanchang Formation, Ordos Basin: Journal of Energy Chemistry, v. 4, p. 512–519.

Williams, J., M. A. Arsenault, B. J. Buczkowski, J. A. Reid, J. G. Flocks, M. A. Kulp, S. Penland, and C. J. Jenkins, 2007, Surficial sediment character of the Louisiana offshore continental shelf region: A GIS Compilation: USGS Open-File Report 2006-1195, 49 p. supplementary online resource, http://pubs.usgs.gov/of/2006/1195/htmldocs/images/chart.pdf

Yang, J., K. Li, D. Zhang, and S. Liu, 1992, Petroleum geology of China, Changqing oil field: Beijing, Petroleum Industry Publishing House, v. 12, 490 p.

Yang, Y., W. Li, and L. Ma, 2005, Tectonic and stratigraphic controls of hydrocarbon systems in the Ordos basin: A multicycle cratonic basin in central China: AAPG Bulletin, v. 89, p. 255–269.

Yang, Z., Y. Cheng, and H. Wang, 1986, The geology of China: Oxford, Clarendon Press, 303 p.

Yao, J., X. Deng, Y. Zhao, T. Han, M. Chu, and J. Pang, 2013, Characteristics of tight oil in Triassic Yanchang Formation, Ordos Basin: Petroleum Exploration and Development, v. 40, p. 161–169.

Yu, Y., X. Luo, Y. Lei, X. Wang, L. Zhang, C. Jiang, W. Yang, M. Cheng, and L. Zhang, 2016, Characterization of lacustrine shale pore structure: The Upper-Triassic Yanchang Formation, Ordos Basin, China: Journal of Natural Gas Geoscience, v. 1, p. 299–308.

Yuan, X., S. Lin, Q. Liu, J. Yao, L. Wang, H. Guo, H., X. Deng, and D. Cheng, 2015, Lacustrine fine-grained sedimentary features and organic rich shale distribution pattern: A case study of Chang 7 Member of Triassic Yanchang Formation in Ordos Basin, NW China: Petroleum Exploration and Development, v. 42, p. 37–47.

Zhang, X., C.-M. Lin, Y.-F. Cai, C.-W. Qu, and Z.-Y. Chen, 2012, Pore-lining chlorite cements in lacustrine-deltaic sandstones from the Upper Triassic Yanchang Formation, Ordos Basin, China: Journal of Petroleum Geology, v. 35, p. 273–290.

Zhang, M., L. Ji, Y. Wu, and C. He, 2015, Palynofacies and geochemical analysis of the Triassic Yanchang Formation, Ordos Basin: Implications for hydrocarbon generation potential and the paleoenvironment of continental source rocks: International Journal of Coal Geology, v. 152, p. 159–176.

Zhang, T., J. Zhang, and K. L. Milliken, 2017, Pore size distribution of Triassic organic-rich Yanchang Formation by using N_2 adsorption isotherms: Interpretation, v. 5, p. SF41–SF61.

Zhao, W., Z. Wang, M. Chen, and H. Zheng, 2005, Formation mechanism of the high quality Upper Paleozoic natural gas reservoirs in the Ordos Basin, Acta Geological Sinica (English Edition), v. 79, p. 843–855.

Zhao, J., N. P. Mountney, C. Liu, H. Qu, and J. Lin, 2015, Outcrop architecture of a fluvio-lacustrine succession: Upper Triassic Yanchang Formation, Ordos Basin, China: Marine and Petroleum Geology, v. 68, p. 394–413.

Zou, C., X. Zhang, P. Luo, L. Wang, Z. Luo, and L. Liu, 2010, Shallow-lacustrine sand-rich deltaic depositional cycles and sequence stratigraphy of the Upper Triassic Yanchang Formation, Ordos Basin, China: Basin Research, v. 22, p. 108–125.

GENERAL CONCLUSIONS

This research advances the current understanding of the interplay of depositional, diagenetic, and hydrocarbon generation processes in the origin and evolution of OM-rich mudrock pores. This was accomplished by carrying out laboratory pyrolysis simulation on immature rocks, investigating controls of pores in different suites of subsurface mudrock samples, and integrating petrography with geochemistry, mineralogy, and sedimentology. High-resolution FE-SEM was used for describing and characterizing multiscale mudrock properties. Results of this research led to not only fundamental, process-based understanding of origin and control of different pore types but the establishment of a link between sediments and depositional processes to pore system variations.

OM pores are related to types of kerogen and macerals, and subsequent thermal maturation processes which are determined by generation kinetics and activation energy distribution of each maceral type. Four main categories of OM pores comprise the OM-pore network: primary OM pore, convoluted OM pore, OM bubble pore, and OM spongy pore, with the latter two related to thermal maturation processes.

Pore evolution models of mature mudrocks and a classification scheme of OM pores were developed from this investigation. The original interparticle and intraparticle mineral pores, which are a function of depositional and early diagenetic processes, determined the mineral pore network before petroleum generation, expulsion, and migration began. The mineral pore network constrained petroleum migration and OM redistribution, controlling the modified-mineral-pore and OM-pore network after thermal

maturation of OM. Petroleum migrated more pervasively in mudrocks composed of predominantly interparticle pores than in mudrocks composed of mainly intraparticle pores. After OM maturation, the pore evolution was closely related to OM conversion. The morphology of mineral and OM pores vary with stages of OM maturation. Predominant pore types change from primary mineral pores at the immature stage, to modified mineral pores containing relic OM at the bitumen maturation stage, to coexisting modified mineral pores, OM bubble pores, and OM spongy pores at the oil window maturation stage, and finally to OM spongy pores at the gas maturation stage. Pre-oil solid bitumen was observed to have migrated into initial primary mineral pore networks in studied mudrock samples. The volume of primary mineral pores decreases and the pore volume composed of modified mineral pores and OM pores increases at higher levels of thermal maturation.

Pore sizes in OM-rich mudrocks range across at least five orders of magnitude (from 1 nm to approximately 100 μm). In general, sizes of OM pores are smaller than those of mineral pores. Mineral-hosted pores are related to sediment sources, depositional, and diagenetic (compaction, cementation, dissolution, and replacement) processes. Primary mineralogy, grain assemblage, texture, and fabric determine the strength of mineral frameworks and affect subsequent diagenetic alteration such as compaction and cementation. A mudrock with well-sorted and coarser grains has higher mineral porosity. A mudrock with abundant early calcite and quartz cementation retards compaction and adds brittleness to the rock. A mudrock without early cementation contains smaller OM pores than mudrocks with abundant cements. Primary mineralogy,

texture, and fabric could indirectly affect sizes of OM pores up to two orders of magnitude differences.

REFERENCES

Afsharpoor, A. and F. Javadpour, 2016, Liquid slip flow in a network of shale noncircular nanopores: Fuel, v. 180, p. 580–590.

Alldredge, A. L., and M. W. Silver, 1988, Characteristics, dynamics, and significance of marine snow: Progress in Oceanography, v. 20, p. 41–82.

Ambrose, R. J., R. C. Hartman, M. D. Campos, I. Y. Akkutlu, and C. H. Sondergeld, 2010, New pore-scale considerations for shale gas in place calculations: Society of Petroleum Engineers Unconventional Gas Conference, Pittsburgh, Pennsylvania, February 23–25, 2010, SPE Paper 131772, 17 p.

Aplin, A. C., and J. H. S. Macquaker, 2011, Mudstone diversity: Origin and implications for source, seal, and reservoir properties in petroleum systems: AAPG Bulletin, v. 95, p. 2031–2059.

ASTM D2797, 2016a, Standard practice for preparing coal samples for microscopical analysis by reflected light: Annual book of ASTM standards, Petroleum products, lubricants, and fossil fuels; Gaseous fuels; coal and coke, sec. 5, v. 5.06: ASTM International, West Conshohocken, PA, 542–546.

ASTM D7708, 2016b, Standard test method for microscopical determination of the reflectance of vitrinite dispersed in sedimentary rocks: Annual book of ASTM standards, Petroleum products, lubricants, and fossil fuels; Gaseous fuels; coal and coke, sec. 5, v. 5.06: ASTM International, West Conshohocken, PA, p. 923–932.

Aufill, M., 2007, High resolution magnetic susceptibility of the Oklahoma Woodford Shale and relationships to variations in outcrop spectral gamma-ray response: MS thesis, Oklahoma State University, Stillwater, Oklahoma, 165 p.

Bastow, T. P., B. G. K. van Aarssen, and D. Lang, 2007, Rapid small-scale separation of saturate, aromatic, and polar components in petroleum: Organic Geochemistry, v. 38, p. 1235–1250.

Bernard, S., and B. Horsfield, 2014, Thermal maturation of gas shale systems: Annual Review of Earth and Planetary Sciences, v. 42, p. 635–651.

Bernard, S., B. Horsfield, H.-M. Schulz, A. Schreiber, R. Wirth, T. T. A. Vu, F. Perssen, S. Könitzer, H. Volk, N. Sherwood, and D. Fuentes, 2010, Multi-scale detection of organic and inorganic signatures provides insights into gas shale properties and evolution: Chemie der Erde - Geochemistry, v. 70, no. S3, p. 119–133.

Bernard, S., B. Horsfield, H.-M. Schulz, R. Wirth, A. Schreiber, and N. Sherwood, 2012a, Geochemical evolution of organic-rich shales with increasing maturity: A STXM and TEM study of the Posidonia Shale (Lower Toarcian, northern Germany): Marine and Petroleum Geology, v. 31, p. 70–89.

Bernard, S., R. Wirth, A. Schreiber, H.-M. Schulz, and B. Horsfield, 2012b, Formation of nanoporous pyrobitumen residues during maturation of the Barnett Shale (Fort Worth Basin): International Journal of Coal Geology, v. 103, p. 3–11.

Bernard, S., R. Wirth, A. Schreiber, L. Brown, A.C. Aplin, E. J. Mathia, H.-M. Schulz, and B. Horsfield, 2013, FIB-SEM and TEM investigations of an organic-rich shale maturation series from the Lower Toarcian Posidonia Shale, Germany: Nanoscale pore system and fluid-rock interactions, in E. D. W. Camp, and B. Wawak, eds., Electron microscopy of shale hydrocarbon reservoirs: AAPG Memoir 102, p. 53–66.

Bertrand, P. J.-L. Pittion, and C. Bernaud, 1986, Fluorescence of sedimentary organic matter in relation to its chemical composition: Organic Geochemistry, v. 10, p. 641–647.

Blakey, R., 2009, Paleogeography and geologic evolution of North America, Late Devonian (360 Ma), map: http://jan.ucc.nau.edu/~rcb7/namD360.jpg, accessed September 2016.

Bohacs, K. M., Q. M. Passey, M. Rudnicki, W. L. Esch, and O. R. Lazar, 2013, The spectrum of fine-grained reservoirs from "shale-gas" to "shale oil"/tight liquids: essential attributes, key controls, practical characterization: International Petroleum Technology Conference (IPTC), Beijing, China, March 26–28, 2013, IPTC Paper 16676, 16 p.

Bowker, K. A., 2007, Barnett Shale gas production, Fort Worth Basin: Issues and discussion: AAPG Bulletin, v. 91, p. 523–533.

Burwood, R., 1999, Angola: source rock control for Lower Congo Coastal and Kwanza basin petroleum systems, *in*: N. R. Cameron, R. H. Bate, and V. S. Clure eds., The Oil and Gas Habitats of the South Atlantic, Geological Society (London), Special Publication 53, p. 181–194.

Bustin, R., A. Bustin, A. Cui, and D. Ross, 2008, Impact of shale properties on pore structure and storage characteristics: Society of Petroleum Engineers Shale Gas Production Conference, Fort Worth, Texas, USA, November 16–18, 2008, SPE Paper 119892, 28 p.

Cao, H., X. Shan, P. Sun, H. Chi, and S. Du, 2016, Geochemical characteristics of oil shale in the Triassic Chang7 subsection, southern Ordos basin, China, and palaeo-environment reconstruction: Journal of Mineralogy and Geochemistry, 193, p. 45–57.

Cardott, B. J., and J. R. Chaplin, 1993, Guidebook for selected stops in the Western Arbuckle Mountains, southern Oklahoma, Oklahoma Geological Survey Special Publication 93-3, 61 p.

Cardott, B. J., 2011, Four distinct Woodford Shale plays in Oklahoma—gas, condensate, oil, and biogenic methane: AAPG Hedberg Conference, http://www.searchanddiscovery.com/abstracts/pdf/2011/hedberg-texas/abstracts/ndx_cardott.pdf, accessed 1/23/2016.

Cardott, B. J., C. R. Landis, and M. E. Curtis, 2015, Post-oil solid bitumen network in the Woodford Shale, USA — A potential primary migration pathway: International Journal of Coal Geology, v. 139, p. 106–113.

Carroll, A. R., S. A. Graham, and M. E. Smith, 2010, Walled sedimentary basins of China: Basin Research, v. 22, p. 17–32.

Chalmers, G. R., R. M. Bustin, and I. M. Power, 2012, Characterization of gas shale pore systems by porosimetry, pycnometry, surface area, and field emission scanning electron microscopy/transmission electron microscopy image analyses: Examples from the Barnett, Woodford, Haynesville, Marcellus, and Doig units: AAPG Bulletin, v. 96, p. 1099–1119.

Clarkson, C. R., N. Solano, R. M. Bustin, A. M. M. Bustin, G. R. L. Chalmers, L. He, Y. B. Melnichenko, A. P. Radliński, and T. P. Blach, 2013, Pore structure characterization of North American shale gas reservoirs using USANS/SANS, gas adsorption, and mercury intrusion: Fuel, v. 103, p. 606–616.

Comer, J. B., 2007, Lithologic characeristics and gas production potential of Woodford Shale in the southern midcontinent, abstract, GSA Annual Meeting, Denver, 28–31 October 2007.

Cook, A. C., and N. R. Sherwood, 1991, Classification of oil shales, coals, and other organic-rich rocks: Organic Geochemistry, v. 17, p. 211–222.

Curiale, J. A., 1986, Origin of solid bitumens, with emphasis on biological marker results: Organic Geochemistry, v. 10, p. 559–580.

Curtis, M. E., Cardott, B. J., Sondergeld, C. H. and Rai, C.S., 2012, Development of organic porosity in the Woodford Shale with increasing thermal maturity: International Journal of Coal Geology, v. 103, p. 26–31.

Curtis, M. E., R. J. Ambrose, C. H. Sondergeld, and C. S. Rai, 2010, Structural characterization of gas shales on the micro- and nano-scales: Canadian Unconventional Resources and International Petroleum Conference, Calgary, Alberta, Canada, October 19–21, 2010, CUSG/SPE Paper 137693, 15 p.

Curtis, M. E., C. H. Sondergeld, R. J. Ambrose, and C. S. Rai, 2012, Microstructural investigation of gas shales in two and three dimensions using nanometer-scale resolution imaging: AAPG Bulletin, v. 96, p. 665–677.

Dahl, J., R. T. Chen, and I. R. Kaplan, 1989, Alum Shale bitumen maturation and migration: implications for Gotland's Oil: Journal of Petroleum Geology, v. 12, p. 465–476.

Day-Stirrat, R. J., P. B. Flemings, Y. You, A. C. Aplin, and B. A. van der Pluijm, 2012, The fabric of consolidation in Gulf of Mexico mudstones: Marine Geology, v. 295–298, p. 77–85.

Denne, R. A., R. E. Hinote, J. A. Breyer, T. H. Kosanke, J. A. Lees, N. Engelhardt-Moore, J. M. Spaw, and N. Tur, 2014, The Cenomanian-Turonian Eagle Ford Group of South Texas: Insights on timing and paleoceanographic conditions from geochemistry and micropaleontologic analyses: Palaeogeography, Palaeoclimatology, Palaeoecology, v. 413, p. 2–28.

Derenne, S., P. Metzger, C. Largeau, P. F. van Bergen, J. P. Gatellier, J. S. Sinninghe Damste, J. W. de Leeuw, C. Berkaloff, 1992, Similar morphological and chemical variations of *Gloeocapsomorpha prisca* in Ordovician sediments and cultured *Botryococcus braunii* as a response to changes in salinity: Organic Geochemistry, v. 19, 299–313.

Desbois, G., J. L. Urai, and P. A. Kukla, 2009, Morphology of the pore space in claystones- Evidence from BIB/FIB ion beam sectioning and cryo-SEM observations: Earth, v. 4, p. 15–22.

Dewhurst, D. N., S. C. Aplin, J.-P. Sarda, and Y. Yang, 1998, Compaction-driven evolution of porosity and permeability in natural mudstones: an experimental study: Journal of Geophysical Research, v. 103, p. 651–661.

Dewhurst, D. N., Y. Yang, and A. C. Aplin, 1999, Permeability and fluid flow in natural mudstones, in A. C. Aplin, A. J. Fleet, and J. H. S., Macquaker, eds., Muds and mudstones: Physical and fluid flow properties: Geological Society (London) Special Publication 158, p. 23–43.

Driskill, B., N. Suurmeyer, S. Rilling-Hall, A. Govert, and A. Garbowicz, 2012, Reservoir Description Of The Subsurface Eagle Ford Formation, Maverick Basin Area, South Texas, USA: Society of Petroleum Engineers Europec/EAGE Annual Conference & Exhibition, Copenhagen, Denmark, June 4–7, 2012, SPE Paper 154528, 23 p.

Driskill, B., J. Walls, S. W. Sinclair, and J. DeVito, 2013, Applications of SEM imaging to reservoir characterization in the Eagle Ford Shale, south Texas, U.S.A., in W. Camp, E. Diaz, B. Wawak, eds., Electron microscopy of shale hydrocarbon reservoirs: AAPG Memoir 102, p. 115–136.

Durand, B., 1980, Kerogen: Insoluble organic matter from sedimentary rocks: Paris, Technip, 519 p.

Eldrett, J. S., C. Ma, S. C. Bergman, A. Ozkan, D. Minisini, B. Lutz, S.-J. Jackett, C. Macaulay, A. M. Kelly, 2015, Origin of limestone-marlstone cycles: Astronomic forcing of organic-rich sedimentary rocks from the Cenomanian to early Coniacian of the Cretaceous Western Interior Seaway, USA: Earth and Planetary Science Letters, v. 423, p. 98–113.

Ergene, S. M., 2014, Lithologic heterogeneity of the Eagle Ford Formation, South Texas: Austin, The University of Texas at Austin, 203 p.

Espitalié, J., M. Madec, and B. Tissot, 1980, Role of mineral matrix in kerogen pyrolysis: Influence on petroleum generation and migration: AAPG Bulletin, v. 64, p. 59–66.

Espitalié, J., K. Senga Makadi, and J. Trichet, 1984, Role of the mineral matrix during kerogen pyrolysis: Organic Geochemistry, v. 6, p. 365–382.

Fairbanks, M. D., S. C. Ruppel, and H. Rowe, 2016, High-resolution stratigraphy and facies architecture of the Upper Cretaceous (Cenomanian–Turonian) Eagle Ford Group, Central Texas: AAPG Bulletin, v.100, p. 379–403.

Fishman, N. S., P. C. Hackley, H. A. Lowers, R. J. Hill, S. O. Egenhoff, D. D. Eberl, and A. E. Blum, 2012, The nature of porosity in organic-rich mudstones of the Upper Jurassic Kimmeridge Clay Formation, North Sea, offshore United Kingdom: International Journal of Coal Geology, v. 103, p. 32–50.

Fishman, N. S., G. S. Ellis, S. T. Paxton, A. R. Boehlke, and S. O. Egenhoff, 2013, Gas storage in the Upper Devonian–Lower Mississippian Woodford Shale, Arbuckle Mountains, Oklahoma: How much of a role do chert beds play?, *in* J. Chatellier and D. Jarvie, eds., Critical assessment of shale resource plays: AAPG Memoir 103, p. 81–107.

Folk, R. L., 1980, Petrology of sedimentary rocks: Hemphill Publication Company, Austin, Texas 78703.

Fowler, M. G., L. D. Stasiuk, M. Hearn, and M. Obermajer, 2004, Evidence for *Gloeocapsomorpha prisca* in Late Devonian source rocks from southern Alberta, Canada: Organic Geochemistry, v. 35, p. 425–441.

Frébourg, G., S. C. Ruppel, R. G. Loucks, and J. Lambert, Depositional controls on sediment body architecture in the Eagle Ford/Boquillas system: Insights from outcrops in West Texas, USA: AAPG Bulletin, v. 100, p. 657–582.

Goldstein, T. P., 1983, Geocatalytic reactions in formation and maturation of petroleum: AAPG Bulletin, v. 67, p. 152–159.

Guo, H., W. Jia, P. Peng, Y. Lei, X. Luo, M. Cheng, X. Wang, L. Zhang, and C. Jiang, 2014, The composition and its impact on the methane sorption of lacustrine shales from the Upper Triassic Yanchang Formation, Ordos Basin, China: Marine and Petroleum Geology, v. 57, p. 509–520.

Hackley, P. C., C. V. Araujo, A. G. Borrego, A. Bouzinos, B. Cardott, A. C. Cook, C. Eble, D. Flores, T. Gentzis, P. A. Gonçalves, J. G. Mendonça Filho, M. Hámor-Vidó, I. Jelonek, K. Kommeren, W. Knowles, J. Kus, M. Mastalerz, T. R. Menezes, J. Newman, M. Pawlewicz, W. Pickel, J. Potter, P. Ranasinghe, H. Read, J. Reyes, G. De La Rosa Rodriguez, I. V. Alves Fernandes de Souza, I. Suarez-Ruiz, I. Sýkorová, B. J. Valentine, 2014, Standardization of reflectance measurements in dispersed organic matter: results of an exercise to improve interlaboratory agreement: Marine and Petroleum Geology, v.59, p. 22–34.

Hackley, P. C., and B. J. Cardott, 2016, Application of organic petrography in North American shale petroleum systems: A review: International Journal of Coal Geology, v. 163, p. 8–51.

Hackley, P. C., Fishman, N., Wu, T., and Baugher, G., 2016, Organic petrology of mudrocks from the lacustrine Lucaogou Formation, Santanghu Basin, northwest China: application to lake basin evolution: International Journal of Coal Geology, v 168, p. 20–34.

Hackley, P. C., and J. Kus, 2015, Thermal maturity of Tasmanites microfossils from confocal laser scanning fluorescence microscopy: Fuel, v. 142, p. 343–350.

Hackley, P. C., and J. R. SanFilipo, 2016, Organic petrology and geochemistry of Eocene Suzak bituminous marl, north-central Afghanistan: depositional environment and source rock potential: Marine and Petroleum Geology, v. 73, p. 572–589.

Hackley, P. C., L. Zhang, and T. Zhang, 2017, Organic petrology of peak oil maturity Triassic Yanchang Formation lacustrine mudrocks, Ordos Basin, China: Interpretation, v. 5, p. SF211–SF223.

Ham, W. E., 1973, Regional geology of the Arbuckle Mountains, Oklahoma: The Geological Society of America, compiled by T. L. Rowland, 62p.

Han, S., B. Horsfield, J. Zhang, Q. Chen, N. Mahlstedt, R. di Primio, and G. Xiao, 2014, Hydrocarbon generation kinetics of lacustrine Yanchang Shale in southeast Ordos Basin, North China: Energy & Fuels, v. 28, p. 5632–5639.

Harbor, R. L., 2011, Facies Characterization and stratigraphic architecture of organic-rich mudrocks, Upper Cretaceous Eagle Ford Formation, South Texas: Austin, The University of Texas at Austin, 195 p.

Hart, B. S., J. H. S. Macquaker, and K. G. Taylor, 2013, Mudstone ("shale") depositional and diagenetic processes: Implications for seismic analyses of source-rock reservoirs: Interpretation, v. 1, p. B7–B26.

Hemes, S., G. Desbois, J. L. Urai, B. Schröppel, and J.-O. Schwarz, 2015, Multi-scale characterization of porosity in Boom Clay (HADES-level, Mol, Belgium) using a combination of X-ray μ-CT, 2D BIB-SEM and FIB-SEM tomography: Microporous and Mesoporous Materials, v. 208, p. 1–20.

Hetényi, M., 1995, Simulated thermal maturation of type I and III kerogens in the presence, and absence, of calcite and montmorillonite: Organic Geochemistry, v. 23, p. 121–127.

Honarpour, M. M., N. R. Nagarajan, A. Orangi, F. Arasteh, and Z. Yao, 2012, Characterization of critical fluid, rock, and rock-fluid properties – impact of reservoir performance of liquid-rich shales: Society of Petroleum Engineers Annual TechnicalConference and Exhibition, San Antonio, Texas, USA, October 8–10, 2012, SPE Paper 158042, 22 p.

Horsfield, B., and A. G. Douglas, 1980, The influence of minerals on the pyrolysis of kerogen: Geochimica et Cosmochimica Acta, v. 44, p. 1119–1131.

Houben, M. E., G. Desbois, and J. L. Urai, 2013, Pore morphology and distribution in the Shaly facies of Opalinus Clay (Mont Terri, Switzerland): Insights from representative 2D BIB-SEM investigations on mm to nm scale: Applied Clay Science, v. 71, p. 82–97.

Houben, M. E., G. Desbois, and J. L. Urai, 2014, A comparative study of representative 2D microstructures in Shaly and Sandy facies of Opalinus Clay (Mont Terri, Switzerland) inferred form BIB-SEM and MIP methods: Marine and Petroleum Geology, v. 49, p. 143–161.

Huizinga, B. J., E. Tannenbaum, and I. R. Kaplan, 1987a, The role of minerals in the thermal alteration of organic matter: III. Generation of bitumen in laboratory experiments: Organic Geochemistry, v. 11, p. 591–604.

Huizinga, B. J., E. Tannenbaum, and I. R. Kaplan, 1987b, The role of minerals in the thermal alteration of organic matter: IV. Generation of n-alkanes, acyclic isoprenoids, and alkenes in laboratory experiments: Geochimica et Cosmochimica Acta, v. 51, p. 1083– 1097.

Hunt, J. M., 1996, Petroleum geochemistry and geology: New York, New York, W. H. Freeman and Company, 746 p.

Ichaso, A. A., and R. W. Dalrymple, 2009, Tide- and wave-generated fluid mud deposits in the Tilje Formation (Jurassic), offshore Norway: Geology, v. 37, p. 539–542.

Jennings, D. S., and J. Antia, 2013, Petrographic characterization of the Eagle Ford shale, south Texas: mineralogy, common constituents, and distribution of nanometer-scale pore types, in W. Camp, E. Diaz, B. Wawak, eds., Electron microscopy of shale hydrocarbon reservoirs: AAPG Memoir 102, p. 101–113.

Ji., L.-M., F.-W. Meng, J. D. Schiffbauer, J.-L. Xu, K. Yuan, and J.-W. Shu, 2008, Correlation between highly abundant oil-prone leiosphaerid acritarchs and hydrocarbon source rocks from the Triassic Yanchang Formation, eastern Gansu Province, Northwestern China: Gondwana Research, v. 14, p. 554–560.

Ji, L.-M., K. Yan, F.-W. Meng, and M. Zhao, 2010, The oleaginous Botryococcus from the Triassic Yanchang Formation in Ordos Basin, northwestern China: Morphology and its paleoenvironmental significance: Journal of Asian Earth Sciences, v. 38, p. 175–185.

Jiang, F., D. Chen, Z. Wang, Z. Xu, J. Chen, L. Liu, Y. Huyan, and Y. Liu, 2016, Pore characteristic analysis of a lacustrine shale: A case study in the Ordos Basin, NW China: Marine and Petroleum Geology, v. 73, p. 554–571.

Johns, W. D., 1979, Clay mineral catalysis and petroleum generation: Annual Review Earth Planetary Science, v. 7, p. 183–198.

Kanitpanyacharoen, W., F. B. Kets, H.-R. Wenk, and R. Wirth, 2012, Mineral preferred orientation and microstructure in the Posidonia shale in relation to different degrees of thermal maturity: Clay and Clay Minerals, v. 60, p. 315–329.

Katz, B., and F. Lin, 2014, Lacustrine basin unconventional resource plays: Key differences: Marine and Petroleum Geology, v. 56, p. 255–265.

Kim, B., S. Gupta, S. Lee, S. Kim, and V. Sahajwalla, 2008, Devolatilization and cracking characteristics of Australian lumpy coals: Energy & Fuels, v. 22, p. 514–522.

Kirkland, D. W., R. E. Denison, D. M. Summers, and J. R. Gormly, 1992, Geology and organic geochemistry of the Woodford Shale in the Criner Hills and western Arbuckle Mountains, *in* K. S. Johnson and B. J. Cardott, eds., Source rocks in the southern Midcontinent, 1990 symposium: Oklahoma Geological Survey Circular 93, p. 38–69.

Klaver, J., G. Desbois, J. L. Urai, and R. Littke, 2012, BIB-SEM study of the pore space morphology in early mature Posidonia Shale from the Hils area, Germany: International Journal of Coal Geology, v. 103, p. 12–25.

Ko, L. T., T. Zhang, R. G. Loucks, S. C. Ruppel, and D. Shao, 2014, Boquillas (Eagle Ford) Formation pore evolution results from laboratory heating experiments: Unconventional Resources Technology Conference (URTeC), Denver, Colorado, August 25–27, 2014, URTeC 1935124, 7 p.

Ko, L. T., T. Zhang, R. G. Loucks, S. C. Ruppel, and D. Shao, 2015, Pore evolution in the Barnett, Eagle Ford (Boquillas), and Woodford mudrocks based on gold-tube pyrolysis thermal maturation, AAPG 2015 Annual Convention and Exhibition, Denver, Colorado, May 31–June 3rd, Search and Discovery Article #51228 (2016)

Ko, L. T., R. G. Loucks, T. Zhang, S. C. Ruppel, and D. Shao, 2016, Pore and pore network evolution of Upper Cretaceous Boquillas (Eagle Ford-equivalent) mudstone: Results from gold-tube pyrolysis experiments: AAPG Bulletin, v. 100, p. 1693–1722.

Ko, L. T., R. G. Loucks, S. C. Ruppel, T. Zhang, S. Peng, 2017, Origin and characterization of Eagle Ford pore networks in the south Texas Upper Cretaceous shelf: AAPG Bulletin, v. 101, p. 387–418.

Krystyniak, A. M., 2005, Outcrop-based gamma-ray characterization of the Woodford Shale of south-central Oklahoma: Master's thesis, Oklahoma State University, Stillwater, Oklahoma, 145 p.

Kulia, U., M. Prasad, A. Derkowski, and D. K. McCarty, 2012, Compositional controls on mudrock pore-size distribution: an example from Niobrara Formation: Society of Petroleum Engineers Annual Technical Conference and Exhibition, San Antonio, Texas, USA, October 8–10, 2012, SPE Paper 160141, 16 p.

Kulia, U., 2013, Measurement and interpretation of porosity and pore-size distribution in mudrocks: the whole story of shales: dissertation thesis: Golden, Colorado, Colorado School of Mines, 238 p.

Kulia, U., and M. Prasad, 2013, Specific surface area and pore-size distribution in clays and shales: Geophysical Prospecting 61, p. 341–362.

Lazar, O. R., K. M. Bohacs, J. H. S. Macquaker, J. Schieber, and T. M. Demko, 2015, Mudstone primer: Lithofacies variations, diagnostic criteria, and sedimentologic/stratigraphic implications at lamina to bedset scale: Concepts in Sedimentology and Paleontology, v. 12, SEPM, 198 p.

Lambert, M. W., 1993, Internal stratigraphy and organic facies of the Devonian-Mississippian Chattanooga (Woodford) Shale in Oklahoma and Kansas: Source rocks in a sequence stratigraphic framework: Chapter 11, AAPG Studies in Geology, v. 37, p. 163–176.

Lao, Y., J. Korth, J. Ellis, and P. T. Crisp, 1989, Heterogeneous reactions of 1-pristene catalyzed by clays under simulated geological conditions: Organic Geochemistry, v. 14, p. 375–379.

Lewan, M. D., 1983, Effects of thermal maturation on stable organic carbon isotopes as determined by hydrous pyrolysis of Woodford Shale: Geochimica et Cosmochimica Acta, v. 47, p. 1471–1479.

Lewan, M. D., 1987, Petrographic study of primary petroleum migration in the Woodford shale and related rock units, in B. Doligez Ed., Migration of Hydrocarbons in Sedimentary Basins: Paris, Editions Technip, p. 113–130.

Lewan, M. D., 1993, Laboratory simulation of petroleum formation, hydrous pyrolysis, in M. S. A. Engel M.H., ed., Organic Geochemistry Plenum Press, p. 419–442.

Lewan, M. D., M. P. Dolan, and J. B. Curtis, 2014, Effects of smectite on the oil-expulsion efficiency of the Kreyenhagen Shale, San Joaquin Basin, California based on hydrous-pyrolysis experiments: AAPG Bulletin, v. 98, p. 1091–1109.

Li, S., S. Yang, and T. Jeryzkiewicz, 1995, Upper Triassic–Jurassic foreland sequences of the Ordos Basin in China, *in* S. L. Dorobek and G. M. Ross, eds., Stratigraphic evolution of foreland basins: SEPM Special Publication 52, p. 233–241.

Li, J., S. Zhou, Y. Li, Y. Ma, Y. Yang, C. Li, 2016, Effect of organic matter on pore structure of mature lacustrine organic-rich shale: A case study of the Triassic Yanchang Shale, Ordos Basin, China: Fuel, v. 185, p. 421–431.

Liu, B., Y. Wang, and X. Qian, 1997, Two Ordovician unconformities in north China: Their origins and relationships to regional carbonate-reservoir characteristics: Carbonates and Evaporites, v. 12, p. 177–184.

Liu, S., 1998, The coupling mechanism of basin and orogeny in the western Ordos Basin and adjacent regions of China: Journal of Asian Earth Sciences, v. 16, p. 369–383.

Löhr, S. C., E. T. Baruch, P. A. Hall, and M. J. Kennedy, 2015, Is organic pore development in gas shales influenced by the primary porosity and structure of thermally immature organic matter?: Organic Geochemistry, v. 87, p. 119–132.

Loucks, R. G., R. M. Reed, S. C. Ruppel, and D. M. Jarvie, 2009, Morphology, genesis, and distribution of nanometer-scale pores in siliceous mudstones of the Mississippian Barnett Shale: Journal of Sedimentary Research, v. 79, p. 848–861.

Loucks, R. G., R. M. Reed, S. C. Ruppel, and U. Hammes, 2012, Spectrum of pore types and networks in mudrocks and a descriptive classification for matrix-related mudrock pores: AAPG Bulletin, v. 96, p. 1071–1098.

Loucks, R. G., and R. M. Reed., 2014, Scanning-electron-microscope petrographic evidence for distinguishing organic-matter pores associated with depositional organic matter versus migrated organic matter in mudrocks: GCAGS Journal, v. 3, p. 51–60.

Loucks, R. G., and S. C. Ruppel, 2007, Mississippian Barnett Shale: Lithofacies and depositional setting of a deep-water shale-gas succession in the Fort Worth Basin, Texas: AAPG Bulletin, v. 91, p. 579–601.

Loucks, R. G., S. C. Ruppel, L. T. Ko, P. Smith, S. Peng, and T. Zhang, 2017, Pore types, pore-network analysis, and pore quantification of the lacustrine shale-hydrocarbon system in the Late Triassic Yanchang Formation in the southeastern Ordos Basin, China: Interpretation, v. 5, p. SF63–SF79.

Lucia, F. J., 2007, Carbonate reservoir characterization: An integrated approach, 2nd ed.: New York, Springer-Verlag, 336 p., doi: 10.1007/978-3-540-72742-2.

Luffel, D. L., and C. W. Hopkins, 1993, Matrix permeability measurement of gas productive shales: Society of Petroleum Engineers (SPE) Annual Technical Conference and Exhibition, October 3-6th, Houston, Texas, SPE-26633-MS, p. 261–270.

Macquaker, J. H. S., and A. E. Adams, 2003, Maximizing information from fine-grained sedimentary rocks: An inclusive nomenclature for mudstones: Journal of Sedimentary Geology, v. 73, p. 735–744.

Macquaker, J. H. S., and R. L. Gawthorpe, 1993, Mudstone lithofacies in the Kimmeridge Clay Formation, Wessex Basin, southern England: Implications for the origin and controls of the distribution of mudstones: Journal of Sedimentary Petrology, v. 63, p. 1129–1143.

Macquaker, J. H. S., and J. K. Howell, 1999, Small-scale (<5.0 m) vertical heterogeneity in mudstones: Implications for high-resolution stratigraphy in siliciclastic mudstone successions: Journal of Geological Society, London, v. 156, p. 105–112.

Macquaker, J. H. S., M. A. Keller, and S. J. Davies, 2010, Algal blooms and "marine snow": Mechanisms that enhance preservation of organic carbon in ancient fine-grained sediments: Journal of Sedimentary Research, v. 80, p. 934–942.

Macquaker, J. H. S., K. G. Taylor, and R. L. Gawthorpe, 2007, High-resolution facies analyses of mudstones: Implications for paleoenvironmental and sequence stratigraphic interpretations of offshore ancient mud-dominated successions: Journal of Sedimentary Research, v. 77, p. 324–339.

Mancini, E. A., R. M. Mink, J. W. Payton, and B. L. Bearden, 1987, Environments of deposition and petroleum geology of Tuscaloosa Group (Upper Cretaceous), south Carton and Pollard Fields, southwestern Alabama: AAPG Bulletin, v. 71, p. 1128–1142.

Mastalerz, M., and M. Glikson, 2000, In-situ analysis of solid bitumen in coal: Examples from the Bowen Basin and the Illinois Basin: International Journal of Coal Geology, v. 42, p. 201–220.

Mastalerz, M., A. Schimmelmann, A. Drobniak, and Y. Chen, 2013, Porosity of Devonian and Mississippian New Albany Shale across a maturation gradient: Insights from organic petrology, gas adsorption, and mercury intrusion: AAPG Bulletin, v. 97, p. 1621–1643.

Mastalerz, M., A. Schimmelmann, G. P. Lis, A. Drobniak, and A. Stankiewicz, 2012, Influence of maceral composition on geochemical characteristics of immature shale kerogen: Insight from density fraction analysis: International Journal of Coal Geology, v. 103, p. 60–69.

McAllister, R. T., K. G. Taylor, and B. Garcia-Fresca, 2015, Diagenetic evolution of the Eagle Ford Formation, SW Texas: Impacts upon reservoir quality and rock properties: Unconventional Resources Technology Conference (URTeC), San Antonio, Texas, July 20–22, 2015, URTeC 2153115, 12 p.

Meckel. L. D., D. G. Smith, and L. A. Wells, 1992, Ouachita foredeep basins: Regional paleogeography and habit of hydrocarbons: Foreland basins and foldbelts: Chapter 15, AAPG Memoir 55, Tulsa, Oklahoma, p. 427–444.

Meissner, F. E, 1978, Petroleum geology of the Bakken Formation, Williston basin. North Dakota and Montana, in The economic geology of the Williston basin: Montana Geological Society 24th Annual Conference; 1978 Williston Basin Symposium, p. 207–227.

Milliken, K. L., 2013, SEM-based cathodoluminescence imaging for discriminating quartz types in mudrocks: Unconventional Resources Technology Conference (URTeC), Denver, Colorado, August 12–14, 2013, URTeC 1582467, 9 p.

Milliken, K. L., S.-J. Choh, P. Papazis, and J. Schieber, 2007, "Cherty" stringers in the Barnett Shale are agglutinated foraminifera: Sedimentary Geology, v. 198, p. 221–232.

Milliken, K. L., R. J. Day-Stirrat, P. K. Papazis, and C. Dohse, 2012a, Carbonate lithologies of the Mississippian Barnett Shale, Fort Worth Basin, Texas, *in* J. A. Breyer, ed., Shale reservoirs—Giant resources for the 21st century: AAPG Memoir 97, p. 290–321.

Milliken, K. L., S. M. Ergene, and A. Ozkan, 2016, Quartz types, authigenic and detrital, in the Upper Cretaceous Eagle Ford Formation, south Texas, USA: Sedimentary Geology, v. 339, p. 273–288.

Milliken, K. L., W. L. Esch, R. M. Reed, and T. Zhang, 2012, Grain assemblages and strong diagenetic overprinting in siliceous mudrocks, Barnett Shale (Mississippian), Fort Worth Basin, Texas: AAPG Bulletin, v. 96, p. 1553–1578.

Milliken, K. L., L. T. Ko, M. Pommer, and K. M. Marsaglia, 2014, SEM petrography of eastern Mediterranean sapropels: Analogue data for assessing organic matter in oil and gas shales: Journal of Sedimentary Research, v. 84, p. 961–974.

Milliken, K. L. and S. E. Laubach, 2000, Brittle deformation in sandstone diagenesis as revealed by scanned cathodoluminescence imaging with application to characterization of fractured reservoirs, in: M. Pagel, V.B., P. Blanc, and D. Ohnenstetter (Ed.), Cathodoluminescence in Geosciences, Springer Berlin Heidelberg, p. 225–243.

Milliken, K. L., M. Rudnicki, D. N. Awwiller, and T. Zhang, 2013, Organic matter-hosted pore system, Marcellus Formation (Devonian), Pennsylvania: AAPG Bulletin, v. 97, p. 177–200.

Milliken, K. L., Y. Shen, L. T. Ko, and Q. Liang, 2017, Grain composition and diagenesis of organic-rich lacustrine tarls, Triassic Yanchang Formation, Ordos Basin, China: Interpretation, v. 5, p. SF189–SF210.

Montgomery, S. L., D. M. Jarvie, K. A. Bowker, and R. M. Pollastro, 2005, Mississippian Barnett Shale, Fort Worth Basin, northcentral Texas: Gas-shale play with multi-trillion cubic foot potential: AAPG Bulletin, v. 89, no. 2, p. 155– 175.

Mukhopadhyay, P. K., and J. R. Gormly 1984, Hydrocarbon potential of two types of resinite: Organic Geochemistry, v. 6, p. 439–454.

Nicholas, R. L., and R. A. Rozendal, 1975, Subsurface positive elements within Ouachita foldbelt in Texas and their relation to Paleozoic cratonic margin: AAPG Bulletin, v. 59, p. 193– 216.

Myrow, P. M., and J. B. Southard, 1996, Tempestite deposition: Journal of Sedimentary Research, v. 66, p. 875–887.

Pan, C., A. Geng, N. Zhong, and J. Liu, 2010, Kerogen pyrolysis in the presence and absence of water and minerals: Steranes and triterpenoids: Fuel, v. 89, p. 336–345.

Pan, S., B. Horsfield, C. Zou, and Z. Yang, 2016, Upper Permian Junggar and Upper Triassic Ordos lacustrine source rocks in northwest and central China: Organic geochemistry, petroleum potential, and predicted organofacies: International Journal of Coal Geology, v. 158, p. 90–106.

Passey, Q. R., K. M. Bohacs, W. L. Esch, R. Klimentidis, and S. Sinha, 2010, From oil-prone source rock to gas-producing shale reservoirs - geological and petrophysical characterization of unconventional shale-gas reservoirs: Society of Petroleum Engineers CPS/SPE International Oil and Gas Conference and Exhibition, Beijing, China, June 8–10, 2010, SPE Paper 131350, 29 p.

Paxton, S. T., and B. J. Cardott, 2008, Oklahoma gas shales, field trip guidebook: Oklahoma Geological Survey Open File Report 2-2008, 87 p.

Peng, S. and R. G. Loucks, 2016, Permeability measurements in mudrocks using gas-expansion methods on plug and crushed-rock samples: Marine and Petroleum Geology, v. 73, p. 299–310.

Pepper, A. S., and P. J. Corvi, 1995, Simple kinetic models of petroleum formation. Part 1: oil and gas generation from kerogen: Marine and Petroleum Geology, v. 12, p. 291–319.

Pierce, J. D., S. C. Ruppel, and D. F. Stockli, 2016, U-Pb geochronology of the Late Cretaceous Eagle Ford Shale, Texas: Defining chronostratigraphic boundaries and volcanic ash source, GCAGS Journal, *in press*.

Plint, A. G., 2014, Mud dispersal across a Cretaceous prodelta: Storm-generated, wave-enhanced sediment gravity flows inferred from mudstone microtexture and microfacies: Sedimentology, v. 61, p. 609–647.

Pollastro, R. M., D. M. Jarvie, R. J. Hill, and C. W. Adams, 2007, Geologic framework of the Mississippian Barnett Shale, Barnett–Paleozoic total petroleum system, Bend arch–Forth Worth Basin, Texas: AAPG Bulletin, v. 91, p. 405–436.

Pommer, M. E., 2014, Quantitative assessment of pore types and pore size distribution across thermal maturity, Eagle Ford Formation, South Texas: Austin, The University of Texas at Austin, 239 p.

Pommer, M., and K. Milliken, 2015, Pore types and pore-size distribution across thermal maturity, Eagle Ford Formation, southern Texas: AAPG Bulletin, v. 99, p. 1713–1744.

Potter, P. E., B. Maynard, and P. J. Depetris, 2005, Mud and mudstones: Introduction and overview: Berlin; London, Springer, 297 p.

Pradier, B., B. Bertrand, L. Martinez, and F. Laggoun-Defarge, 1991, Fluorescence of organic matter and thermal maturity assessment: Organic Geochemistry, v. 17, p. 511–524.

Redmond, L., 2016, Lithofacies, depositional environments, and depositional model of the Mississippian Barnett Formation in the southern Fort Worth Basin, Master's Thesis, University of Texas at Austin, Austin, Texas, 162 p.

Reed, R.M., and R. G. Loucks, 2007, Imaging nanoscale pores in the Mississippian Barnett Shale of the northern Fort Worth Basin (abs): American Association of Petroleum Geologists, Annual Convention, Abstracts Volume, v. 16, p. 115.

Reed, R. M., R. G. Loucks, and K. L. Milliken, 2012, Heterogeneity of shape and microscale spatial distribution in organic-matter-hosted pores of gas shales: AAPG Annual Convention and Exhibition.

Revill, A. T., J. K. Volkman, T. O'Leary, R. E. Summons, C. J. Boreham, M. R. Banks, and K. Denwer, 1994, Hydrocarbon biomarkers, thermal maturity, and depositional setting of tasmanite oil shales from Tasmania, Australia: Geochimica et Cosmochimica Acta, v. 58, p. 3803–3822.

Rine, J. M., and R. N. Ginsburg, 1985, Depositional facies of a mud shoreface in Suriname, South America—A mud analogue to sandy, shallow-marine deposits: Journal of Sedimentary Petrology, v. 55, p. 633–652.

Roduit, N., 2008, JMICROVISION Version 1.2.7: Image analysis toolbox for measuring and quantifying components of high-definition images: http://www.jmicrovision.com (accessed November 1, 2012).

Romero-Sarmiento, M.-F., J. -N. Rouzaud, S. Bernard, D. Deldicque, M. Thomas, and R. Littke, 2014, Evolution of Barnett Shale organic carbon structure and nanostructure with increasing maturation: Organic Geochemistry, v. 71, p. 7–16.

Roof, J. G., 1970, Snap-off of oil droplets in water-wet pores: Society of Petroleum Engineers Journal, v. 249, p. 85–90.

Ross, D. J. K., and R. M. Bustin, 2009, The importance of shale composition and pore structure upon gas storage potential of shale gas reservoirs: Marine and Petroleum Geology, v. 26, p. 916–927.

Rowe, H., X. Wang, B. Fan, T. Zhang, K. L. Milliken, Y. Shen, and J. Zhang, 2015, Chemostratigraphy of the Triassic Yanchang fluvio-lacustrine succession, Ordos Basin, Shaanxi Province, China: AAPG Annual Convention and Exhibition, Denver, Colo., abstract.

Ruppel, S. C., and R. G. Loucks, 2008, Black mudrocks: Lessons and questions from the Mississippian Barnett Shale in the southern Midcontinent: The Sedimentary Record, v. 6, p. 4–8.

Ruppel, S. C., and H. Rowe, 2017, Facies, rock attributes, stratigraphy, and depositional environments of the Upper Triassic Yanchang Formation, Ordos Basin, China: Interpretation, v. 5, p. SF15–SF29.

Ruppert, L. F., R. Sakurovs, T. P. Blach, L. He, Y. B. Melnichenko, D. F. R. Mildner, and L. Alcantar-Lopez, 2013, A USANS/SANS study of the accessibility of pores in the Barnett Shale to methane and water: Energy & Fuels, v. 27, p. 772–779.

Selby, D., R. A. Creaser, K. Dewing, M. Fowler, 2005, Evaluation of bitumen as ^{187}Re-^{187}Os geochronometer for hydrocarbon maturation and migration: A test case from Polaris MVT deposit, Canada: Earth and Planetary Science Letters, v. 235, p. 1–15.

Schieber, J., 1996, Early diagenetic silica deposition in algal cysts and spores: A source of sand in black shales?: AAPG Bulletin, v. 66, 175–183.

Schieber, J., 1999, Distribution and deposition of mudstone facies in the Upper Devonian Sonyea Group of New York: Journal of Sedimentary Research, v. 69, p. 909–925.

Schieber, J., 2010, Common themes in the formation and preservation of intrinsic porosity in shales and mudstones—Illustrated with examples across the Phanerozoic: Society of Petroleum Engineers Unconventional Gas Conference, Pittsburgh, Pennsylvania, USA, February 23–25, SPE Paper 132370, 10 p.

Schieber, J., J. B. Southard, and K. Thaisen., 2007, Accretion of mudstone beds from migrating floccule ripples: Science, v. 318, p. 1760–1763.

Schieber, J., and J. B. Southard, 2009, Bedload transport of mud by floccule ripples – Direct observation of ripple migration processes and their implications: Geology, v. 37, p. 483-486.

Schieber, J., 2010, Common themes in the formation and preservation of intrinsic porosity in shales and mudstones -illustrated with examples across the Phanerozoic: Society of Petroleum Engineers Unconventional Gas Conference, Pittsburgh, Pennsylvania, USA, February 23–25, SPE Paper 132370, 10 p.

Schieber, J., J. B. Southard, P. Kissling, B. Rossman, and R. Ginsburg, 2013, Experimental deposition of carbonate mud from moving suspensions: Importance of flocculation and implications for modern and ancient carbonate mud deposition: Journal of Sedimentary Research, v. 83, p. 1025–1031.

Schieber, J., J. B. Southard, and A. Schimmelmann, 2010, Lenticular shale fabrics resulting from intermittent erosion of water-rich muds – Interpreting the rock record in the light of recent flume experiments: Journal of Sedimentary Research, v. 80, p. 119–128.

Schieber, J., W. Zimmerle, and P. S. Sethi, 1998, Shales and mudstones: Petrography, Petrophysics, Geochemistry, and Economic Geology, v. 2: Stuttgart, E. Schweizerbart, 296 p.

Schneider, J. P. B. Flemings, R. J. Day-Stirrat, and J. T. Germaine, 2011, Insights into pore-scale controls on mudstone permeability through residimentation experiments: Geology, v. 9, p. 1011–1014.

Silver, M. W., A. L. Shanks, and J. D. Trent, 1978, Marine snow: Microplankton habitat and source of small-scale patchiness in pelagic populations: Science, v. 201, p. 371–373.

Slatt, R. M., and N. R. O'Brien, 2011, Pore types in the Barnett and Woodford gas shales: Contribution to understanding gas storage and migration pathways in fine-grained rocks: AAPG Bulletin, v. 95, p. 2017–2030.

Smith, P., L. T. Ko, and T. Zhang, 2016, High-resolution microscopic analysis of mineral and organic-matter components in the Upper Triassic Yanchang lacustrine shale deposits in southeastern Ordos Basin, China, 2016 SEPM-AAPG Hedberg Research Conference “Mudstone Diagenesis”, October 16-19, Santa Fe New Mexico, USA

Sondergeld, C. H., R. J. Ambrose, C. S. Rai, and J. Moncrieff, 2010, Micro-structural studies of gas shales: SPE Unconventional Gas Conference, Pittsburgh, Pennsylvania,

USA, Society of Petroleum Engineers Unconventional Gas Conference, Pittsburgh, Pennsylvania, USA, February 23-25, SPE Paper 131771, 17 p.

Sone, H. and M. D. Zoback, 2013, Mechanical properties of shale-gas reservoir rocks – Part 1: static and dynamic elastic properties and anisotropy: Geophysics, v. 78, p. D381–D392.

Stow, D. K. V., J.-C. Faugeres, J. A. Howe, C. J. Pudsey, and A. R. Viana, 2002, Bottom currents, contourites, and deep-sea sediment drifts: current state-of-the-art: Geological Society, London, Memoirs 2002, v. 22, p. 7–20.

Suárez-Ruiz, I., D. Flores, J. G. M. Filho, P. C. Hackley, 2012, Review and update of the applications of organic petrology: Part 1, geological applications: International Journal of Coal Geology, v. 99, p. 54–112.

Sun, S., Q. Liang, C. Jiang, D. Enriquez, T. Zhang, and P. C. Hackley, 2017, Liquid hydrocarbon characterization of lacustrine Yanchang Formation, Ordos basin: Organic matter source variation and maturity: Interpretation, v. 5, p. SF225–SF242.

Sun, X., T. Zhang, Y. Sun, K. L. Milliken, and D. Sun, 2016, Geochemical evidence of organic matter source input and depositional environments in the lower and upper Eagle Ford Formation, south Texas: Organic Geochemistry, v. 98, p. 66–81.

Sundararaman, P., S. C. Teerman, R. G. Mann, and B. Mertani, 1988, Activation energy distribution: a key parameter in basin modeling and a geochemical technique for studying maturation and organic facies, Proc. 17th Annu. Indones. Pet. Assoc. 1, p. 169–185.

Tang, X., J. Zhang, X. Wang, B. Yu, W. Ding, J. Xiong, Y. Yang, L. Wang, and C. Yang, 2014, Shale characteristics in the southeastern Ordos Basin, China: Implications for hydrocarbon accumulation conditions and the potential of continental shales: International Journal of Coal Geology, v. 128–129, p. 32–46.

Tannenbaum, E., and I. R. Kaplan, 1985, Role of minerals in the thermal alteration organic matter—I: Generation of gases and condensates under dry condition Geochimica et Cosmochimica Acta, v. 49, p. 2589–2604.

Tannenbaum, E., B. J. Huizinga, and I. R. Kaplan, 1986, Role of minerals in thermal alteration of organic matter—II: A material balance: AAPG Bulletin, v. 70, p. 1156–1165.

Taylor, G. H., and S. Y. Liu, 1989, Micrinite — its nature, origin, and significance: International Journal of Coal Geology, v. 14, p. 29–46.

Teichmüller M., 1986, Organic petrology of source rocks, history and state of the art: Organic Geochemistry, v. 10, p. 581–599.

Tissot, B. P., B. Durand, J. Espitalie, and A. Combaz, 1974, Influence of nature and diagenesis of organic matter in formation of petroleum: AAPG Bulletin, v. 58, p. 499–506.

Tissot, B. P., R. Pelet, Ph. Ungerer, 1987, Thermal history of sedimentary basins, maturation indices, and kinetics of oil and gas generation: AAPG Bulletin, v. 71, p. 1445–1466.

Tissot, B. P., and D. H. Welte, 1984, Petroleum formation and occurrence, 2nd ed.: Berlin, Heidelberg, Germany, Springer-Verlag, 699 p.

Thompson, D. M., 1988, Fort Worth basin, in L. L. Sloss, ed., The geology of North America: Geological Society of America, v. D-2, p. 346–352.

Tyson, R. V., 1995, Sedimentary organic matter: organic facies and palynofacies, Chapman & Hall, Univ. California, 615 p.

Vigran, J. O., A. Mork, A. W. Forsberg, H. M. Weiss, and W. Weitschat, 2008, *Tasmanites* algae—contributors to the Middle Triassic hydrocarbon source rocks of Svalbard and the Barents Shelf: Polar Research, v. 27, p. 360–371.

Volkman, J. K., Z. Zhang, X. Xie, J. Qin, and T. Borjigin, 2015, Biomarker evidence for *Botryococcus* and a methane cycle in the Eocene Huadian oil shale, NE China: Organic Geochemistry, v. 78, p. 121–134.

Walters, C. C., 2007, The origin of petroleum, in book: Practical Advances in Petroleum Processing, Chapter 2, p.79–101.

Wang, X., 2012, The exploration discovery and key technologies of continental shale gas, Yanchang Petroleum: http://www.uschinaogf.org/Forum12/pdf/21%20-%20Xiangzeng%20-%20Shaanxi%20Yanchang%20Petroleum-EN.pdf (accessed November 7, 2015).

Wang, X., L. Zhang, C. Jiang, and B. Fan, 2015a, Hydrocarbon storage space within lacustrine gas shale of the Triassic Yanchang Formation, Ordos Basin, China: Interpretation, v. 3, p. SJ15–SJ23.

Wang, Y., Y. Zhu, H. Wang, and G. Feng, 2015b, Nanoscale pore morphology and distribution of lacustrine shale reservoirs: Examples from the Upper Triassic Yanchang Formation, Ordos Basin: Journal of Energy Chemistry, 4, p. 512–519.

Wei, Z., J. M. Moldowan, J. Dahl, T. P. Goldstein, and D. M. Jarvie, 2006a, The catalytic effects of minerals on the formation of diamondoids from kerogen macromolecules: Organic Geochemistry, v. 37, p. 1421–1436.

Wei, Z., J. M. Moldowan, and A. Paytan, 2006b, Diamondoids and molecular biomarkers generated from modern sediments in the absence and presence of minerals during hydrous pyrolysis: Organic Geochemistry, v. 37, p. 891–911.

Wignall, P. B., 1994a, Black shales: Oxford monographs on geology and geophysics, v. 30: New York, Oxford University Press Inc., 127 p.

Wignall, P. B., 1994b, Mudstone lithofacies in the Kimmeridge Clay Formation, Wessex Basin, Southern England: Implications for the origin and controls of the distribution of mudstones—Discussion: Journal of Sedimentary Research, v. a64, p. 927–929.

Williams, J., M. A. Arsenault, B. J. Buczkowski, J. A. Reid, J. G. Flocks, M. A. Kulp, S. Penland, and C. J. Jenkins, 2007, Surficial sediment character of the Louisiana offshore continental shelf region: A GIS Compilation: USGS Open-File Report 2006-1195, 49 p. supplementary online resource, http://pubs.usgs.gov/of/2006/1195/htmldocs/images/chart.pdf

Wood, S. G., 2013, Lithofacies, depositional environments, and sequence stratigraphy of the Pennsylvanian (Morrowan-Atokan) Marble Falls Formation, central Texas, Master's Thesis, University of Texas at Austin, Austin, Texas, 276 p.

Wood, J. M., H. Sanei, M. E. Curtis, and C. R. Clarkson, 2015, Solid bitumen as a determinant of reservoir quality in an unconventional tight gas siltstone play: International Journal of Coal Geology, v. 150–151, p. 287–295.

Yang, J., K. Li, D. Zhang, and S. Liu, 1992, Petroleum geology of China, Changqing oil field: Beijing, Petroleum Industry Publishing House, 12, 490 p.

Yang, Y., W. Li, and L. Ma, 2005, Tectonic and stratigraphic controls of hydrocarbon systems in the Ordos basin: A multicycle cratonic basin in central China: AAPG Bulletin, v. 89, p. 255–269.

Yang, Z., Y. Cheng, and H. Wang, 1986, The geology of China: Oxford, Clarendon Press, 303 p.

Yao, J., X. Deng, Y. Zhao, T. Han, M. Chu, and J. Pang, 2013, Characteristics of tight oil in Triassic Yanchang Formation, Ordos Basin: Petroleum Exploration and Development, v. 40, p. 161–169.

Young, R. N., and J. B. Southard, 1978, Erosion of fine-grained marine sediments: Sea-floor and laboratory experiments: Geological Society of America Bulletin, v. 89, p. 663–672.

Yu, Y., X. Luo, Y. Lei, X. Wang, L. Zhang, C. Jiang, W. Yang, M. Cheng, and L. Zhang, 2016, Characterization of lacustrine shale pore structure: The Upper-Triassic Yanchang Formation, Ordos Basin, China: Journal of Natural Gas Geoscience, v. 1, p. 299–308.

Yuan, X., S. Lin, Q. Liu, J. Yao, L. Wang, H. Guo, H., X. Deng, and D. Cheng, 2015, Lacustrine fine-grained sedimentary features and organic rich shale distribution pattern: A case study of Chang 7 Member of Triassic Yanchang Formation in Ordos Basin, NW China: Petroleum Exploration and Development, v. 42, p. 37–47.

Zhang, T., G. S. Ellis, K. Wang, C. C. Walters, S. R. Kelemen, B. Gillaizeau, and Y. Tang, 2007, Effect of hydrocarbon type on thermochemical sulfate reduction: Organic Geochemistry, v. 38, p. 897–910.

Zhang, M., L. Ji, Y. Wu, and C. He, 2015, Palynofacies and geochemical analysis of the Triassic Yanchang Formation, Ordos Basin: Implications for hydrocarbon generation potential and the paleoenvironment of continental source rocks: International Journal of Coal Geology, v. 152, p. 159–176.

Zhang, X., C.-M. Lin, Y.-F. Cai, C.-W. Qu, and Z.-Y. Chen, 2012, Pore-lining chlorite cements in lacustrine-deltaic sandstones from the Upper Triassic Yanchang Formation, Ordos Basin, China: Journal of Petroleum Geology, v. 35, p. 273–290.

Zhang, T., J. Zhang, and K. L. Milliken, 2017, Pore size distribution of Triassic organic-rich Yanchang Formation by using N_2 adsorption isotherms: Interpretation, v. 5, p. SF41–SF61.

Zhao, W., Z. Wang, M. Chen, and H. Zheng, 2005, Formation mechanism of the high quality Upper Paleozoic natural gas reservoirs in the Ordos Basin, Acta Geological Sinica (English Edition), v. 79, p. 843–855.

Zhao, J., N. P. Mountney, C. Liu, H. Qu, and J. Lin, 2015, Outcrop architecture of a fluvio-lacustrine succession: Upper Triassic Yanchang Formation, Ordos Basin, China: Marine and Petroleum Geology, v. 68, p. 394–413.

Zou, C., X. Zhang, P. Luo, L. Wang, Z. Luo, and L. Liu, 2010, Shallow-lacustrine sand-rich deltaic depositional cycles and sequence stratigraphy of the Upper Triassic Yanchang Formation, Ordos Basin, China: Basin Research, v. 22, p. 108–125.

Supplemental Data

Data used for these studies, such as core descriptions, thin section photographs, SEM images, JMicrovision files, XRD and XRF data can be obtained from the author.